Magnetic Textures and Magnetization Reversal Processes in Arrays of Ferromagnetic and Exchange-Biased Hollow Hemispheres

Dissertation

zur Erlangung des akademischen Grades
Doktorin der Naturwissenschaften (Dr. rer. nat.)

eingereicht im Fachbereich 10 - Mathematik und Naturwissenschaften
der Universität Kassel im Mai 2022

vorgelegt von **M.Sc. Meike Reginka**

Gutachter	Prof. Dr. Arno Ehresmann
	Prof. Dr. Manfred Albrecht
Prüfer	Prof. Dr. Thomas Giesen
	Prof. Dr. Gustavo Miguel Pastor

Tag der Disputation 25. Oktober 2022

Abstract

The main objective of this thesis is to investigate hemispherical caps prepared by thin film deposition of magnetic material compositions on top of nano- and micrometer sized silica spheres. When compared to flat magnetic discs, these microcaps differ in their magnetic properties due to the curved and therefore three-dimensional shape. However, under certain conditions, both microstructures have previously been proven to express the famous magnetic vortex texture because of the confinement into a circular shape. Vortices, in which the magnetic moments curl around the object's center, are not only fundamentally studied to this day but are also traded as potential information carriers in spintronic devices.

Aside of purely ferromagnetic caps, the focus of this thesis lies on cap structures exhibiting an exchange bias (EB). This effect emerges as an additional unidirectional magnetic anisotropy due to exchange coupling when a thin antiferromagnetic and ferromagnetic material share an interface. While it is aimed to study whether the effect's characteristics known from flat bilayers are influenced when the film is structured into an array of curved microobjects, it shall also be investigated how the remagnetization of the caps - including the passing through various characteristic magnetization textures - is altered by the presence of EB. Throughout the work, the structural and magnetic properties of assembled magnetic cap arrays are experimentally studied to identify methods to tailor the exhibition of specific magnetic textures and remagnetization paths: e.g., the cap's diameter, the ferromagnetic material, the presence or absence of EB, and post-deposition treatments. But most importantly, the caps' magnetization reversal is studied in dependence on the ferromagnetic thickness which turned out to be a key parameter influencing both the EB strength and the demagnetization energy of the magnetic states expressed within the microcaps. Last but not least, it is found that the thickness of the antiferromagnetic layer determines whether the macroscopic magnetization reversal of the caps follows a biased, i.e., simply shifted hysteresis, or whether they remagnetize viscously instead.

The applied magnetic characterization techniques include magnetometry exploiting the magneto-optic Kerr effect (MOKE) and visualization techniques utilizing the X-ray magnetic circular dichroism (XMCD) in order to laterally resolve the microscopic magnetic textures on the nanoscale. Additionally, it is shown that MOKE recordings of first-order reversal curves (FORC) allow to disentangle the distribution of magnetic properties and reversal paths within the studied cap arrays. While a macroscopic measurement of the full magnetization reversal represents only the averaged characteristics of the measured cap array, the introduced FORC diagrams can not only be interpreted as magnetic fingerprints of the investigated sample/specimen, but further resolve the behavior of individual entities and cap subsets within the array.

Although the majority of the thesis studies the behavior of close-packed cap arrays, one chapter is dedicated to effects of EB in individual magnetic half shells. Herein, XMCD contrast images of single caps and dynamic cantilever magnetometry measurements in combination with micromagnetic simulations are presented. As an outlook for the potential use of magnetically functionalized particles in microfluidic applications, actuation concepts for both magnetically capped particles and superparamagnetic beads are briefly covered at the thesis' end.

Contents

Terms and Abbreviations

The following list summarizes frequently used abbreviations, terms, and symbols which are found throughout the thesis.

b	Backward/ascending hysteresis branch under increasing magnetic field
Bead	(Micro-)Particle
BMP	Biofunctionalized magnetic particle
D	Particle diameter
DCM	Dynamic cantilever magnetometry
DW	Domain wall
EB	Exchange bias (also eb)
f	Forward/descending hysteresis branch under decreasing magnetic field
FC	Field cooling
FORC	First order reversal curve
FIB	Focused ion beam
H_{ann}	Vortex annihilation field
H_{C}	Coercive field
H_{EB}	Exchange bias field shift
H_{nuc}	Vortex nucleation field
HIM	Helium ion microscope
LOC	lab-on-a-chip
L-MOKE	Longitudinal magneto-optical Kerr effect
JP	Janus Particle
M	Magnetization (usually longitudinal M)
M_{L}	Longitudinal magnetization
M_{R}	Remanent (longitudinal) magnetization
M_{T}	Transversal magnetization
MOKE	Magneto-optical Kerr Effect
MFM	Magnetic force microscopy
φ	Azimuthal angle between magnetic field and the sample's main anisotropy axis
PEEM	Photoemission electron microscope
SD	Single domain
SEM	Scanning electron microscope
SPP	Superparamagnetic particle
t_{AF}	Ferromagnetic thickness
t_{F}	Antiferromagnetic thickness
w%	Percent weight fraction
V-MOKE	Vectorial magneto-optical Kerr effect
VSM	Vibrating sample magnetometer
XMCD	X-ray magnetic circular dichroism
XPEEM	X-ray photoemission electron microscope
ZFC	Zero field cooling

1. Introduction

Over the recent three decades, the roadmap of curvilinear nanomagnetism started off with the investigations on two-dimensional curved objects such as disks,[CKA99,LLN01,PNB02,SHZ00,Shi00,GNO02] ellipses,[KKL98,WWB02,SBP08], rings,[LPN01,RKLD01,BBV02,KVLD03,LEA06,VKB06,WRZ10] and other geometries like parabolic stripes,[VKM19] where some are under investigation until today. On this journey, the reasonable next step to dive deeper towards understanding the impact of curvature on magnetism was to extend the investigated objects into the third dimension. More and more interest has developed to theoretically and experimentally study the magnetism in curvilinear three-dimensional shapes: spherical,[KSS12,KRV16,SKS13,SKS12,AHG05,ALS10,MBUS08] toroidal,[VNA16,TCSV19] tubular[BMC09,OLLV12,YAK12,SLM14,USK16] and even more complex geometries like helices[PLG14,EGR14]. These geometries exhibit non-collinear magnetic textures, like vortices, spin spirals, chiral domain walls or skyrmions[SVM17] which are not only appealing in terms of fundamental research, but may also be explored as information carriers for logic or memory devices in the field of spintronics.[BKD08,YAS21,MVK22]

Just as advanced micromagnetic models are required to theoretically approach these micro- and nanometer sized magnetic architectures with the help of numerical simulations on the one hand, it is inevitable to establish fabrication and characterization methods in order to experimentally study their magnetic characteristics on the other hand. Specifically, optical or electron beam lithography serve as fabrication techniques for flat objects but also as a prerequisite for tubes where lithographically prepared thin film patches are rolled up via strain engineering.[BMC09] Other sophisticated methods have been developed, where, e.g., glancing angle deposition allowed for the fabrication of helices[EGR14] and focused electron-beam induced deposition was successfully applied to prepare a Co double helix from a precursor gas[SHHRD20]. Furthermore, two photon lithography is a promising candidate to generate arbitrarily shaped cast molds on the micrometer scale that can be filled by a magnetic material[WHB18] or template architectures like scaffolds for subsequent magnetic film deposition[PDD20,MSvdB21]. In terms of financial expense, effort and scalability, however, all of these approaches are outperformed by the simple and fast path of combining the self-assembly of template objects with the subsequent deposition of a magnetic film. Especially, nano- or microspheres can be assembled over large sample areas, which offers a great opportunity to generate magnetic hemispherical shells in a hexagonal arrangement, e.g., by sputter deposition.[AHG05,MBUS08,ZWM09,TRH21] Depending on the layer thickness of the deposited material, these samples may either be perceived as composed of touching magnetic caps or, in the case of large thicknesses and small sphere diameters, as a magnetic film with a patterned curvature modulation.[SKR16]

Once fabricated, the nano- or microobjects need to be characterized in terms of the magnetic textures formed within and their remagnetization behavior. Typically, the magnetization is macroscopically determined during the reversal process driven by an external magnetic field, with techniques based either on magneto-optical Kerr effect (MOKE), a superconducting quantum interference device (SQUID) or vibrating sample magnetometry (VSM). These techniques deliver information on the integral magnetization, but do, however, not allow to reconstruct local microscopic magnetization textures. Here, magneto-sensitive visualization methods come into play. These include magnetic force microscopy (MFM),[Shi00,SBP08,AHG05,SKR16,ABR21] Lorentz transmission electron microscopy (LTEM),[SHZ00,SHO02,TPLH09] off-axis electron holography,[BGLB13] or MOKE microscopy[SLM14]. Additionally, techniques based on the X-ray magnetic circular dichroism (XMCD) have advanced in the recent years. Representatives are magnetic transmission X-ray microscopy (MTXM)[SHI15,Nis16,SHHRD20] or the combination of the XMCD with photoemission electron microscopy (PEEM)[SKS12,SHK14,SKR16], for which also a tomography variant has been reported[SKF15].

Focusing on assembled spherical and magnetically capped microparticles, further application potential for microfluidic lab-on-a-chip devices lies in the possibility to collect the magnetically functionalized particles from the substrate and disperse them in an anlatye liquid. Due to the particles' appearance, where one side is covered and the other is not, they have been named magnetic Janus particles, which reminds of the Roman god with two faces.[De 92] Especially Janus particles with one magnetic side and one side possessing an analyte sensitive surface functionalization, e.g., an immobilized protein, may serve as carriers for biomolecular cargo and as probes to detect biological processes.[YSG16] As an example, the detection of glucose has been realized by magnetic Janus particles to which an enzyme, i.e. a receptor, was immobilized: The biofunctionalized side catalyzes the oxidation of the target molecule glucose and the obtained reaction product is subsequently detected in a second step.[LLL15] As compared to static analytic concepts, the possibility for magnetic field driven actuation of these particles does not only enhance the probability of target-receptor contacts and thereby the sensitivity to detect a biological event,[CGS19] but also facilitates the remote-controlled transport of the collected biomaterial to a sensor unit.[LYY16,HRT21] Designing these two-sided microprobes, however, requires to build up knowledge on how to deliberately tune their magnetic behavior. For a precise motion control, this is necessary, as the magnetic characteristics of the Janus particles determine how their translatory and rotatory motion can be initiated by magnetic fields exerting magnetic force and torque, respectively.[HRT21]

It shall be emphasized that the motivation for fundamental research of magnetically capped particles branches into these different fields of applications, including both the design of magnetic probes for lab-on-a-chip purposes and the development of logic devices from precisely ordered nanoobjects exhibiting non-collinear magnetization textures for spintronics.

Therefore, this thesis aims to fundamentally study the **remagnetization processes of magnetic thin films with in-plane anisotropy shaped into the simple yet not trivial geometry of hemispherical caps**. They have proven to exhibit the magnetic vortex, onion or other non-collinear textures. In literature, individual entities of these spherical half shells have previously been explored with the help of numerical simulations .[SKS13,YKS15] The effects of

arrangement in rows[HDY09] or hexagonal arrays[VSF17,VFP16,SEG12] have mainly been simulated for magnetic disks instead of caps due to the computational effort that goes along with the spatial discretization of three-dimensional bodies. Regarding the influence of magnetostatic and exchange coupling, **micromagnetic simulations** of the angular-dependent magnetization reversal have been performed for this thesis, where a hexagonal lattice of ferromagnetic caps and a single cap are compared. In the simulations, the cap geometry, size and material was selected based on the ferromagnetic caps in the focus of the performed experiments.

Finding inspiration in experimental studies on the geometry-dependent (thickness and diameter) properties of both individual ferromagnetic caps[SKS12] and cap arrays,[SMK12,SKR16,NMK15] this thesis investigates the possibilities to tailor the thin hemispherical shells' magnetic characteristics by the **implementation of exchange bias**. The exchange bias effect arises due to exchange coupling when a thin antiferromagnetic and ferromagnetic material share an interface and is expressed as an additional unidirectional magnetic anisotropy. Besides the cap geometry, this interface effect is consequently expected to be a set screw when engineering the magnetic caps' remagnetization behavior which is governed by the sum of the prevailing anisotropic energy contributions. In this thesis, sputter deposition onto self-assembled microparticles was consequently used to fabricate ferromagnetic and exchange-biased cap arrays, where for the latter IrMn was chosen as a material with a stable antiferromagnetic order at room temperature. Hence, the magnetic characteristics of magnetic cap arrays composed of a material system prominently used in industrial applications exploiting the exchange bias can be compared to the case of purely ferromagnetic cap arrays. For both cap types, CoFe and, to a lesser extent, NiFe were used as representative ferromagnetic alloys typically exhibiting a weak and a strong intrinsic magnetic anisotropy, respectively. As a second aspect, the experimental studies performed within the present thesis investigate whether the curvature of the cap may in turn affect the expression of the exchange bias as compared to flat bilayers. Especially, changes in the remagnetization behavior related to the **variation of the participating layers' thicknesses** are in the focus of the presented studies. The fact that the thickness of a ferromagnetic cap already crucially affects its remagnetization process[NMK15] adds complexity to these thickness dependencies, which are well reported for flat and extended exchange-biased systems in literature.[MKS87,RZ07,MRH22] Further aiming to modify the exchange bias in the caps, different **post-deposition annealing** procedures will be discussed being popularly employed to set or modify the strength as well as the direction of the associated unidirectional anisotropy.

In terms of characterization, mainly MOKE magnetometry is used to differentiate the arrays' macroscopic **magnetization reversal processes** by either recording the samples' major loop or by analyzing first-order reversal curves additionally addressing microscopic magnetic states that are enclosed by the complete hysteresis. In contrast, XMCD-PEEM images have been acquired to microscopically **visualize magnetization configurations** in the individual caps situated in an array in dependence on the sample's magnetic history. Because the exchange bias in polycrystalline systems - that are naturally formed in the case of sputter deposition - crucially depends on the **film's microscopic structure** and granularity, helium ion microscopy is utilized to study the caps' surface in comparison with the flat system. As an additional magnetic characterization technique, dynamic cantilever magnetometry is introduced to measure

the **hysteresis loop of single caps**, both ferromagnetic and exchange-biased. With an outlook towards applications, Janus particles are collected from the particle arrays capped with an exchange bias bilayer in order to demonstrate their capability to be actuated to perform a **rotational motion** driven by external magnetic fields.

Altogether, this thesis aims to experimentally as well as theoretically investigate the magnetization reversal of individual but mainly arrays of assembled ferromagnetic and exchange-biased caps in order to identify characteristic magnetic textures and remagnetization paths. Subsequent to structural investigations, magnetic characterization techniques are applied that do not only probe the macroscopic magnetization reversal, but also allow to visualize the laterally resolved microscopic magnetic textures of the caps. Furthermore, first-order reversal curves are recorded and analyzed with the help of an established mathematical formalism to disentangle the distribution of magnetic properties and reversal paths within the studied arrays. While a macroscopic measurement of the magnetization reversal represents only the averaged characteristics of the whole measured magnetic cap array, the presented FORC diagrams can be interpreted as magnetic fingerprints resolving the behavior of individual entities within the array. Finally, the complementary use of different magnetic and structural characterization techniques in combination with micromagnetic simulations shall contribute to a better understanding of the remagnetization behavior of ferromagnetic and exchange-biased caps assembled in an array and eventually sketch possible routes to engineer their - but also other three-dimensional structure's - magnetic textures and remagnetization paths.

2. Magnetism

Throughout this first chapter, fundamentals of magnetism shall be introduced in view of extended thin films and micro- or nanostructured objects. In section 2.1, magnetic anisotropies will be discussed in the scope of the micromagnetic description. Next, the process of a magnetic object's magnetization reversal is described in section 2.2. In section 2.3, the origin of magnetic domains is discussed alongside a model for a single-domain body, before the focus is changed to the phenomenology and modeling of exchange bias - as an important anisotropy for this work - in section 2.4.

2.1 Micromagnetic Description and Magnetic Anisotropies

In order to theoretically study the magnetization processes of a magnetic object on the micron scale, the micromagnetic description offers a mesoscopic approach: The equilibrium state of the magnetization is found by minimizing the torque that is exerted by an effective magnetic field $\vec{H}_{\mathrm{eff}}$ arising from the sum of all energetic contributions.[HS98,Abe19] The magnetization dynamics of a magnetic material, i.e. its temporal evolution, can be described by the Landau-Lifschitz-Gilbert equation, which describes the temporally resolved motion of the magnetization in an effective field. In short, the magnetization performs a precessional motion around $\vec{H}_{\mathrm{eff}}$ which is combined with the dissipative motion towards $\vec{H}_{\mathrm{eff}}$. However, for the calculation of the magnetization in the case of static problems it is sufficient to minimize the system's total free energy. One example is the computation of hysteresis curves via steepest-descent methods, where for each applied step of a magnetic field sequence the nearest local energy minimum needs to be found by adjusting the magnetization configuration with respect to the previous field step.[Abe19] Energy contributions that are typically considered in the micromagnetic description of a ferromagnetic system shall be introduced in the following:

Starting from classical electromagnetics, a magnetic object in an external magnetic field $\vec{H}_{\mathrm{ext}}$ has the **Zeeman energy**

$$E_{\mathrm{Z}} = -\mu_0 M_{\mathrm{s}} \int \vec{m} \cdot \vec{H}_{\mathrm{ext}} \, \mathrm{d}V \tag{2.1.1}$$

with the vacuum permeability μ_0, the saturation magnetization M_{s} and the vector field $\vec{m} = \vec{M}/M_{\mathrm{s}}$, describing the magnetization contribution.

As a second contribution, the so-called **exchange energy** is added. A ferromagnet can exhibit - in contrast to paramagnetic materials - a remanent magnetization at room temperature that does not vanish in the absence of a magnetic field, i.e. it possesses a magnetic order. This collective order of the magnetic moments occurs for temperatures below the ordering temperature of the material, while above paramagnetic behavior is found. The ordering temperature of ferromagnets is called CURIE temperature T_C and it is named NÉEL temperature T_N in the case of antiferromagnets.[BKS05] The occurrence of this long-range collective magnetic ordering is mediated by the exchange interaction, which is a quantum mechanic effect based on the fact that electrons as fermions are indistinguishable. The associated PAULI's exclusion principle requires that the total wave function of an electronic system is antisymmetric upon the particles' exchange. Hence, the total wave function of two neighboring electrons needs to be a combination of a symmetric spatial function with an antisymmetric spin function or a vice versa, which results in singlet ($\uparrow\downarrow$ or $\downarrow\uparrow$) or triplet states ($\uparrow\uparrow$ or $\downarrow\downarrow$). For triplet spin orientation, the spatial wave functions are forbidden to coincide and as a consequence the spatial separation of two electrons sharing the same spin reduces the COULOMB interaction.[Get08] However, this enhances the kinetic energy by the necessity of the electrons to occupy higher energetic levels. Consequently, the parallel spin alignment mediating ferromagnetism is only favored if the COULOMB energy reduction exceeds this kinetic energy increase, otherwise an antiferromagnetic ordering is observed.[BKS05]

The exchange coupling in solid state materials can be addressed by the isotropic HEISENBERG model with the Hamiltonian

$$\mathcal{H} = -\sum_{ij} J_{ij}\, \mathcal{S}_i \cdot \mathcal{S}_j \tag{2.1.2}$$

summing up all exchange interaction contributions of nearest neighbor spins i, j with the exchange integral $J_{i,j}$ for all pairs of spinvectors $\mathcal{S}_i$ and $\mathcal{S}_j$.[Get08] Here, positive J result in ferromagnetic and negative J in antiferromagnetic coupling.[BKS05]

The exchange energy can be expressed via the material specific and temperature dependent exchange constant A determined by J:[HS98]

$$E_\mathrm{ex} = A \int (\nabla \vec{m})^2 \,\mathrm{d}V. \tag{2.1.3}$$

As the exchange interaction tends to orient neighboring magnetic moments parallel for positive J, it can macroscopically be understood as a stiffness favoring uniform magnetization, which is reflected by synonymously using the term exchange stiffness constant for A.[HS98]

When introducing the **stray field energy** (or demagnetization energy) as a third energetic contribution, the origin of magnetic stray fields needs to be determined. In general, the magnetization $\vec{M}$ of a sample and the demagnetization field $\vec{H}_\mathrm{d}$ relate to the magnetic flux density $\vec{B} = \mu_0 \vec{H}_\mathrm{d} + \vec{M}$ inside the sample volume. With MAXWELL's equation $\mathrm{div}\vec{B} = 0$, describing that the field of a magnetic flux is divergence free in the absence of electric currents, it becomes apparent that any divergence in $\vec{M}$ has to create a magnetic field H_d determined by[HS98,Abe19]

$$\mu_0 \mathrm{div}\vec{H}_\mathrm{d} = -\mathrm{div}\vec{M}. \tag{2.1.4}$$

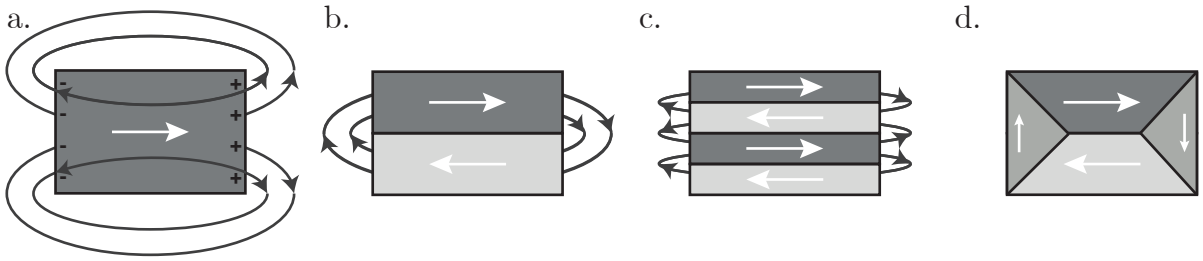

Figure 2.1: Formation of magnetic domains as a consequence of stray field minimization with magnetization vectors (white) and stray field lines (black). From left to right the stray field energy is reduced, whereas the exchange energy increases. d presents a flux-closure pattern that is also called *Landau* state which occurs in low anisotropic materials, whereas high anisotropic materials would form the open domain structures b and c. If the exchange stiffness is much more dominant than all other contributions, the ferromagnet would remain in the monodomain state a.

The sources and sinks of this auxiliary demagnetization field can be interpreted as magnetic charges, as depicted in figure 2.1 a. Unlike electric charges, these can never be isolated but always appear balanced by opposing charges. The demagnetization energy is given by: [Abe19,HS98,Get08]

$$E_{\mathrm{d}} = -\frac{\mu_0}{2} \int \vec{H}_{\mathrm{d}} \cdot \vec{M} \, \mathrm{d}V. \tag{2.1.5}$$

Only in a spherical body with zero magnetocrystalline anisotropy (s. below) the demagnetization energy would be isotropic, whereas any other shape results in one (e.g. in a wire) or more directions along which magnetizing the sample is energetically favored. [Get08] This is called shape anisotropy and is very well known from thin magnetic films favorably exhibiting in-plane magnetization configuration. For an infinitely extended xy-plane the demagnetization energy can be expressed by

$$E_{\mathrm{d,plate}}(\theta) = \frac{\mu_0}{2} \cdot M^2 \sin^2 \theta \tag{2.1.6}$$

in dependence of the polar angle θ between $\vec{M}$ and the z-axis. [Get08] While it may be possible to analytically express the demagnetization energy for this and other rather simple geometries, stray field calculations become too complex for arbitrary shapes, which makes numerical calculations based on finite-element or finite-difference methods inevitable. However, Equation 2.1.6 is comparable to a uniaxial anisotropy, hence the term

$$K_{\mathrm{d}} = 1/2 \cdot \mu_0 \cdot M^2 \tag{2.1.7}$$

can be extracted as a parameter which can be compared with anisotropy constants in the case of thin magnetic films. [HS98]

The magnetocrystalline anisotropy representing the fourth energy contribution describes that a single crystalline ferromagnet's energy depends on the orientation of $\vec{M}$ with respect to the materials structural axes typically determined by the crystal lattice, which results from the spin-orbit interaction. [HS98] The electronic orbitals of different shape are aligned with the crystallographic axes of the material. When the exchange-coupled electronic spins are rotated, a

torque is exhibited on the orbital moments due to spin-orbit coupling. However, in transition metals the distribution of d-electrons, that cause the ferromagnetic behavior, is anisotropic which makes the orientation of orbital moments direction depended, and, consequently results in a changed overlap of wave functions of neighboring atoms when they are rotated.[BKS05] Hence, the spin-orbit coupling causes the directional dependence of the ferromagnet's free energy and the orientation of the magnetization is energetically preferred along certain axes of the crystallographic structure, called easy axes. This is expressed in the **magnetocrystalline anisotropy energy**. Generally, the magnetization direction of a magnetic moment can be expressed by

$$\vec{m} = \begin{pmatrix} \alpha_x \\ \alpha_y \\ \alpha_z \end{pmatrix} = \begin{pmatrix} \cos\theta\cos\varphi \\ \cos\theta\sin\varphi \\ \sin\theta \end{pmatrix} \tag{2.1.8}$$

with $\vec{m}^2 = 1$ and the polar angle θ reaching 0 at the equator in the respective spherical coordinate system.[HS98] Based on this definition of direction cosines α_x, α_y and α_z, it is common to define the magnetocrystalline anisotropy energy $\mathcal{E}_{\mathrm{an}}$ by a power series expansion at α_i with $i = x$, y and z. Since there is no energy difference between opposite magnetization directions, excluding odd terms yields:

$$\mathcal{E}_{\mathrm{an}} = \mathcal{E}_0 + \sum_{ij} b_{ij}\alpha_i\alpha_j + \sum_{ijkl} b_{ijkl}\alpha_i\alpha_j\alpha_k\alpha_l \tag{2.1.9}$$

In a cubic crystal it becomes

$$\begin{aligned} \mathcal{E}_{\mathrm{an,cub}} =& K_{\mathrm{c0}} + K_{\mathrm{c1}}(\alpha_x^2\alpha_y^2 + \alpha_x^2\alpha_z^2 + \alpha_y^2\alpha_z^2) + K_{\mathrm{c2}}\alpha_x^2\alpha_y^2\alpha_z^2 \\ =& K_{\mathrm{c0}} + (K_{\mathrm{c1}} + K_2\sin^2\theta)\cos^4\theta\cos^2\varphi\sin^2\varphi + K_{\mathrm{c1}}\cos^2\theta\sin^2\theta, \end{aligned} \tag{2.1.10}$$

with magnetocrystalline anisotropy constants K_{ci} that are functions of the coefficients b_{ij} and b_{ijkl},[Get08,HS98] where the lower line of the equation indicates the directional dependence. Cubic crystals may have easy directions along the $< 100 >$ axes or the $< 111 >$ axes, where the first case is described by a positive sign of K_{c1} and the latter by a negative.[HS98] In magnetic films with dominant in-plane shape anisotropy, Equation 2.1.10 can furthermore be simplified, as $\theta = 0$:

$$\mathcal{E}_{\mathrm{an,cub,ip}} = K_{\mathrm{c0}} + K_{\mathrm{c1}}\sin^2 2\varphi. \tag{2.1.11}$$

However, in three-dimensional magnetic films, like magnetic cap structures the shape anisotropy does not allow for this simplification, as it may favor orientations different from the xy-plane. From the sine's argument in Equation 2.1.11 the biaxial character of the anisotropy becomes readily obvious. Both, in ferromagnets and antiferromagnets, magnetocrystalline anisotropy is found. Note, that this cubic anisotropy can be superposed with a stronger uniaxial term,[HS98]

$$\mathcal{E}_{\mathrm{u}} = K_{\mathrm{u0}} + K_{\mathrm{u1}}\sin^2\gamma + K_{\mathrm{u2}}\sin^4\gamma \tag{2.1.12}$$

that depends on the angle γ between an **induced anisotropy** axis and the magnetization direction. Such an induced anisotropy can for example be initialized when an alloy sample has undergone a treatment like annealing/heating in an applied magnetic field.[CG97] Annealing the famous face-centered-cubic (fcc) structured alloy Permalloy (Py), $Ni_{80}Fe_{20}$, which typically exhibits a neglectable anisotropy ($K_{c1} \approx 0$), in an external magnetic field can induce a uniaxial anisotropy with $K_{u1} \approx 140\,\mathrm{J/m^3}$.[CO55] At temperatures below the ferromagnet's Curie temperature, the alloy's randomly distributed atoms are thermally activated and undergo diffusion within the lattice. The external magnetic field causes a reorientation of the atomic positions favoring field-aligned pairs of iron atoms, which results in an order that is kept during the cool down of the sample.[Coe10a] In polycrystalline samples a similar structure can be initialized when the film deposition is performed in an external magnetic field.[Coe10a]

Often, the strength of magnetic anisotropy is given by a material parameter $Q = K/K_d$ as the ratio between the predominant anisotropy constant and the stray field energy constant. High-anisotropic and low-anisotropic materials materials are characterized by $Q \gg 1$ and $Q \ll 1$, respectively.[HS98]

In exchange-biased systems a ferromagnetic thin film shares an interface with an antiferromagnet. The resulting exchange bias, which will be discussed in detail in section 2.4, adds an **exchange bias energy** contribution in the form of a unidirectional anisotropy:[NS99]

$$\begin{aligned} E_{EB} &= -\int J_{EB}\,\cos(\alpha)\,\mathrm{d}S \\ &= -\mu_0 M_S \int \vec{H}_{EB}\cdot\vec{m}\,\mathrm{d}V, \end{aligned} \tag{2.1.13}$$

with the unidirectional anisotropy constant J_{EB} and the angle α between the anisotropy axis and the ferromagnet's magnetization. While the previously introduced energy contributions were given as volume integrals over an energy density, the exchange bias as an interface effect finds its representation by the integration of the energy area density over the shared interface S. Alternatively, a volume integral (lower line of Equation 2.1.13) can be defined for the ferromagnet's vector field of magnetization directions $\vec{m}$ inside the exchange bias field $\vec{H}_{EB}$ as an effective field describing the unidirectional character in a similar manner like for the Zeeman term (cf. Equation 2.1.1).

Finally, the sum of all contributions in a thin film system of cubic crystallinity can be summed, when neglecting magnetoelastic effects:[HS98]

$$\begin{aligned} E_{tot} = \int [&-\mu_0\vec{H}_{ext}\cdot\vec{M} + A(\nabla\vec{m})^2 + \frac{\mu_0}{2}\vec{H}_d\cdot\vec{M} \\ &+ F_{an}(\vec{m}) - \mu_0\vec{H}_{EB}\cdot\vec{M}]\,\mathrm{d}V. \end{aligned} \tag{2.1.14}$$

Note, that $F_{an}(\vec{m})$ collects all energy density contributions from magnetocrystalline and induced anisotropy.

As numerical computations based on the micromagnetic description require a discretization of the magnetic object's volume, it is assumed that the magnetic moments are aligned parallel on a

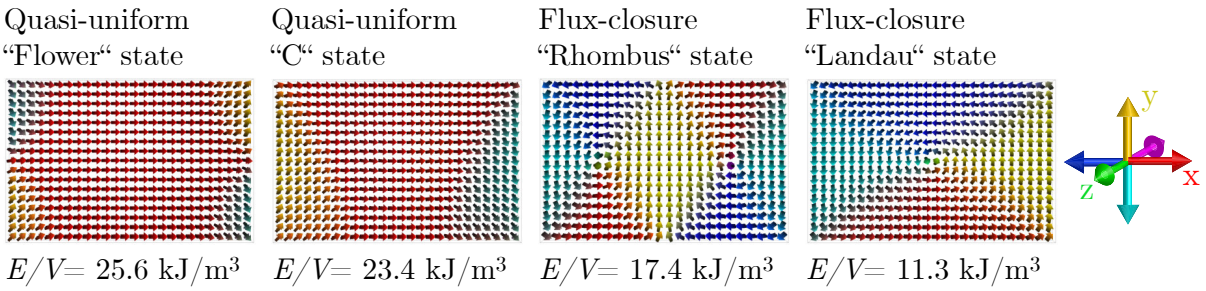

Figure 2.2: Possible magnetization textures in soft-magnetic rectangles (230 nm x 350 nm) with a thickness of 30 nm obtained by micromagnetic simulations conducted with the software *Boris*.[Lep20] The resulting total energy density, taking the stray field energy and the exchange energy into account, is shown for all configurations. For the chosen dimensions, the energy is minimized in the Landau state.

characteristic length scale, which is taken as the maximum width (length, height) of one cell within the discretized volume. More precisely, correctly resolving structures like a domain wall requires a discretization beyond the material's so-called exchange length

$$l_{\mathrm{ex}} = \sqrt{A/K_{\mathrm{eff}}} \tag{2.1.15}$$

with the effective anisotropy constant K_{eff} and the exchange coupling constant A.[Abe19] K_{eff} is usually taken as the sum of K_{d} and the magnetocrystalline anisotropy constant K_{u}.[Abe19]

Exemplary magnetic textures have been simulated for a 30 nm thick Py rectangle (230 nm x 350 nm) with the micromagnetic simulation package *Boris Computational Spintronics*[Lep20] and are presented in Figure 2.2. For simplicity, only the stray field energy and the exchange energy have been considered with a discretization of the volume into cells with dimensions of $(5\,\mathrm{nm})^3$. From the resulting total energy densities it becomes obvious that the rectangular object will decompose into magnetic domains. Towards larger sizes the rhombus state becomes energetically more relevant while the quasi-uniform states can be found in rectangles of small dimensions, i.e. they are energetically favored in a rectangle of the same thickness and aspect ratio but the dimensions 50 nm x 75 nm. Similar examples for another aspect ratio are presented in Ref. [Get08]. The origin of domains and the respective limits for homogeneously magnetized single-domain states shall be further discussed in section 2.3.

2.2 Magnetization Reversal

Ferromagnets are susceptible to magnetic fields, which means that their magnetization can be changed by applying a magnetic field. In order to observe how this affects a ferromagnetic specimen, magnetization reversal curves are usually recorded as the magnetization's projection onto the direction of an applied magnetic field, while it is altered. Due to the formation of domains within a ferromagnet the reversal may be complex, as different processes take place.[CG97] A demagnetized material, that has $M = 0$ as it decomposed into domains to reduce its stray field energy, is magnetized when a magnetic field is applied as seen in the virgin curve in Figure 2.3 until it reaches saturation, i.e. $M = M_{\mathrm{S}}$. From here, the magnetization follows the often called

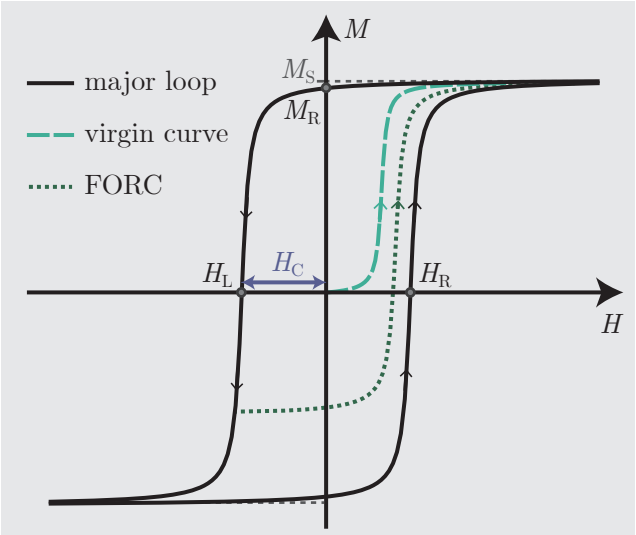

Figure 2.3: Schematic hysteresis curve $M(H)$. A major loop (continuous line) is recorded by ramping the magnetic field that saturates the ferromagnet (M_S) to zero and then inverting it to reach negative saturation ($-M_S$). The virgin curve (dashed line) indicates how a previously demagnetized body is magnetized.

descending or *forward* hysteresis branch: when decreasing the magnetic field to zero, a residual magnetization of the ferromagnetic material remains, called remanent magnetization M_R. Upon lowering the magnetic field to negative values, the magnetization first reaches zero at a magnetic field $H = H_L$, which in this case is the coercivity, before it again reaches saturation ($M = -M_S$) at large enough magnetic fields. When again increasing the magnetic field towards the positive direction, the magnetization follows the *ascending* or *backward* branch. In general, different remagnetization processes may contribute to the ferromagnet's **major reversal loop**:

- *coherent rotation*: Magnetic moments rotate coherently and the magnetization changes continuously.
- *nucleation*: Small domains with a magnetization that opposes the surrounding are formed.
- *domain wall motion*: Nucleated domains grow via the propagation of their domain walls.

For objects of circular geometry three processes may be added (discussed later in section 3.1):

- *vortex nucleation*
- *motion of the vortex core*
- *vortex annihilation.*

While some of the named transitions like vortex core motion and coherent rotation are reversible processes, nucleation processes are highly irreversible. In order to study the reversibility of the transitions throughout the full major loop, **minor loops** can probe portions of the reversal. [RSB03] For these measurements, the magnetization is measured up to a magnetic field with an absolute value smaller than the saturating field. [NSL05]

2.2.1 First-Order Reversal Curves

A specific type of minor loop is the so-called first-order reversal curve (FORC). Here, the magnetization is first driven from the specimen's positive saturation towards a *reversal* field H_{rev} on the descending branch. A FORC as shown in Figure 2.3 is then the ascending magnetization curve recorded when monotonically increasing the magnetic field from H_{rev} until positive saturation is again reached.[RHZ14] Typically, a family of FORCs with evenly varied H_{rev} is measured, where the individual curves fill the interior of the major loop.[DLR07] The magnetization data $M(H_{\mathrm{rev}}, H_{\mathrm{ext}})$ at consecutive magnetic fields on consecutive FORCs may be used to determine the FORC distribution commonly defined as

$$\rho(H_{\mathrm{rev}}, H_{\mathrm{ext}}) = -\frac{1}{2}\frac{\partial^2 M(H_{\mathrm{rev}}, H_{\mathrm{ext}})}{\partial H_{\mathrm{rev}} \partial H_{\mathrm{ext}}}, \tag{2.2.1}$$

which is a mixed second derivative defined for $H_{\mathrm{rev}} \leq H_{\mathrm{ext}}$.[RHZ14,DLR07] The FORC distribution is then plotted using a false color map as a function of the two coordinates H_{rev} and H_{ext}. These FORC diagrams are often referred to as magnetic *fingerprints* or *signatures* because irreversible switching processes may be identified where $\rho(H_{\mathrm{rev}}, H_{\mathrm{ext}})$ takes non-zero values, while purely reversible components correspond to $\rho(H_{\mathrm{rev}}, H_{\mathrm{ext}}) = 0$.[DLR07] With the help of FORC diagrams it is possible to distinguish different magnetization processes within one sample that consists of magnetic entities with varying properties which is often unfeasible from the sole analysis of ensemble averaged major hysteresis loops. Hence, FORC is often used in paleomagnetism to study the magnetic compartments in rocks or sediments, where it was even shown possible to identify remains of magnetotactic bacteria.[RHZ14] On the other hand, FORC is a useful tool to study magnetic recording media or other samples composed of magnetic entities like dot, pillar or particle arrays.[DLR07,PRS05,GYV15,BRG13]

In order to determine the FORC distribution ρ at each measured data point $M(H_{\mathrm{rev}}, H_{\mathrm{ext}})$, a second-order polynomial is fitted numerically using a local grid of $N = (2 \cdot SF + 1)^2$ points around $(H_{\mathrm{rev}}, H_{\mathrm{ext}})$ specified by the smoothing factor SF. For this, a least-squares fit of the polynomial

$$a_1 + a_2 \cdot H_{\mathrm{rev}} + a_3 \cdot H_{\mathrm{rev}}^2 + a_4 \cdot H_{\mathrm{ext}} + a_5 \cdot H_{\mathrm{ext}}^2 + a_6 \cdot H_{\mathrm{rev}} \cdot H_{\mathrm{ext}} \tag{2.2.2}$$

with the fit parameters a_i to the data within the chosen fit space allows a direct extraction of the FORC distribution via $\rho(H_{\mathrm{rev}}, H_{\mathrm{ext}}) = -a_6/2$, because a_6 represents the mixed second order derivative of the polynomial itself as defined in Equation 2.2.1. The fit space may either be a square grid or an arbitrarily shaped region of N nearest neighbors in which the data points are weighted depending on their distance to the evaluated point in order to assign higher importance to closer points.[RHZ14,MHR21] Accordingly, small SF values may result in noisy distributions whereas high values may smooth the data so strongly that key features can get lost.[RHZ14]

Two types of representation for FORC diagrams are usually found in literature: Either the triangular shaped $\rho(H_{\mathrm{rev}}, H_{\mathrm{ext}})$ or the distribution $\rho(H_{\mathrm{i}}, H_{\mathrm{C}})$, i.e. the distribution of local

interaction (or bias) fields and local coercive fields, H_i and H_C, is depicted.[RHZ14] For the latter, the coordinate system is rotated counterclockwise bv 45° using the transformation of H_ext and H_rev to $H_\mathrm{i} = (H_\mathrm{ext} + H_\mathrm{rev})/2$ and $H_\mathrm{C} = (H_\mathrm{ext} - H_\mathrm{rev})/2$.[DLR07,MHR21]

2.3 The Emergence of Magnetic Domains

In macroscopic samples, the formation of areas with parallel aligned magnetization, so-called domains separated by boundaries called domain walls, is observed, which is a result of the competing energy terms contributing to the ferromagnet's total free energy. In order to reduce the stray field energy, a magnetic system favors a demagnetized state, if it was only subjected to dipole-dipole interactions.[Abe19] However, as discussed in section 2.1, the exchange energy prefers a parallel alignment of magnetic moments and the magnetocrystalline anisotropy prefers the orientation of magnetic moments along specific anisotropy axes. Consequently, a magnetic state will be occupied which minimizes the sum of all energy contributions. This typically results in different magnetic domain patterns as shown in Figure 2.1.

The formation of domains causes the emergence of domain walls, in which the magnetization direction transitions between the orientations of two adjacent domains. In an infinite medium, two domains of opposite magnetization are separated by a 180° wall in which the magnetic moments can either rotate around an axis perpendicular to the wall plane, which is called a *Bloch wall*, or they rotate around an axis that lies within the wall plane, which is referred to as *Néel wall*. In contrast to an infinite material, where a Bloch wall is stray-field free and is therefore energetically favored, thin magnetic films with an in-plane anisotropy usually form Néel walls, if the film thickness is comparable to the wall width.[HS98] For both types, the rotation sense within the wall can be energetically degenerate, so that substructures in the walls may be formed that are divided by so-called *Bloch lines*.[HS98]

In general, a simple expression of the domain wall width can be found being proportional to $\sqrt{A/K}$, where a high anisotropy constant K favors thinner walls and a high exchange constant A results in wider walls. When a magnetic object is reduced in its dimensions, the energy associated with the domain walls increases in importance within the total energy due to its dependence on the wall area, i.e. there exists a critical single-domain (SD) size below which no domains are formed.[HS98] For small objects with low anisotropies, this critical size determines the transition from high-remanence or single-domain configuration of the object's magnetization to a low-remanence state above l_SD which is the prominent stray-field reducing vortex texture, where the magnetization curls around the center (further discussed in section 3.1). Micromagnetic computations revealed single-domain sizes l_SD for soft magnetic objects that scale with the factor $\Delta_\mathrm{d} = \sqrt{A/K_\mathrm{d}}$ and define the edge length of an equivalent cube with the object's volume: $l_\mathrm{SD} \approx 7\Delta_\mathrm{d}$ was found for cubic geometry and $l_\mathrm{SD} \approx 4\Delta_\mathrm{d}$ for spheres.[HS98] Elongating the object was further found to cause higher l_SD.[Aha88]

2.3.1 Hysteresis of a Single-Domain Magnetic Body

When working below the single-domain limit, it is a valid approach to model the free energy of a single-domain particle by a so-called Stoner-Wohlfarth approach, as the ferromagnet is

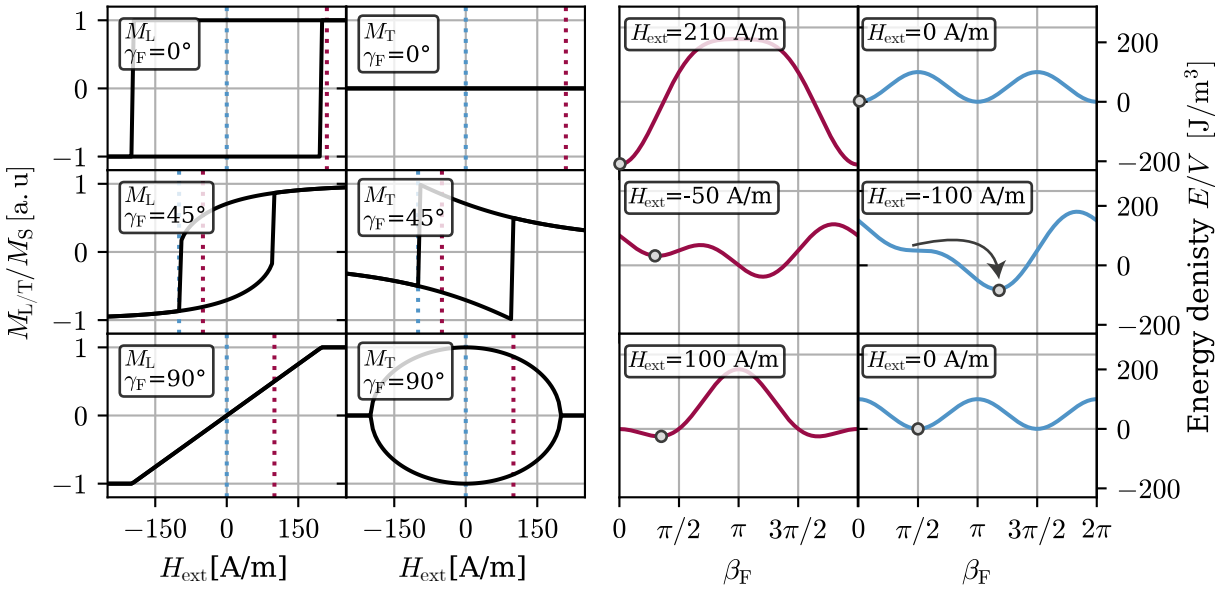

Figure 2.4: Magnetization reversal curves (left) calculated using a STONER-WOHLFARTH approach for three different angles between the magnetic field and anisotropy axis, defined by the angles $\alpha_{ext} = 0°$ and $\gamma_F = 0$, 45° and 90°: The magnetization components along and perpendicular to the applied field axis (M_L, M_T) are derived by minimizing the energy density in Equation 2.3.1 with respect to the magnetization angle β_F. The respective course of the energy density is shown for specific magnetic fields (indicated by the dashed lines on the left), whereby the circles point to the populated minimum. While a typical easy axis curve results for $\gamma_F = 0°$, a hard axis is found at $\gamma_F = 90°$.

suspected to reverse its magnetization only via coherent rotation and that no domains nucleate and extend throughout the body. Assuming all moments are aligned parallel, allows to neglect exchange energy and to describe the magnetization, the anisotropy axes and the external field orientation via the angles β_F, γ_F and α_{ext} with respect to the chosen coordinate system. [SW48] The free energy of the ferromagnet with a volume V_F is described by a Zeeman term, representing the potential energy of the magnetization inside H_{ext}, and a term considering a uniaxial anisotropy K_F which may include magnetocrystalline, induced and shape anisotropies: [SW48]

$$E = -\mu_0 M_s V_F H_{ext} \cos(\beta_F - \alpha_{ext}) + K_F V_F \sin^2(\beta_F - \gamma_F). \tag{2.3.1}$$

Minimizing Equation 2.3.1 with respect to β_F allows for the simulation of hysteresis loops upon variation of H_{ext}, i.e. magnetization reversal processes. For magnetic fields that do not saturate the ferromagnet, two minima are found due to the uniaxial anisotropy character. However, the ferromagnet's orientation is kept in the minimum populated in the previous step of the magnetization history and β_F can be chosen for each next field step such that it is not allowed to overcome the energy barrier between the two minima by excluding external energy inputs like thermal fluctuations. Hence, the magnetization only switches to the global energetic minimum when the second derivative of the energy changes from being positive (before switching) to or below zero. Based on the preceding description, magnetic reversal curves for a material with $K_F = 100$ J/m^3 are presented in Figure 2.4. The magnetization reversal curves with $M_L/M_s = \cos(\beta_F)$, $M_T/M_s = \sin(\beta_F)$ and the angular dependence of the energy for

specific magnetic fields are shown for three orientations of the anisotropy axis with the azimuths $\gamma_F = 0$, 45° and 90°. Typically, M_L is referred to as the longitudinal and M_T as the transversal magnetization component. Easy axis reversal curves at $\gamma_F = 0°$ are hysteretic, meaning M_x has two different remanent magnetizations, which refers to the two states at zero magnetic field, and symmetric switching fields, while the hard axis reversal at $\gamma_F = 90°$ shows purely rotational behavior and M_L at zero field is independent of the magnetic field history.

2.4 Exchange Bias

The exchange bias (EB) effect, as already shortly introduced by its energy contribution (Equation 2.1.13) for the micromagnetic description, was first reported in 1956 by Meiklejohn and Bean.[MB56] They had observed a lateral shift of the ferromagnetic hysteresis loop of oxidized Co nanoparticles after cooling the sample inside an external magnetic field down to a temperature of 77 K, which is below the oxide's Néel temperature T_N.[MB56] The horizontal shift H_{EB} is named EB shift and can be perceived as an additional effective magnetic field, which affects the ferromagnet's magnetic moments at the interface shared with an antiferromagnetic material (e.g. CoO). Besides, they observed an increase in the sample's coercivity H_C.[MB56] Both, H_{EB} and H_C can be extracted from experimental magnetization reversal loops via the intersections H_L and H_L of the hysteresis with the external magnetic field axis:

$$H_{EB} = \frac{H_L + H_R}{2} \ , \ H_C = \frac{H_L - H_R}{2}. \tag{2.4.1}$$

The origin of the effect lies in the exchange interaction of magnetic moments at the common interface of the ferromagnetic and the antiferromagnetic material. The antiferromagnet has a very low susceptibility and (neglecting uncompensated moments) no macroscopic net magnetization, and hence, it is unaffected by external magnetic fields. Consequently, for rectangular shaped easy axis hysteresis curves the ferromagnet may exhibit only one remanent magnetization if $|H_{EB}|$ is greater than H_C. This unique feature renders EB systems very useful in applications for magnetic recording media and magnetic sensing technologies.[NS99] A prominent example are spin valves in read heads of magnetic hard disks that exploit the giant magnetoresistance (GMR) effect for the detection of stray fields from the hard disk (which determines the stored information) and make use of an EB bilayer as a reference electrode.[Was12,Get08]

The initialization of the effect in antiferromagnet/ferromagnet bilayers is done either by applying an external magnetic field during the system's deposition process or by an annealing process after the fabrication, often referred to as field cooling (FC). As depicted in Figure 2.5, the EB system with $T_C > T_N$ is heated to a temperature $T_C > T > T_N$, for which the ferromagnetic spins align in an applied magnetic field, whereas the antiferromagnet enters a paramagnetic state. Saturating the ferromagnet while cooling down will result in a parallel alignment of the antiferromagnetic moments with respect to the neighboring ferromagnetic moments at the interface due to exchange interaction, building up an antiferromagnetic order throughout the antiferromagnetic layer exhibiting uncompensated moments at the interface.[RZ07] Reversing the ferromagnetic magnetization will now acquire higher magnetic fields, as their coupling to the antiferromagnetic moments needs to be overcome. Consequently, an effective torque acts on the

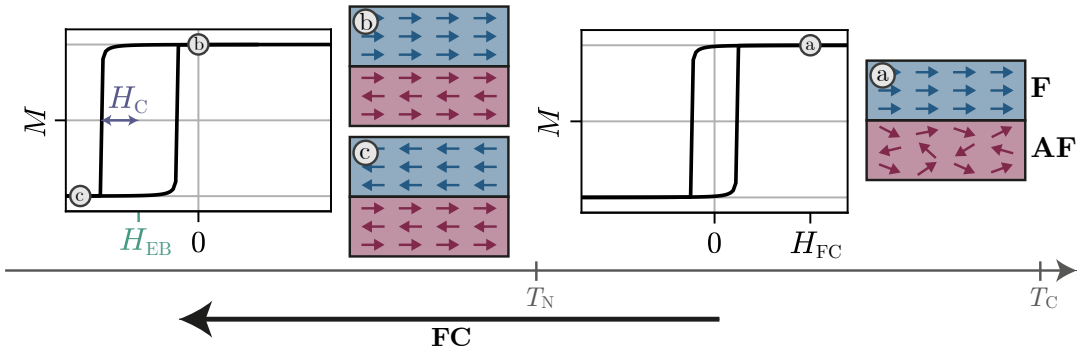

Figure 2.5: Schematic depicting the field cooling (FC) process of an EB bilayer system, with the magnetic moments of the ferromagnetic layer (blue) and antiferromagnetic layer (red), from right to left: a) Above T_N the antiferromagnet is in a paramagnetic state and the ferromagnet's magnetization curve is symmetric with respect to zero magnetic field. During the process, the sample is cooled below T_N (arrow), while the ferromagnet is saturated by H_{FC}. b) After FC, the ferromagnetic moments are exchange coupled to the uncompensated antiferromagnetic interface moments. c) When a negative external magnetic field with $|H_{ext}| > |H_{EB}| + H_C$ is applied, the ferromagnet's magnetization can be reversed. Note, that in this simplified picture the antiferromagnetic moments are purely rigid and cannot realign during the ferromagnet's reversal. Inspired by [RZ07].

ferromagnetic moments if the ferromagnetic magnetization is not aligned with the direction of the EB. This direction is defined by the external field applied during FC, and hence, the macroscopic hysteresis is shifted by H_{EB} which takes negative values. [RZ07] Again heating the sample to above T_N will cause the shift to vanish and by repeating the procedure, the EB direction can be redefined.

As an alternative, the annealing procedure can be realized via the bombardment of an EB sample with light ions in an external magnetic field. [MPF01] For instance, He+ ions with energies in the keV regime can be used to modify the EB locally, i.e. only in the irradiated region. In combination with lithographic masks, this allows to create microstructured patterns with areas of different EB directions and consequently different remanent magnetization. [EEW06] Based on this, magnetic domain patterns generating specific magnetic stray field landscapes can be designed which can subsequently be used as topographically flat substrates by which the motion of magnetic particles can be controlled in microfluidic applications. [HKB15,EKH15,HRT21] These domain patterns are therefore promising candidates for lab-on-a-chip applications in which bio-functionalized magnetic particles are utilized as catchers and carriers for biological analytes such as antibodies. [EKH15,RLL16]

An often observed effect when performing consecutive reversal measurements with EB systems, is the training effect, which describes that H_{EB} decreases upon hysteresis loop cycling. Besides the pronounced athermal training after the first loop, a thermal (or 'slow') training is also evident for the second and subsequent hysteresis loops which is due to thermal activation processes in the antiferromagnet. [OFOVF10] For reproducibility of experiments, typically the first measured loop after EB initialization is omitted to exclude the athermal training effect. It is expected to be associated to non-collinearly arranged antiferromagnetic moments that are irreversibly rearranged to a collinear orientation during the ferromagnet's first reversal. [Hof04]

2.4.1 Modeling Exchange Bias

The first approach presented by Meiklejohn and Bean to model their experimental findings is based on the following assumptions: The ferromagnet in a single-domain state rotates as a whole. The single-domain antiferromagnet is supposed to be magnetically rigid and does not change its magnetization during the ferromagnet's reversal. [MB57] At the interface which is assumed to be atomically smooth, the antiferromagnetic moments are fully uncompensated. [MB57] The exchange coupling can be modeled by a positive parameter J_{EB} representing the exchange coupling energy area density.

Based on these assumptions, the Stoner-Wohlfarth model introduced in subsection 2.3.1 can be extended with a term accounting for the interfacial exchange coupling energy under consideration of the uncompensated interface moment's angle β_{AF}. In this ideal Meiklejohn and Bean model, the ferromagnet's free energy area density can be expressed as

$$\begin{aligned}\frac{E(\beta_{\mathrm{F}})}{A} = &- \mu_0\, M_{\mathrm{s}}\, t_{\mathrm{F}}\, H_{\mathrm{ext}}\, \cos(\beta_{\mathrm{F}} - \alpha_{\mathrm{ext}}) \\ &+ K_{\mathrm{F}}\, t_{\mathrm{F}}\, \sin^2(\beta_{\mathrm{F}} - \gamma_{\mathrm{F}}) \\ &- J_{\mathrm{EB}}\, \cos(\beta_{\mathrm{F}} - \beta_{\mathrm{AF}})\end{aligned} \tag{2.4.2}$$

with the ferromagnetic thickness t_{F}. [MB57,RZ07] For the easy axis in the case of an parallel alignment of the ferromagnet's uniaxial anisotropy axis and the EB direction, i.e. $\beta_{\mathrm{AF}} = \alpha_{\mathrm{ext}} = \gamma_{\mathrm{F}} = 0$, analytic expressions H_{EB} and H_{C} can be derived: [RZ07]

$$H_{\mathrm{EB}} = -\frac{J_{\mathrm{EB}}}{\mu_0\, M_{\mathrm{s}}\, t_{\mathrm{F}}} \qquad \text{and} \qquad H_{\mathrm{C}} = \frac{2K_{\mathrm{F}}}{\mu_0\, M_{\mathrm{s}}}. \tag{2.4.3}$$

Equation 2.4.3 indicates a linear dependence of the characteristic H_{EB} shift on the interfacial coupling constant J_{EB} and the inverse dependence on the ferromagnetic layer thickness t_{F}. This originates from the interfacial nature of the effect itself and was experimentally proven, [MKS87] however the absolute values for H_{EB} determined via this relation differ significantly from the experimental findings. [RZ07,Mal87] Additionally, the enhancement of the coercivity is not reflected by the term for H_{C} in Equation 2.4.3 as it is identical with H_{C} resulting from the classical Stoner-Wohlfarth model (subsection 2.3.1) and scales only with the ferromagnetic material parameters. [RZ07]

As a first approach to further develop the model and to consider the antiferromagnetic layer's characteristics, the authors extended their model with a term that describes the ability of the ideally uncompensated antiferromagnetic interface moment to rotate as a whole. [Mei62] In this so-called realistic Meiklejohn and Bean model, a uniaxial anisotropy of the antiferromagnet with the anisotropy constant K_{AF} contributes to the bilayer's total free energy

$$\begin{aligned}\frac{E(\beta_{\mathrm{F}})}{A} = &- \mu_0\, M_{\mathrm{s}}\, t_{\mathrm{F}}\, H_{\mathrm{ext}}\, \cos(\beta_{\mathrm{F}} - \alpha_{\mathrm{ext}}) \\ &+ K_{\mathrm{F}}\, t_{\mathrm{F}}\, \sin^2(\beta_{\mathrm{F}} - \gamma_{\mathrm{F}}) \\ &+ K_{\mathrm{AF}}\, t_{\mathrm{AF}}\, \sin^2(\beta_{\mathrm{AF}} - \gamma_{\mathrm{AF}}) \\ &- J_{\mathrm{EB}}\, \cos(\beta_{\mathrm{F}} - \beta_{\mathrm{AF}})\end{aligned} \tag{2.4.4}$$

with the antiferromagnet's thickness t_{AF}, the angle of its interface moment β_{AF} and the angle of its anisotropy γ_{AF}.[Mei62,RZ07] Depending on the ratio between $K_{\mathrm{AF}}t_{\mathrm{AF}}$ and J_{EB}, the antiferromagnet rotates either reversibly or irreversibly with the ferromagnet, which affects the strength of H_{EB} and H_{C}. When the antiferromagnetic anisotropy is much larger than the exchange coupling, this model coincides with the previous ideal Meiklejohn and Bean model.[RZ07,Mei62]

2.4.2 Modeling Exchange Bias in Polycrystalline Systems

While the above described models treat both supposedly monocrystalline layers in a single-domain approach, many realistic samples are of polycrystalline character which is caused by commonly used fabrication techniques like sputter deposition in which the layers are not formed by epitaxial growth. Besides structural properties like the interface roughness and a variation of stoichiometry, especially the variation of antiferromagnetic grain sizes affects the EB in these samples. Consequently, the single-domain character of the antiferromagnet will be discarded and its granular nature needs to be included in the model. An early proposed granular model was presented by Fulcomer and Charap called *thermal fluctuation aftereffect model*:[FC72]

It is assumed that the antiferromagnet consists of non-interacting single-domain grains i which are exchange coupled to the uniformely magnetized ferromagnet and that the system's total free energy is given by

$$E(\beta_{\mathrm{F}}, \{\beta_{\mathrm{AF},i}\}) = E_{\mathrm{F}}(\beta_{\mathrm{F}}) + \sum_{i=1}^{N} E_{\mathrm{AF},i}(\beta_{\mathrm{AF},i}), \tag{2.4.5}$$

where N is the total number of antiferromagnetic grains.[FC72] Here, E_{F} can be expressed by the Stoner-Wohlfarth model in Equation 2.3.1. Each antiferromagnetic grain i with an in-plane interface moment defined via the azimuthal angle $\beta_{\mathrm{AF},i}$ contributes with an energy term composed of the local exchange coupling to the ferromagnet via the surface area $S_{\mathrm{AF,i}}$ and the microscopic coupling constant $J_{\mathrm{EB},i}$, as well as its individual anisotropy that depends on $K_{\mathrm{AF},i}$, the respective angle $\gamma_{\mathrm{AF},i}$ and its volume $V_{\mathrm{AF},i}$:[FC72]

$$\begin{aligned} E_{\mathrm{AF,i}}(\beta_{\mathrm{AF,i}}) =& K_{\mathrm{AF},i}\, V_{\mathrm{AF},i}\, \sin^2(\beta_{\mathrm{AF},i} - \gamma_{\mathrm{AF},i}) \\ & - J_{\mathrm{EB},i}\, c\, S_{\mathrm{AF},i}\, \cos(\beta_{\mathrm{F}} - \beta_{\mathrm{AF},i}). \end{aligned} \tag{2.4.6}$$

Note, that the exchange coupling term further depends on the parameter c, which was added by the authors as a contact fraction to reflect the circumstance that two grains with the same interface area can have different surface moment depending on the contact site: If the contact area shows only one type of antiferromagnetic sublattice, $c = 1$, whereas a coupling site with two equally represented sublattices yields $c = 0$.[FC72] Hence, $c \cdot S_{\mathrm{AF},i} = A_{\mathrm{AF},i}$ represents an effective interface area.

The antiferromagnetic grain's free energy can be visualized by a two-level model for $K_{\mathrm{AF},i}\, V_{\mathrm{AF},i} > J_{\mathrm{EB},i}\, A_{\mathrm{AF},i}$, with the energetic minima being degenerate for the extreme case of zero exchange coupling at the interface ($J_{\mathrm{EB},i} = 0$). The relation of the grain's anisotropy and its exchange

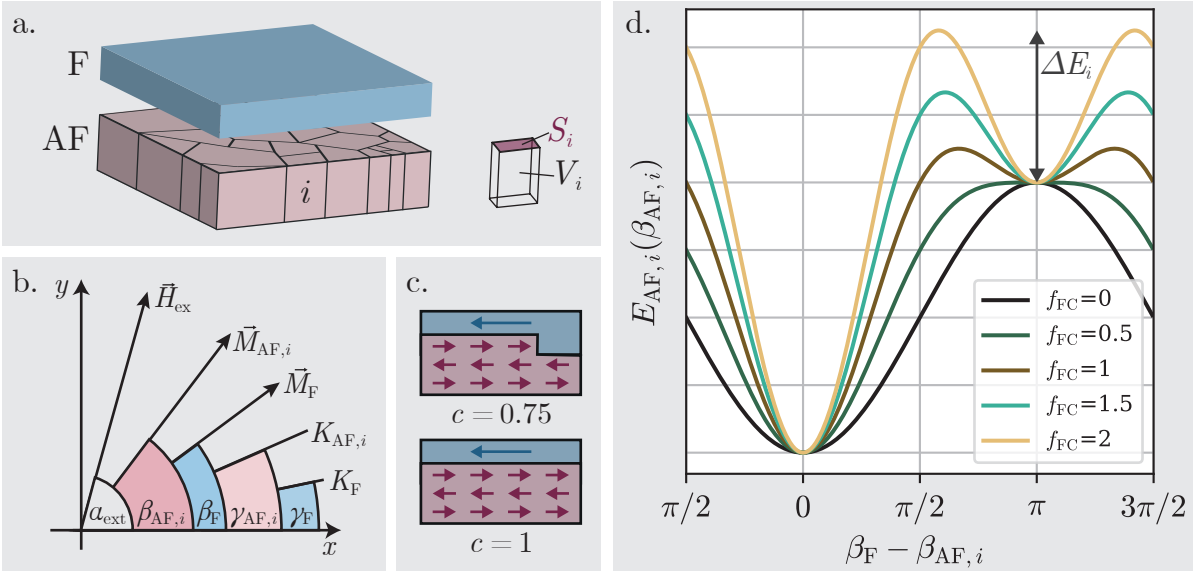

Figure 2.6: Schematic depiction visualizing the *thermal fluctuation aftereffect model* [FC72]: a. The individual grains i of the granular antiferromagnet (AF) have a volume $V_{AF,i}$ and an effective interface area $A_{AF,i}$ that they share with the single-domain ferromagnet (F). b. The relevant angles for the involved anisotropy axes, the magnetic field vector and the magnetic moment of the ferromagnet as well as the antiferromagnet are denoted. c. Imperfections in the crystal surface cause different coupling strengths for the same interface ares which is reflected by the contact fraction parameter c. d. For the special case, that the ferromagnetic moment is aligned parallel to the external magnetic field ($\alpha_{ext} = \beta_F = \gamma_{AF,i} = \gamma_F = 0$) the course of the energy of an individual grain is shown for a variation of the parameter f_{FC}. For $f_{FC} < 0.5$, only one energetic minimum is present, while for $0 < f_{FC} > 0.5$, a two-level system results, where the global ($\vec{M}_F \uparrow\uparrow \vec{M}_{AF,i}$) and the local minimum ($\vec{M}_F \uparrow\downarrow \vec{M}_{AF,i}$) are separated by an energy barrier ΔE_i. Inspired by [FC72,EJE05]

coupling can be quantified by the parameter

$$f_{FC} = \frac{K_{AF,i}\, V_{AF,i}}{J_{EB,i}\, A_{AF,i}}. \tag{2.4.7}$$

The influence of f_{FC} on the antiferromagnetic grain's free energy depending on its uncompensated interface moment's direction with respect to the ferromagnetic magnetization ($\beta_F - \beta_{AF,i}$) is depicted in Figure 2.6 for the special case with a parallel alignment of $\vec{H}_{ext}$, $\vec{M}_F$ and the uniaxial anisotropy axes of the ferromagnet K_F and the antiferromagnetic grain $K_{AF,i}$ ($\alpha_{ext} = \beta_F = \gamma_{AF,i} = \gamma_F = 0$). When the exchange coupling dominates over the grain's anisotropy for $0 < f_{FC} < 0.5$, one energetic minimum is found. For $f_{FC} > 0.5$, a global ($\vec{M}_F \uparrow\uparrow \vec{M}_{AF,i}$) and a local minimum ($\vec{M}_F \uparrow\downarrow \vec{M}_{AF,i}$) arise, that are separated by an energy barrier ΔE_i. In the case of a strong anisotropy ($f_{FC} \gg 1$), this barrier can in first order be described by $\Delta E_i \approx K_{AF,i}\, V_{AF,i}$, which indicates that the energy required to switch from the local to the global minimum linearly scales with the grain volume for constant $K_{AF,i}$.[ESW11] Hence, thermal activation can lead to the transition from the local to the global minimum for which a relaxation time

$$\tau_i = 1/\nu_0 \exp\left(\frac{\Delta E_i}{k_B T}\right) \tag{2.4.8}$$

is defined under consideration of single spin precession frequency ν_0 that is usually assumed to be $1 \times 10^9\,\mathrm{s}^{-1}$.[FC72,ESW11] In this context, the blocking temperature $T_{\mathrm{B},i}$ of an individual grain may be introduced as the temperature below which its magnetization cannot relax to a global energy minimum on the timescale of the experiment.[FC72] Above $T_{\mathrm{B},i}$ of the largest grain, all grains in the polycrystalline sample behave paramagnetic and the loop shift of the sample's hysteresis vanishes, rather than at the Néel temperature ($T_\mathrm{N} > T_\mathrm{B}$).[FC72]

As the antiferromagnetic layer needs to be described as an ensemble of grains with a grain volume distribution, these grains consequently show a distribution of energy barriers, relaxation times and blocking temperatures. Finally, the macroscopic magnetic characteristics of the sample depend on the superposed population of the global and local energy minima of the antiferromagnetic grains.

Antiferromagnetic Grain Classification

In order to relate the relaxation behavior of the antiferromagnetic grains to their volume, a classification of the grains' thermal stability depending on their volume can be made under the assumption that $\Delta E_i \approx K_{\mathrm{AF},i} V_{\mathrm{AF},i}$ and $K_{\mathrm{AF},i} = \text{const.}$, where the class boundaries depend on the experimental conditions:[OFOVF10,MGM16]

- **Class I**: For energy barriers ΔE_i being smaller than thermal energy $k_\mathrm{B}T$ at the chosen measurement temperature, the grains behave superparamagnetic as their moments are disordered. These grains are classified as thermally unstable, therefore they do not influence the ferromagnet and contribute neither to the EB shift not to the coercive field.[OFOVF10,MGM16]

- **Class II**: The grains of this class are also connected to small energy barriers, i.e. the relaxation time being in the order of the observation time scale. During a hysteresis cycle, these grains relax into the global energy minimum depending on the ferromagnet's magnetization direction, which changes throughout the reversal process. These *rotatable* antiferromagnetic grains follow the ferromagnetic magnetization with a certain delay and, thus, they contribute to the ferromagnet's coercivity H_C.[MGM16]

- **Class III**: Grains with larger volume and consequently a relaxation time above the hysteresis duration are characterized by an energy barrier that does not allow for thermal activated relaxation during the hysteresis. However, the energy barrier may be overcome during a FC procedure in which the grains are transferred to the global energy minimum which is defined by the external magnetic field saturating the ferromagnet. As a result, the grains of this class are also called *rigid* or *pinned* as they mediate the unidirectional anisotropy, i.e. the shift H_EB.[EJE05,MGM16]

- **Class IV**: Within this class, the grains' energy barriers even exceed the thermal energy input during the FC process. Therefore, these grains cannot be set deliberately and do not contribute to the EB as their interface moments are assumed to be statistically distributed.[MGM16,OFOVF10]

Note that the boundaries between the grain classes depend on thermal influences. Hence, they are affected by experimental conditions like temperature and times for the measurements and the storage of the polycrystalline sample. The boundaries are further not to be understood discretely but rather as continuous transitions.[OFOVF10]

Although the antiferromagnetic grain classification described above is capable to explain a significant portion of the phenomenology of EB in polycrystalline systems, it does not allow for an easy calculation of hysteresis curves as compared to the Stoner-Wohlfarth model as it requires the implementation of each individual grain's influence. For this reason, Müglich *et al.* developed a model based on the Stoner-Wohlfarth formalism that abstracts the contribution of thermally stable and unstable grains (classes II and III) in two terms that reflect the average anisotropy per class.[MGM16,Müg16] Herein, the thermally stable and thereby EB mediating grains of class III are represented by a macroscopic unidirectional anisotropy (UDA) with the effective exchange coupling constant $J_{\mathrm{EB}}^{\mathrm{III}}$. The rotatable grains of class II that affect the ferromagnet's coercivity are represented by a time-dependent rotatable magnetic anisotropy (RMA) term.[MGM16] The term *rotatable* refers to a description previously introduced by Stiles and Mc Michael where the anisotropy changes its easy axis orientation throughout the hysteresis, as the magnetization of the ferromagnet changes and, thus, applies a magnetic torque on the antiferromagnetic uncompensated interface moment.[SM99] The antiferromagnetic grains react to the ferromagnetic changes within their relaxation time, which makes the RMA dependent on the magnetic history of the ferromagnet. Based on the described definitions of the macroscopic UDA and RMA, Müglich *et al.* proposed an extended Stoner-Wohlfarth ansatz representing the free energy of the ferromagnet as[MGM16]

$$\begin{aligned}\frac{E(\beta_{\mathrm{F}}(t))}{A} =& -\mu_0\, M_{\mathrm{s}}\, t_{\mathrm{F}}\, H_{\mathrm{ext}}\, \cos(\beta_{\mathrm{F}} - \alpha_{\mathrm{ext}}) \\ &+ K_{\mathrm{F}}\, t_{\mathrm{F}}\, \sin^2(\beta_{\mathrm{F}}(t) - \gamma_{\mathrm{F}}) \\ &- J_{\mathrm{C}}^{\mathrm{II}}\, \cos(\beta_{\mathrm{F}}(t) - \gamma_{\mathrm{RMA}}(t)) \\ &- J_{\mathrm{EB}}^{\mathrm{III}}\, \cos(\beta_{\mathrm{F}}(t) - \gamma_{\mathrm{UDA}})\end{aligned} \tag{2.4.9}$$

with the effective exchange energy constant $J_{\mathrm{EB}}^{\mathrm{III}}$ summarizing all interactions of the ferromagnet with the thermally stable grains resulting in an effective UDA with the azimuthal angle γ_{UDA}, representing the direction of all superposed grains within class III. Accordingly, $J_{\mathrm{C}}^{\mathrm{II}}$ describes the summed contributions of all grains within class II and $\gamma_{\mathrm{RMA}}(t)$ is the time dependent angle of the RMA which depends on the average relaxation time $\tau_{\mathrm{C}}^{\mathrm{II}}$ of class II grains, which is proposed to be:[MGM16]

$$\gamma_{\mathrm{RMA}}(t) = \beta_{\mathrm{F}}(t - \tau_{\mathrm{C}}^{\mathrm{II}}). \tag{2.4.10}$$

In the view quantitatively extracting model parameters, Müglich *et al.* simulated angular-dependent values for H_{EB} and H_{C} depending on the angle of the externally applied magnetic field that were in agreement with experimentally determined angular-dependent values of H_{EB} and H_{C} obtained by magneto-optical Kerr magnetometry.[MGM16] The authors further mention

the importance of reproducible experimental conditions like the temperature and the magnetic sweep rate during hysteresis measurements, because they are crucially determining the grain class boundaries.[MGM16,Müg16] The model was further successfully applied by Merkel *et al.* to disentangle magnetic anisotropy contributions in EB systems where the deposition rate dependent impact on the antiferromagnetic grain size distribution was used to tune the contribution of thermally stable and thermally unstable grains.[MHR20] The authors further studied first-order reversal curves of EB systems with a high portion of thermally unstable grains (thin antiferromagnetic layer) revealing that these rotatable grains may be dragged by the ferromagnet during its magnetization reversal which is reflected by a viscous behavior of the system: Upon increasing external magnetic field, the ferromagnetic magnetization viscously decreases.[MHR21]

Although the model does not give insights regarding the microscopic structure of the antiferromagnet and the interface of the bilayer, a quantitative comparison of experimental and simulated data can provide information about averaged grain class specific microscopic parameters and their impact on macroscopic magnetic properties of the sample.[Müg16]

3. Magnetism in Curved Geometries

In chapter 2, fundamentals about magnetism were introduced, among which the shape anisotropy plays an essential role in the formation of magnetization textures in three-dimensional magnetic objects. This chapter focuses on the effects of this anisotropy on flat microstructured magnetic objects with circular geometry. Within section 3.1, magnetization textures in magnetic disks and rings and the connected magnetization reversal mechanisms will be presented. Next, the recent research regarding magnetic hollow hemispheres, which are at the heart of this thesis, will be reviewed in section 3.2. Finally, micromagnetic simulations that have been performed to approach the reversal behavior of ferromagnetic caps are presented in chapter 4.

3.1 Magnetism in Circular Disks and Rings

Unlike rectangles, where a flux closure domain pattern exhibits domain walls in order to prohibit surface charges, a circular geometry allows for the alignment of moments parallel to the circumference for reducing the stray field energy: In the famous **vortex** texture, the magnetic moments curl around the circular object's center. Hence, this structure which is neither a single-domain nor a multi-domain configuration is the counter piece of a single-domain configuration.
Starting around the turn of the millennium, magnetic disks and the textures within have been studied driven by the interest to potentially use nano-magnets, which are desired to stably populate single-domain states, for magnetoelectric devices such as nonvolatile magnetic memory.[Cho97,CKA99] When the first nano-scaled disks made from Py[CKA99] and Co[LLN01,PNB02] were fabricated with the help of electron beam lithography, their magnetization reversal for both materials was studied in dependence of the dimensions, i.e. the element's radius (50-1000 nm) and thickness (6-50 nm).[CKA99,PNB02] From hysteresis measurements in combination with micromagnetic calculations, phase diagrams for the occurrence of either vortex or single-domain states in dependence of the disk radius r and thickness t were derived, where the phase boundary from the experimental data describes a transition from the vortex to the single-domain state when the diameter falls below 200 nm (100 nm) in 6 nm (15 nm) thick Py disks,[CKA99] and below 500 nm in 15 nm thick Co disks.[PNB02] Accordingly, the phase boundary between a single-domain (SD) and vortex (V) can be studied by numerically finding solutions for t and r (typically scaled via the exchange length) when equalizing the energy terms for both textures: $E_{\mathrm{tot}}^{\mathrm{V}}(r,t) = E_{\mathrm{tot}}^{\mathrm{SD}}(r,t)$.[JA04] While anisotropy, exchange and demagnetization energy need to be considered in the vortex case, the single-domain energy can in first approximation be reduced to the demagnetization energy $E_{\mathrm{d}}^{\mathrm{SD}}(r,t)$ when all moments are assumed to be oriented parallel ($E_{\mathrm{ex}} = 0$, $E_{\mathrm{ani}} = 0$).[JA04]

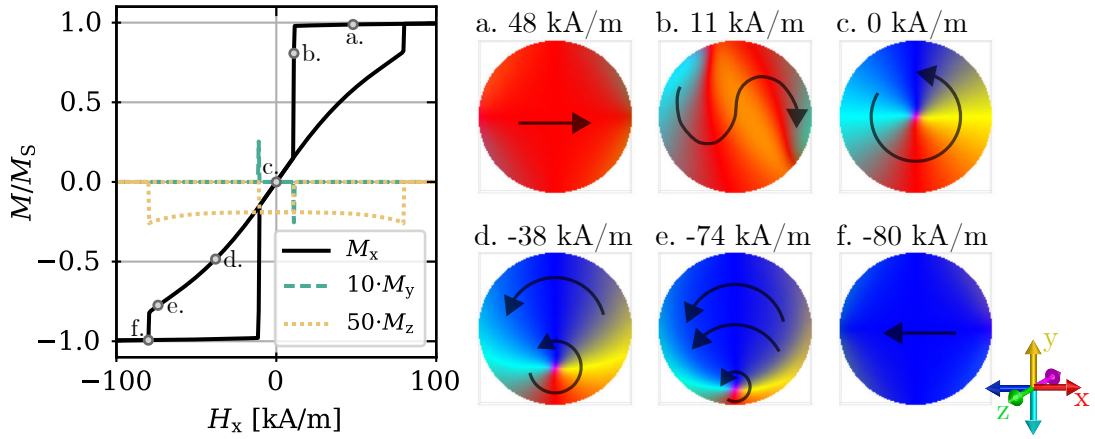

Figure 3.1: Characteristic magnetization reversal of a ferromagnetic disk (Py, 30 nm thick, 300 nm diameter) simulated with the finite-difference based micromagnetic software *Boris*,[Lep20] taking exchange, Zeeman and stray field energy into account. All three magnetization components M_x, M_y and M_z are normalized with respect to saturation, while M_y and M_z are scaled by the factors 10 and 50 for better visualization. Starting from the saturated state (a.), the disk first transits to a S-state when the field is reduced (b.), from which it nucleates a vortex at the nucleation field $H_{nuc} \approx 10$ kA/m . Around zero field this vortex is centered (c.), and towards negative magnetic fields the center of the vortex moves in a direction perpendicular to H_{ext} (d. and e.). At the annihilation field $H_{ann} \approx -80$ kA/m the vortex annihilates, meaning it is expelled and the reversed uniform state is reached (f.).

Since then, the reversal behavior of disks has been vastly studied, not only with integral methods for the characterization of the magnetization reversal but also with spatially resolved imaging techniques. Especially, magnetic force microscopy (MFM)[Shi00,PNB02] and Lorentz transmission electron microscopy (LTEM)[SHZ00] performed at characteristic magnetic fields during the reversal could proof the existence of two different main reversal types: Either remagnetization via vortex nucleation, motion and annihilation or via coherent rotation of a single-domain state could be observed. A characteristic vortex type reversal is depicted in Figure 3.1: When lowering the magnetic field from positive saturation, a sudden decrease of magnetization occurs at the so-called nucleation field H_{nuc} that indicates the formation of a flux-closure state. At zero field, the magnetization is zero when pinning, e.g. due to surface roughness, can be neglected, as the disk's state is majorly determined by the stray field energy and the vortex is perfectly centered. When further decreasing the magnetic field towards negative values, the vortex texture is deformed and its core is pushed perpendicular to the magnetic field on a straight path away from the disk's center. The reason for this is the competition between magnetostatic energy and the increasing Zeeman energy, which favors to increase the area of parallel aligned magnetic moments to the external field. The direction of the consequently following core motion therefore depends on the circulation sense (also called circularity[IFH17]) of the vortex texture itself. When the magnetic field is eventually decreased towards negative saturation, the vortex becomes finally unstable and the texture annihilates at the annihilation field H_{ann}.[CKA99] Note, that within this thesis, values for the characteristic fields H_{nuc} and H_{ann} are always referring to the decreasing hysteresis branch if not stated otherwise. The vortex nucleation and annihilation fields have been studied

depending on the geometry of the disk: For smaller and/or thicker disks, i.e. for increasing aspect ratio t/r, vortices nucleate at an earlier stage during reversal (at larger positive fields on the descending branch) and annihilate later (at more negative fields).[SHO02,GNO02] Both observations describe that a higher Zeeman energy is necessary to destabilize the vortex structure so that the single-domain state is favored over the vortex with regard to the total free energy. (Accordingly, larger and/or thinner disks nucleate the vortex later during the reversal.[SHO02,GNO02]) In a relatively thick magnetic disk, the mono-domain state is energetically less favorable due to a higher number of surface charges and hence, a higher demagnetization energy as compared to the vortex. When enlarging the disk diameter, however, these positive and negative magnetic charges on the disks sides move apart which lowers the uniform state's demagnetization energy and thereby stabilizes it in the disk. The result is a later nucleation and an earlier annihilation. Contrastingly, small but very thick cylinders, which rather resemble columns than disks, find an energetic minimum for a homogenous magnetization pointing perpendicular to the sample plane, i.e. parallel to the cylinder axis.[PNB02,RHS02]

Eventually, for very small t and r the single-domain state is preferred independent of the external magnetic field, which causes the reversal type to switch from vortex reversal to coherent rotation.[PNB02,CKA99]

In disks reversing via vortex formation, the characteristic fields H_{nuc} and H_{ann} have been shown to be temperature-dependent: While at low temperatures, the processes depend on thermal activation over an energy barrier, the temperature dependence of M_{s} determines the course of the critical fields at elevated temperatures.[MP10]

In Figure 3.1, the disk transitions to the vortex state via a so-called S-state , while another known transition includes a C-state. This transition is not a general or necessary characteristic of vortex reversal but can occur as a distinct kink in magnetization curves. It is for example not visible in the hysteresis curves in Refs. [CKA99, PNB02] but has been theoretically predicted both by micromagnetic simulations[GNO02,RSB03] and an analytical description[GNO02]. Both quasi-uniform states were imaged by means of LTEM[SHO02,TPLH09] and the related kink in the hysteresis curve just before the vortex nucleation was recorded at temperatures below 5 K.[RSB03] Another possible precursor state besides the S- and C-state is a double-vortex which was found during the reversal of disks larger than 700 nm[RSB03,PSN00] and as a remanent state in soft magnetic ellipses previously magnetized along their long axis.[VZM04]

For the sake of clarity, it shall be mentioned that in disks characterized by a reversal via vortex nucleation, motion and annihilation, the remanent state at zero field does not necessarily have to be a vortex but can be a mono-domain texture. Therefore, when comparing phase diagrams in literature, it is important to differentiate whether the study refers either to simulated ground states, i.e. textures with minimized energy,[PNB02] to the occurrence of the typical vortex-shape of the measured reversal curves[CKA99] or the extractable remanent states at zero field[HHK03].

In a magnetic disk or cylinder, a strictly in-plane curling vortex texture would cause a singularity in the center, that leads to a distinct increase of exchange energy. Hence, the local impact

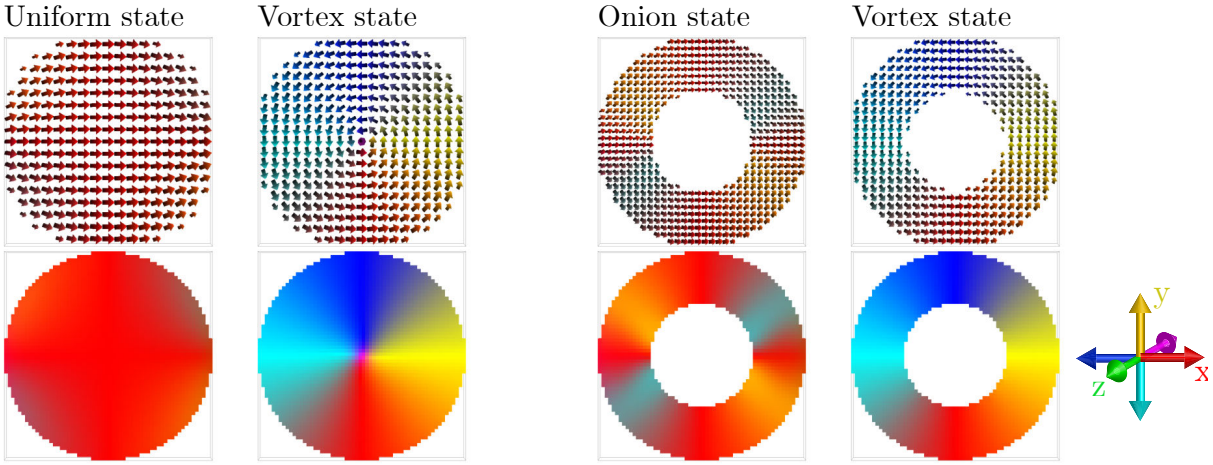

Figure 3.2: Magnetization textures in ferromagnetic disks (left) and rings (right) obtained by micromagnetic simulations performed with the software *Boris*.[Lep20] The disk/ring outer diameter was chosen to be $D = 300\,\text{nm}$ with a thickness of 30 nm. The resulting total energy density, taking the stray field energy and the exchange energy into account, is shown for all configurations. For both, the ring and the disk with the specified geometry, a vortex would be the desired texture due to the minimized energy. (The upper and lower row of images depict the same states and just offer a different visualization.)

of exchange coupling is stronger than the dipolar forces which results in a magnetization *swirl* that avoids the singularity as the moments turn perpendicular to the surface in the center of the vortex.[HS98] The existence of the so-called **vortex cores** was verified by means of MFM.[Shi00] Its lateral dimensions were not only addressed analytically[JA04,AEL07] but were also experimentally investigated. For the determination of their size MFM is however unsuited, as the lateral resolution is limited to 20 nm at best and because of possible interactions of the magnetic tip's and the vortex core's stray fields. Instead, a spin-polarized scanning tunneling microscope (SP-STM) with atomic resolution was used to resolve the out-of-plane magnetization profile across the vortex core of sub-micrometer Fe islands, from which a core width of 9 nm was derived.[WWB02] The core dimensions were shown to depend on the ratio between demagnetization energy and the exchange energy in materials with zero anisotropy, i.e. it scales with $\sqrt{A/K_\text{d}}$ in the thin film limit ($t \to 0$), similar as the width of domain walls does.[Get08,FT65] X-ray imaging further revealed that the vortex core diameter increases for increasing disk thickness.[FIK11]

Due to its core, the vortex texture in a disk is not completely stray field free. Contrastingly, in a ring structure, where the core part is removed, the vortex related stray fields are reduced dramatically,[KVLD03] as it can be seen from Figure 3.2 where the total energy density of a ring and a disk can be compared for two prominent textures. For a soft magnetic material such as Py in the here chosen geometry, with an outer radius of 150 nm, an inner radius of 75 nm and with a thickness of 30 nm, the vortex state is expected to be energetically favored, which is in agreement with the thickness and radius dependent phase diagrams by Landeros *et al.*.[LEA06] However, it has been observed that an often stabilized remanent state in these rings is the higher-energetic **onion** state, which was attributed to defects and edge roughness.[VKB06,LPN01]

This texture - the onion state - was at first differently addressed in literature, where it appeared *simultaneously* as a 'single domain'[LPN01] as well as a 'bi-domain' state[RKLD01] (one domain in the upper and one in the lower part of the ring with opposing flux direction) in the same volume of *physical review letters* in 2001. The different naming can be reasoned from the observations made: In the simulations of relatively wide rings investigated in Ref. [LPN01], the moments rotate relatively smoothly within the pole regions at which the two halved of the ring with opposing flux meet which reminds of a 'single-domain' state. Contrastingly, the slimmer rings in Ref. [RKLD01] showed distinct head-to-head and tail-to-tail domain walls at these poles, giving rise to the term 'bi-domain'. As the observed magnetization texture reminded of the "cross-section of an onion when it is cut from top to bottom"[RKLD01], the term onion texture is nowadays commonly used - not only for ring structures but also for a similar three-dimensional textures in hollow spheres.[KSS12] During the reversal of these rings, the magnetization first decreases from the saturated state towards the onion state in which the moments follow the curvature, from where the transition into a vortex state with a sharp drop of the magnetization to $M = 0$ is expected at the switching field H_{nuc}. However, it has been shown that magnetization reversal curves of arrayed rings indicate a switching field distribution as the rings successively nucleate and later annihilate the vortex in contrast to a single ring, for which a sharp transition was measured, exclusively.[BBV02]

This smooth transitioning in the hysteresis has also been observed in the vortex-reversal of disks arrays.[LLN01,OSO02] Further studies revealed a so-called **configurational anisotropy** which connects the existence of magnetic easy axes in periodic arrays of circular shaped objects with the lattice symmetry exhibited by the arrays: While thin disks prefer in-plane orientation of the magnetization (shape anisotropy), with no further anisotropy within this plane, the anisotropy constant derived for a square lattice in which the disks couple magnetostatically is four-fold in the sample plane and depends on the inter-dot distance.[Gus01,IIP12] This configurational anisotropy manifests itself by the disk-distance dependent changes in the nucleation and annihilation field of vortex reversing disks.[NGS02] Compared to an isolated disk, the disks in a square lattice both, nucleate and annihilate at smaller magnetic fields, respectively, as their magnetostatic coupling stabilizes the mono-domain state.[NGS02] This vortex destabilization has not only been shown for arrays but also for two coupled disks depending on their distance.[JRA09,LDS14] An arrangement of two soft magnetic disks clearly showed that the vortex is stable along a shorter field range when the reversal is probed parallel to the long axis of the disk pair.[JRA09] Furthermore, the magnetostatic coupling affects the circulation direction of the vortex in the disks: While the circulation sense (clock- or counterclockwise) and polarity (core up or down) are randomly generated during vortex nucleation in an isolated disk, in a disk pair an alternating (same) circulation sense is observed after saturating the pair in a field perpendicular (parallel) to its long axis.[JRA09] This is due to the coupling of the intermediate states (*C*-, *S*-state and shifted vortex) as these posses surface charges that allow for magnetostatic coupling. In diagonally aligned disk pairs (45° to field axis), alternating circulation directions are found for the same reason, cf. Figure 3.3. Consequently, in a periodic lattice of similarly diagonally arranged disks, which is a honeycomb lattice, purely alternating circulation sense of nucleated vortices is expected and was confirmed by X-ray microscopy techniques.[VSF17] These magnetostatic forces aiming for flux

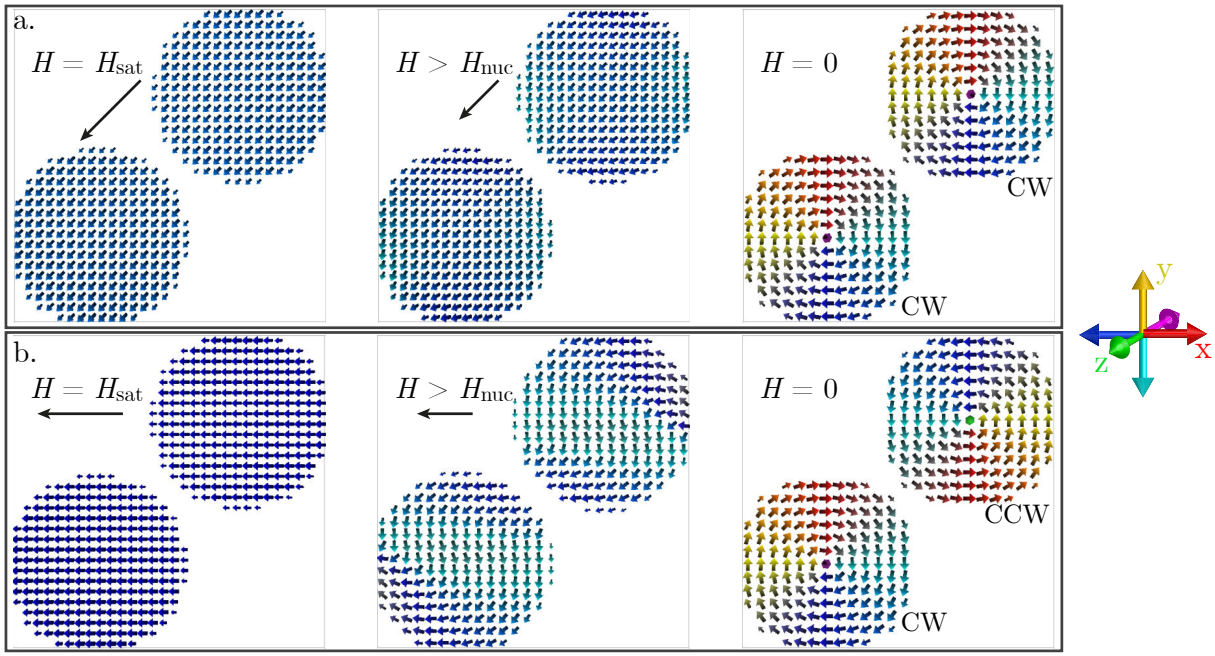

Figure 3.3: The nucleation process in two magnetostatically coupled Py disks with $D = 300\,\text{nm}$ and $t_F = 30\,\text{nm}$. In a. the external magnetic field previously saturating the disk is aligned parallel to the doublets long axis, while in b. it is oriented in a 45° angle. As the disks transition via magnetostatically coupled S-states in b. allowing for an inter-disk flux closure, the vortices in remanence have alternating circulation sense. Simulated with *Boris*,[Lep20] inspired by[VSF17].

closure are also present in a hexagonal lattice, however, in this case circulation frustration arises as the perfect alteration of diagonal neighbors cannot be achieved anymore. The result is an alternating line pattern whose lateral extension scales with the distance between the disks.[VSF17] In simulations, configurational anisotropy can be considered by the use of periodic boundary conditions. However, this cannot represent finite array dimensions which were found to add a **global configurational anisotropy**.[VFS14] Experimental and micromagnetic studies on arrays of 16 x 16 ferromagnetic disks (Py, $t_F = 13\,\text{nm}$, $r = 315\,\text{nm}$, periodicity of 400 nm) reveal that this global configurational anisotropy causes that the array reversal starts at its boundaries and then expands towards the lattice center with intermediate global states of similar magnetized chains, i.e., the corner dots nucleate vortices first and annihilate them at last.[VFS14] For the finite number of 256 disks, the magnitude of the in-plane magnetization can be visualized for each disk within the lattice. From this, the distribution of populated magnetization states and different reversal routes was analyzed for the simulated hysteresis with different disk thickness.[VFS14]

In addition to the effects of magnetostatic coupling, also exchange coupling of disk elements was shown to have an impact on their reversal by the fabrication of disk rows (Py, $t_F = 40\,\text{nm}$, $r = 300\,\text{nm}$) in which 50 nm long bridges of different width connected the individual disks.[HDY09] In contrast to non-exchange-coupled disks, the vortex nucleation in these samples is suppressed and the coupled disks show overall non-zero remanence. Likewise to arrays with global configurational anisotropy, in these coupled chains, the vortices nucleate sequentially throughout the hysteresis from the outer to the inner disks.[HDY09]

3.1.1 Exchange Bias in Circular Disks

Aside of the effects introduced by magnetostatic interaction or exchange coupling of disks in an array, a further way to affect and finally tune reversal processes and remanent textures in magnetic disks was studied: The introduction of EB as an additional unidirectional anisotropy term for each individual disk opened a new field of research.

At first, competing EB and demagnetization effects in disks composed of an antiferromagnet-ferromagnet bilayer were found to add an angular dependency for the reversal process as it is the case for extended films. Sort *et al.* observed a suppression of the vortex reversal type for hysteresis measurements with magnetic fields applied at an angle larger than $\theta_c = 80°$ with respect to the EB direction, where the disks reversed via coherent rotation over the EB direction instead.[SHC05] This critical angle is related to the EB strength, as the vortex can only nucleate if the absolute value of the effective field, i.e. the superposition of $\vec{H}_{EB}$ and $\vec{H}_{ext}$, falls below the nucleation field, otherwise the reversal takes place via coherent rotation.[SHC05] The characteristic vortex nucleation/annihilation fields are likewise angular-dependent, whereby only the nucleation field of the ascending (backward) branch $H_{nuc,b}$ linearly decreases with rising angle, while the nucleation on the descending (forward) branch ($H_{nuc,f}$) remains unaffected.[SHC05] The authors of Ref. [SHC05] reasoned the experimentally determined course of the angular-dependent nucleation field with the help of a geometrical model. They state that the vortex nucleation occurs when the effective field $\vec{H}_{eff} = \vec{H}_{EB} + \vec{H}_{ext}$ equals the vortex nucleation field $H_{nuc,0}$ if no EB was present, As indicated in Figure 3.4. By geometric calculation, the branch-specific nucleation fields $H_{nuc,f}$ and $H_{nuc,b}$ become[SHC05]

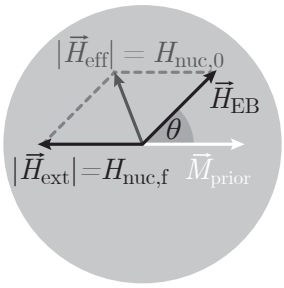

Figure 3.4: Sketch for Equation 3.1.1[SHC05] describing the nucleation of a disk previously magnetized along M_{prior}.

$$H_{nuc,f/b}(\theta) = H_{EB}\cos(\theta) \pm \sqrt{H_{nuc,0}^2 - H_{EB}^2 \sin^2(\theta)}, \tag{3.1.1}$$

considering H_{EB} as the EB shift at $\theta = 0$ and $H_{nuc,0}$ as the nucleation field if no EB was present.

In a next step, Sort *et al.* modified the strength of the EB in their disks.[SSAB06] Although the EB can be tuned via its dependence on the ferromagnetic thickness (Equation 2.4.3), this kind of modification is not desired as a change of the disk's aspect ratio simultaneously affects the demagnetization energy of the disk and thus its reversal. Hence, two subsequent FC steps are used for tailoring the EB: The first step sets the maximum EB, while the choice of annealing temperature in a second step with opposing external field is used to successively reduce the EB in its magnitude.[SSAB06] This study could prove that the strength of the EB determines the critical angle θ_c beyond which the vortex nucleation is suppressed. The larger H_{EB}, the smaller θ_c.[SSAB06]

A second and important finding was the effect of zero field cooling (ZFC). This annealing procedure in the absence of an external field was shown to stabilize the existence of vortices over a wider magnetic field regime in the EB disks due to an increase of the nucleation and annihilation fields when compared to unbiased disks.[SSAB06] This can be explained by supposing that the ZFC

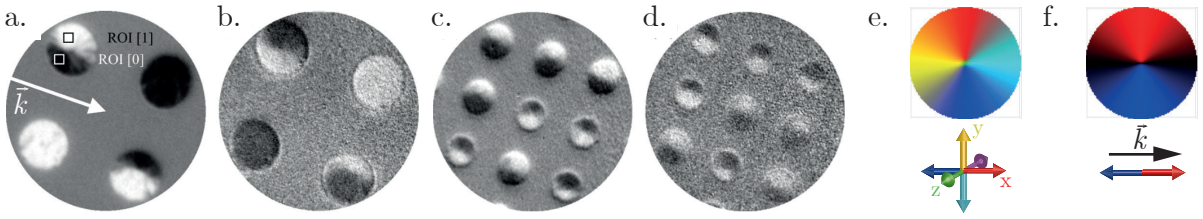

Figure 3.5: Magnetic contrast of 2 µm (a.,b.) and 1 µm sized EB disks (IrMn/NiFe) after ZFC acquired by XMCD-PEEM, where a. and c. show the ferromagnetic texture and b. and d. give the texture of antiferromagnetic moments at the interface. The dipolar contrast indicating vortex textures as shown in e. arises as the PEEM image displays the magnetization projected onto the direction of incident light (f.). Note, that the red-to-blue color map in f. translates to the white-to-black color map in the shown microscopy data. a. to d. are reprinted from [SAKS09], with the permission of AIP Publishing.

process 'imprints' the vortex texture into the antiferromagnetic layer, which phenomenologically adds a vortex-shaped effective pinning field after cool-down. Applying this procedure does not result in a hysteresis loop shift, but lowers the coercivity in the reversal loop as compared to field-cooled EB disks.[TPLH09] The vortex textured alignment of uncompensated interfacial antiferromagnetic moments imprinted by ZFC was experimentally proven by means of X-ray photoemission electron microscopy and magnetic circular dichroism (XMCD-PEEM):[SAKS09] A vortex texture can be identified by a dipolar contrast of the disks, as the technique is sensitive to the magnetization components aligned either parallel or antiparallel to direction of the incident light, or in other words, to the projection of the magnetization onto the light's k-vector. By choosing the correct X-ray energy for imaging, either a magnetic contrast of the Fe in the ferromagnetic layer or of the uncompensated moments of the antiferromagnet at the interface is received. Hence, the results of Ref. [SAKS09] depicted in Figure 3.5 revealed vortex textures in both cases, but with opposite contrast indicating an antiparallel coupling of the two layers.[SAKS09] Measurements of the vortex nucleation performed with in-field LTEM could prove that ZFC EB disks from Py and IrMn consistently nucleate the vortex with a fixed circularity rather than at a fixed nucleation site. The latter process was contrastingly found to dominate in Py disks as the two circularities have the same energy so that the disk's microstructure is the only factor defining the nucleation site. Contrastingly, the ZFC causes that this degeneracy is canceled and that the only circulation sense entered during the reversal is the one which was present prior to the ZFC.[TPLH09]

A third option is the annealing in an unsaturated state, realized by the application of non-zero magnetic fields insufficient for saturating the disks during FC. In case the ferromagnetic texture is a displaced vortex during the FC process, this texture is again imprinted into the antiferromagnet, with the core shifted perpendicular to the FC direction. The vortex reversal mechanism is in general preserved but nevertheless, it is modified as described in the following: Due to the imprinted shifted vortex, the ferromagnet's remanent texture is also a shifted vortex with non-zero magnetization, which was found to be tunable via the strength of the applied magnetic field during FC.[SBN06] For magnetization reversal measurements parallel to the FC direction ($\theta = 0°$), the longitudinal magnetization component consequently does not reach vanish zero field. Performed perpendicular to the FC direction ($\theta = 90°$), the reversal is again performed

by vortex nucleation, motion and annihilation, but the path described by the core position during the reversal is no longer linear but follows a curved trajectory.[SBN06] At this hard axis measurements, the longitudinal magnetization component vanishes at remanence, while the transversal takes non-zero values due to the vortex core's shift.

Reversal Modes in EB Disks

In an unbiased, purely ferromagnetic disk, the vortex hysteresis with its characteristic irreversible features, nucleation and annihilation, is symmetric around $H_{\text{ext}} = 0$ (*unbiased vortex reversal*). In extended thin EB bilayers, the additional antiferromagnetic layer causes a shift of the hysteresis curve by H_{EB}, generally accompanied by an increased coercive field (section 2.4).

In EB disks, the effects are more complex. However, if first assuming that only pinning antiferromagnetic grains of class III affect an EB disk's reversal, the uncompensated antiferromagnetic moments at the interface would either exhibit a homogeneous orientation or an imprinted and shifted vortex (after FC in non-saturating magnetic field). If the ferromagnet only depended on the exchange coupling among ferromagnetic and uncompensated antiferromagnetic interfacial moments, its remanent state would likewise be either uniform or a shifted vortex and the magnetization reversal curve would be symmetric around H_{EB} (*biased vortex reversal*). However, in a realistic disk the exchange coupling at the interface competes with the demagnetization energy of the ferromagnetic layer which can be expected to cause a non-uniform configuration of magnetic moments along the disk's normal axis. This was first identified for nanodots ($r \ll 40\,\text{nm}$) by Monte-Carlo simulations performed on the atomic level, which resulted in asymmetric hysteresis curves.[MLSA05] Guslienko and Hoffmann incorporated this finding in an analytical model for the vortex reversal where the effective EB shift is described as a depth-dependent property: Directly at the interface at $z = 0$, H_{EB} is larger than for the top layer of the ferromagnet at $z = t_{\text{F}}$.[GH06] Hence, the ferromagnetic vortex will be shifted at the bottom layer according to the antiferromagnetic interface moments but more centered at the top layer, and hence, the vortex core will be a tilted or curved Bloch line as depicted in Figure 3.6 c.[GH06] Consequently, on the decreasing (forward) hysteresis branch, the vortex annihilation will start at the free surface layer and will propagate towards the bottom layer, i.e. the characteristic field of total vortex annihilation is defined by the bottom layer. This irreversible feature is shifted with respect to the absolute annihilation field of the unbiased vortex H^0_{ann} as follows:[GH06]

$$H_{\text{ann,f}} = -H^0_{\text{ann}} - H_{\text{EB}}(z = 0) \tag{3.1.2}$$

On the ascending (backward) branch, it is vice versa $H_{\text{ann,b}} = H^0_{\text{ann}} - H_{\text{EB}}(z = t_{\text{F}})$. Together, they result in an average annihilation field $\overline{H}_{\text{ann}} = (H_{\text{ann,f}} + H_{\text{ann,b}})/2$. For a system with $H_{\text{EB}}(z = 0) = H_{\text{EB}}(z = t_{\text{F}}$, this average value would not differ from the unbiased case, i.e. $H^0_{\text{ann}} = \bar{H}_{\text{ann}}$. The authors further introduce the parameter

$$\Delta H_{\text{ann}} = \overline{H}_{\text{ann}} - H^0_{\text{ann}} = \frac{H_{\text{EB}}(0) - H_{\text{EB}}(t_{\text{F}})}{2} \tag{3.1.3}$$

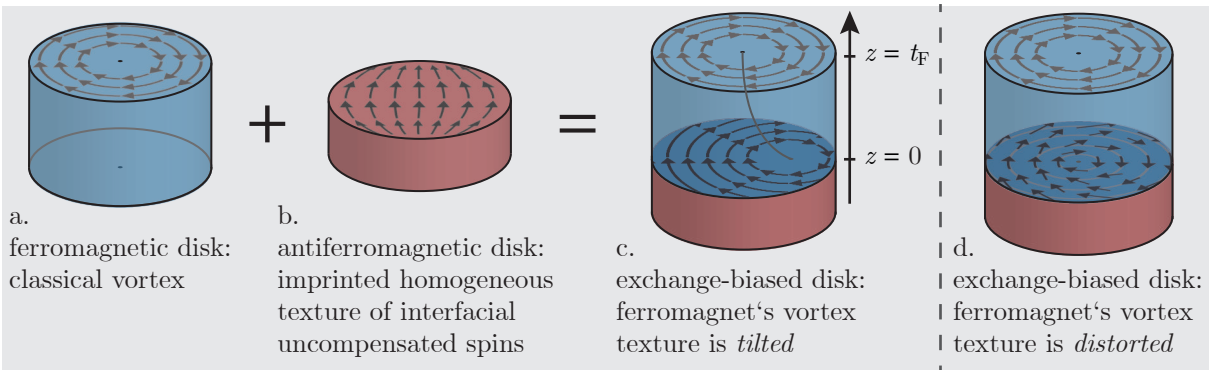

Figure 3.6: The vortex state in a ferromagnetic disk is symmetric around the disk's center (a.). In an exchange-biased disk, the imprinted magnetization texture of the antiferromagnet's interfacial moments (b.) pins the ferromagnetic moments close to the interface ($z = 0$) more strongly than the moments at the layer's top ($z = t_F$). Thus, the lateral position of the vortex core is depth dependent, when the ferromagnetic bottom 'layer' forms a perfectly circular vortex with a shifted center (c.).[GH06] Alternatively, the lowermost layer of the ferromagnet possesses a rather distorted vortex texture, in which the core is centered but the moments curling around it are tilted in order to align with the antiferromagnetic texture (d.).[GYV15]

that, if it is unequal to zero, accounts for the asymmetry in the so-called *tilted vortex reversal*.[GH06] The hysteresis loop's asymmetry is expected to rise when increasing the ferromagnetic film thickness t_F.[GH06] Note, that the here mentioned asymmetry is not to be confused with the angular-dependent asymmetric magnetization reversal observed for extended EB films , which originates from the competition between the uniaxial and the unidirectional anisotropy.[CSH05]

An additional asymmetry of the nucleation field is not covered by the model, which the authors explain by stating that the vortex nucleation takes place as soon as the saturated state, which cannot vary along z, becomes unstable.[GH06] Despite the theoretical prediction, this very asymmetry with $\Delta H_{nuc} \neq 0$ was later experimentally evidenced and reproduced in micromagnetic simulations of EB disks.[GYV15] It was found to be pronounced for small antiferromagnetic film thicknesses, at which according to the grain classification (subsection 2.4.2) a high portion of thermally unstable grains is present. In extended films, these rotatable grains promote an enhanced coercivity and small EB shift. Unstable antiferromagnetic interface moments are dragged by the ferromagnet which, in turn, changes the energetic landscape of the ferromagnet throughout the reversal process. In the case of EB disks, the configuration of interfacial uncompensated antiferromagnetic moments (both, pinning and rotatable), differs for the two hysteresis branches when lowering the magnetic field from saturation, which explains the nucleation field asymmetry in this so-called *viscous vortex reversal*.[GYV15] Note, that prior to nucleation the antiferromagnet's pinned and rotatable moments are parallel on the descending branch. The unpinned moments rotate during the reversal towards negative saturation so that afterwards, on the ascending branch pinned and rotatable moments do not share the same orientation. Hence, the ferromagnetic disk nucleates asymmetrically as it is exposed to different textures of antiferromagnetic interface moments when inverting the direction of reversal. Micromagnetic simulations of these EB disks performed by the authors further reveal that the magnetization texture within the ferromagnet changes along the $z-$direction as follows: At the

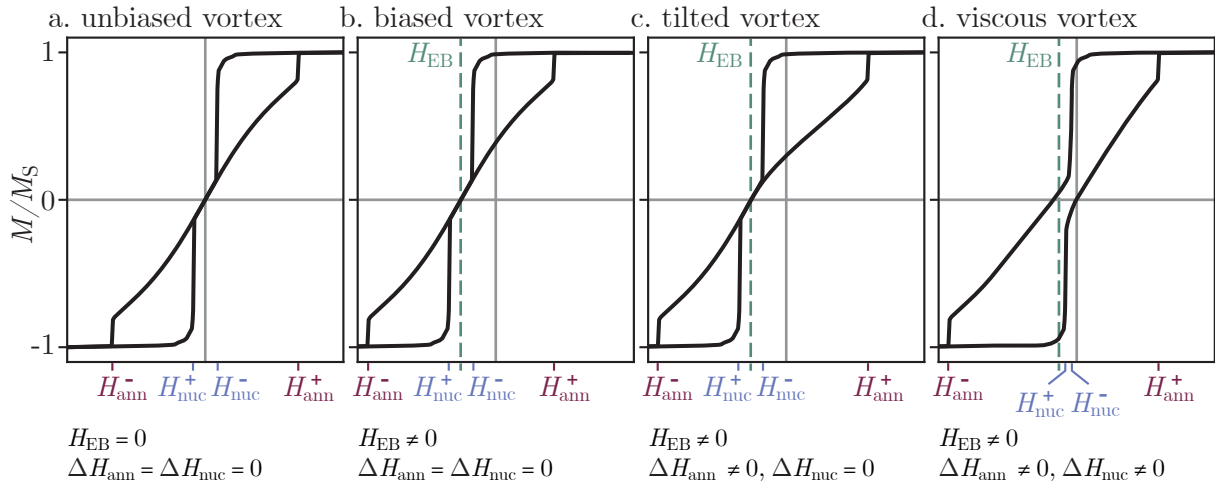

Figure 3.7: The different vortex reversal types possible for (EB) disks. Both, nucleation and annihilation fields of the two hysteresis branches are symmetric around zero field or the EB field in the unbiased and the biased vortex reversal, respectively. In contrast, the annihilation fields are asymmetric with respect to H_{EB} for the tilted vortex reversal. In disks with thin antiferromagnetic films, a viscous vortex reversal takes place: When the antiferromagnetic grain ensemble contains less pinning and more rotatable grains, the EB shift is reduced, while the coercivity is enhanced and both, nucleation and annihilation fields appear to be asymmetric with respect to H_{EB}.[GYV15] Inspired by[GYV15]

top, it creates a perfectly symmetric vortex and at the interface it experiences a complex energy landscape due to the presence of both pinned and rotatable uncompensated moments of the antiferromagnet.[GYV15] The result is a distorted, non-uniform vortex texture within this bottom layer, where the moments are tilted towards the EB direction although the vortex core is laterally centered. Hence, the ferromagnet's texture does not show the core tilt but is described by the term *distorted vortex* (cf. Figure 3.6 d.), where the degree of distortion was seen to differ along the two respective hysteresis branches.[GYV15]

In conclusion, the asymmetries of nucleation and annihilation with respect to the EB shift can be quantified by

$$\Delta H_{nuc} = H^+_{nuc} + H^-_{nuc} - 2 \cdot H_{EB} \quad \text{and} \quad \Delta H_{ann} = H^+_{ann} + H^-_{ann} - 2 \cdot H_{EB}. \tag{3.1.4}$$

Figure 3.7 summarizes how a measured hysteresis can be assigned to one of the four vortex reversal types described as unbiased, biased, tilted and viscous based on the introduced asymmetries ΔH_{nuc} and ΔH_{ann}.[GYV15]

Finally, both distorted and tilted vortices have been imaged by means of magnetic fore microscopy in viscously reversing disks ($R = 4\,\mu m$, $t_F = 40\,nm$) where a thin IrMn layer of varied thickness was deposited on top of the NiFe disks.[ABR21] Hereby, a centered starlike pattern with spatially alternating contrast was attributed to the distorted vortex type for $4\,nm < t_{AF} < 5.5\,nm$, which was not found in purely ferromagnetic disks.[ABR21] Furthermore, the displacement of the vortex core indicated the proposed tilt because the measured charge contrast originated mainly from the pinned side of the ferromagnetic disk. Only with sufficient pinning strength of the antiferromagnet, i.e. in the case $t_{AF} \geq 5.5\,nm$, the core position was found shifted.[ABR21]

3.2 Magnetism in Hollow Hemispheres

When aiming to extend circular two-dimensional geometries of thin films like disks and rings to the third dimension, the logically resulting shapes are of spherical or toroidal shape. Although some theoretical investigations were made for, e.g., hollow spheres in Ref. [GKS14], from an experimental point of view, a more easily accessible geometry is a spherical half shell, i.e. a magnetic cap. These three-dimensionally curved objects can easily be fabricated by the deposition of magnetic thin film on top of spherical template particles. [AHG05,MBUS08,ZWM09] Usually, assembled templating particles form hexagonal arrays and therefore mostly groups of possibly interacting magnetic caps have been investigated. In general, a lot of knowledge gained from magnetic disks can be applied. However, the introduced curvature in spherical half shells changes some characteristics as compared to their planar counterparts. Apart from the curvature, it was early on discovered that these caps cannot be simply perceived as hollow hemispheres with constant thickness, but that they rather have a crescent shaped cross-section due to the directional deposition with a variation of the film thickness from the cap's top towards its rim (thickness gradient). [AHG05]

Motivated to explore topographically patterned magnetic films for their applications in data storage media, it was found that self-assembly techniques for the creation of particle arrays are less cost-intensive than lithographic structuring. Research on magnetic caps started with the focus on out-of-plane anisotropy materials, like Co/Pd multilayers. [AHG05,UMH06,KKP10,ALS10] First studies revealed a dependence of the coercivity on the caps' diameter, where H_c was found to be increased for smaller diameters which was accompanied by wider reversal field distributions. [AHG05,MBUS08] Transmission electron microscopy (TEM) on sputter deposited multilayer caps further revealed a clustering of the contained materials at the small interconnecting sites where the multilayer stack's thickness is reduced. This clustering causes the loss of the ferromagnetism within this region and results in a magnetic exchange decoupling of the individual caps. [KKP10]

Interestingly, it was observed that the curvature of hemispherical half shells modifies the magnetic anisotropy of in-plane materials, e.g. in Fe/Gd multilayers, resulting in a geometry-driven spin reorientation transition (SRT) where caps below a certain diameter are out-of-plane magnetized. [ALS10] In comparison to disks, where an out-of-plane magnetization results in strong stray fields, the demagnetization energy of a cap with a perpendicular-to-equatorial-plane texture is reduced because this configuration causes the cap's side to be parallel-to-film magnetized. [ALS10]

Individual Magnetic Caps with in-plane Anisotropy

Similar to magnetic disks with in-plane anisotropy, magnetic caps typically possess either a vortex texture or a mono-domain state depending on the competition between the demagnetization energy on the one hand and exchange and uniaxial anisotropy energy on the other hand. Although the cap analogon for the mono-domain texture in disks may look similar in the top view, it is characterized by a tangential alignment of the magnetic moments with the shell's surface as illustrated in Figure 3.8. Again, the course of the magnetic moments reminds of a layer of

an onion cut in half. Hence, this texture is referred to as an onion texture in line with the nomenclature for magnetic rings, because its in-plane cross-section close to the equator has the same appearance as an onion texture in a ring with two poles.

A ground state phase diagram for individual hemispherical half shells of soft magnetic material with constant thickness was obtained via energy minimization from micromagnetic simulations with two distinct phases for the onion and the vortex state.[SKS13] Here, the onion texture is the equilibrium state for either very thin caps with $t_F = 2.5\,\text{nm}$ and diameters up to $D = 140\,\text{nm}$ or for very small caps ($D = 20\,\text{nm}$) at thicknesses up to $t_F = 15\,\text{nm}$. A similar phase diagram presented in Ref. [SKS12] has been derived under consideration of the mentioned thickness gradient, where the implementation of the latter shifts the phase boundary between onion and vortex state towards larger diameters.[1] Apart from the vortex and onion phase, a third phase with a uniform magnetic texture perpendicular to the equatorial plane arises for thick but relatively small individual caps with aspect ratios $t_F/D \approx 1$, e.g. for $t_F = 40\,\text{nm}$ and $D = 40\,\text{nm}$.[SKS12] Within the computed diagram, the phase boundaries between vortex and onion differ slightly from phase diagram that the authors obtained for magnetic disks, i.e. the equilibrium state in a 15 nm thick cap with $D = 35\,\text{nm}$ is an onion state, while the flat counterpart with the same t_F and D already stabilizes a vortex texture.[SKS12] This trend is in agreement with the simulations presented in Ref. [BRG13], where a FePt cap of 100 nm diameter reversed via coherent rotation of an onion state while the corresponding disk of same diameter and thickness reversed via vortex nucleation, motion and annihilation. To summarize, it can generally be expected that for thin magnetic layers and small caps an onion texture is developed, whereas for thicker layers and larger caps a vortex is stabilized.

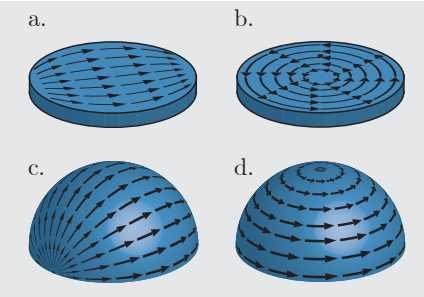

Figure 3.8: In-plane textures in magnetic disks (single domain in a. and vortex in b.) and hemispherical shells (onion in c. and vortex in d.).

For geometries, e.g. disks or hemispherical half shells, that allow vortex nucleation during reversal, micromagnetic simulations further reveal that the magnetic field range over which a vortex texture is stabilized, i.e. the range between the nucleation and the annihilation filed, strongly depends on the chosen geometry. This can be observed in micromagnetic simulations that are depicted in Figure 3.9. These simulations were conducted by using a finite difference method based on the magnetic object's discretization into cubic cells (edge length here: 2.5 nm). Note, that finite-element methods using tetrahedral instead of cubic cells would be rather suitable for a realistic discretization of a curved geometry,[TRH21,PGR21] for which, however, the available open-source packages only make use of central processing units (CPUs) but do not enhance the computation speed with the help of graphical processing units (GPUs).[Abe19] Consequently, for the calculations in this thesis, the well-documented and rather new finite-difference based open-source software *Boris*[Lep20] was used, because it utilizes GPUs and thus, also allows to compute larger volumes (e.g. multiple magnetic caps in a row) in a reasonable amount of

[1] From the simulations of Py caps with crescent cross-sections, the onion state is the equilibrium texture in 5 nm thick caps up to D =130 nm.[SKS12]

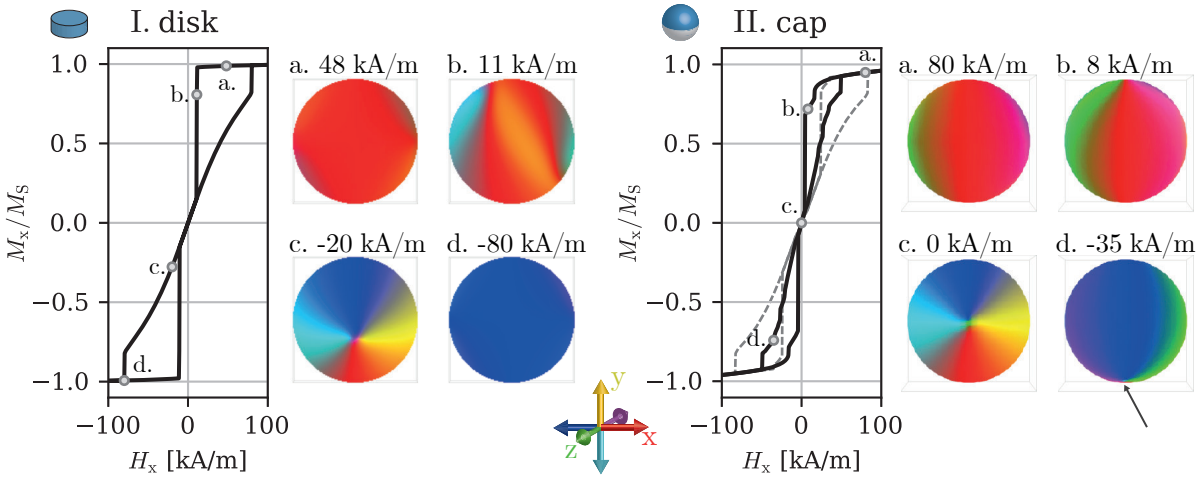

Figure 3.9: Characteristic longitudinal magnetization reversal along the indicated x-axis of the ferromagnetic disk shown in Figure 3.1 (I. Py, $t_F = 30\,\text{nm}$, $D = 300\,\text{nm}$) and a magnetic cap (II.) of the same inner diameter and the same material. Considering a thickness gradient, the cap's thickness is varied from 30 nm at the top to 12 nm at the rim (black line). The two simulations differ in their overall hysteresis shape, and the vortex texture is stabilized in a larger magnetic field regime for the disk. This is indicated as the annihilation fields show a significant difference ($H_{\text{ann,disk}} \approx -80$ kA/m, $H_{\text{ann,cap}} \approx -50$ kA/m), whereas the nucleation fields vary only slightly ($H_{\text{nuc,disk}} \approx 10$ kA/m, $H_{\text{nuc,cap}} \approx 7$ kA/m). Note, that the false-color images referring to specified magnetic fields on the descending branch represent both shapes in a top view. Hence, the cap's vortex core in d. can only barely be seen on the lower end of the picture (arrow) as it has already moved across the shell. The gray dashed line in II. depicts the reversal of a hemispherical shell without thickness gradient. The differences between the two curves in II. are severe and they illustrate how important it is to consider the geometric details. The cap with constant thickness nucleates a vortex even before the disk at $\approx 24\,\text{kA/m}$ and also annihilates it at a even smaller field of $\approx -84\,\text{kA/m}$.

time. With *Boris*, a steepest-descent solver can be used to minimize the energy throughout the calculation of the magnetization reversal (here: step size 0.5 kA/m). In Figure 3.9 II., the magnetization reversal of two different cap geometries are shown alongside characteristic magnetic textures populated at specific magnetic fields (a.-d.). For comparison, the magnetization reversal and the respective characteristic textures of a disk are shown in Figure 3.9 I. (same as in Figure 3.1). All simulations have been conducted for the same series of magnetic fields applied under consideration of the same energy contributions, material parameters and discretization length. While the disk (I.) has a diameter of 300 nm and a thickness of 30 nm, the cap (II.) with an inner diameter of 300 nm was once simulated with a constant thickness of 30 nm (gray dashed line) and once with a thickness gradient, i.e. 30 nm at the top which is reduced to 12 nm at the rim (black line). This thickness reduction down to 40 % was chosen based on layer thickness estimates by analyzing focused ion beam milled cross-sections of capped particles.[TRH21] Firstly, it can be observed that the cap with constant thickness stabilizes a vortex texture over a field range that is larger than for the magnetic disk, as it already nucleates the vortex at higher magnetic fields but annihilates is at more negative fields (see caption of Figure 3.9 for values). In a curvature dependent micromagnetic study, it has similarly been reported that the required magnetic field to eliminate a vortex, i.e. its annihilation field, rises when tuning from a flat

disk towards a spherical half shell.[MZK21] However, when considering the realistic geometry, in which the thickness gradually decreases towards the rim, the field regime of a stable vortex is reduced in comparison to the disk geometry. The fact that the cap with a thickness gradient has smaller absolute annihilation fields is not due to the fact that the vortex becomes energetically less favorable, but much more due to the fact that the onion becomes already more favorable, i.e. its magnetostatic energy is overcompensated by Zeeman energy, at lower absolute field strengths. The reduction of the onion state's magnetostatic energy is attributed to the fact that it is mostly governed by edge charges in the equatorial region, whose density is reduced due to the thickness gradient.

For selected cap geometries, the two prominent textures, vortex and onion, could be successfully imaged by means of XMCD-PEEM in capped particles.[SKS12] In contrast to comparable measurements on flat disks where a dipolar contrast pattern indicates a magnetic vortex state (cf. Figure 3.5), the three-dimensional geometry of a hollow hemisphere partly allows for the transmission (besides absorption) of X-rays through the object. Here, the helicity dependent absorption (cf. subsection 6.3.1) causes a contrast inversion on the backside of the object which results in quadrupolar rather than dipolar patterns for the vortex state. Note, that for the measurement geometry in PEEM with a large angle of incidence (e.g. 74° in the cited work), the cast shadow of a three-dimensional object being imaged is longer than the object itself. Based on this, the authors of Ref. [SKS12] successfully demonstrated the advantage of analyzing this elongated shadow, in which the contrast is also inverted: The shadow's magnetic texture can be interpreted even for objects with a size in the range of or even below the spatial resolution of the electron microscope.[SKS12] Both, the cap's and its shadow's contrast can further indicate the shifted position of the vortex core when a magnetic field is applied. The authors further tracked the summed XMCD signal for a range of applied magnetic fields, which gave rise to a single cap hysteresis.[SKS12]

Arrays of Magnetic Caps with in-plane Anisotropy

Just like the above described experiment, hysteresis measurements of individual nano- or microobjects are very demanding and, thus, often large arrays are investigated instead. In general, the reversal behavior of both, magnetic cap and disks arrays, cannot be directly compared with the magnetic reversal of the respective individual objects, e.g. from simulations. Furthermore, when analyzing hysteresis measurements of ensembles it always needs to be considered that the data reflects integral information of the probed area only and that the magnetization reversal of an individual object within this array cannot be retrieved from this data. While magnetic disks can lithographically be designed with desired lattice symmetry (square, hexagonal) and spacing, the fabrication of arrays of magnetic caps by self-assembly of the templating particles only allows for hexagonal arrays with zero spacing between the caps. The consequently present magnetostatic interaction effects are therefore correlated to the observation of the phase boundary between the onion and the vortex state being shifted towards much larger cap diameters as compared to individual caps. For this, Streubel *et al.* studied hysteresis measurements of differently sized

Py caps in arrays and determined the corresponding thickness-dependent phase diagram from the shape of the reversal curves.[Str15,SKR16] Magnetic reversal behavior governed by coherent rotation may be assigned to the onion phase and reversal curves with a distinct pinch to the vortex phase. The authors state, that the caps may possibly reverse their magnetization via vortex reversal but remain in the onion state at remanence due to the magnetostatic coupling in the lattice. Therefore, they divide the vortex phase into two regions within the phase diagram: One for which the vortex is the transition state during the reversal, although it shows an onion at remanence ($H_{\mathrm{nuc}} < 0$), while thicker caps within the second phase nucleate a vortex before zero field is reached ($H_{\mathrm{nuc}} > 0$, $M(H_{\mathrm{ext}} = 0) \approx 0$). Please note, that the fields are representative for the decreasing field branch of the caps' hysteresis starting out from positive saturation. At 300 K, arrays of caps with a diameter of $D = 330\,\mathrm{nm}$ exhibit a vortex reversal for thicknesses above $t_{\mathrm{F}} = 15\,\mathrm{nm}$, but only populate vortices at remanence for $t_{\mathrm{F}} \geq 40\,\mathrm{nm}$.[Str15] Contrastingly, another study on Py caps of same diameter presents hysteresis curves in which a remanent vortex state is only visible for thicknesses $t_{\mathrm{F}} \geq 60\,\mathrm{nm}$.[NMK15] Although both groups investigated a critical thickness below which the remanent state of vortex reversing caps is an onion state, the corresponding absolute values differ significantly. Accordingly, the obtained value for the annihilation field at room temperature for $D = 330\,\mathrm{nm}$ and $t_{\mathrm{F}} = 40\,\mathrm{nm}$ is also significantly smaller in Ref. [NMK15] than in Refs. [Str15, SFK16]. Nevertheless, the nucleation field generally rises with increasing film thickness while the annihilation field shifts further to more negative values, which is in accordance with a larger field regime for vortex stability.[NMK15] By decreasing the temperature during the recording of the reversal measurements, Nissen *et al.* could observe a slight decrease in the nucleation field, while the annihilation field increased. Consequently, the vortex can be stabilized over a broader field range at lower temperatures, while it is destabilized at elevated temperatures.[NMK15]

The previously mentioned phase for individual caps magnetized perpendicular to the equatorial plane[SHI15] is omitted in the phase diagram for cap arrays, since thick magnetic films on particle arrays rather form modulated in-plane magnetized films than arrays of coupling out-of-plane magnetized caps.[Str15]

Imaging the magnetization textures in cap arrays (Py, $D = 330\,\mathrm{nm}$, $t_{\mathrm{F}} = 40\,\mathrm{nm}$) by XMCD-PEEM further revealed a circularity coupling of the nucleating vortices, that causes the formation of chains of caps with vortices of same circulation sense, in which for each cap four of the six neighbors have opposite circulation sense.[SKR16] Straight chains were favored when the magnetic field was ramped from saturation to zero along a direction close to the main symmetry axis of the lattice (4°), while zigzag lines formed at remanence after saturating with a field oriented at −20° with respect to this symmetry axis.[SKR16] Hence, the frustration effects that were discussed for magnetic disks[VSF17] also play a role when magnetic caps are arranged in a hexagonal lattice. Especially, the intercap exchange interaction which depends on the thickness of the film was found to affect which states are exhibited: After demagnetization, hexagonally arranged Co nanocaps ($D = 290\,\mathrm{nm}$) homogeneously formed vortex states when $t_{\mathrm{F}} = 30\,\mathrm{nm}$ was chosen, whereas they occupied a mixture of vortex and onion states at $t_{\mathrm{F}} = 60\,\mathrm{nm}$ due to the enhanced exchange coupling.[SEG12] Additionally, a coupling between the vortex circularity and the polarity of its

core could not be experimentally shown,[SKR16] although it had been theoretically predicted for spherical shells.[GKS14] Similarly, larger areas of coupling vortices with same circulation sense were observed by Nissen *et al.* for arrays of caps with a similar geometry (Py, $D = 330\,\mathrm{nm}$, $t_\mathrm{F} = 50\,\mathrm{nm}$), while, again, no circularity-polarity coupling was found across the array.[NMK15] Nevertheless, an individual coupling of polarity and sense of circulation was indicated within each individual cap of an array.[Nis16] In this study, thicker Py caps ($D = 850\,\mathrm{nm}$, $t_\mathrm{F} = 130\,\mathrm{nm}$) observed by magnetic transmission X-ray microscopy (MTXM) kept a fixed chirality each time they nucleate vortices, so that an inversion of the circularity was always accompanied by an inverted core polarity.[Nis16]

3.2.1 Exchange Bias in Hollow Hemispheres

As in the case of disks, also particles capped with an EB bilayer were investigated. At first, depositing a thin film system contianing an antiferromagnet and a ferromagnetic layer on top of the arranged spherical particles was observed to significantly affect the strength of the EB: The caps showed a higher EB shift H_EB alongside higher coercivity as compared to the flat film, which the authors attributed to the inverse thickness dependency (Equation 2.4.3) and the gradually decreasing film thickness of the caps.[ZWM09] Furthermore, both the EB strength as well as the coercivity were shown to increase for reduced cap diameter.[WYW11] With enhanced curvature (i.e. towards smaller diameters) the authors mention that the interfacial roughness could be larger towards the cap's rim, and that therefore the enhanced EB and coercivity could be explained by an increased number of uncompensated antiferromagnetic interface moments in this region.[WYW11]

However, also for non-thickness modulated microsturctured objects, the dimensions like the width w of a micro- or nanowire were observed to affect the EB in a similar manner (e.g., $H_\mathrm{EB} \propto 1/w$)[NSL05,NOK99], and hence, it would be desirable to rather compare a flat disk, a thickness-modulated but flat disk and a cap in order to disentangle the origin of the effect.

A detailed FC study on exchange-biased cap arrays was presented by Nissen *et al.* in Ref. [NKM16]: Firstly, they evidence that - just like it had been shown for disks,[SSAB06] - the vortex texture can be stabilized in the caps by a ZFC procedure, increasing the nucleation field as well as the absolute annihilation field.[NKM16] Accordingly, they performed FC procedures at different external magnetic fields H_FC, which stabilized a shifted vortex state at small H_FC or a C-state, when H_FC was larger than the annihilation field of the unbiased cap $H_{\mathrm{ann},0}$.[NKM16] These cooling fields are large enough to align the pinning antiferromagnetic moments along the FC direction during the procedure, however, after the second hysteresis cycle some of these moments were seen to have again rearranged following the ferromagnet's vortex configuration. Although the first hysteresis loop might indicate a remanent C-state, the displaced vortex texture in the antiferromagnet causes the occurrence of remanent vortex states in the ferromagnet in subsequent loops. On the other hand, larger antiferromagnetic film thicknesses allow for the imprinting of a stable mono-domain texture by using adequately large H_FC, which remain pinned due to the higher stability (cf. grain classification subsection 2.4.2) for several subsequently measured hysteresis loops. Hence, the relative change in EB strength between first and second loop is smaller for thicker antiferromagnetic layers. Building of the analysis of the characteristic field's

asymmetries with respect to the loop shift (ΔH_{nuc} and ΔH_{ann}, cf. Equation 3.1.4) proposed for disks,[GYV15] the authors identified that the caps reversed via the formation of distorted viscous vortices, while the asymmetry depended on the antiferromagnetic thicknesses.[NKM16]

Overall, it may be desired to stabilize vortices in small magnetic entities when aiming to introduce them in high density data storage applications.[BKD08] Alternatively, there may also be the interest to stabilize onion states over a wide range of cap dimensions. From the previously discussed phase diagrams for individual soft magnetic disks and caps, remanent onion states are only expected when the objects are smaller than 100 nm. There are however applications, in which a capped particle shall serve as a micro object with a defined magnetic moment, e.g. in lab-on-a-chip scenarios where magnetic torque is used to manipulate the object.[HRT21,EMS16]

Ultimately, we could show in Ref. [TRH21] that EB can be used to design magnetic caps with a stable onion configuration at dimensions where this would be energetically unfavorable in case of pure ferromagnetic caps. Starting from these first investigations, this thesis will concentrate in more detail on the influence of differently designed EB bilayers on the caps' magnetic reversal.

4. Micromagnetic Simulations of Ferromagnetic Hollow Hemispheres

As it has been observed in measurements and simulations, significant differences are obtained between the magnetization reversal characteristics of single magnetic disks on the one hand and disk arrays on the other (cf. section 3.1), which is a result of the magnetostatic coupling between the disks in the lattice.[NGS02] In order to approach this effects of coupling for hemispherical magnetic caps, micromagnetic simulations have been performed for the present thesis with the finite-difference based micromagnetic simulation software *Boris* (Version 3.0 - released 18.12.2020),[Bor,Lep20], version 3.0. An advantage of this software is that simulations can be accelerated due to the use of the graphical processing unit (GPU), as the simulations can otherwise become too computationally demanding due to the three-dimensional nature of the studied objects. The simulations within this chapter focus on CoFe caps with a diameter of $D = 500\,\mathrm{nm}$, as the simulated magnetic caps shall reflect the cap arrays mainly studied in the experiments of this work. An exemplary ferromagnetic thickness of $t_\mathrm{F} = 30\,\mathrm{nm}$ was chosen, for which a magnetization reversal via vortex nucleation, motion and annihilation is expected.

4.1 Geometry Discretization, Material Parameters and Simulation Settings

Starting with a single cap (I), the simulation mesh was generated by the subtraction of two discretized ellipsoids with the help of the scripting module *NetSocks.py* provided for *Boris*.[Bor] Here, the inner ellipsoid is a sphere with diameter D and the outer one has the dimensions according to the ferromagnetic film thickness t_F with the height of $h = 2 \cdot t_\mathrm{F} + D$ and a width and depth of $w = d = 2 \cdot t_\mathrm{F} \cdot g + D$, where g is a factor of 0.4 in order to consider the thickness reduction towards the sides of the cap in accordance to the observations published in Ref. [TRH21] This is an important geometric detail significantly affecting the magnetic characteristics, as shown in Figure 3.9. Half of this hollow sphere is then considered for the simulation of the ferromagnetic cap with $Co_{70}Fe_{30}$ (CoFe) as the material of choice in the present thesis, whose characteristics are reflected by the saturation magnetization $M_\mathrm{S} = 1515\,\mathrm{kA/m}$,[MRH22] the exchange stiffness $A = 1.5 \times 10^{-11}\,\mathrm{J/m}$[PGR21,BBK11] and a uniaxial anisotropy along the x-axis with $K_\mathrm{u} = 3\,\mathrm{kJ/m^3}$[MHR20]. As introduced in section 2.1, the dimension of features like domain walls is in the range of the material's exchange length $l_\mathrm{ex} = \sqrt{A/K_\mathrm{eff}}$ (Equation 2.1.15).[Abe19,HS98] The effective anisotropy as the sum of K_u and $K_\mathrm{d} = 1/2 \cdot {M_\mathrm{S}}^2 * \mu_0$ yields $l_\mathrm{ex} \approx 3.2\,\mathrm{nm}$ in the

case of the here assumed properties of CoFe (cf. Permalloy, $l_{\mathrm{ex}} \approx 5.7\,\mathrm{nm}$). With the intention to accurately resolve the magnetic texture of domain walls and vortices, the cubic cells for the simulations were chosen to have a size of $(2.5\,\mathrm{nm})^3$ - significantly smaller than the exchange length. The cap is therefor represented by 5 cells at its sides and by 12 cells at its top (normal to surface direction). Note, that for three-dimensional objects, the discretization further limits the representation of the geometry, e.g. curved parts. For the simulation of hollow hemispheres, this results in a staircase-like mesh, so that for very small caps the cell size would need to be reduced for the accurate modeling of the shape. Alternatively, one could use finite-element rather than finite-difference method based simulation tools, where a mesh of tetrahedral cells is generated. [TRH21] However, the mesh generation is non-trivial which challenges the implementation of finite-element solvers. [Abe19] Unfortunately, the available open-source packages for finite-element micromagnetics do only run on central processing units (CPU). As a consequence, the finite-difference based software *Boris* was used for the simulations in this thesis due to the available GPU acceleration, the user-friendly appearance and the scripting module for *Python*.

The mesh for the simulation of two coupled caps (II) is created likewise to the individual cap (I) by subtracting two touching spheres from two ellipsoids, both centered with respect to the respective sphere.

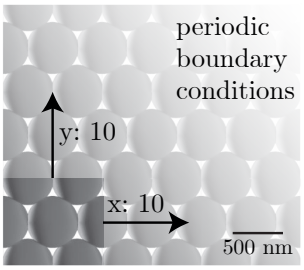

Figure 4.1: Simulated array geometry (periodic boundary conditions).

By this approach, also a reduced cell of a hexagonal array (III) can be generated, in order to mimic experimental conditions, where the caps in a lattice are coupled, with the self-assembled templating spheres being in direct touch. As the so-called supermesh, i.e. the volume in which the simulation takes place, is always cuboid, a geometry of one full cap in the center surrounded by six half caps was chosen, which is then extended in the simulation by the use of periodic boundary conditions as displayed in section 4.1: In the conducted simulations for hexagonal arrays, the chosen finite simulation window is repeated 10 times along both $x-$ and $y-$ direction resulting in a wrap-around effect. [Bor]

In order to calculate the magnetization reversal of the described geometries (I, II and III), i.e. deriving the relaxed magnetization textures at each field step in a specifically chosen sequence of the applied magnetic field H, *Boris* offers a steepest descent solver which is based on the *Barzilai-Borwein* step size selection formulas. [Bor] To determine static solutions of the described micromagnetic problems, the Landau-Lifschitz-Gilbert equation can be solved neglecting the precession term, which corresponds effectively to the minimization of the total energy density $\varepsilon_{\mathrm{tot}} \propto \vec{m} \cdot \vec{H}$ (cf. section 2.1). In contrast, for problems regarding time-dependent magnetization dynamics, the precession term needs to be considered in the Landau-Lifschitz-Gilbert equation, which requires to use another solver to dynamically derive the damping dependent evolution of the magnetic textures. Computing only for the static solutions reduces the computation time, however, it is very important to choose an appropriate stopping criterion for each simulated field step. Here, the criterion is the normalized torque $|\vec{m} \times \vec{H}_{\mathrm{eff}}|$ set to 10^{-10},

meaning that the simulation continues with the next magnetic field value of the sequence once a texture is found for which the normalized torque undergoes this threshold value. Aiming for rather smooth hysteresis curves, the magnetic field step size should be adequately small, and was therefor set to 0.5 kA/m for the present simulations.

The effective field $\vec{H}_{\mathrm{eff}}$ results from the summed contributions of the micromagnetic equation, where all terms that can possibly be implemented are described in Ref. [Lep20]. For the simulations at hand, the energy terms for exchange coupling (Equation 2.1.3), anisotropy energy (Equation 2.1.9), demagnetization energy (Equation 2.1.5) and Zeeman energy (Equation 2.1.1) are considered.

Although the micromagnetic simulations can shed light on differences in the reversal behavior, it is important to realize, that a simulation with periodic boundary conditions is only a first approach to extended arrays but can unfortunately not be used to study global configurational effects as presented, .e.g., in Ref. [VFS14]. Nevertheless, the available computational power and random access memory are the bottleneck for simulations like these.

4.2 Simulated Magnetization Reversal: Single Cap vs. Cap Array

The results of the conducted simulations are summarized in Figure 4.2 for the three above described geometries I, II and III, where the magnetization reversal curves are shown together with exemplary false-color images of the magnetic textures at characteristic points throughout the reversal. For each magnetic field step, the total and individually contributing energy densities ε of the relaxed texture have been exported from *Boris* and are plotted in Figure 4.3 for the course of the decreasing hysteresis branch. Throughout the discussion of the results, the content of both figures will be presented side by side.

The hysteresis curve acquired for a single magnetic cap (I) resembles the same features as for the comparably smaller and soft magnetic cap in Figure 3.9. Starting from positive saturation, the cap shows an onion state, which transits to a C-state, in which it possesses a short side-by-side domain wall at $H_{\mathrm{ext}} = 15\,\mathrm{kA/m}$ and $M_{\mathrm{L}} = 0.7 M_{\mathrm{S}}$. Next, at a magnetic field of 14 kA/m, the cap nucleates a vortex. The nucleation is accompanied by a severe reduction of the demagnetization energy density ε_{d} overcompensating the rise in $\varepsilon_{\mathrm{ex}}$, $\varepsilon_{\mathrm{an}}$ and ε_{Z}, so that the total energy density is reduced. Subsequently, the vortex core is shifted throughout the course of the reversal until it annihilates at an annihilation field of $-88\,\mathrm{kA/m}$, which can be seen from one distinct change in M_{L} (see inset in Figure 4.2, I.). At zero magnetic field, the macroscopic magnetization is zero and the demagnetization energy density reaches a minimum, as the vortex core is fully centered. Driven by a higher demagnetization energy for an onion state as compared to the 300 nm Py cap, the vortex is present over a field range of 102 kA/m, whereas the smaller Py cap stabilized a vortex over a range of 57 kA/m only. It can be concluded, that the course of the hysteresis branch for this individual cap is mainly driven by the interplay of ε_{Z} and ε_{D}, as these two energetic contributions have the highest impact on the total energy, which can be seen from the absolute scale of the values in Figure 4.3.

When the magnetization reversal of two magnetic caps (II) is simulated for magnetic fields

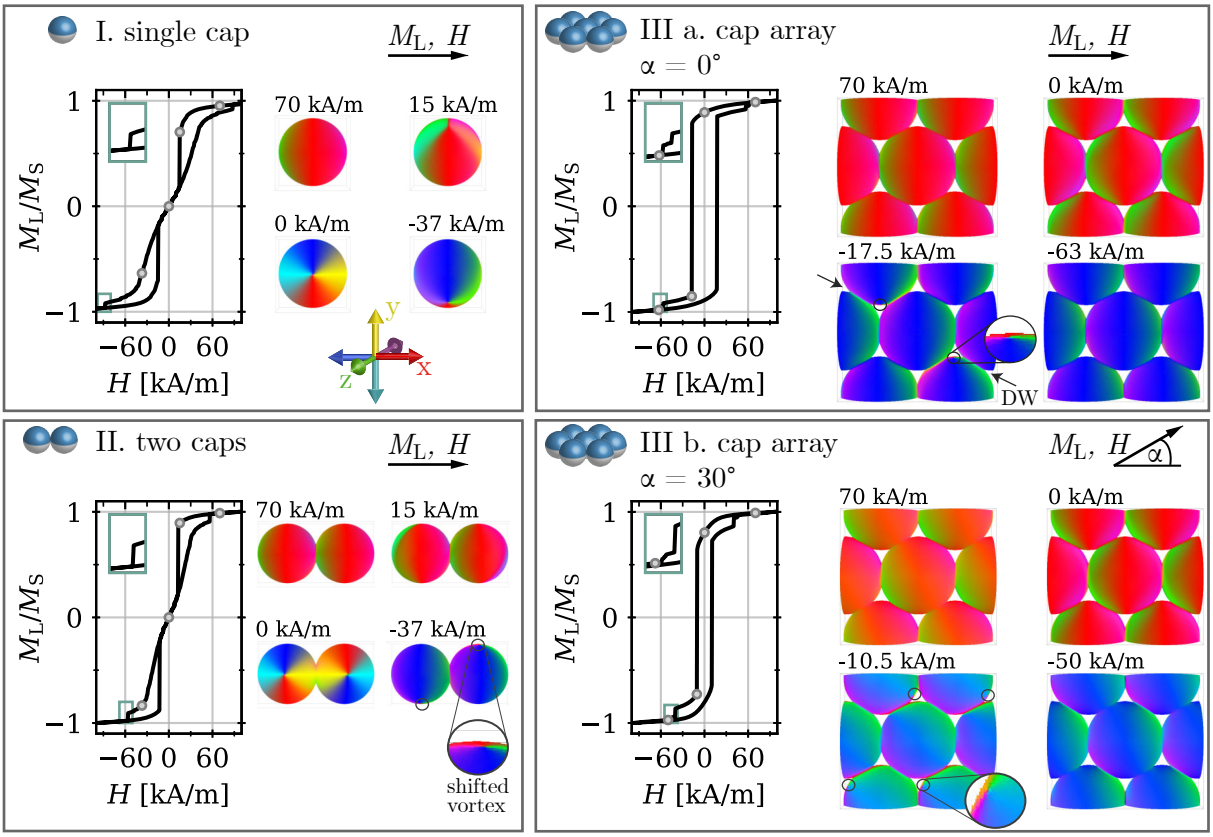

Figure 4.2: Results from micromagnetic simulations for CoFe caps with a diameter of 500 nm and a nominal thickness of 30 nm under consideration of a thickness gradient. The derived magnetization reversal curves are shown alongside false-color images of the simulated mesh in the top view for characteristic states with the given magnetic fields that correspond to the marked data points on the decreasing hysteresis branch. In I., II. and III., the behavior of a single magnetic cap, two touching magnetic caps and an array o touching caps are shown, respectively. For III., periodic boundary conditions have been applied. Note, that M_L denotes the magnetization component parallel to the applied magnetic field H. In III a., H is oriented parallel to the main symmetry axis of the lattice while it is applied in an angle of $\alpha = 30°$ to this symmetry axis in III b. Far shifted vortex cores which are not obviously seen in the top view are marked by gray ellipses, with exemplary detail views. The arrows indicate domain walls referred to in the text. The insets in the hysteresis panels indicate details of the annihilation region: It can be seen, that for the cap doublet both vortices annihilate simultaneously, while for the cap arrays the process is indicated by two or more steps.

along the long axis of this doublet, the hysteresis shape changes in a way, that a pair of vortices with opposing circulation sense is present only between $H_{nuc} = 12\,\mathrm{kA/m}$ and $H_{ann} = -56\,\mathrm{kA/m}$ on the descending branch, which is indicative for a reduction of the vortex stability field regime in comparison to the single cap (I). Based on the observations for magnetostatically coupled disks,[JRA09] vortices of same circulation sense would have been expected for this alignment in which the external magnetic field axis is parallel to the long axis of the doublet. However, the situation here differs in terms of exchange coupling. As the caps are touching each other, they are not only magnetostatically but also exchange coupled which explains why the two vortices have opposing circularity in order to create parallel aligned moments at the caps' physical connection. Note that these differently circulating vortices have also been found when the magnetic field

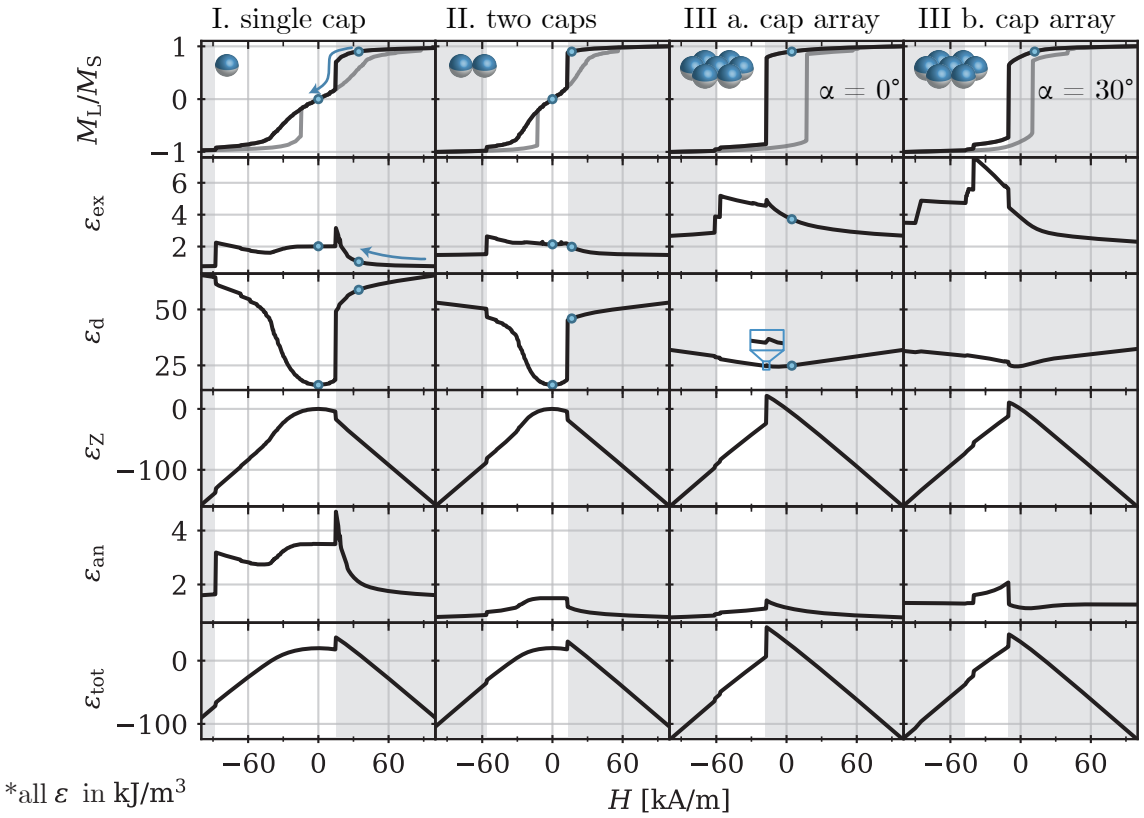

Figure 4.3: Below the simulated magnetization reversal of the different geometries I, II and III, as introduced in Figure 4.2, the evolution of the considered energetic contributions and the total energy density are shown for the descending branch (blue arrows direction, black branch). The gray shaded regions indicate the presence of purely onion states. The blue data points indicate the energy density values extracted in Table 4.1 for vortex ($M_L = 0$) and onion states ($M_L = 90\,\%{\cdot}M_S$).

is applied under an angle of 30° with respect to the doublet's long axis (not shown). Further, the caps do not reach the C-state, as their onion states stabilize each other. This can be understood from the comparison of the energy situation for onion states in both the single cap (I) and the doublet (II): The exchange and demagnetization energy density for onion states with a net magnetization of $M_L = 90\,\%{\cdot}M_S$ in the different simulated geometries are listed in Table 4.1 and indicated by gray data points in Figure 4.3). The exchange energy density is slightly increased for the doublet with two onion states as compared to the single cap, which is probably due to the touching region of the caps, where neighboring magnetic moments of the two caps point in opposite direction at the pole. Nevertheless, this additional exchange energy density is overcompensated by a significantly reduced demagnetization energy for the onion state, because the magnetostatic coupling of both caps causes less stray fields to emerge from the touching region than from the outside poles of both caps. On the other hand, the energetic differences for vortices in a single cap and the doublet are negligible. Consequently, the doublet (II) energetically stabilizes the onion in a way that the vortices nucleate 'later' and annihilate 'earlier' on the descending branch as compared to the single cap (I). The described effect of magnetostatically stabilized onion textures is also observed for the magnetization reversal of a hexagonal array of magnetic caps (III a.) simulated with the magnetic field applied parallel to

Table 4.1: Demagnetization and exchange energy densities of vortex ($M_L = 0$) and onion states ($M_L = 90\,\%{\cdot}M_S$) linked to Figure 4.2 and Figure 4.3. The three configurations are a single CoFe cap (I), two of these caps (II) and a hexagonal array of these caps (III a.). The onion state referred to is aligned with the net magnetization parallel to the main symmetry axis of the array or the long axis of the doublet, respectively.

	Single cap		Two caps		Hexagonal cap array
Energy Density	Onion	Vortex	Onion	Vortex	Onion
ε_d [kJ/m^3]	58.8	16.2	46.0	16.3	24.9
ε_{ex} [kJ/m^3]	1.0	2.0	2.0	2.1	3.7

the lattice's main symmetry axis ($\alpha = 0°$). The demagnetization energy density for a state with only onion textures is even more reduced than in the doublet case and hence, the caps maintain the onion textures until remanence, and even at negative magnetic fields. At $H = -17.5\,\mathrm{kA/m}$, two of the four $(1 + 6/2)$ caps in the reduced lattice nucleate vortices, while the other two caps directly switch to the opposing onion state. The vortices nucleated are already far shifted towards the lower or upper side of the cap (towards $+y$ or $-y$) due to the Zeeman energy. This nucleation process is accompanied by a small reduction of ε_d of about $0.5\,\mathrm{kJ/m^3}$ only (detail view), indicating that the reversal process is not governed by ε_d as it was the case for the single magnetic cap. The vortices nucleate with opposing circulation sense as previously observed for the doublet of caps (II). At a magnetic field of $H_{ann} = -57\,\mathrm{kA/m}$, the vortices are annihilated, resulting in a lattice of caps exhibiting onion states oppositely magnetized with respect to the initial positive saturation. The inset in the hysteresis panel of Figure 4.2 III a. further reveals that the annihilation is a two step process, where both steps are linked to a reduction of the exchange energy density: At first, the vortices are expelled, and secondly two remaining domain walls (see arrows in III a.) between the caps in the upper left and the lower right corner are subsequently annihilated at $H = -62\,\mathrm{kA/m}$.

For the hexagonal array geometry, a second hysteresis was simulated (III b.), this time with the magnetic field applied along a direction between two of the main symmetry axes of the lattice ($\alpha = 30°$). Starting from saturation, all caps show onion textures aligned with H. When approaching zero field, a rotation of these onion textures is observed, as the Zeeman energy becomes zero at $H = 0$ and the orientation of all onions along the hexagonal lattice symmetry axis allows for the reduction of the demagnetization energy. At $H = 0$, the false-color images therefore indicate the same onion textures for both $\alpha = 0°$ and $\alpha = 30°$. One might argue that the rotation of the onion states is further influenced by the parallel alignment of the uniaxial anisotropy with the lattice symmetry axis, however, the lowering of ε_d induced by the rotation of the magnetic onion textures is about one order of magnitude larger as compared to the lowering of ε_{an} (between $M_L = 90\,\%{\cdot}M_S$ and $M(H = 0)$), which implies this process to be driven magnetostatically. At $H = -10.5\,\mathrm{kA/m}$, the central chain of caps in the reduced lattice directly switches to the opposing onion state. Interestingly, the other caps form two vortex cores where one is located in the cap's lower half (top row) and one in the upper half (bottom row). As for III a., $\alpha = 0°$, the annihilation is characterized by multiple steps, where the individual vortices as well as the afterward maintained domain walls annihilate at different magnetic fields.

4.3 Conclusion

To conclude, certain expectations for the magnetization reversal in realistic samples can be concluded from the discussed micromagnetic simulations. At first, severe differences in the behavior of individual magnetic caps and those in an array formation have been derived, and therefore, magnetization reversal loops of samples with assembled layers of magnetically capped particles cannot reveal the nature of an individual cap.

In the array, onion states in the caps are stabilizing each other via magnetostatic coupling. This is responsible for a difference in the macroscopically determined values for the coercive field H_{C} and the remanent magnetization M_{R} of individual caps and those in an array, and consequently for differences in the phase boundaries for the remanent textures as observed in literature (cf. phase diagrams in Refs. [Str15, SKS12]).

A second observation is, that multiple reversal paths are taken by the caps in the array. While the central chain of caps in the simulated hexagonal array directly switches to the opposing onion state, the other caps undergo vortex nucleation. To study this effect in more detail would require a simulation with a mesh representing a larger unit cell, i.e., more than just one full and six half caps.

In realistic measurements, no distinct annihilation field is expected but rather a distribution of observable characteristic fields. Reasons for this are, that the annihilation was seen to take place via multiple steps and that a variety of cap properties is expected within the measured region. Finally, the simulations revealed, that the orientation of the symmetry axes with respect to the applied magnetic field affects the course of the hysteresis and the textures formed within the array. A consequence for hysteresis measurements of realistic magnetic cap arrays is that only the average of all reversal types within a measured region can be resolved. The resulting magnetization reversal curve will contain the superposition of all prevailing orientations of sub-lattices in the case of a non-perfectly self-assembled array of templating particles.

Summarizing, a variety of neighborhood situations, like the orientation of the hexagonal array symmetry with respect to the axes of the anisotropy and the applied magnetic field, influences the investigations of cap arrays. Additionally, other factors which were not accounted for in these simulations, like defects in the lattice and a size distribution of the templating particles, may further add to a distribution of magnetic properties.

It is important to mention that these observations and the drawn conclusions are qualitatively also valid for magnetic caps with EB. Magnetostatic interactions, the exchange interaction at the connecting sites and the array orientation are factors influencing the caps' reversal regardless of the presence of EB. Nevertheless, the EB effect arising when the ferromagnetic cap shares an interface with an antiferromagnetic layer will add complexity to the energetic situation and, therefore according simulations for EB caps would be desirable. In principle, the unidirectional anisotropy could be implemented as an additional field H_{EB} added to the effective field H_{eff} as shown in Ref. [TRH21]. However, it is assumed that the EB follows the curvature of the cap

(cf. subsection 7.2.1) and that in the case of ZFC, circular EB is imprinted. Consequently, the EB would need to be implemented as a local property. Exploring possible methods to realize the latter with the help of the utilized software *Boris* would have been beyond the scope of this thesis. Exemplary approaches for the advanced modeling of EB in micromagnetic simulations are proposed in Refs. [CVA16, DaCR19].

5. Fabrication of Arrays of Magnetic Hollow Hemispheres

The fabrication of samples with magnetically capped particles is a two steps process as sketched in Figure 5.1: A self-assembly of non-magnetic spherical particles similar to the process described in Ref. [MFO95] is followed by the deposition of the desired thin film system on top of the spheres. In the following, both procedures shall be described as they were performed to receive the samples investigated in the thesis at hand.

5.1 Self-Assembly of Spherical Non-Magnetic Particles

With the aim to create samples with close-packed regions of non-magnetic particles, aqueous stock suspensions of silica particles were purchased from *micromod Partikeltechnologie GmbH* with a nominal concentration of 50 mg/ml (sicastar, hydrophilic surface with terminal COOH groups, 0.5, 1 and 1.5 µm in diameter).

At first, the substrate (Si or glass) is placed on a hot plate at a plateau temperature of 35 °C, which is placed with a tilt angle of roughly 9°. Then, a 30 µl droplet of distilled water with 10 vol% ethanol is placed with a microliter pipette in the center of the tilted substrate. Next, 4.5 µl of the stock particle suspension are carefully placed on top of the water-ethanol drop. The evaporation process starts at the upper edge and proceeds towards the lower edge of the droplet,[MFO95] forming a layer of densely packed particle arrays with an extension of several square millimeters surrounded by areas of lower particle density. The latter regions with non-regularly arranged particles are called sub-monolayered areas in the following. While the liquid evaporates, the sample is rotated on the tilted hot plate by 180° around the substrate normal (cf. Figure 5.1) every 3 to 6 minutes which has been seen to qualitatively improve the spatial distribution of mono- and multilayered particle regions on the sample. After 15 minutes the liquid has fully evaporated.

In the case that glass substrates are used, a cleaning procedure precedes the particle assembly to increase the hydrophilic character of the substrate surface. Therefore, the substrate is covered by concentrated sulfuric acid for 24 hours and afterwards stored in ethanol.[MFO95] When the samples are prepared for investigations in an electron microscope, e.g. XMCD PEEM, glass samples are unfavorable, as they are insulating and hence cause strong charging effects. Instead, Si substrates are used for this purpose, where the conductivity of the substrate surface can be further enhanced by an additional layer of sputter deposited Pt.

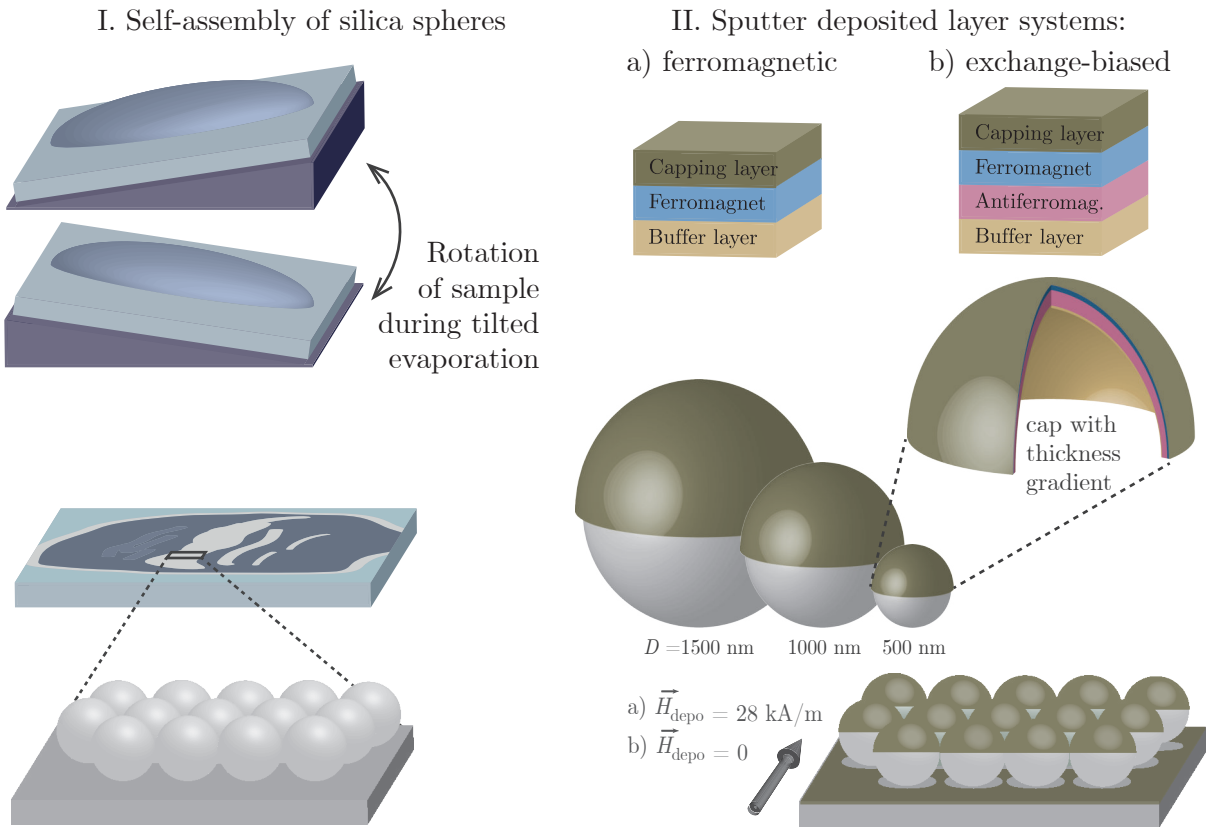

Figure 5.1: Sketch of the fabrication of both ferromagnetically and exchange-biased capped particles: Starting with the self-assembly (I.) procedure, the droplet containing the particle suspension is placed on the tilted sample for evaporation, which results in an arrangement of mono- and multilayered regions of hexagonal close-packed silica particles aside of regions with non-arranged and randomly distributed particles (cf. section 7.1). Next, the chosen magnetic layer system is deposited on the full sample, i.e. on top of the region with sphere arrays, on the areas of plain substrate and also on the substrate through the interstices of the close-packed array (shadow effect). The two investigated thin film systems are shown schematically (not to scale). The three different particle sizes used are shown, with the focus in this work being laid on particles with a diameter of $D = 500\,\mathrm{nm}$. Additionally, the depicted magnetic cap with a segment removed along the azimuthal angle indicates the gradient of the layer thicknesses towards the sphere's equator. Here, the ratio of the individual layers is scaled correctly for an exemplary layer system of Cu(10 nm)/IrMn(30 nm)/CoFe(10 nm)/Al(4 nm) on top of a sphere with $D = 500\,\mathrm{nm}$.

5.2 Metallic Layer Deposition on top of Assembled Particles

The deposition of the metallic layers on top of the non-magnetic spherical particles is realized by radio-frequency (RF) sputter deposition. This physical vapor deposition technique is based on the acceleration of ions onto a target material from which atoms are ejected due to the ions' momentum transfer. These target atoms are subsequently deposited on the substrate to create polycrystalline films.

The ions are delivered by a plasma, in this case from the inert gas Ar, which is ignited inside a vacuum chamber. In this chamber, the target material is connected to the RF alternating current source via a capacitor and the substrate is connected to ground. Hence, the free charge carriers of the plasma move in the electric field spanning the room between the target and the

substrate, where electrons move at higher velocities due to their lower mass as compared to the ions. As these electrons can only be discharged by the substrate but not at the target, a so-called decelerating potential builds up between the target and the substrate, which depends on the capacitance of the capacitor. Consequently, this constant DC potential (between 400 and 800 V) causes the Ar ions to be accelerated towards the negatively charged target (cathode), where they impinge and transfer their kinetic energy to the material from which atoms and clusters are ejected. These are subsequently deposited onto the substrate.

For the fabrication of the samples investigated in this thesis, the deposition of various layer systems on top of non-magnetic particle arrays was realized with the sputter system *Leybold Heraeus Z400*. While the chamber reaches a base pressure below 10^{-6} mbar, the Ar gas flows into the simultaneously pumped chamber at a flow of 140 sccm during the sputter process to set a working gas pressure in the order of 10^{-2} mbar. Within the chamber, permanent magnets can be mounted on the sides of the substrate holder in order to generate a homogeneous magnetic field of $H_{\mathrm{depo}} = 28\,\mathrm{kA/m}$ parallel to the sample surface. This magnetic field determines the orientation of the ferromagnetic anisotropy and can further be used to introduce an initial EB in systems with ferromagnetic and antiferromagnetic layers.[MHR20] As the magnetic field influences the moving charge carriers within the plasma, the deposition rates for constant DC potential differ when the magnets are mounted, as can be seen from the tables summarizing the sputter parameters used for the deposition of various chosen layer stacks on top of the assembled silica spheres (Table 5.1 and Table 5.2). Except stated otherwise, all layer systems discussed throughout the following chapters have been deposited in the presence of a magnetic field.

5.3 (Zero) Field Cooling

For post-modification of the EB within the fabricated arrays of capped particles, an annealing procedure can be applied. For this, the sample is heated to a temperature above the blocking temperature of the antiferromagnetic layer but below the Curie temperature of the ferromagnetic material and, subsequently, cooled down to room temperature. Depending on the aimed modification, it is differentiated between cooling in an external magnetic field (FC) strong enough to saturate the ferromagnet and cooling with zero external magnetic field (ZFC).

The samples are placed face down, with the layer system in direct contact with a heatable sample holder, in a vacuum chamber at a base pressure of 4×10^{-6} mbar. For FC, the magnetic field of $(120 \pm 10)\,\mathrm{kA/m}$ is aligned parallel to the EB direction which had been initialized during the deposition. After heating the sample stage to the desired temperature T_{FC}, this temperature is kept for 60 min before stage and sample are cooled down to room temperature. In the case of ZFC, the samples were previously subjected to a demagnetization procedure in order to minimize the remanent magnetization of the ferromagnet. In this demagnetization routine, an alternating magnetic field with successively reduced field strength is applied. When working with disks or caps, the demagnetization typically results in remanent vortex states, if the objects reverse their magnetization via vortex formation. Consequently, it is possible to imprint a circular EB in a subsequent ZFC process (cf. subsection 3.1.1).

Table 5.1: Sputter parameters for materials deposited on top of the assembled particle arrays with a magnetic field applied during deposition. Here, ranges for the sputter rates are given, as depositions for different sample sets, i.e. at different times with target changes in between, resulted in varied sputter rates. However, samples with the same particle size and thicknesses in the layer stack are still considered comparable.

Material	Sputter rate [nm/min]	Ar gas flow [sccm]	DC potential [V]
Cu	6.0 to 8.8	140	600 to 700
$Ir_{17}Mn_{83}$	4.7 to 6.0	140	700 to 750
$Co_{70}Fe_{30}$	3.2 to 3.5	140	600
$Ni_{81}Fe_{19}$	4.3	140	600
Si	3.7 to 5.1	140	700
Al	1.6 to 2.5	140	600

Table 5.2: Sputter parameters for the materials deposited on top of the assembled particle arrays in the absence of a magnetic field.

Material	Sputter rate [nm/min]	Ar gas flow [sccm]	DC potential [V]
Cu	4.6 to 5.2	140	600
$Ir_{17}Mn_{83}$	2.9 to 3.1	140	750
$Co_{70}Fe_{30}$	1.9	140	600
$Ni_{81}Fe_{19}$	2.3 to 2.4	140	600
Si	1.8 to 2.0	140	700

6. Methods for Characterization

6.1 Structural Characterization: Scanning Electron and Helium Ion Microscopy

In order to structurally characterize microscopic objects like capped particles, different imaging techniques aside of optical microscopy were applied and will therefore be briefly introduced.

The optical resolution in classical light microscopy defines the minimum distance in which two features can be distinguished as individual points. It is limited by diffraction and cannot be pushed below 200 nm in standard light microscopes.[Kub13] When charged particles are used instead as an illumination source, e.g. electrons or helium ions that are accelerated via a voltage U in the kV regime, much higher resolved images can be obtained due to the shortening of the electron's (or ion's) wavelength $\lambda = h/\sqrt{2Umq}$. Here, m is the mass of the particle, h PLANCK's constant and for electrons and singly charged ions the charge q equals the elementary charge e.

For both types of microscopes, scanning electron and Helium ion microscopy (SEM and HIM), the beam of primary electrons or ions is scanned over the sample area by a deflection unit, upon which secondary electrons are created due to inelastic scattering processes. These secondary electrons can then be detected with a so-called Everhardt-Thornley detector, where the mapped intensity, i.e. the brightness, corresponds to the number of emitted electrons. This detector is usually positioned to one side of the sample stage, so that electrons escaping from edges facing the detector have a higher chance to be detected than electrons emitted towards the opposite direction.[Was12] The result is the appearance of shadows.

While the focusing in both microscopes is realized via electrostatic or magnetic lenses, the techniques differ in the generation of the primary particle beam. While for SEM a field emission electron source is used, the HIM makes use of a gas field ion source (GFIS). This source is made of a needle from a single crystal metal. Within the source chamber, this needle is modified to possess a pyramidal structure on its apex by raising the extractor voltage up to the point of field evaporation which rearranges the atoms in the tip.[NWE07] For imaging, the helium gas is admitted close to the needle which is set at high positive voltage, typically around 30 kV. The helium atoms in the apex' vicinity are polarized due to its electric field gradient, which causes the tunneling of electrons from a helium atom into the metal needle and hence, the creation of positively charged helium ions. Due to the pyramidal apex shape, three ion beams emerge, of which one is guided into the microscope column. Owing to the higher mass of a helium ion as compared to electrons, its wavelength is smaller than that of accelerated electrons. Additionally,

the lateral expansion of the ion beam within the sample is smaller than in the case of a SEM, meaning that the ion beam diverges more slowly once it has entered the material. Hence, the resolution is higher as the recorded secondary electrons originate from a smaller area. [NWE07]

In HIM, Helium ions are used as they have a comparably low mass and therefore act only slightly destructive in the sense of sputtering the sample surface in the region under investigation. When changing to higher mass ions, like Gallium, the sputter rate is enhanced, which is nowadays even used as a tool for nanomachining in so-called focused ion beam (FIB) applications. The focused beam of ions can be precisely scanned across the sample which allows to mill parts of the structures, e.g. to create cross-sections or even thin lamellas that can later be studied in transmission electron microscopy (TEM). Often, FIB-SEM crossbeam setups are used, in which the electron and ion beam coincide in the sample plane in order to simultaneously image the milling process with the SEM. [YM05] For cross-sections, usually an additional layer is deposited before milling by either electron-beam-induced or ion-beam-assisted deposition with the help of a gas injection system. It protects the sample surface during the milling in order to achieve steep cuts without damage.

6.2 Magneto-optic Characterization

Magneto-optic phenomena that relate to a sample's magnetization are the circular birefringence and the circular dichroism. [Coe10b] While the latter describes a difference in the sample's absorption coefficients for left and right circular polarized light, a difference in the refractive index n for the two circular polarizations is called circular birefringence.

For visible light, the Faraday effect and the Kerr effect are distinguished, which describe the rotation of the polarization plane of linear polarized light passing through a magnetized material or being reflected from its surface, respectively. Although the Kerr effect is smaller in magnitude, Kerr magnetometry has become a vastly used non-destructive technique for the characterization of non-transparent magnetic samples.

6.2.1 Magneto-optic Kerr Effect

The magneto-optic Kerr effect (MOKE), named after the physicist John Kerr, causes a change in the polarization state of linear polarized light which is reflected from a magnetized sample. The incident linear polarized light can be described as a superposition of two electromagnetic waves with opposing circular polarization. [Coe10b] The magnetized sample possesses different refractive indices for both of these portions (circular birefringence), which causes different propagation velocities in the medium and, thus, a phase shift. Besides the resulting rotation of the polarization plane of the reflected light, the absorption of both circular polarized parts differs in the magnetized sample (circular dichroism). As a consequence, the reflected light is elliptically polarized with the major axis of the ellipse being rotated by the Kerr angle Θ_K with respect to the initial polarization direction.

Macroscopically, the change of the magneto-optical effects may be described by the electric induction $\vec{D}$ via the dielectric displacement law $\vec{D} = \widetilde{\epsilon}\vec{E}$, where the permittivity tensor $\widetilde{\epsilon}$ acts

on the incident light's electric field vector $\vec{E}$. With the permittivity tensor, the influence of the interaction between the incident light and a optically anisotropic and possibly magnetic material on the light's electric field vector can be described. In the case of the magneto-optic Kerr effect and for cubic crystals, the reduced magnetization $\vec{m} = \vec{M}/M_\mathrm{S} = (m_\mathrm{x}, m_\mathrm{y}, m_\mathrm{z})^T$ is found in the off-diagonal elements of this tensor:

$$\widetilde{\epsilon} = \epsilon_0\epsilon_\mathrm{r} \begin{pmatrix} 1 & -iQm_\mathrm{z} & iQm_\mathrm{y} \\ iQm_\mathrm{z} & 1 & -iQm_\mathrm{x} \\ -iQm_\mathrm{y} & iQm_\mathrm{x} & 1 \end{pmatrix}, \tag{6.2.1}$$

when neglecting higher order terms.[HS98] Here, $\epsilon_0\epsilon_\mathrm{r}$ is the permittivity and Q the material specific Voigt constant. As a result, the dielectric displacement law transforms to:[HS98]

$$\vec{D} = \epsilon_0\epsilon_\mathrm{r}(\vec{E} + iQ\vec{m} \times \vec{E}). \tag{6.2.2}$$

A microscopic explanation is related to a difference in the electronic excitation in the magnetic medium by left or right circular polarized light depending on the electron's spin orientation. In a magnetized sample the degeneracy of electronic states is lifted due to the spin-orbit coupling and the exchange interaction. The energy level splitting of spin-up and spin-down states causes the allowed dipole transition (selection rules $\Delta l = \pm 1$, $\Delta s = 0$, $\Delta m = \pm 1$) to differ for right and left circular polarized light.[Kus11]

Phenomenologically, the rotation of the polarization plane can be understood by the picture of light induced electron oscillations parallel to the polarization direction. Besides a regularly reflected portion of the beam R_N owning the same polarization, a secondary, so-called Kerr-amplitude R_K is generated as the oscillating electrons (velocity $\vec{v}$, charge e) experience a Lorentz force $F_\mathrm{L} = e \cdot \vec{v} \times (\vec{M} + \mu_0 \cdot \vec{H})$ due to the magnetization M of the sample. Superposing R_K and R_N yields the magnetization dependent rotated polarization of the reflected beam.[HS98]

In general, three geometries are distinguished that are illustrated in Figure 6.1. The polar MOKE (P-MOKE) senses the magnetization parallel to the sample's surface normal for both, perpendicular and parallel polarized light. [1]

For the longitudinal configuration (L-MOKE), where $\vec{M}$ lies within both the incidence plane and the sample plane, perpendicular and parallel polarization have to be distinguished, for which, contrarily to the P-MOKE, the sense of Kerr-rotation is inverted. At last, the transversal geometry (T-MOKE) occurs for $\vec{M}$ lying in the sample plane but being perpendicular to the plane of incidence. Here, no change of the polarization state is observed, but the reflected light shows a varied amplitude in the case of parallel incident polarization.[HS98]

6.2.2 L-MOKE Magnetometer

The longitudinal Kerr magnetometer (L-MOKE) is often in use when measuring the magnetization reversal of purely in-plane magnetized samples. The longitudinal magnetization component M_L is read out for easy and hard axis hysteresis loops, as the sample can be placed with the main

[1] The polarization is called parallel or perpendicular, if the electric field vector of the electromagnetic wave lies within the plane of incidence or points perpendicular to this plane, respectively.

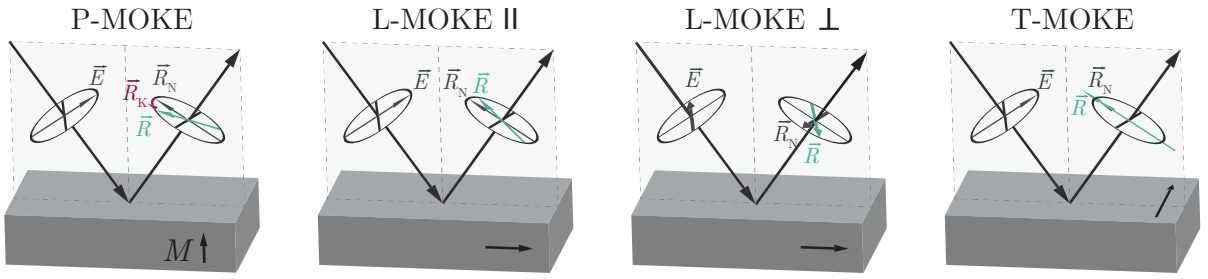

Figure 6.1: Visualization of different MOKE geometries. While $\vec{E}$ denotes the polarization of the incident beam, the reflected light with the rotated polarization plane R is described by the superposition of the regularly reflected electric field amplitude R_{N} and the Kerr amplitude R_{K}. Note that for simplicity R_{K} is only exemplarily depicted for the P-MOKE.

anisotropy axis parallel or perpendicular to the plane of incidence (or under any other angle).

The optical setup utilized in this thesis for the detection of the Kerr rotation being in first order proportional to M_{L} consists of a polarizer, which polarizes the light emitted by a laser ($\lambda = 635$ nm) perpendicularly, the reflective sample placed on a rotatable xy-stage, an analyzing polarizer and a photodiode as a detection unit. Additionally, a lens focuses the light onto the sample with a resulting spot size of approximately 170 µm x 200 µm determined as the FWHM of the Gaussian beam profile. [2] Perpendicular polarized light is used, as it prevents the contribution of the transversal magnetization component M_{T} within the signal (T-MOKE). In order to maximize the longitudinal magneto-optical response in comparison to the polar one, a grazing incident would be optimal. However, the incidence angle of the setup used for the measurements in this thesis is due to practical reasons approximately 50°. As the analyzer is set to an angle close to 90° with respect to the polarizer angle, the intensity measured arises from the Kerr-amplitude R_{K}. When sweeping the magnetic field H_{ext} within the sample plane generated by an electromagnet placed in the sample plane, the magnetization reversal can be measured. The Kerr-amplitude can be directly converted to the reduced longitudinal magnetization component $M_{\mathrm{L}}/M_{\mathrm{S}}$ by normalizing the intensity values to 1 and -1 for $M_{\mathrm{L,sat}+}$ and $M_{\mathrm{L,sat}-}$, respectively.

Note, that a direct conversion between the measured signal and the longitudinal in-plane magnetization component is only valid, if the sample does not possess any perpendicular-to-plane magnetization component, as this would add a PMOKE contribution to the signal.

6.2.3 V-MOKE Magnetometer

Aiming to disentangle the in-plane components M_{L} and M_{T}, i.e. to track the in-plane magnetization vector during the magnetization reversal, a so-called vector Kerr magnetometer as sketched in Figure 6.2 can be utilized. In order to access M_{T}, it is necessary to work with parallel polarized light, as the T-MOKE arises only for this polarization as an intensity alteration. The setup is similar to the L-MOKE case, however, the reflected light is divided by a beam splitter. The two parts can then be analyzed by one detector ('T' detector) in regard of intensity changes and by an anlayzer-detector combination ('L') in regard of the polarization rotation. As also the 'L' detection unit is sensitive to the intensity changes regarding the T-MOKE, the isolated

[2] For this profile, the reflected intensity was measured while the edge of a reflective sample was moved through the beam by the help of the motorized stage, which is commonly known as the *knife edge method*.

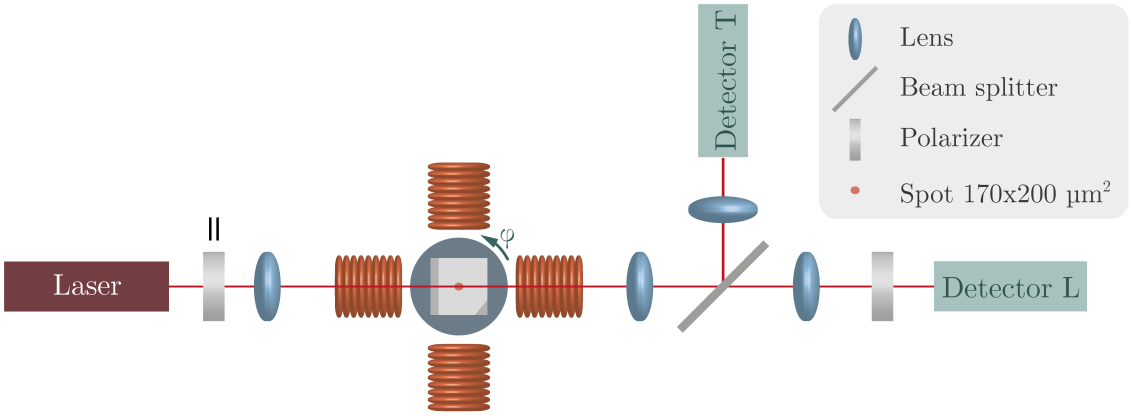

Figure 6.2: Schematic top view of the VMOKE magnetometer setup with a sample placed on the rotatable holder (φ). Components described in the text.

longitudinal component needs to be carefully recalculated from both signals.[Müg16] Therefore, three hysteresis curve are required, which necessitate the use of a quadrupole electromagnet: The magnetic field dependent intensity on the 'L' detector $I_{\mathrm{L}}(H)$ and the intensities $I_{\mathrm{T}}(H)$ and $I_{\mathrm{T}}(H_{\perp})$. The latter, a measurement of the transversal component for a field applied perpendicular is necessary in order to extract the intensity values with respect to the transversal magnetization component in saturation $I_{\mathrm{T}}(H_{\perp,\mathrm{sat}\pm})$ along this rotated axis for normalizing $I_{\mathrm{T}}(H)$ to gain $M_{\mathrm{T}}(H)/M_{\mathrm{S}}$. A detailed explanation of this procedure and additionally the determination of $M_{\mathrm{L}}(H)/M_{\mathrm{S}}$ is described in detail in Ref. [Müg16]. Studying reversal mechanisms in dependence on the angle between the sample axis and the applied magnetic field direction, e.g. for the investigation of anisotropy axes in the sample, requires furthermore that the sample holder angle φ can be altered in an automatized fashion.

6.3 Magnetic Imaging

Besides characterizing integrated magnetic properties of magnetic samples, it is inevitable to also use magnetic imaging techniques on the micro- or nanoscale in order to visualize magnetic textures and to understand processes governing magnetization reversal processes like domain nucleation, growth and domain wall movement. Many techniques have been developed based on various physical principles, of which some shall be named:

- Detecting domains by spatially resolving the magnetization via Kerr microscopy
- Analyzing the spin polarization of secondary electrons emitted in scanning electron microscopy indicating the magnetization direction (SEMPA)
- Sensing magnetic stray fields of a sample by means of magnetic force microscopy (MFM), a scanning probe method.
- Imaging secondary electrons of a sample excited near an absorption edge by monochromatic X-rays (XPEEM)

The last of these methods will be described in the course of this chapter.

6.3.1 X-ray Photoemission Electron Microscopy - XPEEM

In 1988 Tonner and Harp published an article about a microscopy technique to image photoelectrons from soft X-ray absorption with synchrotron radiation where the advantage compared to conventional electron microscopy was the possibility to spatially resolve a sample surface's chemical information.[TH88] About five years later, the first magnetic contrast imaging of a magnetic recording disk was realized by Stöhr *et al.* based on this photoemission electron microscopy (PEEM).[SWH93] Since then, PEEM endstations have been established at most synchrotron facilities, of which the XPEEM station at beamline UE49-PGM located at BESSY II (Berliner Elektronenspeicherring für Synchrotronstahlung, Helmholtz-Zentrum Berlin) was utilized for the experiments within this thesis. The named beamline offers full polarization control and the X-rays entering in an angle of 74 ° with respect to the surface normal are moderately focused to gain a spot size of 20 µm x 10 µm.[KV16] How magnetic information can be acquired via X-ray magnetic circular dichroism will be described in this section after a note on spectromicroscopy is given.

Principle of Spectromicroscopy

For a specific material, the X-ray absorption process in so-called *near edge X-ray absorption fine structure* (NEXAFS) experiments is energy dependent with characteristic absorption edges, e.g. the L_3 edge describing the dipole transition from the core level $2p_{3/2}$ to an empty state in the d valence band above the Fermi level. The absorption is hereby proportional to the number of valence holes, which is often referred to as the charge sum rule.[SS06] A measure for the absorption intensity can either be determined from the transmitted intensity when working with thin samples or it can alternatively be laterally resolved by detecting secondary electrons emitted due to the absorption.[SS06] The absorption in transition elements (e.g. at the L_3 edge) causes the occurrence of core holes. Following absorption, these holes will soon (within attoseconds) be filled via Auger processes, in which an electron from the valence shell fills the hole while the excess energy from this process results in the emission of a so-called Auger electron.[FO15] This escaping electron creates many low energy secondary electrons via scattering within the material. The mean free path of these emitted electrons is only a few nanometers which makes the technique very surface sensitive (sampling depth $\approx$ 5 nm), although the penetration depth of the X-rays is in the range of tens of nanometers.[SS06] It is spoken of spectromicroscopy when a stack of images is recorded while tuning the excitation energy of the X-rays via the undulator of the synchrotron facility, which allows for spatially resolved spectra.

The Origin of X-ray Magnetic Circular Dichroism - XMCD

The term magnetic circular dichroism generally describes that the absorption process of circular polarized light is dependent on the investigated sample's magnetization. Linked to the magneto-optic effects introduced in section 6.2, it is, however, not restricted to visible light but even enhanced near X-ray absorption edges.[Coe10b]

The X-ray magnetic circular dichroism (XMCD) arises due to a difference in the absorption intensity of circularly polarized light of certain helicity by a magnetized sample as shown in the

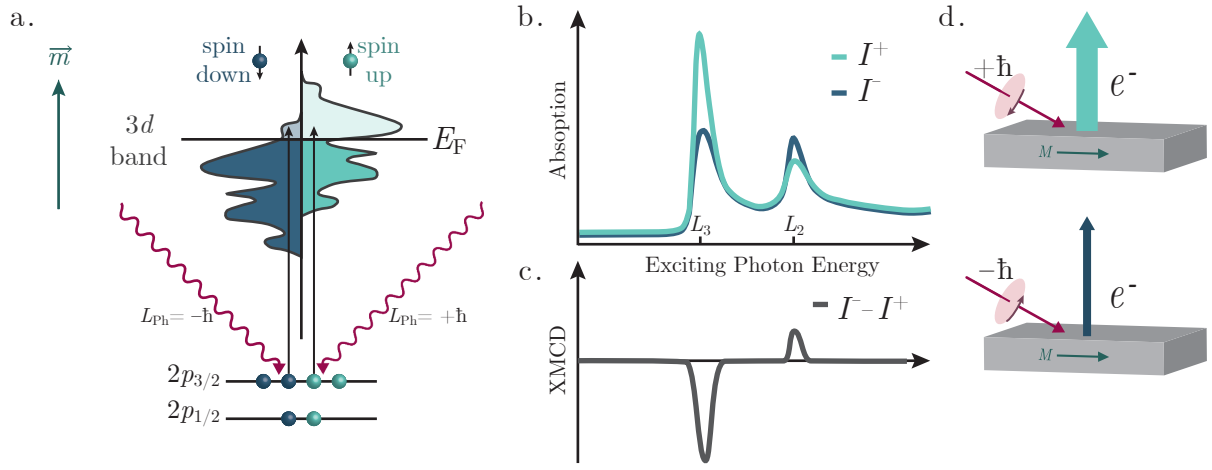

Figure 6.3: Illustration of the absorption at the L_3 edge from the $2p_{3/2}$ level in the unoccupied $3d$ valence band of a magnetic material (a.). Due to the STONER splitting, there is a difference in the density of states in the valence band with respect to the electron spin. The corresponding absorption spectra are sketched in b. for both photon helicities and also including the L_3 edge. Here, I^+ and I^- denote the electron yield I at positive $(+\hbar)$ and negative $(-\hbar)$ helicity of the X-rays. A photon angular momentum parallel to the propagation direction $(\vec{k})$, i.e. $+\hbar$, shows higher L_3 absorption when the sample is magnetized parallel (instead of antiparallel) to the projection of $\vec{k}$ onto the sample plane as shown in d. The difference spectrum in c. indicates the XMCD and its inverse sign for L_2.

schematic spectrum in Figure 6.3. The photon's angular momentum can either point parallel $(\vec{L}_{\text{ph}} = +\hbar)$ or antiparallel $(\vec{L}_{\text{ph}} = -\hbar)$ to the wave vector $\vec{k}$. A collinear arrangement of $\vec{L}_{\text{ph}}$ and the magnetization $\vec{M}$ results in maximum XMCD, while it vanishes for perpendicular alignment.[Bea06] Under the condition of angular momentum conservation, $\vec{L}_{\text{ph}}$ is transferred to the photo-excited electron's angular momentum, i.e. its orbital moment and its spin. This causes a difference in the absorption of right- $(+\hbar)$ and left-handed $(-\hbar)$ circular polarized light in the presence of spin-orbit coupling, as there is an imbalance in the density of unoccupied spin-up and spin-down valence states in the material due to the STONER splitting - a characteristic feature of a ferromagnet. Pure magnetic contrast for domain depiction with eliminated topographic information is derived by calculating the asymmetry ζ_{XMCD} of two PEEM images recorded with opposing helicity of the X-rays:

$$\zeta_{\text{XMCD}} = \frac{I^+ - I^-}{I^+ + I^-}, \tag{6.3.1}$$

where I^+ (I^-) is the spatially resolved electron yield upon illumination with light of positive/ right-handed (negative/ left-handed) helicity.[Bea06]

Besides spatially resolving the magnetization directions in XMCD microscopy, precise analysis of XMCD spectra, including both the L3 and L2 edge, and the application of the sum rules described in chapter 9.6.5 of Ref. [SS06] allows for the quantitative differentiation of spin and orbital magnetic moment per atom in the investigated material.

XPEEM Station at Beamline UE49-PGM (BESSY II)

The important components of the photoemission electron microscope (*Elmitec GmbH* at UE49-PGM) are the objective lens collecting the secondary electrons which are accelerated from the sample at 10 kV. After passing the microscope column containing a stigmator and a deflector, the energy analyzer reduces chromatic abberation and the electrons are magnified by projective lenses onto the detection unit. [SHAR12,KV16]

Working with electrons usually restricts the possibilities to apply magnetic fields due to the electrons' deflection by the acting Lorentz force. However, the setup is equipped with custom sample holders which posses a special yoke geometry as depicted in Figure 6.4 a. and b. and therefore allow for the application of magnetic fields that are spatially confined to minimize electron deflection. [SHAR12,KSR10] At the rear side of the sample, the magnetic yoke has a 500 µm gap and the magnetic field is generated by a pair of symmetric coils. With this yoke design the magnetic field decays to 1/e within 1.5 mm with respect to the sample position (substrate thickness 500 µm). [KSR10] In turn, measurements can only be performed in the very center of the yoke's gap, which makes a pre-characterization of the sample via light microscopy necessary. In this study, microscopic maps of all investigated samples have been recorded like shown in Figure 6.4 c. and e., that helped mounting the sample at the synchrotron facility and later on with the identification of the sample position in the PEEM images. Using an on-site light microscope the sample can be placed at the desired position aligning the anisotropy axis, i.e. the

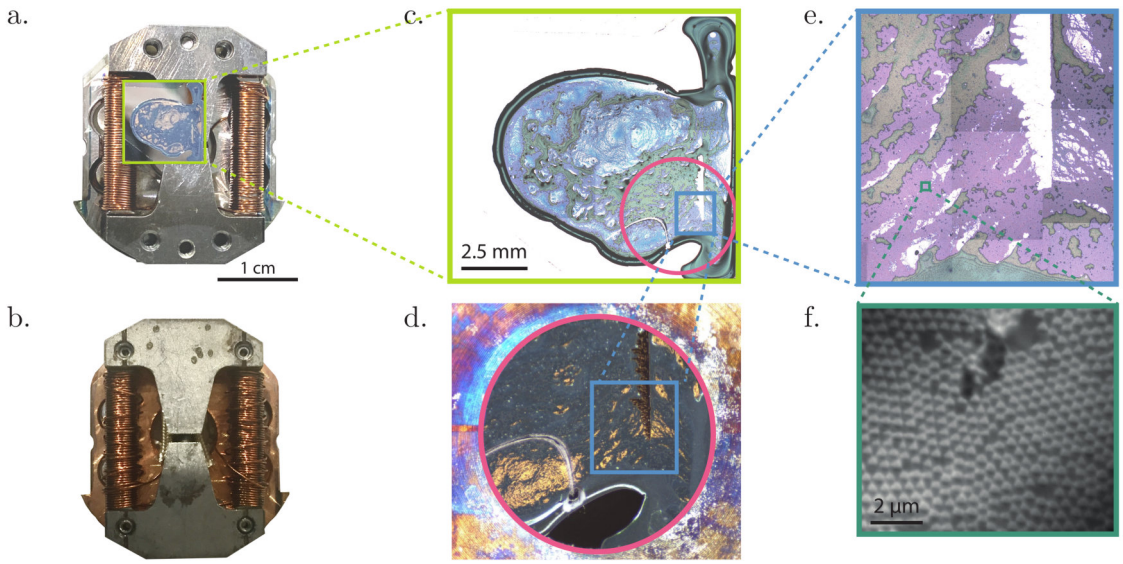

Figure 6.4: The top view photograph in a. shows the sample holder with a mounted sample (light green). The holder is also shown in b. for better visibility of the coils and yoke. In c., a light microscopic map (2.5 x Objective) of the sample is given, with the pink circle indicating the hole of the afterwards mounted capping lid. The microscopic image in d. was taken after the lid was placed (pink). The microscopic map (20 x Objective) in e. was used for orientation on the sample. Monolayers of magnetically capped particles appear in violet and flat film regions in white while particle multilayers cause a gray tone. At last, an image of a capped particle monolayer recorded with the XPEEM after the sample has been inserted to the microscope is shown in f. All images are related to the XPEEM station at beamline UE49-PGM (BESSY II).

EB direction, perpendicular to the yoke's gap to guarantee the application of magnetic fields along the easy axis during image acquisition. As an electric contact between the sample and the holder is necessary to reduce charging effects, the sample is fixated with conductive silver paste and the aluminum lid is placed on top to clamp the sample (Figure 6.4 c.). Once the sample is mounted and transferred to the PEEM, alignment is usually performed with a UV lamp as an additional light source illuminating a larger field of view in comparison to the probing X-rays.

7. Morphological Characterization of Magnetically Capped Particles

An important step when investigating microstructured samples is their structural or morphological characterization in order to set the subsequent magnetic characterization into context. Besides micrographs of the overall sample morphology, the structural characteristics of individual caps shall be analyzed. This includes the visualization of the thickness gradient by scanning electron microscopy which was performed on a cross-section of the capped spheres. In section 7.2, the granular structure of the deposited film is analyzed from helium ion microscopic images.

7.1 A Typical Sample's 'Landscape'

For the samples with magnetically capped particles (diameter $D = 500\,\mathrm{nm}$) fabricated for this thesis, the lightmicrographs and images from scanning electron microscopy (SEM) in Figure 7.1 give a first impression of the sample's 'landscape' or its topography. Due to the self-assembly process of spherical template particles, different regions are found on the sample: The particles either form mono- (e.) or multilayers (f.) with predominantly hexagonal lattice structure, where depending on the quality of the substrate surface and the homogeneity of the particles within the suspension defects and holes in the array are found (a., b.). Furthermore, the samples show regions of purely flat thin film system where no templating particles had settled (d. top). Sub-monolayers represent an intermediate type of region, where the particles do not form an extended lattice but either distanced particles or distributed particle islands of various expansion on the surface, hence, building a region of capped particles surrounded by planar film (c.).

In order to characterize the curved metallic film on a capped particle, a focused ion beam was used to mill parts of exemplary particles of 1 µm diameter and a total film thickness of 55 nm (layer stack: Cu(5 nm)/IrMn(30 nm)/CoFe(10 nm)/Si(10 nm)). The cross-section was afterwards imaged with SEM and is depicted in Figure 7.1 g., cf. Ref. [TRH21]. In the obtained images, the cap appears brighter than the particle, which is due to the fact that the non-conductive silica particle can charge up from the impinging primary electrons, while the metallic layer is conductive. A thickness gradient of the metallic film was determined, where at the caps' side the thickness is in the range of 30 to 40 % of the thickness at the caps' top.[TRH21,Reg18] Assuming that the reduction is scalable to the individual layers, the reduction of the film thicknesses of the ferro- and antiferromagnet can be estimated, which is rendered important for the magnetic characterization.

Additionally, the images reveal that the caps of neighboring particles are physically connected, which becomes also obvious from the highly resolved helium ion micrographs in Figure 7.1 h. and i., where the connecting sites between the caps in the lattice are visible. Hence, the caps cannot be perceived as individual entities but rather as an ensemble of caps that interact not only magnetostatically but potentially also via exchange interaction if the film at the contact points is thick enough.

In addition to the SEM images, micrographs recorded with a helium ion microscope (HIM) reveal a highly resolved picture of the particles, e.g. for the monolayer shown in Figure 7.1 h. The utilized microscope is a *ORION NanoFab* from *Zeiss*, where the gas field ion source for the generation of the helium beam for imaging was set to 30 kV, which in turn corresponds to an acceleration energy of 30 keV of the singly charged helium ions. With the enhanced resolution, a more detailed view of the connecting junctions between the particles and of the granular surface can be obtained at higher magnification. In the area recorded in Figure 7.1 i., the conjunctions seem to be rather thick, while they were found less pronounced in other regions of the sample.

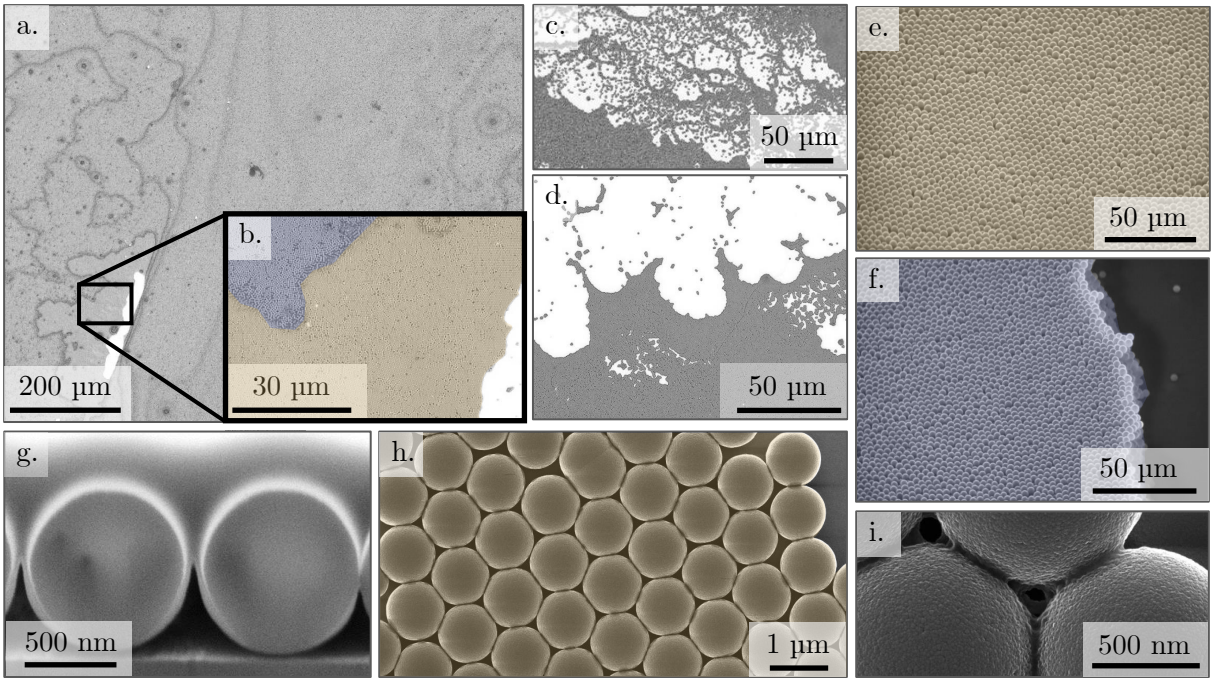

Figure 7.1: Lightmicroscopic images with different magnification taken at various positions on a sample with particles of 500 nm diameter indicating the sample's overall 'landscape' (a. - d.). Mono- and multilayered regions can be distinguished in b., recorded with a 100 x objective lens, and are colored in yellow and blue, respectively. Further, SEM images may resolve mono- (e.) and multilayers (f.) in more detail. The SEM image in g. shows a cross-section of capped particles with a diameter of 1 µm that were previously milled with a focused ion beam. At last, the high resolution images h. and i. of these capped 1 µm particles were recorded with a helium ion microscope (HIM).

7.2 Grain Size Analysis of Curved EB Films on Particles

As presented HIM images were recorded for particles functionalized with a polycrystalline EB layer system, the visible granular appearance of the caps' surface is expected to represent the layer system's grain structure. Regarding the antiferromagnetic layer, the distributions of grain sizes crucially determines the strength of the EB and the coercivity in the picture of the antiferromagnetic grain classification (cf. subsection 2.4.2). It is important to note that, although the imaged surface in the HIM data is not the antiferromagnetic layer itself, the grain radii distributions presented in the following are assumed to resemble the antiferromagnet in good approximation as it has been shown that the metallic layer growth during sputter deposition is controlled by the respective underlayers.[Gau17,VFT05,VGG05,JDM03] Thus, the surface topography of the imaged films' capping layer is expected to reflect the antiferromagnet's granular structure. Recently, the topography of comparable Cu/IrMn/CoFe samples was measured by means of atomic force microscopy (AFM).[MRH22] The results show the same grain radii distributions for the two sample types *buffer/antiferromagnet* and *buffer/antiferromagnet/ferromagnet*, evidencing that the antiferromagnetic grain structure is inherited by the layer above.[MRH22]

In order to compare the curved with the planar polycrystalline thin film, images of these two regions on one exemplary sample have been analyzed with the open source software *Gwyddion* (V2.59)[NK12] with regard to the grain size distribution. For this purpose, the noise in the images was first reduced by a two dimensional Gaussian filter with a full width at half maximum (FWHM) reflecting the measurement resolution. Next, the watershed algorithm[SV90] was used to identify the grains in the full size HIM image of the flat layer (2 x 2 µm^2).[1] The process includes a step to localize valleys in the transformed topography by placing 'water drops' that follow a steepest decent path and a subsequent segmentation step in which the valleys are 'filled' up to the grain boundaries. In contrast to the image of the planar EB film, the images regarding the the curved film were cut to a size of approximately 380 x 380 nm^2 around the particle's center before the algorithm was applied. For the analysis of the grain sizes, an additional circular mask was applied, in order to only evaluate grains within a certain opening angle. Thereby, a region of ±23° around the central axis is considered which is defined by the sample tilt during imaging as sketched in Figure 7.2 c. From the area of each grain identified with the watershed algorithm, the software allows to extract the equivalent grain radius r_{eq}, i.e. the radius of a circle with the same area, if the nominal image resolution is known. Grains with $r_{eq} > 19$ nm have been omitted for the further analysis, as it was seen that for larger sizes the algorithm in some cases had identified two grains as one. Similarly, the imaging resolution and the applied Gaussian filter do not allow to analyze grains with $r_{eq} < 3$ nm. For all evaluated images, the parameters for the localization of grains were kept constant:

1. Smoothing	2. Grain localization			3. Segmentation		4. Grain filtering	
Gauss (FWHM)	n_{steps}	Drop size	Threshold	n_{steps}	Drop size	min.	max.
2.5 nm	10	8 %	20 px^2	200	10 %	3 nm	19 nm

[1] Note, that Gwyddion is a software designed for AFM data. The color values of an image are transferred into height, i.e. bright pixels are shallow and dark pixels elevated regions. In fact, the realistic topography cannot be retrieved from a HIM image, as the grains become valleys and grain boundaries become elevations. However, this transformation allows to localize the grains by the watershed algorithm.

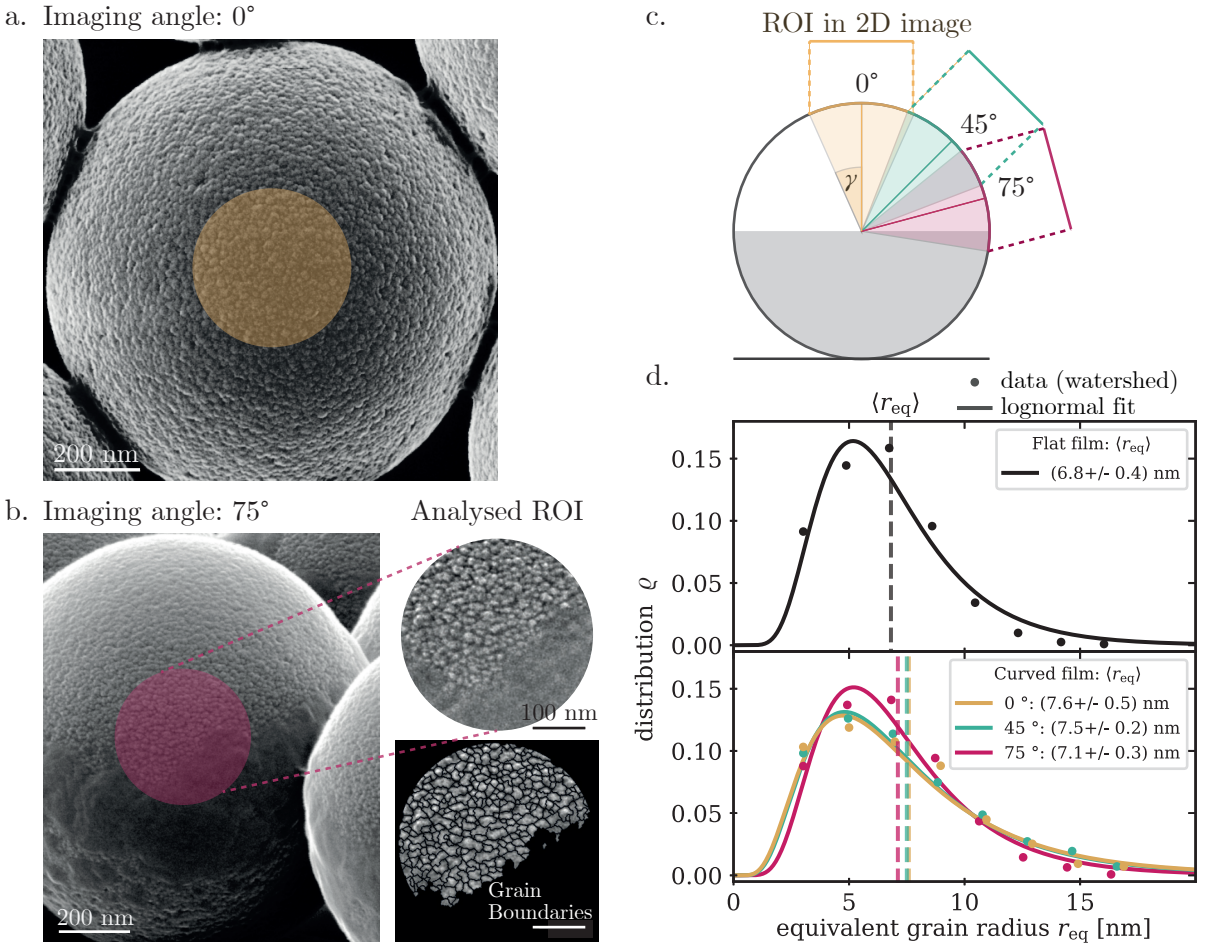

Figure 7.2: High resolution images of the capped 1 µm particles from helium ion microscopy (HIM) with different sample tilts 0° (a. top view), 45° and 75° (b. side view). Due to the projection of the capped particle surface on the image plane, the grain size analysis was performed only within the shaded circular area in order to reduce the error from this distortion (cf. sketch in c.). Distributions of equivalent disc radii are shown in d. for the analyzed EB caps depending on the imaging perspective alongside the result from an image of the layer stack on the flat Si substrate. In all cases, Equation 7.2.1 was fitted to the extracted histograms in order to extract the mean grain radius $\langle r_{\mathrm{eq}} \rangle$.

Subsequently, the probability density for the occurrence of grains with a certain radius r_{eq} is derived as a normalized histogram, for which the binning was chosen to match the FWHM of the Gaussian filter (2.5 nm). The data follows a logarithmic normal (lognormal) distribution, which reproduces the findings for polycrystalline antiferromagnetic layers analyzed with AFM [MHR20] or TEM [OFOVF10] and can therefore be approximated by the function

$$\rho(r_{\mathrm{eq}}, \mu, s) = \frac{1}{\sqrt{2\pi} s \cdot r_{\mathrm{eq}}} \exp\left\{ -\frac{(\ln(r_{\mathrm{eq}}) - \mu)^2}{2s^2} \right\}, \tag{7.2.1}$$

with the parameters μ and s. [MHR20,VFT05] According to common structure zone models, [BA98,Kus19] a columnar growth of crystallites is enabled above a threshold deposition rate. [MHR20] Hence, the distribution of grain radii can be directly correlated to a distribution of grain volumes, which in in the case of the granular antiferromagnetic layer relates to the division of the total

polycrystalline ensemble into grain classes (cf. subsection 2.4.2), as an antiferromagnetic grain's volume dictates its thermal stability and consequently its capability to pin the ferromagnet at the shared interface (class III) for constant magnetocrystalline anisotropy of the grain.[MGM16] After fitting Equation 7.2.1 to the extracted histograms for different sample tilts, the average equivalent disc radius of the grains can be derived from the fit parameters as the distribution's expectation value[VFT05]

$$\langle r_{\mathrm{eq}} \rangle = \int r_{\mathrm{eq}} \rho(r_{\mathrm{eq}}, \mu, s)\, \mathrm{d}r_{\mathrm{eq}} = \exp\left(\mu + \frac{s^2}{2}\right). \tag{7.2.2}$$

For three imaging perspectives representing sample tilts of 0°, 45° and 75°, as well as for the layer stack deposited on the flat substrate (0°), the extracted histograms are depicted in Figure 7.2 d., where additionally the corresponding fits from the lognormal distribution in Equation 7.2.1 are shown. Note, that the statistics for the data differs quite strongly, as more than 16.000 grains were identified for the flat film, while at maximum 2200 and at minimum 600 grains were evaluated for the curved film on the particles.

The results shown in Figure 7.2 d. can be compared with the characteristics of EB samples presented in Ref. [MHR20], which were deposited in the same sputter system as the samples of this thesis. Within the named publication, the surface of antiferromagnetic layers (t_{AF} =30 nm) deposited on a 5 nm thick Cu buffer (on Si substrate) was investigated by means of AFM and a similar grain size analysis based on the watershed algorithm was conducted.[MHR20] For a comparable sputter rate of the antiferromagnetic layer η_{AF} as compared to the one used for the deposition of the sample analyzed by HIM, the authors derived $\langle r_{\mathrm{eq}} \rangle = (7.1 \pm 1.5)$ nm (η_{AF} =(5.16 ± 0.12) nm/min),[MHR20] which is within the margins of uncertainty in very good agreement with the value of (6.8 ± 0.4) nm (η_{AF} =(4.87 ± 0.15) nm/min) derived from HIM on the flat layer stack.

Furthermore it may be argued that a change of the grain radii across the particle's surface can be expected, as the layer growth may vary when the deposition angle changes towards a glancing angle deposition on the particle's side due to the following hypothesis: During the deposition, atoms (and clusters) physiosorbed on the particle's side carry less kinetic energy than those atoms hitting the particle's top, because they must have undergone scattering processes in order to change their direction along the path from the target to the sample. Hence, their potential for surface diffusion after the adsorption is reduced. This could lead to a higher number of nucleation sites as the adatoms cannot 'reach' other already existing nuclei where they could then be chemisorbed. Although the values for $\langle r_{\mathrm{eq}} \rangle$ show a general tendency to be reduced towards the equatorial region of the magnetic cap, no significant change in the mean grain size can be observed by considering the corresponding margins of uncertainty. Note, that the HIM images for 45 and 75° only picture capped particles at the outer boundary of a hexagonally arranged particle ensemble, which does not allow for the analysis of grain sizes on the particle's side in the proximity to a neighboring particle.

7.2.1 Conclusion

Overall, the grain size distributions for the curved EB film on the particles are seen to be comparable with the flat film deposited on the plain substrate - regardless of the deposition angle, i.e. the polar angle on the spherical object. As a result, it is inferred that the antiferromagnetic layer is generated by columnar growth at the chosen sputter rate, where the nucleated crystallites grow along a direction parallel to the surface normal. It is further assumed that the Cu buffer layer promotes a (111) crystal orientation in the antiferromagnetic layer which correlates with a large magnetocrystalline anisotropy of the antiferromagnetic grains.[MHR20] In combination with the *perpendicular-to-surface growth direction*, this leads to the hypothetical conclusion, that the EB direction successively follows the sphere's curvature as illustrated in Figure 7.3. When the ferromagnetic texture setting the EB in a field-free deposition scenario is an onion state, the EB would gradually change along the sphere from parallel-to-(substrate)plane at its top towards perpendicular-to-(substrate)plane at the equator, thus, resulting in an onion textured EB. However, a magnetic field is typically applied during the deposition or in a post-deposition field cooling procedure to induce the anisotropy direction. This would contrarily promote that the EB evolves parallel to the substrate plane due to the exchange coupling between the saturated ferromagnetic layer and the addressed uncompensated magnetic moments of the antiferromagnet at the interface. Hence, a competition of a global in-plane EB and the locally changing, i.e., onion textured EB is expected.

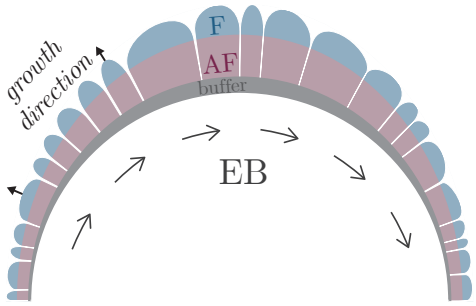

Figure 7.3: Sketch for the proposed perpendicular-to-surface growth and the inheritance of the grain structure. Arrows indicate that the EB direction is assumed to follow the cap's curvature.

8. How to Analyze Typical Remagnetization Measurements on Cap Arrays?

An established method for magnetization reversal measurements in dependence of an external magnetic field is the vibrating sample magnetometry (VSM). In these magnetic hysteresis measurements, the sample moves periodically back and forth as it is mounted on an oscillating holder. Then, a lock-in amplifier is used to measure the voltage that the oscillating magnet induces in a pair of pick-up coils.[Fon59] Hence, the measured signal originates from the entire sample and therefore integrates over the magnetic properties of all components of a sample. In the case of the samples investigated in this thesis, we may expect contributions from both, the magnetic caps and the planar film, as the signal contains information of mono-, multi- and submonolayers as well as from the residual flat film surrounding the particle area. In the following, magnetization reversal measurements of two samples that differ in the particle size and in the magnetic layer stack will be shown. Both VSM and MOKE data will be carefully analyzed with regard to the described superposition.

8.1 Exemplary Hysteresis of Ferromagnetic Caps with $D = 500$ nm and $t_F = 40$ nm

A resulting VSM hysteresis curve for an exemplary sample is shown in Figure 8.1 d. (topmost, green circles). Alongside the magnetization reversal, a map of the full sample is shown in a. which was acquired by stitching together 63 images from a light microscope with a 10 x objective lens. For the chosen sample, the templating silica particles are 500 nm in diameter and the magnetic cap deposited consists of a 10 nm thick Cu buffer layer, 40 nm of CoFe as a ferromagnet and a 4 nm thick Al capping. The substrate below is a silicon wafer piece with a layer of Pt sputtered in order to enhance its conductivity for later XPEEM measurements.

The VSM curve clearly indicates different reversal processes by the presence of different slopes, where the steepest part around the center is attributed to the residual thin film contribution. Note, that VSM measurements of similar shape can also be found in literature,[WYW11,SMK12,NKM16,TRH21] which is reasonable when considering that perfectly assembled particles over the full sample area would be required to gain pure capped particle signal from an integral technique like VSM.

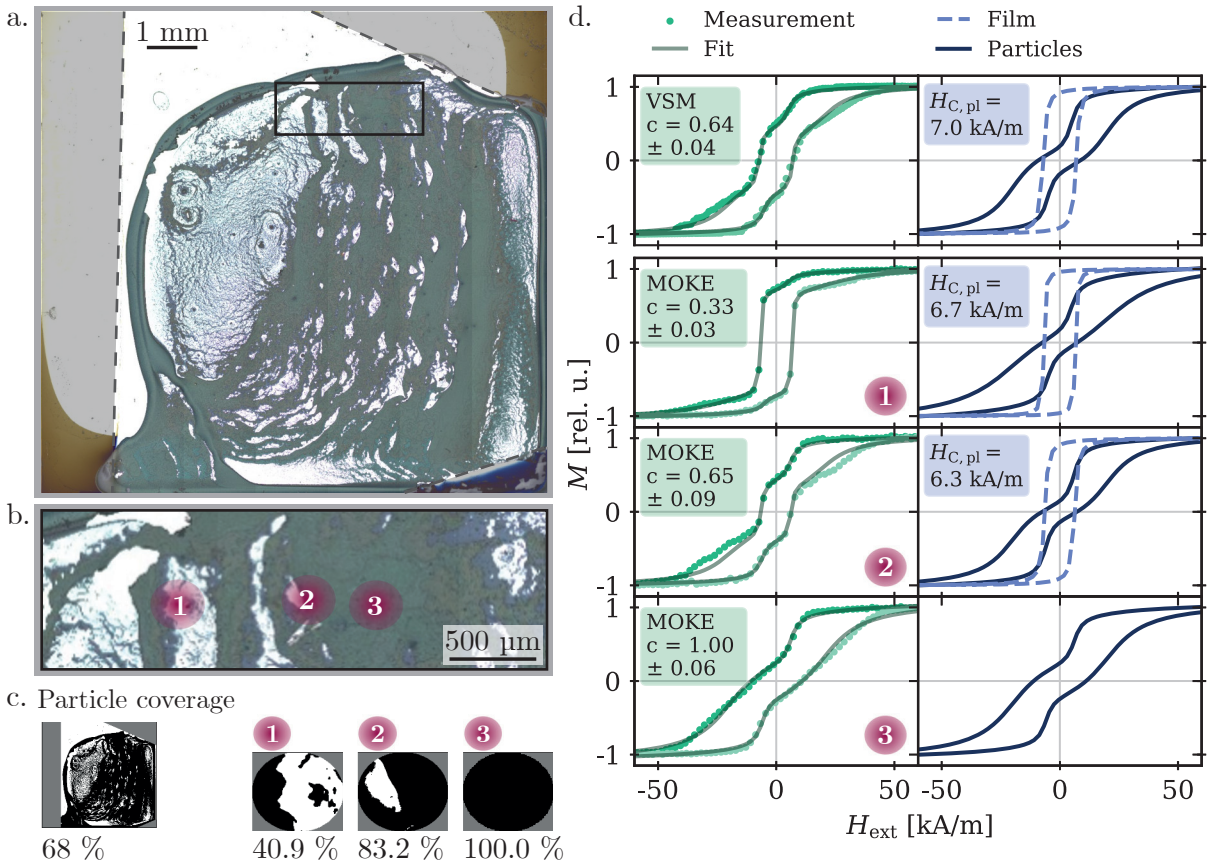

Figure 8.1: Analysis of the magnetization reversal of a characteristic sample with 500 nm particles capped with 40 nm of CoFe. A microscopic map consisting of 63 individual microscopic images (a.) is shown alongside different measurements of the sample's magnetization reversal (left column in d.). The data of the top most panel was recorded with a VSM which integrates over the full sample volume, while the three measurements below originate from MOKE measurements with different laser positioning. The corresponding spots were identified from photographs and are marked in b. (zoomed rectangle indicated in a.). Besides the normalized experimental data, the approximating fit function (Equation 8.1.1) is shown for each measurement in the left column of d., while the right column contains the extracted reversal curves for both, the flat film and the magnetic cap array. The parameter c resembles the signal contribution of the particle array that results from the fitting procedure. The dashed lines in a. indicate areas which are not magnetic as they were covered by adhesive tape to fixate the sample during sputter deposition. In c. binarized images of the full sample as well as the three spots measured in the LMOKE are shown with the corresponding particle coverage evaluated from the images' histograms.

In order to study magnetic properties of only capped particles, it is necessary to distinguish the fabrication-dependent characteristic areas on the sample. An approach to exclude sample areas with residual flat film can be done with MOKE magnetometry, which is convenient since the signal only emanates from the area on the sample that is hit by the light. Therefore, the measurement area depends on the optical components focusing the laser beam.[1] In order to assign the recorded LMOKE measurements depicted in Figure 8.1 d. to the regions on the sample from which they originate, the laser spot's position is marked in the microscopic image (b.). For this, a neutral density filter (ND 1, i.e. 10 % transmittance) was placed in the optical path in order to

[1]The laser spot size in the sample plane is 170 µm x 200 µm for the L-MOKE setup used for this thesis.

take a photograph of the laser spot position on the sample, which was subsequently matched to the microscopic map (a.). With the chosen sample, three remagnetization measurements were recorded at slightly different positions. The corresponding hystereses loops in Figure 8.1 d. have significantly different shapes. While measurement 3 resembles a classical vortex reversal curve which is expected for the chosen ferromagnetic thickness of 40 nm, measurements 1 and 2 exhibit a rather steep part, which is accounted to the thin film contribution. In order to quantify how much of the measured signal originates from the magnetic cap array, a fit function is determined which approximates the data for both the descending (forward, f) and ascending (backward, b) branch individually. The branches' characteristic shape can be modeled with the help of a function that superposes three *regularly* shaped hysteresis loops, of which each is described by an arctan function:

$$M(H_{\mathrm{ext,f/b}}) = \sum_i c_i \cdot \frac{2}{\pi} \cdot \arctan[a_i(H_{\mathrm{ext,f/b}} - H_{\mathrm{EB},i} \pm H_{\mathrm{C},i})] \text{ for } i \in \{\mathrm{film}, 1, 2\}. \tag{8.1.1}$$

with the fit parameters a_i, $H_{\mathrm{C},i}$, $H_{\mathrm{EB},i}$ and c_i. The vortex hysteresis of the cap ensemble is reflected by two arctan functions with the subscript 1 and 2 in order to account for the different slopes of the nucleation and the vortex core motion regime (c.f. Figure 3.1). The contribution of the flat layer system is indicated by the subscript 'film'. Note, that $c_1 + c_2 + c_{\mathrm{film}} = 1$ and hence, the relative signal contributions of the film and the cap array are c_{film} and $c = c_1 + c_2 = 1 - c_{\mathrm{film}}$, respectively. In the left column of Figure 8.1 d, the data for the VSM and the three MOKE measurements is shown alongside the corresponding fits in which $H_{\mathrm{EB},i}$ was chosen to be zero as the magnetic layer stack did not include any EB. The derived hollow hemisphere contributions range from $(33 \pm 3)\,\%$ over $(65 \pm 9)\,\%$ to $(100 \pm 6)\,\%$ for the MOKE measurements 1, 2 and 3. These signal contributions c follow the same trend as the values for the particle coverage that have been determined from the microscopy images. Here, the images were binarized and cut to ellipses according to the laser spot position extracted from the photographs, as shown in Figure 8.1 c., and the coverage was determined from the number of pixels for particles (black) and flat film (white), respectively. However, the magnetic cap contribution c determined via the fitting procedure yields smaller values than the areal coverage. Exemplarily, measurement 1 was performed at a laser spot position with 41 % particle coverage from although only 33 % of the the MOKE signal is linked to the caps.

Note, that a direct comparison of the coverage ratio determined from the microscopy images and the signal contribution in the LMOKE measurement may be misleading as the latter rather depends on the *local* coverage because the laser beam is characterized by a Gaussian intensity profile. An array defect, i.e. an area with residual thin film, will contribute less planar information to the MOKE signal if it is located in the spot's periphery. Additionally, the MOKE sensitivity for the mono- and multilayered regions is assumed to be comparably lower than the sensitivity of the measurement on the flat film. Reasons are, that the light is not strictly reflected towards the detector but is partly scattered from the particle array and that multilayer regions can result in a shadowing effect.

The same procedure has been applied to the VSM data, where the cap contribution of $(64 \pm 4)\,\%$ derived from the fit agrees with the analysis of the full binarized microscopic map yielding a coverage of 68 % since the VSM measurement captures the magnetization of the sample's total magnetic volume. Contrastingly, the signal contribution is limited in the optical MOKE setup because the signal, i.e. the light reflected towards the detector, is obliged to shadow effects, light scattering and the opening angle of the detector. It is important to note that the different sample portions superposed in the measured data *do* have different reversal fields, and that consequently the observed remanent magnetization $M_{\mathrm{R,meas}} \approx 0.50 \cdot M_{\mathrm{S}}$ represents a superposition of the still saturated thin film ($M_{\mathrm{film,fit}} = 0.92 \cdot M_{\mathrm{S}}$) and the caps that have already nucleated vortices ($M_{\mathrm{caps,fit}} = 0.19 \cdot M_{\mathrm{S}}$).

Aiming to disentangle flat thin film and magnetic cap contribution the parameters from the fit procedure with Equation 8.1.1 were separately used to plot a function with one arctan element for the film hysteresis (dashed light blue line) and another function with two arctan elements for the hemispherical cap arrays' hysteresis (blue line) in the right column of Figure 8.1 d. The fitting procedure led to comparable flat film coercivity, which is a good indication for the validity of the method. Further, the extracted cap hystereses are similar in shape and show comparable nucleation fields $\overline{H}_{\mathrm{nuc}}$ in the range of 4.8 kA/m to 5.9 kA/m which were determined from the average of both branches' maximum absolute susceptibility, i.e. the highest gradient. Nevertheless, they differ slightly in the slope of the vortex core motion region and the saturation field. Henceforth, it should be attempted to only record the pure magnetic cap signal without thin film contributions superposed (like measurement 3) in order to gain data that is quantitatively comparable without the need to subtract the thin film contribution, e.g., in terms of the remanent magnetization.

8.2 Exemplary Hysteresis of an EB Cap Array with $D = 1$ µm and $t_{\mathrm{F}} = 10$ nm

Taking the above described aspects into account, further MOKE measurements were performed to study the magnetization reversal of exchange-biased hemispherical shells on particles with a diameter of 1 µm. The layer stack consists of a 10 nm thick Cu buffer layer, 30 nm of IrMn as an antiferromagnet, 10 nm of CoFe as a ferromagnet and a 10 nm thick Si capping. In accordance with the data shown in Figure 8.1, it was found that the reversal loop shape crucially depends on the laser spot positioning.[TRH21] As an example, one of the measurements is depicted in Figure 8.2 c. alongside a microscopic map in a. of the sample where the laser spot position has been localized with the help of a photograph. Again, Equation 8.1.1 can be fitted to the data, however, this time as a superposition of two arctan functions, i.e. with $i \in \{\mathrm{film}, \mathrm{caps}\}$ and $c_{\mathrm{caps}} = 1 - c_{\mathrm{film}}$ because no classical vortex reversal could be identified for these caps with a thinner ferromagnet. Hence, the cap contribution can be modeled with a single arctan function. The extracted parameters with regard to coercivity and EB of both the flat film and the monolayered cap region were comparable between the different measurements.[TRH21] The derived signal contribution of the caps in the shown measurement is $c_{\mathrm{caps}} = (66 \pm 2)\,\%$, whereas the areal coverage from the microscopic image (b.) was evaluated to be 99.7 %.

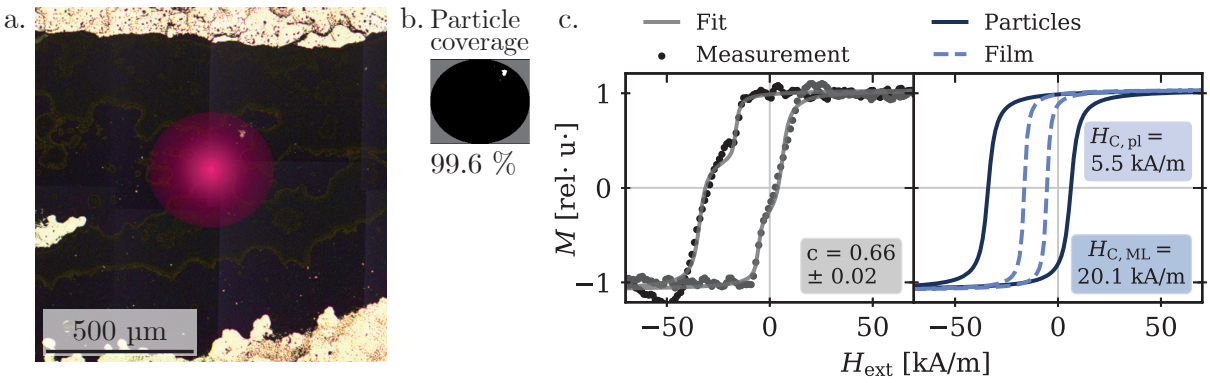

Figure 8.2: Microscopic map (a.) of the sample area alongside the measured area's particle coverage indicated by binarized laser spot area (b.). The magnetization reversal curve recorded with the L-MOKE setup (c.) is shown together with the corresponding fit functions, from which the planar layer and the caps' contribution is extracted on the right. The templating silica particles are 1 µm in diameter and the magnetic cap consists of a 10 nm thick Cu buffer layer, 30 nm of IrMn as an antiferromagnet, 10 nm of CoFe as a ferromagnet and a 10 nm thick Si capping.

8.2.1 Ray Optics Considerations

As compared to the MOKE measurements on the smaller type of capped particles the relative error between the areal coverage and the signal contribution ratio is enhanced. This deviation may be explained to a certain extent when we consider how ray optics determine the Kerr magnetometry's sensitivity for both the planar film and the magnetic cap arrays.

At first, we ascribe the sensitivity $f_{\text{film}} = 1$ to the flat magnetic film, as all light being specularly reflected from the sample will reach the detecting unit. On the other hand, the particles' curvature is responsible for the fact that only from a very small area A_{sens} around the magnetic caps' top the light will be reflected towards the detector which is sketched in Figure 8.3. As there is a focusing lens in the optical path between the sample and the detection unit (analyzer and photo diode), the radius r_{lens} of this lens and its distance L to the magnetic cap with radius $R = D/2$ determine the maximum central angle β from which a signal can be expected, because $\beta = 0.5 \cdot \arctan(r_{\text{lens}}/L)$. As a consequence, each cap has an area

$$A_{\text{sens}} = 2\pi \cdot R^2(1 - \cos\beta) \tag{8.2.1}$$

from where light can be collected on the detector. However, under the assumption of a hexagonal particle lattice, the cap array covers an area of connected hexagons, where each hexagon with

$$A_{\text{hex}} = 6 \cdot \sqrt{3} \cdot R^2 \tag{8.2.2}$$

includes $n_{\text{hex}} = 3$ particles. The ratio of the area covered by particles and the measured area of all caps therefore determines the MOKE setup's sensitivity for the magnetic cap arrays and for the flat film, respectively:

$$f_{\text{caps}} = \frac{n_{\text{hex}} A_{\text{sens}}}{A_{\text{hex}}}\ ,\ f_{\text{film}} = 1. \tag{8.2.3}$$

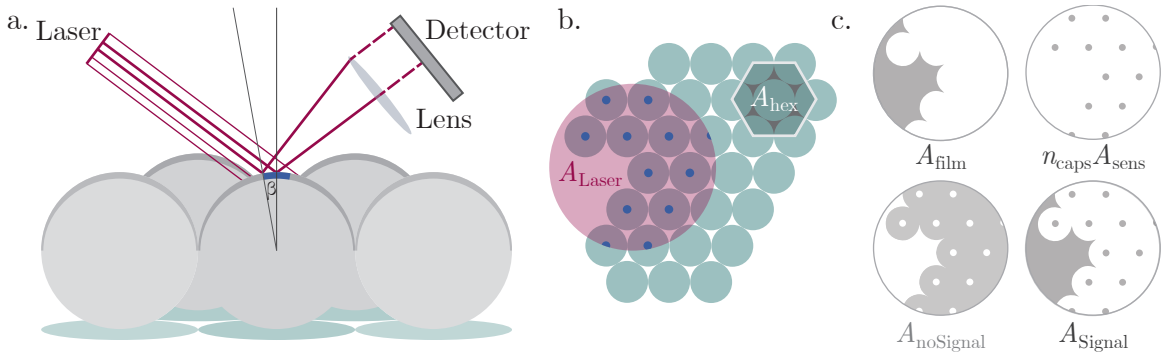

Figure 8.3: Sketch for the visualization of the laser light's specular reflection on the curved surface of the capped particles (a.). Top view indicating exemplary areal contributions of particles and flat film within the laser spot region (b.). c. Individual areas are defined within the text in order to retrieve areal coverages of particles within the measured spot from the fit parameter c_{caps}. It is assumed that light cannot be specularly reflected towards the detector from the small triangular thin film regions within the hexagonal array, as the particles will cast a shadow. (Sketches are not drawn to scale: For a hexagonal array of 1 µm caps, the laser spot would cover $A_{\text{laser}} \cdot n_{\text{hex}}/A_{\text{hex}} \approx 123000$ particles.)

The fit parameters c_{caps} and $c_{\text{film}} = 1 - c_{\text{caps}}$ denote signal contributions in the actual measurement data. They connect to the full area from which a signal can be detected $A_{\text{signal}} = A_{\text{film}} + n_{\text{caps}}A_{\text{sens}}$ as follows:

$$c_{\text{caps}} = \frac{n_{\text{caps}}A_{\text{sens}}}{A_{\text{signal}}} \;,\; c_{\text{film}} = \frac{A_{\text{film}}}{A_{\text{signal}}}, \tag{8.2.4}$$

with n_{caps} being the number of particles within the laser spot area measured and A_{film} being the area which is not covered by the particle array. Note, that within this model the full no-covered area of thin film is assumed to contribute to the thin film signal. As the laser incidence angle is $\approx 45°$, the length of the shadows created by the particles is in the same order of magnitude as the particles itself, and hence, this *shadow effect aside the monolayer edge* is neglected. The laser spot itself, however, is assigned the area

$$\begin{aligned} A_{\text{laser}} =& A_{\text{film}} + \frac{n_{\text{caps}}}{n_{\text{hex}}}A_{\text{hex}} \\ =& A_{\text{signal}}(1 - c_{\text{caps}}) + \frac{c_{\text{caps}}A_{\text{signal}}A_{\text{hex}}}{A_{\text{sens}}n_{\text{hex}}} \end{aligned} \tag{8.2.5}$$

where for the second row n_{caps} has been replaced by rearranging Equation 8.2.4. Now, we can further reformulate Equation 8.2.5 by inserting the sensitivity factors from Equation 8.2.3:

$$A_{\text{laser}} = A_{\text{signal}}\left(\frac{1 - c_{\text{caps}}}{f_{\text{film}}} + \frac{c_{\text{caps}}}{f_{\text{caps}}}\right), \tag{8.2.6}$$

which weights the signal contributions. Solving the set of linear equations

$$\begin{aligned} A_{\text{laser}} =& \frac{A_{\text{hex}}}{n_{\text{hex}}}n_{\text{caps}} + A_{\text{film}} \\ \frac{A_{\text{laser}}}{\frac{1-c_{\text{caps}}}{f_{\text{film}}} + \frac{c_{\text{caps}}}{f_{\text{caps}}}} =& A_{\text{sens}}n_{\text{caps}} + A_{\text{film}} \end{aligned} \tag{8.2.7}$$

for the variables n_{caps} and A_{film} allows to retrieve information on the areal particle coverage

$$\lambda_{\mathrm{caps}} = \frac{n_{\mathrm{caps}} A_{\mathrm{hex}}}{n_{\mathrm{hex}} A_{\mathrm{laser}}} \tag{8.2.8}$$

within the measurement spot.

For the present data with $c_{\mathrm{caps}} = (66 \pm 2)\,\%$ an areal coverage of $\lambda_{\mathrm{caps}} = (99.7 \pm 0.1)\,\%$ results, which matches the coverage value determined from the microscopic images in Figure 8.2b. In order to estimate the uncertainty of λ_{caps}, one could consider the uncertainty of the fit parameter c_{caps} as well as of the geometrical parameters r_{lens}, L. However, it is assumed that the error included due to the assumption that both, flat film and cap array signal is independent of its local origin within the laser spot area, is even more severe. This is connected to the fact that the laser spot has a Gaussian beam profile but is only modeled with continuous intensity within the area of $A_{\mathrm{laser}} = \pi \cdot a \cdot b$, where a and b are estimated from the profile's full width at half maximum (170 µm and 200 µm) that has been previously determined with the knife edge method.

One could now argue that the same approach can be applied to the MOKE measurements 1 and 2 presented in Figure 8.1, however, the strong deviation between λ_{caps} (99.7 % and 99.9 %, respectively) and the coverage from the microscopic images (40.9 % and 83.2 %, respectively) indicates that the technique is not applicable for the particles with a diameter of 500 nm. A reason for this could be that the wavelength of the used layer is with 635 nm in the same range as the particle size and, hence, ray optics might fail to explain how light is reflected from the curved object.

8.2.2 'Artifacts' from Misleading Interpretation of MOKE Measurements

It shall further be mentioned that the magnetization reversal in Figure 8.2 measured in the L-MOKE setup contains an unusual feature: Around −50 kA/m on the decreasing branch and around 20 kA/m on the increasing branch, the magnetization reaches values beyond saturation level. Upon variation of the external magnetic field, it is physically not meaningful, that the MOKE signal linked to the sample's magnetization firstly exceeds and subsequently approaches saturation.[2] Hence, the observation is accounted to be an artifact arising when the measured Kerr amplitude is erroneously interpreted to be directly proportional to the longitudinal magnetization component M_{L}. This assumption of a pure longitudinal MOKE is usually made when in-plane magnetized samples are probed with perpendicularly polarized light (c.f. section 6.2). One reason for the artifact can therefore lie in small deviations from the perfectly perpendicular alignment of the polarizer. A slight deviation can cause unwanted contributions of the transversal components to the Kerr amplitude, as the polarization becomes 'partly' parallel.

Another hypothetical explanation for additional magnetization components contributing to the here recorded MOKE signal may be found in the cap's geometry. One important aspect is, that due to the curvature, the surface normal of the magnetic film locally changes its direction

[2] Note that there is an exception to this: If the magnetic sample contains two ferromagnetic materials with opposing sense of Kerr rotation, like Co and Tb in Ref. [FKCO20], the described course of the signal is possible.

with respect to the polarization angle within the polarization reference plane. Hence, the upper assumption about perpendicularly polarized light is (even for a perfect polarizer setup) not valid over the whole cap area. Furthermore, an onion textured cap with a magnetization following the curvature exhibits all three magnetization components (M_x, M_y, M_z). Only at the cap's exact geometrical center, M_y and M_z are zero. Similarly, possibly nucleated vortices with cores hosting perpendicular-to-surface magnetic moments can add to either of the three MOKE effects depending on the core's position on the cap. In contrast to a flat film, this can result in the simultaneous occurrence of all MOKE effects for caps and consequently hampers the interpretation that the Kerr signal is directly proportional to M_L in a standard LMOKE setup. Consequently, for a curved magnetic thin film, the direct conversion of polar MOKE signal into out-of-surface and longitudinal/transversal MOKE signal into parallel-to-surface magnetization is not valid.

Additionally, it should be mentioned that in standard magneto-optical applications 'cross terms' of the magnetization components, e.g. $M_x M_y$, are considered to be negligible,[Ham03] although they may manifest in the so-called vicinal interface sensitive MOKE (VISMOKE) proposed by Hamrle *et al.*. Herein, the standard magneto-optical effects interfere with an additional optostructural perturbation that arises from the lowered symmetry at the reflecting surface when it exhibits steps.[HHF03] As the curvature of a cap also causes a symmetry breaking of the probed surface, similar effects might affect the here discussed measurements, so that it may be misleading to neglect these mixed terms. As a result, an in-depth analysis of the interaction of the incident light with the curved film in dependence of the local magnetization would be required to pinpoint the origin of the specifically indicated artifact which however, exceeds the scope of this thesis.

Interestingly, this feature arose even more strongly in MOKE measurements on larger magnetically capped particles as shown in Figure 8.4 but was contrastingly not identified in any of the measurements on the capped 500 nm sized particles with the same layer stack Cu(10)/IrMn(30)/CoFe(10)/Si(10 nm). This can possibly again be related to the similar magnitude of the incident light's wavelength and the smaller particle size. Overall, the observable measurement artifact unfortunately complicates the analysis of the measured magnetization reversal. Finally, the absence of the artifact emphasizes why throughout the course of this thesis mainly magnetic cap arrays with templating particles with a diameter of 500 nm are selected to be investigated.

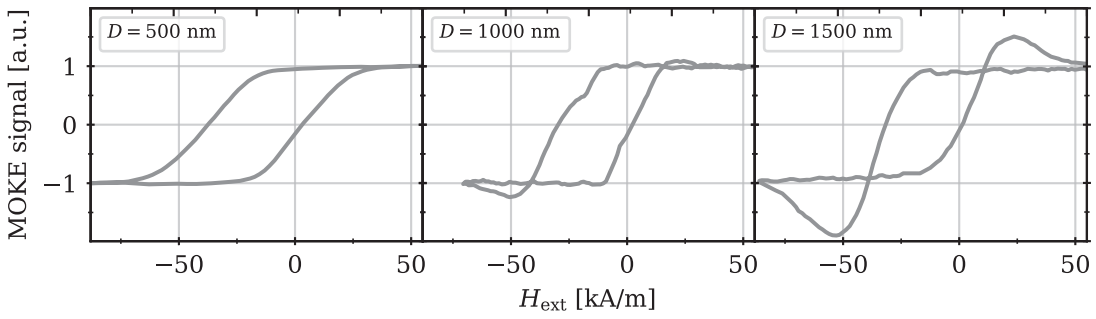

Figure 8.4: LMOKE measurements of EB cap arrays with different particle diameters D but composed of the same layer stack as in Figure 8.2.

8.3 Conclusion

In summary, the discussion of the exemplary measurements in this section points out that a careful analysis of measured magnetization curves of any microstructured sample with regions of different properties, like dimensions and/or curvature, is inevitable. For both VSM and MOKE, it was shown that the measured data can be ambiguous with regard to the analysis of the remagnetization path and the magnetic properties of the investigated capped particles. A hysteresis containing superposed signal contributions could falsely be interpreted as a vortex reversal due to different slopes on the loop's branches, if the contribution of possibly present residual flat film is not considered. As a result, the superposition of information can lead to a misinterpretation of the particles reversal mechanism and their magnetic properties, like the remanent magnetization.

Hence, it has been established to pre-characterize the sample's landscape in order to only consider areas fully covered with capped particles in the subsequently performed L- and V-MOKE measurements.

9. Magnetization Reversal in Ferromagnetic Cap Arrays

9.1 Remagnetization in Arrays of Ferromagnetic Caps in Dependence on the Ferromagnetic Layer's Thickness t_F

After important considerations for the analysis of measurement data related to the magnetization reversal of cap arrays have been discussed in the previous chapter, now, ferromagnetic thickness dependent changes for the reversal of ferromagnetically capped particle arrays shall be investigated. A thickness dependency in the reversal has been reported previously in literature on particles capped with a soft magnetic layer (Py) by NISSEN *et al.* and STREUBEL *et al.*[NMK15,SKR16,Str15] Both observe a transition in the reversal mode from coherent rotation towards vortex reversal around thicknesses of 20 nm for a particle diameter of $D = 330\,\text{nm}$.[NMK15,Str15] Within the thickness range for the vortex reversal, it may even be differentiated between cap arrays that possess a remanent vortex state with nucleation fields $H_{\text{nuc,f}} > 0$, and arrays in which $H_{\text{nuc,f}} < 0$ where the remanent state is an onion texture.

In view of these phase transitions, magneto-optic Kerr magnetometry was performed on samples with CoFe capped particles with $D = 500\,\text{nm}$ for varying ferromagnetic thickness t_F. The ferromagnetic layer has been deposited onto a 10 nm Cu buffer layer and has been capped by 4 nm Al. In Figure 9.1, the reversal curves along the samples' easy axis are indicated for both the longitudinal and transversal magnetization components (M_L and M_T) as determined from VMOKE measurements. A similar trend as described above for the 330 nm soft magnetic caps[Str15,NMK15] is observed here: While for $t_F = 10\,\text{nm}$ the curve's shape resembles magnetization rotation governed reversal processes, the characteristic vortex reversal shape indicating nucleation, motion and annihilation of a vortex as described in section 3.2 can be recognized for $t_F = 50\,\text{nm}$. For the latter case, the transversal magnetization M_T remains zero throughout the full reversal, as the magnetization does not rotate, and the nucleated vortices possess zero net transversal magnetization. When their cores are shifted, only the longitudinal component changes. Note, that for $t_F = 10\,\text{nm}$ non-zero values have been measured for M_T which underpins the nature of the overall remagnetization process incorporating most probably incoherent rotation of the individual caps' onion textures. The absolute values of M_T are however smaller than 10 % of M_S, which agrees with the fact that there is no distinct preference for the sense of rotation within the measured array of caps as it should be the case for a non-biased layer system.

From the shown remagnetization curves, certain characteristics were extracted that are depicted in Figure 9.2. At first, the coercivity H_C is determined from the two branches' intersections with the field axis (cf. Equation 2.4.1) and the remanent magnetizations $M_{R,f/b} = M_L(H_{ext} = 0)$ are retrieved for both branches. For increased thicknesses, H_C is reduced rather linearly because the vortex characteristics become more prominent which is underpinned as both $M_{R,f}$ and $M_{R,b}$ approach zero.

Further, the vortex annihilation fields $H_{ann,f/b}$ were defined as the magnetic fields beyond which M_L exceeds 95 % M_S, whereas the vortex nucleation fields $H_{nuc,f/b}$ result from the maximum susceptibility, i.e. steepest point along $M_L(H_{ext})$. For this, the numerically determined derivative is plotted as a dashed line in Figure 9.1 for each t_F. It is important to mention that the evaluation of H_{nuc} and H_{ann} is only reasonable for reversal curves that clearly indicate the vortex reversal. Although the values can mathematically also be determined for $t_F = 10$ nm, they are physically not meaningful as the caps are understood to neither nucleate nor annihilate a vortex. In this respect, also the data for 20 nm should be treated with caution as the reversal process cannot be clearly identified. However, the descending branch shows a smaller slope after a slightly steeper change around the retrieved nucleation field and hence, it is possible that the characteristic fields are just not as distinct, as e.g. for magnetic discs, but rather show a distribution of nucleation fields. Consequently, the nucleation process would be less prominently visible in the hysteresis.

Nevertheless, the trend of both nucleation fields in Figure 9.2 reproduces the trend of a broadening of the magnetic field regime for vortex stability for thicker films, which has previously been evidenced for cap and disk arrays.[NMK15,GNO02,SHO02] However, the additionally reported reduction of $H_{ann,f}$ and $-H_{ann,b}$ further enlarging the vortex stability range for disks[GNO02,SHO02]

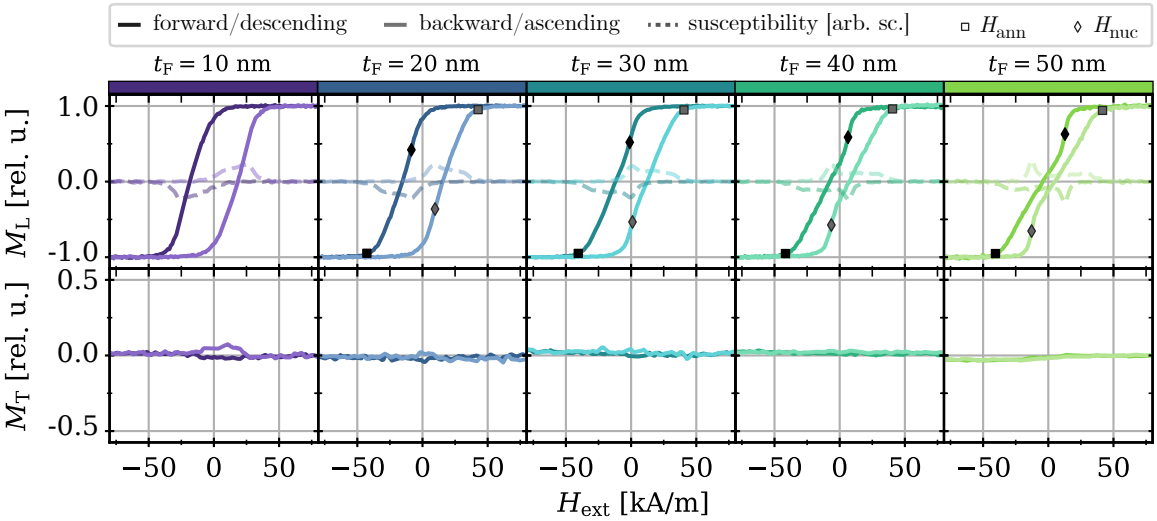

Figure 9.1: Remagnetization curves of CoFe capped particle arrays with $D = 500$ nm with t_F ranging from 10 to 50 nm. From the VMOKE data measured along the samples' easy axis, the longitudinal and transversal magnetization components (M_L and M_T) are extracted, while the darker (lighter) color corresponds to the descending/forward (ascending/backward) hysteresis branch. Dashed lines indicate the arbitrarily scaled (arb.sc.) course of the field-dependent magnetic susceptibility, i.e. the gradient of M_L. The fields at the susceptibilities' absolute maxima are extracted as the nucleation fields $H_{nuc,f/b}$ (♦ / ♦). The annihilation fields $H_{ann,f/b}$ (■ / ■) were determined via the threshold of 95 % M_S.

is not captured by the presented data. Here, both annihilation fields remain rather unaffected by the thickness change, although a slight reduction has been reported for Py caps. [NMK15]

An additional important observation is, that all hysteresis curves are symmetric since $M_{\mathrm{R,f}} \approx -M_{\mathrm{R,b}}$, $H_{\mathrm{nuc,f}} \approx -H_{\mathrm{nuc,b}}$ and $H_{\mathrm{ann,f}} \approx -H_{\mathrm{ann,b}}$ which allows to exclude the presence of a bias or other competing anisotropies.

In conclusion, the three phases, rotation of onion textures (I), vortex reversal with remanent onion states (IIa) and vortex reversal with remanent vortex states (IIb), can be assigned to the ferromagnetic cap arrays in dependence on the ferromagnetic layer thickness as it is indicated in Figure 9.2 by differently colored regions. Note, that $t_{\mathrm{F}} = 30\,\mathrm{nm}$ is within the transition between regions IIa and IIb, as M_{R} is already reduced down to 0.6 although the nucleation field is slightly smaller than zero. This reduction prior to the vortex nucleation speaks for the presence of either a transition state, like C- and S-states, or for a mixture of textures (onion, vortex, transition states) reflected by an average magnetization of 0.6 within the cap array that exhibits a broad nucleation field distribution. The absolute thicknesses for the transitions agree well with the phase boundary positions for $D = 500\,\mathrm{nm}$ caps in Ref. [Str15], despite the difference regarding the utilized ferromagnetic materials' anisotropies.

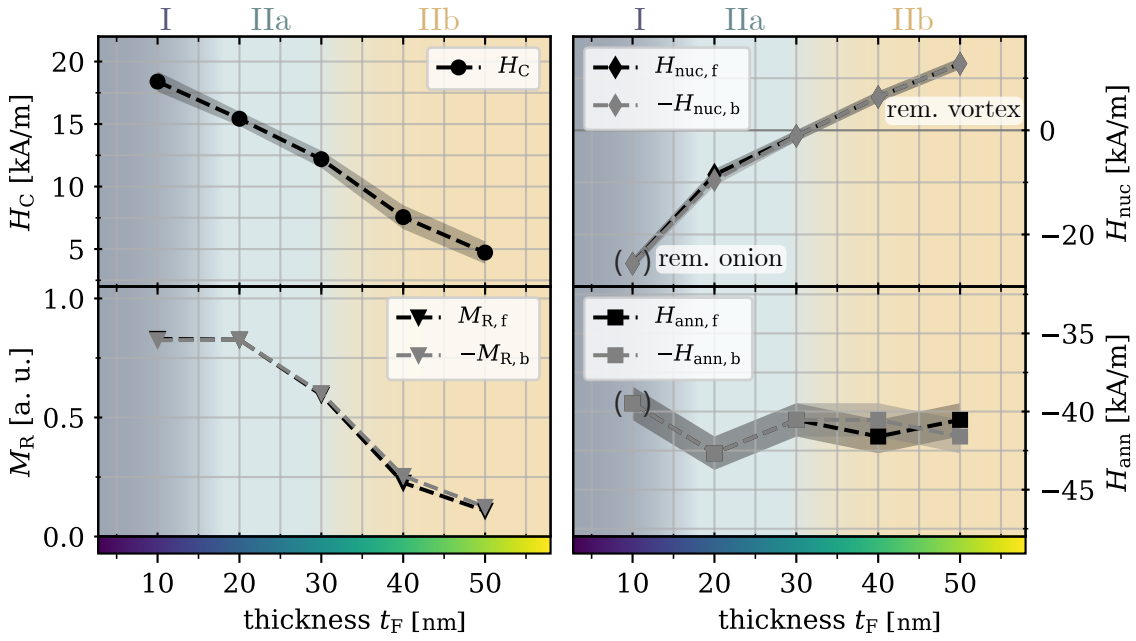

Figure 9.2: Characteristic properties of the ferromagnetically capped particle arrays extracted from the hysteresis curves in Figure 9.1 as functions of the CoFe thickness: The coercive field H_{C}, the remanent longitudinal magnetization M_{R}, the nucleation and annihilation fields H_{nuc} and H_{ann}. The subscripts f and b indicate the respective branches, i.e. the forward (descending) and the backward (ascending) branch. Note, that the parentheses around the data points for 10 nm indicate that for thin CoFe layers, the evaluation of H_{nuc} and H_{ann} is not reasonable, as the reversal does not take place via vortex nucleation and annihilation but magnetization rotation of an onion texture (Phase I). Additionally, the phase transition between remanent onion (IIa) and remanent vortex (IIb) arises at the zero-crossing of H_{nuc}. Based on these observations, shaded regions are added to indicate the phase transitions between I, IIa and IIb.

9.1.1 Analysis of FORC Fingerprints for Ferromagnetic Cap Arrays

In Figure 9.2, the three phases are not depicted to have sharp boundaries as a separation but rather smooth transitions for two reasons: At first, because no data had been acquired for the intermediate thicknesses and second, because the determination of nucleation fields as the magnetic field with the highest hysteresis gradient only reveals the average behavior of the ensemble measured. Especially, the major loop in Figure 9.1 for $t_F = 20\,\text{nm}$ with its large coercivity was accounted to resemble a vortex reversal, although it could possibly also arise from a superposition of vortex reversing caps and caps reversing via coherent rotation of their onion textures.

In order to resolve more details in the reversal processes of subsets within the ensemble, first-order reversal curves (FORC, cf. subsection 2.2.1) have been recorded with the LMOKE setup for three exemplary samples with $t_F = 10$, 20 and 40 nm. Thus, it is aimed to probe the distribution of caps with varying magnetic properties within the measured region.

Both the collected FORC sets as well as the subsequently derived FORC distributions are depicted in Figure 9.3. For all measurements, the experimental conditions, like the magnetic

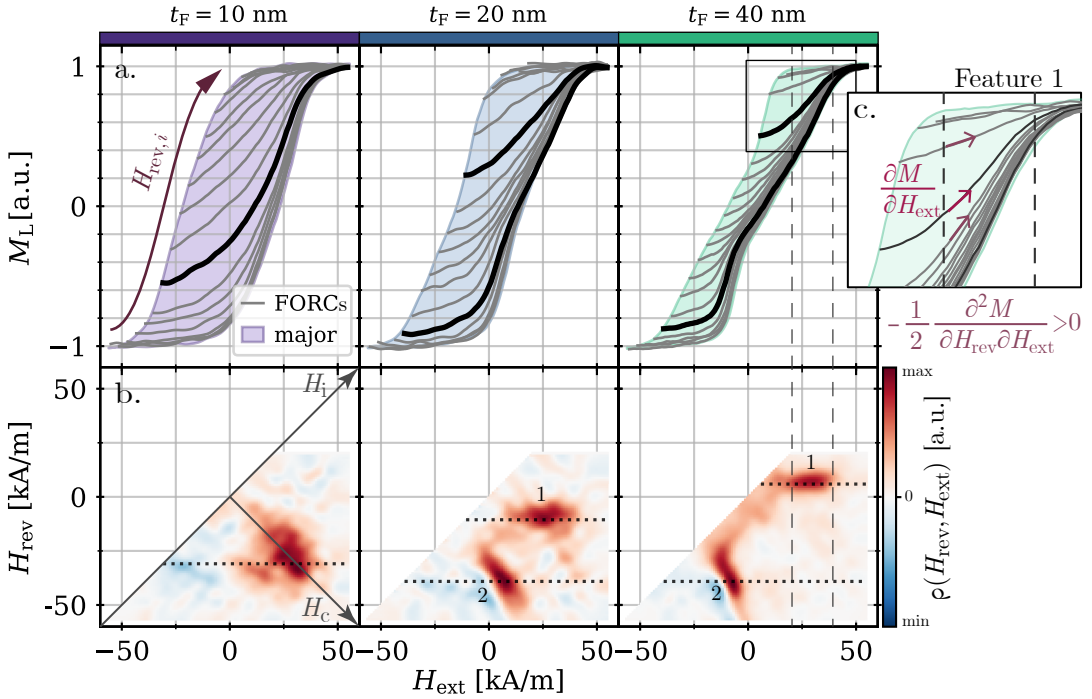

Figure 9.3: FORC analysis for CoFe cap arrays: For the three thicknesses t_F, the families of FORCs $M(H_{rev}, H_{ext})$ measured along the samples' easy axis are shown in a. with the corresponding FORC distributions $\rho(H_{rev}, H_{ext})$ in b. The shading in a. indicates the full major loop and the dotted lines in b. shall help for the orientation in the FORC diagram, as they correspond to the course of H_{ext} of a specific H_{rev} for which the related FORCs $M(H_{rev}, H_{ext})$ in a. are the bold lines. The diagonal arrows in b. shall illustrate the relationship between the coordinate spaces (H_{rev}, H_{ext}) and (H_i, H_C). (cf. Figure 9.4) The detail view in c. exemplarily illustrates the origin of feature 1: As the gradient of each FORC decreases in between the dashed lines (20 kA/m< H_{ext} <40 kA/m) surrounding feature 1 when H_{rev} increases from 5 to 15 kA/m, the FORC distribution is positive (cf. Equation 9.1.1).

field resolution of $\Delta H_{\mathrm{ext}} = 1\,\mathrm{kA/m}$, the measurement time per point $\Delta t_{\mathrm{meas}} = 20\,\mathrm{ms}$ and the sweep rate of $25\,\mathrm{kA/m/s}$ were kept constant. In order to reduce the signal-to-noise ratio of the measurement, the reproducible individual FORCs were averaged from multiple measurements N with $N =$ 7, 5 and 3 for $t_{\mathrm{F}} = 10$, 20 and 40 nm, respectively. To collect a family of n FORCs, the reversal field $H_{\mathrm{rev},i}$ was successively increased as indicated by the arrow in a. from $H_{\mathrm{rev},0}$ at negative saturation towards $H_{\mathrm{rev},n}$ with a step width of $\Delta H_{\mathrm{rev}} = 1\,\mathrm{kA/m}$. Next, the measured FORCs were filtered with the help of a Savitzky-Golay filter,[Sav64] by which polynomials of a certain degree (here 3) are successively fitted to consecutive windows of adjacent data points (here 5). From the hereby smoothed data, the FORC distribution $\rho(H_{\mathrm{rev}}, H_{\mathrm{ext}})$ was calculated as described in subsection 2.2.1 with a smoothing factor $SF = 8$ for all measurements. For this, a software developed by Merkel *et al.* for the FORC analysis of extended EB films was applied.[MHR21] Due to the measurement protocol, meaningful data arises only in the triangular region where $H_{\mathrm{ext}} \geq H_{\mathrm{rev}}$.

Each individual FORC of an acquired family reveals the reversal of the cap ensemble in the probed sample region starting from a specific state, i.e. each magnetic cap performs the reversal from a texture it had reached throughout the forward branch stopping at H_{rev}. Hence, each FORC resembles different starting conditions which allows to resolve the distribution of certain characteristic features. In the false color depiction of the FORC distribution in b. - which is often referred to as a sample's *magnetic fingerprint or signature* - clear changes in the distribution can be identified when the ferromagnetic thickness is increased.

At $\boldsymbol{t_{\mathrm{F}} = 10\ \mathrm{nm}}$, a single rather broadened feature is visible in the quadrant of negative H_{rev} and positive H_{ext}. The feature is stretched along the diagonal with $H_{\mathrm{rev}} = -H_{\mathrm{ext}}$ and has been related to the coherent rotation processes of soft magnetic disks' and caps' individual magnetic textures in literature.[DLR07,BRG13] Hence, the FORC diagram supports the indication of cap-specific coherently rotating onion states in phase I of Figure 9.2.

A FORC diagram $\rho(H_{\mathrm{i}}, H_{\mathrm{C}})$ with transformed axes of the caps with $t_{\mathrm{F}} = 10\,\mathrm{nm}$ is shown in Figure 9.4. Therein, the width of the ridge feature along the interaction field axis H_{i} is known to be connected to the strength of magnetostatic interactions between the object's net magnetization.[RHZ14] Dumas *et al.* show a ridge which is narrow along the H_{i} axis but stretched along the coercivity axis for Fe nanodots with a diameter of 52 nm.[DLR07] From Figure 9.4, it can be deduced, that the individual magnetic caps of the ensemble within the measurement spot interact magnetostatically (and possibly also via exchange coupling at the inter-cap connections) and that the ensemble exhibits a distribution of local coercive fields. Here, the value $H_{\mathrm{C}} = (25 \pm 10)\,\mathrm{kA/m}$ is extracted from the maximum of the FORC distribution's integral with respect to the interaction field as a function of H_{C} with the uncertainty determined by the FWHM. This emphasizes the advantages of FORC compared to standard hysteresis measurements: The major loop, from which zero-crossings a coercivity value of $H_{\mathrm{C}} = (22 \pm 1)\,\mathrm{kA/m}$ can be extracted, does bot reveal the nature of the studied sample sufficiently, as the distribution of magnetic properties cannot be probed.

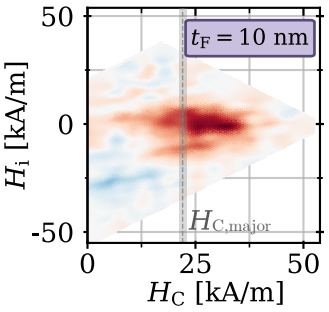

Figure 9.4: FORC distribution $\rho(H_{\mathrm{i}}, H_{\mathrm{C}})$.

Contrastingly, the described feature along the diagonal $H_{\mathrm{rev}} = -H_{\mathrm{ext}}$ cannot be found in the FORC diagram of CoFe caps with $\boldsymbol{t_F = 40\ \mathrm{nm}}$. Instead, two other features show up: One is stretched along H_{ext} from 16 to 34 kA/m for $H_{\mathrm{rev}} \approx 6\,\mathrm{kA/m}$ (1), while the other is located around $H_{\mathrm{rev}} \approx -35\,\mathrm{kA/m}$ and $H_{\mathrm{ext}} \approx -10\,\mathrm{kA/m}$ (2). These features resemble characteristic switching processes, because non-zero values of ρ relate to the degree of irreversibility.[DLR07] In order to correlate the extracted magnetic fingerprints to switching events in the measured FORC family, the two dotted lines which were added in b. and correspond to the bold FORCs in a. shall be analyzed in the following.

1. Starting with the upper scan line across feature 1, the magnetic cap array reverses from a magnetic field $H_{\mathrm{rev}} = 6\,\mathrm{kA/m}$, where vortices have already nucleated in the majority of caps, which matches the average nucleation field of 6.5 kA/m derived from the descending branch of the major loop (cf. Figure 9.2). The connection between the individual FORCs and the derived distribution is illustrated in Figure 9.3 c. When increasing the reversal field from 5 to 15 kA/m, the slope $\partial M/\partial H_{\mathrm{ext}}$ decreases, which in turn speaks for a negative mixed second derivative. Due to the definition of the FORC distribution (cf. subsection 2.2.1)

$$\rho(H_{\mathrm{rev}}, H) = -\frac{1}{2}\frac{\partial^2 M(H_{\mathrm{rev}}, H)}{\partial H_{\mathrm{rev}} \partial H}, \tag{9.1.1}$$

   feature 1 is consequently linked to positive values of the FORC distribution. This positive feature, which is connected to the nucleation of vortices, their motion and their subsequent annihilation, has likewise been recognized in FORC diagrams of magnetic nanodots,[DLR07] disks[GYV15] and hemispherical caps.[BRG13]

2. The lower scan line through feature 2 starts at $H_{\mathrm{rev}} = -43\,\mathrm{kA/m}$, where most of the magnetic caps have already been negatively saturated since the net magnetization is M = -0.88. When H_{ext} is increased, the caps re-nucleate vortices which is accompanied by a maximum in ρ at $H_{\mathrm{ext}} = -9\,\mathrm{kA/m}$. From the major loop's ascending branch in Figure 9.1, $H_{\mathrm{nuc,b}} = -6\,\mathrm{kA/m}$ was determined which also suggests vortices in remanence after negative saturation. The re-nucleation related FORC feature 2 spans from $-20\,\mathrm{kA/m}$ to $-1\,\mathrm{kA/m}$ when projecting $\rho(H_{\mathrm{rev}}, H_{\mathrm{ext}})$ onto the H_{ext} axis. Hence, the FORC diagram supports the presence of remanent vortices as indicated by the phase boundaries in Figure 9.2. It shall be mentioned that feature 2 is accompanied by a region of negative values, which seems irritating when thinking about the physical meaning of the term *distribution* at first. It is, however, reasonable from the mathematical definition of $\rho(H_{\mathrm{rev}}, H_{\mathrm{ext}})$ as the mixed second derivative of $M(H_{\mathrm{rev}}, H_{\mathrm{ext}})$ (Equation 2.2.1). Negative values of the distribution therefore indicate an increase in the slope of successive FORCs for rising H_{rev}.[RHZ14,GYV15] Further following the scan line, ρ remains to be zero, as it is expected for the reversible motion of the vortex cores during the remagnetization process. Likewise to feature 1, feature 2 (with both positive and negative region) has also been observed earlier for nanodots, disks and magnetic caps.[DLR07,GYV15,BRG13] Note, that within the cited work an additional maximum was related to the annihilation of re-nucleated vortices, which is, however, not found in the described scan line of the CoFe capped particles in this thesis. A reason for

this is found in the inset of Figure 9.3 c. The slope change necessary for a non-zero ρ is clearly visible for a specific set of reversal fields (width of feature 1 along H_{rev}) connected to vortices nucleated on the descending branch. For the vortices which re-nucleate on the ascending branch, however, the corresponding FORCs are tightly packed with similar slope in-between the dashed lines. Consequently, no additional feature arises in the shown FORC diagrams. Nonetheless, a thorough physical explanation for the feature being absent in the present thesis but (faintly) visible in other work [DLR07,GYV15,BRG13] is still pending.

When now qualitatively comparing the FORC fingerprints for the three thicknesses, it can be concluded that the reversal mechanism for CoFe caps with $\boldsymbol{t_{\mathrm{F}} = 20\ \mathrm{nm}}$ includes vortex nucleation, motion and annihilation. The ridge feature along the diagonal H_{C} axis is not found, however, features 1 and 2 are clearly visible, although wider than in the case of 40 nm. An additional difference is, that at 20 nm the majority of feature 2 is localized at positive values of H_{ext} which suggests that vortices nucleate at positive magnetic fields on the ascending branch. This agrees well with the classification presented in Figure 9.2, where a remanent onion state with $M_{\mathrm{R}} = 0.83$ was assigned to the major loop of caps with in with $t_{\mathrm{F}} = 20\,\mathrm{nm}$.

9.2 Angular-Dependent Magnetization Reversal in Arrays of Ferromagnetic Caps

In a ferromagnetic cubic crystal material with in-plane shape anisotropy (e.g. thin films) the anisotropy energy density depends on $\sin^2(2\varphi)$ with the azimuthal angle φ as described for Equation 2.1.11. Hence, easy axes along 0° and 90° are expected for thin CoFe films. [KHP12] However, this cubic anisotropy can be superposed by a uniaxial anisotropy that originates from anisotropic growth conditions, like the application of a magnetic field during deposition. [Kus11] The samples fabricated for this thesis were sputtered in an external magnetic field of 28 kA/m, which causes a difference in the two minima of the anisotropy energy, where the uniaxial anisotropy axis aligns with one of the cubic axes. The consequently arising azimuthal dependence of the coercivity is displayed in Figure 9.5 b., where the maxima at 0° and 180° indicate the main anisotropy axis and the local maxima at 90° and 270° indicate the second axis. The course in b. was extracted from angular resolved MOKE measurements of the magnetization reversal for a CoFe film sputtered on Si with a thickness of $t_{\mathrm{F}} = 10\,\mathrm{nm}$. Accordingly, the same measurement was performed for an array of particles capped with this magnetic film and is plotted in a. It is immediately apparent that the expression of the major and minor easy axis found for the thin film is not reproduced for the cap array. Instead, the coercivity determined from the hystereses' intersections with the abscissa (Equation 2.4.1) is generally higher in the case of caps with barely visible maxima at 0° and 180°. While H_{C} spans a range of 2.8 kA/m between easy and hard axis for the planar film, it only changes by 0.6 kA/m along the coercive field's course for the cap array. However, please note that the ferromagnetic film is expected to grow differently on a silica sphere than on a Si substrate: A defined cubic crystal structure cannot be promoted from the particle surface, which explains the absence of the weaker anisotropy axis along 90°. Nevertheless, the sputtering in an external magnetic field applies to both film and caps and still results in a

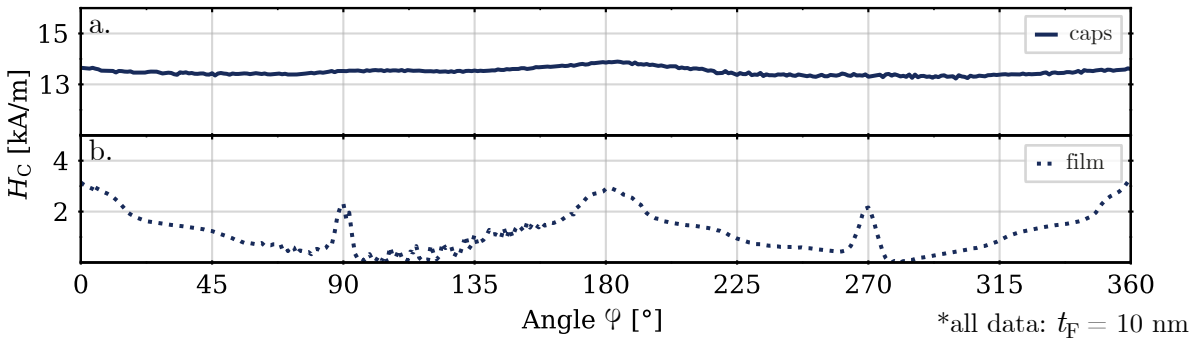

Figure 9.5: The coercive field $H_C(\varphi)$ was extracted from angular resolved magnetization reversal measurements for both CoFe capped particle arrays (a.) and the corresponding flat film (b.) with $t_F = 10\,\text{nm}$. Note, that the H_C axes are equally scaled except for a constant offset.

uniaxial anisotropy along the direction of this magnetic field although it is only slightly visible for the caps.

Thus, the angular dependence of the coercivity is clearly weakened in the case of ferromagnetic caps, as the crystal structure is expected to be less uniform due to the growth on a silica particle. It is further probably overshadowed by the large distribution of switching fields that was previously recognized during the analysis of easy axis FORCs and the corresponding FORC distributions (cf. Figure 9.4).

9.3 Conclusion

As a result, the ferromagnetically capped particle arrays clearly show a thickness dependence with regard to their remagnetization behavior. This relates to a change in the dominating reversal process from coherent rotation of onion states to a vortex reversal upon increasing layer thickness. The analysis of the acquired FORC diagrams of CoFe capped particle arrays in the scope of *fingerprint characteristics* supports the t_F related phase transitions indicated in Figure 9.2 and adds information about the distribution of magnetic properties. Between 10 and 20 nm, the caps' remagnetization route changes from rotation of magnetic onion states to vortex reversal and between 30 and 40 nm the remanent state switches from onion to vortex. Besides these insights, it is important to note that the caps' coercivity as a quantity extracted as half the width of the hysteresis at $M = 0$ cannot be interpreted as a quantity purely connected to the ferromagnet's anisotropy, as it is in principle the case for a thin film. This was seen from the difference in the film's and the caps' angular dependence of H_C as well as from the broad ridge feature in the cap ensemble's FORC diagram. The ensemble of caps underlies a distribution of particle sizes and lattice alignments resulting in a distribution of magnetic properties.

10. Magnetization Reversal in Exchange-Biased Cap Arrays

In the view of engineering magnetically capped particle arrays, the analysis of the caps' reversal with respect to the ferromagnetic thickness in section 9.1 revealed a clear influence of the cap geometry. With enhanced cap thickness t_F the demagnetization energy density of an onion state rises, which causes a transition from coherent rotation of onion states to a reversal defined by vortex nucleation, motion and annihilation. Another factor governing the reversal processes was discussed in chapter 4: The magnetostatic coupling of the onion textured caps in their respective array formation lowers the demagnetization energy, and hence, their hysteresis curves strongly differ from the hysteresis of an individual magnetic cap.
For the present chapter, an antiferromagnetic layer is added to the layer system sputtered on the templating particles, in order to create arrays of exchange-biased (EB) caps. The effects of this induced unidirectional anisotropy on the remagnetization processes will be studied alongside reversal curves of extended films of the same EB layer systems. As introduced in section 2.4, the strength of the EB can be correlated with the displacement of the hysteresis H_{EB} (Equation 2.4.1), and according to Equation 2.4.2 this quantity scales inversely proportional with the layer thickness of the ferromagnet.[MKS87] Moreover, the antiferromagnetic thickness t_{AF} alters H_{EB} (and H_C): The t_{AF} dependent analysis yields a plateau for H_{EB} above a threshold thickness, below which the EB decreases abruptly before it reaches zero for thin enough antiferromagnetic layers.[Mei62,JCJ94] Both thickness dependencies have been exceedingly investigated for extended EB thin films[Mei62,MKS87,JCJ94,NS99] but only to a small extend for EB cap arrays[NKM16]. As compared to ferromagnetic cap arrays, in which the thickness and the lattice geometry have already been identified as influencing properties, it can therefore be expected that the t_F and t_{AF} dependent EB characteristics further add complexity to the remagnetization processes in EB cap arrays.

In order to investigate whether the curved modulation affects the general behavior of an EB bilayer with respect to the antiferromagnetic thicknesses, samples with $t_F = 10\,\text{nm}$ and $t_{AF} = 0$, 5, 7 and 30 nm have been studied. $|H_{EB}|$ and H_C have been extracted from magneto-optically acquired easy axis hysteresis loops measured once on the sample's flat film region and once on a region of purely arranged caps. The data is displayed in Figure 10.1 alongside values of both quantities from a more detailed thickness dependent study of EB thin films presented by Merkel *et al.*.[MRH22]. At first, the results show that the unidirectional anisotropy is also present in the cap arrays, as they show a loop shift which is comparable with the thin film values from Ref. [MRH22]. Further, the strength of the caps' EB clearly depends on t_{AF} as it is also the case

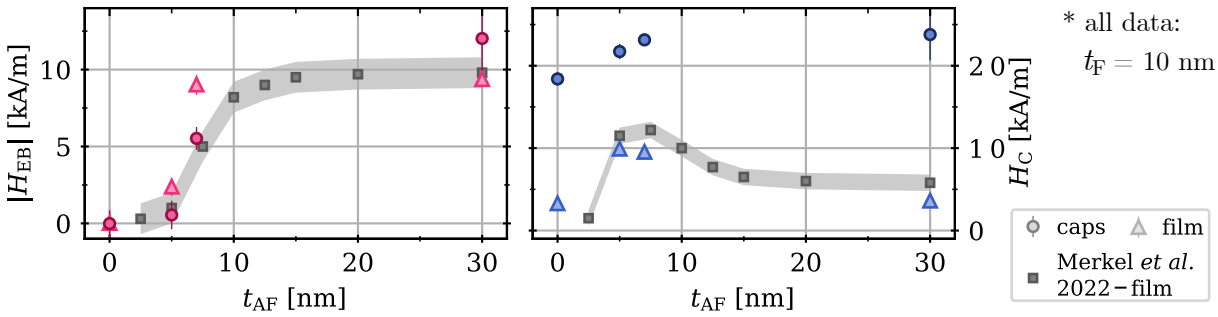

Figure 10.1: Easy-axis values of $|H_{EB}|$ and H_C in dependence of the antiferromagnetic thickness t_{AF} for both the flat film and the cap array with a ferromagnetic thickness of $t_F = 10\,\text{nm}$ are plotted together with values determined by MERKEL *et al.* (gray squares) for comparison.[MRH22] Note, that each data point stems from one sample only, while for the EB cap arrays of $t_{AF} = 30\,\text{nm}$ they were averaged over four samples.

for the thin film: Caps with an IrMn thickness of 0 or 5 nm do not possess an EB, while the onset of EB is visible from 7 nm and the maximum EB shift is reached at 30 nm. Contrastingly, the coercivity of the EB cap arrays, which is determined from the width of the hysteresis, is significantly higher than the flat film's H_C for all chosen thicknesses. For the EB thin films, the coercivity reaches a maximum at the IrMn thickness for which $|H_{EB}|$ shows the highest slope and subsequently H_C decreases when $|H_{EB}|$ reaches its plateau. This behavior can be explained for these polycrystalline films prepared under sputter conditions for which columnar grain growth can be expected (cf. Ref. [MHR20]) because a rise in t_{AF} is accompanied by a gradual shift of the antiferromagnet's average grain size distribution to larger volumes. In the scope of the stability classification for the antiferromagnetic grains presented in subsection 2.4.2, the number of thermally stable grains (class III) increases with increasing t_{AF} while the number of unstable/rotatable grains (class II) is reduced. In Ref. [MRH22], the two grain classes' fractions have been extracted by fitting model calculations based on an extended STONER-WOHLFARTH ansatz to angular resolved hysteresis measurements. The derived proportions of class II and III as functions of t_{AF} agree with the thickness dependent progression of $|H_{EB}|$ and H_C which are the macroscopic magnetic quantities that are essentially proportional to the number of thermally stable and unstable grains, respectively.

Note, that the values derived for the flat film region on the samples of this thesis (triangles) differ slightly in both $|H_{EB}|$ and H_C from the referenced literature values, however, this is likely to be related to the difference in the sample substrate: While Si wafer pieces were used in Ref. [MRH22], the samples studied here with flat film and cap array region were deposited on glass substrates.

The similarity of the $|H_{EB}|$ course for cap arrays and the flat film from Ref. [MRH22] can be related to the similarity in the grain size distributions, as the mean grain radius of $\langle r_{eq} \rangle = (7.6 \pm 0.5)\,\text{nm}$ acquired from HIM images on the caps (Figure 7.2) and the value of $\langle r_{eq} \rangle = (7.0 \pm 0.3)\,\text{nm}$ presented for the flat EB film on Si[MRH22] do not differ significantly. This is in turn indicative for columnar grain growth of the polycrystalline layers on the templating particles and that the antiferromagnetic grains' volumes may be scaled with t_{AF} for the selected deposition rate. As a consequence, the above mentioned dependence of the thermally stable and unstable grains'

fractions on t_{AF} in EB films does also apply for the EB caps.

Overall, the cap arrays' EB seems to be qualitatively interpretable within the scope of established models. Also for the curved film geometry, the t_{AF} dependence applies, although this is not the case for the coercivity. The latter does not decrease for thicker antiferromagnetic layers as it is the case for the flat film. This is accounted to the generally enhanced width of the magnetic cap ensemble's hysteresis curve, as it has also been observed for purely ferromagnetic caps in Figure 9.2 ($t_{AF} = 0$, $t_F = 10\,\text{nm}$). Hence, the distribution of magnetic properties like the coercivity which has previously been discussed based on the FORC analysis of the ferromagnetic cap arrays (cf. Figure 9.4), suppresses the expected t_{AF} dependence for H_C in EB cap arrays.

For the following sections, an antiferromagnetic thickness of 30 nm is chosen which guarantees a stable unidirectional anisotropy in flat films and is therefore rendered a good staring point to study the effects of EB in hemispherical cap arrays. Later, the vortex characteristics of EB caps with thinner antiferromagnetic layers will be discussed in section 10.3.

10.1 Angular-Dependent Magnetization Reversal in Arrays of EB Caps

Flat EB bilayer systems are characterized by an easy direction which is aligned parallel to the direction of the applied magnetic field during deposition or in a post-fabrication field cooling (FC) process. Consequently, the samples show a distinct azimuthal dependence of the coercivity, where the hard axis aligns perpendicular to the FC direction and the easy axis parallel to this direction. In angular resolved magnetization reversal measurements, where for different azimuthal angles φ, hysteresis loops are recorded, the easy axis is indicated by maxima in H_C at $\varphi = 0°$and 180°, while the respective minima at 90° and 270° indicate the hard axis. On the other hand, the hysteresis shift H_{EB} is zero at the hard axis but reaches maximum absolute values around 0° and 180° with opposing signs. Note that this holds true only for a certain set of deposition parameters. However, the here applied conditions during deposition of the investigated cap arrays are comparable to the deposition parameters for which this typical angular dependence of the EB shift and the coercive field was observed in the case of flat films of he same material composition.[MHR20]

In order to compare the azimuthal dependence for the cap arrays and the flat film area of the fabricated samples with $t_{AF} = 30\,\text{nm}$, angular resolved VMOKE measurements have been performed. Exemplary hysteresis loops of both EB cap arrays (a.) and the flat film (b.) are shown in Figure 10.2 for characteristic angles $\varphi = 0°$, 45° and 90° and for three different ferromagnetic thicknesses $t_F = 10$, 30 and 50 nm. The evaluated courses of $H_C(\varphi)$ (c.) and $H_{EB}(\varphi)$ (d.) are depicted in the range from 0° to 180° alongside two additional properties: The maximum value of the transversal magnetization component $M_{T,max}$ reached throughout the remagnetization as a measure for coherent rotation (e.) and a value describing the asymmetry (Ref. [CSH05], s. below) between the two branches of the hysteresis (f.).

For caps with $t_F = 10\,\text{nm}$, EB shift's angular dependence of the flat films is in principle reproduced by the cap arrays for all investigated t_F with slightly larger absolute values. This not only observed here and in Figure 10.1 for $t_{AF} = 30\,\text{nm}$, but was also reported in literature,[ZWM09]

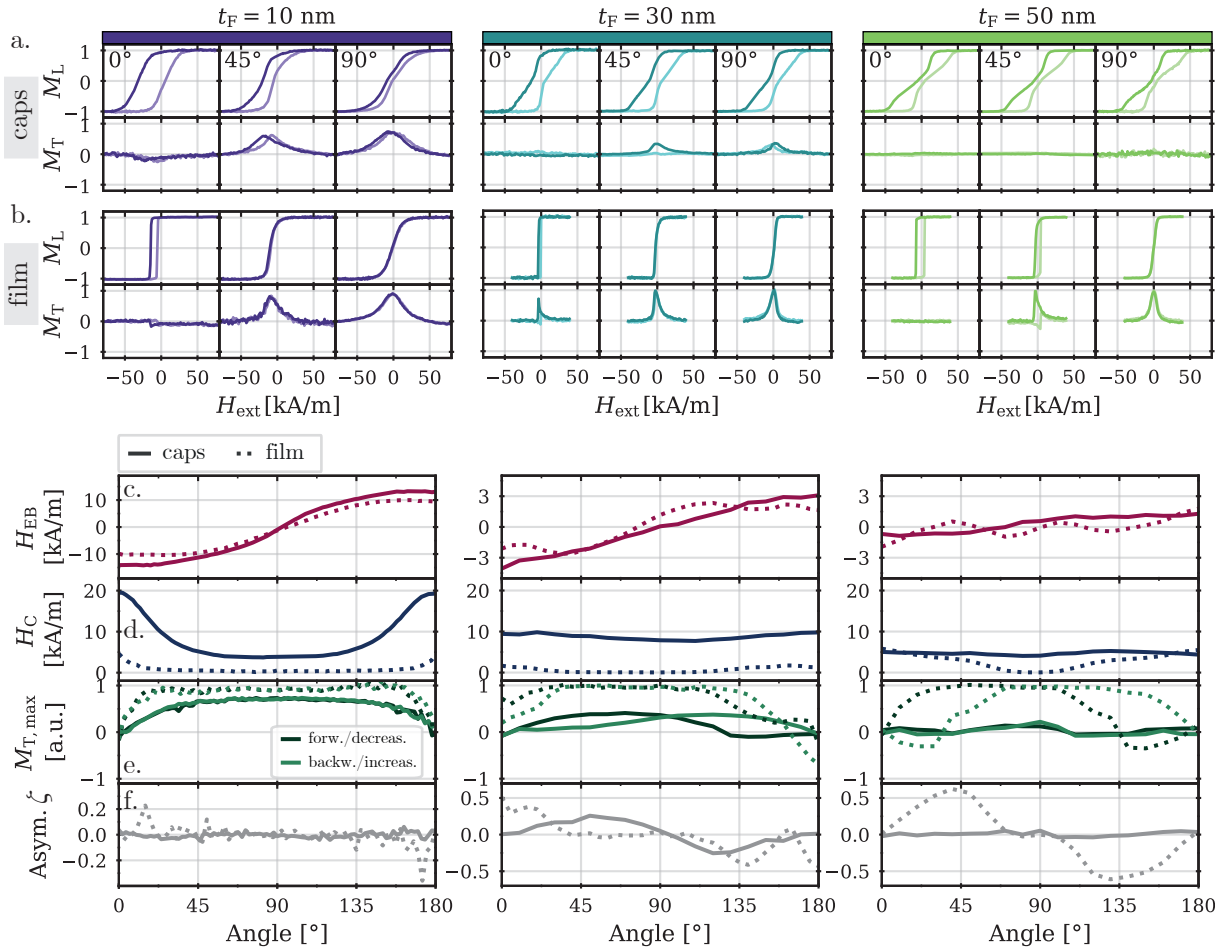

Figure 10.2: For the three exemplary thicknesses $t_F = 10$, 30 and 50 nm, the angular dependence of the remagnetization process is illustrated regarding the flat EB film and the EB film deposited on particle arrays, both with an antiferromagnetic thickness $t_{AF} = 30$ nm. The longitudinal and the transversal magnetization components M_L and M_T are plotted as functions of the external magnetic field H_{ext} for the three angles $\varphi = 0$, 45 and 90° (with respect to the induced EB direction), where the backward (ascending) branch has a lighter color than the forward (descending) branch. The upper row (a.) shows the VMOKE measurements on the cap arrays, while the lower row (b.) presents the data acquired for planar EB layers of the same thicknesses. From all hysteresis curves gained for the angles ranging from 0 to 180 °, the following characteristics were extracted and are plotted in c.-f.: The EB field shift H_{EB} (c., red), the coercivity H_C (d., blue), the maximum value of the transversal component $M_{T,max}$ reached on both branches of the hysteresis measured at $\varphi = 90°$ (e., green) and the asymmetry ζ (f., gray). For all plots, the dotted line depicts the angular resolved data for the flat film, while the continuous line represents the cap arrays.

where the effect of enhanced EB strength is ascribed to the gradually decreasing thickness of the ferromagnet towards the cap's side. As however discussed in subsection 3.2.1, the effect can also originate from the microscopic structuring of the bilayer.[NSL05,NOK99] Also, the course of $H_C(\varphi)$ is qualitatively comparable between caps and film, with the difference that it is generally larger for the caps. It is important to note, that the caps are not just characterized by a higher H_C but also by a broader magnetic field regime in which the reversal takes place. This has previously been referred to as a large switching field distribution which was not only observed in hysteresis

measurements of magnetic rings[BBV02], EB disks[LPE05] and caps[ZWM09], but also matches the stretched appearance of the purely ferromagnetic caps' FORC distribution along the H_C axis in Figure 9.4. In contrast to the flat film,[MHR20] the cap array's coercivity is distinctly enlarged at measurement angles around the hard axis (90°).

For angles close to the hard axis, the flat film is characterized by purely rotational behavior. This can be seen from $M_{T,max}$ which is small around the easy axis where the reversal is dominated by domain nucleation and domain wall motion but reaches values close to 0.95 between 20° and 160° (i.e. the magnetization vector mainly rotates from longitudinal positive saturation over the transversal direction). The transversal magnetization M_T of the cap array, on the other hand, reaches values around 70 % of the saturation magnetization between 45° and 135°, which can possibly be related to other reversal processes than the rotation of onion states. More specifically, if some caps in the ensemble nucleate vortices, the transversal magnetization cannot reach 1. Nevertheless, rotational processes in the reversal of both caps and flat film take place as $\vec{M}$ rotates only over the EB direction, i.e. M_T takes only positive values between 0° and 180°, but negative between 180° and 360°. For a remagnetization along the easy axis, i.e. at 0° and 180°, the film nucleates domains which extend through the film with a vanishing net transversal magnetization component and a steep gradient of the reversing M_L. Also for the cap array, the measured net M_T approaches zero for $\varphi = 0°$ and 180°, which is contrastingly accompanied by M_L gradually changing. At these angles, no direction is preferred for the rotation of the onion states, such that a possible explanation is the equally preferred rotation over both directions. Whether this is accompanied by a fraction of the ensemble reversing via vortex nucleation cannot be deduced, and hence, a FORC analysis shall shed light onto this question in subsection 10.2.2.

The additionally plotted asymmetry ζ is defined as the difference between $M_{T,max}$ on the forward/descending and the backward/ascending hysteresis branch. While the asymmetry vanishes for the caps with $t_F = 10\,\text{nm}$ at all angles, small positive/negative values just after 0° / before 180° can be observed for the flat film. This asymmetry between the reversal pathways on the two branches has been studied previously by Camarero *et al.* and is rated to be an intrinsic property of EB systems.[CSH05] More specifically, ζ describes whether one branch reverses more preferably via magnetization rotation than the other. This asymmetry has been shown to originate from the competition of anisotropies, where the angular range of the asymmetry's presence and its magnitude depend on the ratio between the intrinsic ferromagnetic anisotropy K_F and the strength of the unidirectional anisotropy J_{EB}.[CSH05] In a depth-dependent micromagnetic study, this asymmetry was further found to be connected to the emergence of local incomplete domain walls in the ferromagnetic layer during the descending hysteresis branch.[LPM06] This depth dependence of domain walls in extended EB films has the same origin like the tilt of a vortex core in EB disks where the ferromagnetic moments close to the interface shared with the antiferromagnet are more strongly pinned (cf. Ref. [GH06]).

When increasing the ferromagnetic thickness, the cap arrays' remagnetization behavior is tuned towards vortex reversal as it has been previously observed for ferromagnetic caps (Figure 9.1). Additionally, the inverse proportionality between H_{EB} and t_F (cf. section 2.4) becomes apparent in the remagnetization of both, the cap arrays and flat film, as the absolute values of H_{EB} at

0° and 180° are reduced upon increasing ferromagnetic layer's thickness. Moreover, for the flat film, the two hysteresis branches differ such that the asymmetry is higher at $t_F = 30$ and 50 nm and also spans a larger angular range than for $t_F = 10$ nm. A hypothetical explanation for that lies in the reduction of the interfacial exchange coupling with increasing t_F,[MRH22] which alters the competition between the ferromagnet's uniaxial anisotropy and the interfacial coupling energy mediating the EB. At $t_F = 30$ nm, the asymmetry is also present in the measurement of the cap arrays, however, it vanishes at $t_F = 50$ nm. This is related to the fact, that the cap array's magnetization reversal indicates either no or completely incoherent rotational processes at this thickness of 50 nm and is instead only characterized by vortex nucleation, motion and annihilation. For $t_F = 30$ nm, pure vortex reversal cannot be the case, as the non-zero values of $M_{T,max}$ demonstrate. The data implies, that the ensemble hosts caps with a distribution of properties, which will be studied in more detail via FORC analysis in subsection 10.2.2.

10.2 Remagnetization in Arrays of EB Caps in Dependence on the Ferromagnetic Thickness t_F

In addition to the angular resolved data, the main characteristics of the easy axis measurements, i.e., $|H_{EB}|$, H_C, the remanent magnetizations $M_{R,f}$ and $M_{R,b}$ as well as the maximum transversal magnetization $M_{T,max}$ for the hard axis measurement shall be summarized in Figure 10.3 for a variety of ferromagnetic thicknesses at a fixed antiferromagnetic thickness of $t_{AF} = 30$ nm. The values of all quantities have been averaged per thickness over the number of samples N investigated as summarized in the following table:

t_F [nm]	5	7.5	10	15	20	30	40	50
N (cap arrays)	1	1	2	2	1	4	2	2
N (flat film)	1	1	2	2	1	3	1	2

For $|H_{EB}|$ and H_C, the uncertainties for each measurement result from the magnetic field resolution. The uncertainty of magnetization values for $M_{R,f/b}$ and $M_{T,max}$ is estimated from the scattering of the respective magnetization component at high magnetic fields saturating the sample. For this, the doubled standard deviation of M_L around 1 and M_T around zero was used. Per quantity and per thickness, the sum of the maximum uncertainty of all respective measurements and the averaged values' standard deviation is displayed by the shaded regions.

In a., both flat film and cap array clearly represent an inverse t_F dependency, which is underpinned by the dashed lines representing fits $\propto 1/t_F$ (cf. Equation 2.4.3). For all t_F, the values for H_{EB} of the caps and the film agree considering the given uncertainties, and hence, the thickness gradient of the cap geometry seems to not affect the EB strength significantly. The inverse t_F dependency matches the results presented in Ref. [MRH22], where further the coercive field is evidenced to possess a $1/t_F$ dependence. From the ideal Meiklejohn and Bean model, this is not expected (cf. Equation 2.4.3) as all antiferromagnetic interface moments coupled to the ferromagnet are assumed to be rigid. Contrarily, in the extended models for polycrystalline EB, thermally unstable and therefore rotatable grains contribute to the coercivity of an EB

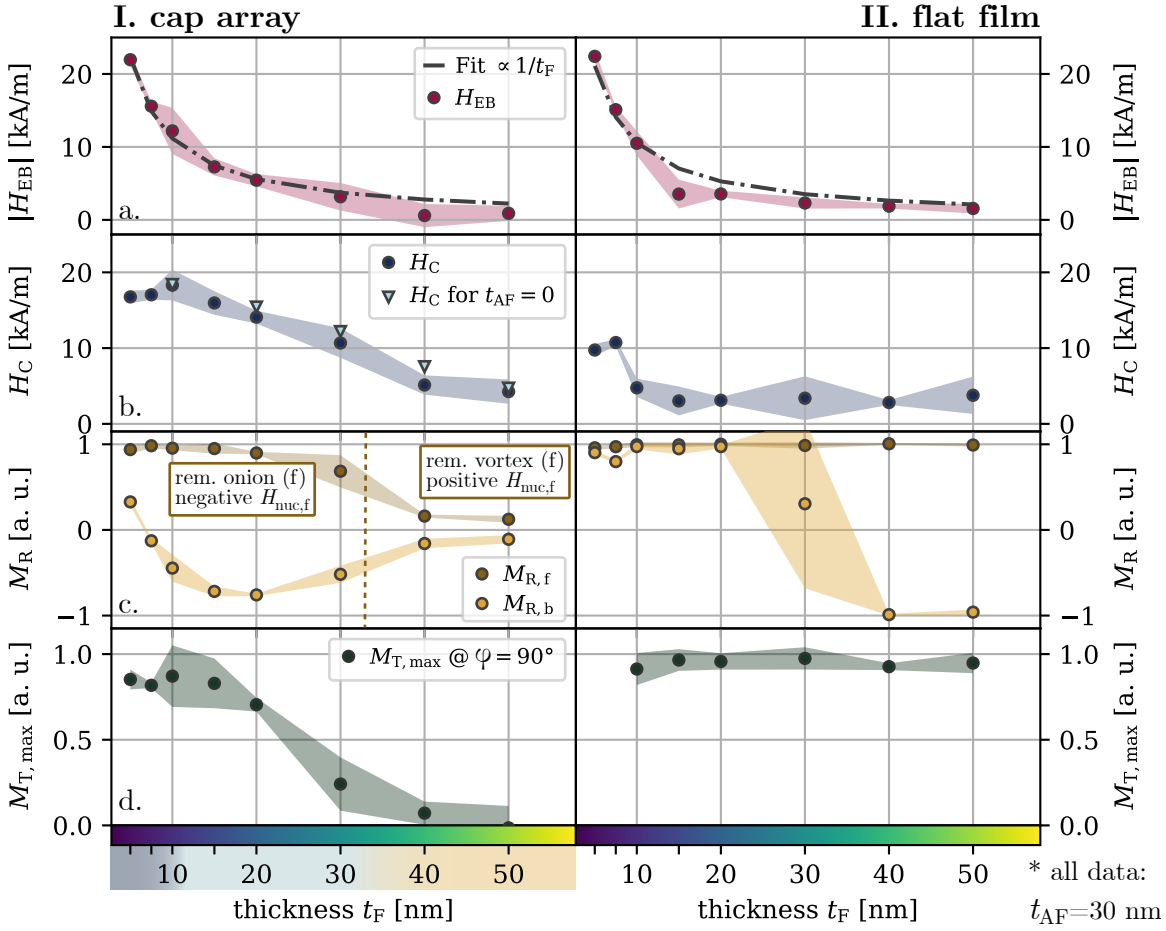

Figure 10.3: Summarized characteristics of the easy axis magnetization reversal ($\varphi = 0°$) of both EB cap arrays and a flat EB film with $t_{AF} = 30\,\text{nm}$ in dependence of the ferromagnetic thickness t_F: The absolute EB field $|H_{EB}|$ (a., red), the coercivity H_C (b., blue) and the remanent longitudinal magnetization M_R with respect to the two hysteresis branches (c., ocker). The dashed vertical line represents the transition from negative to positive values of the nucleation field on the descending branch. This in turn indicates the transition between remanent onion and remanent vortex state and agrees with the values of $M_{R,F}$. Additionally, the maximum value of the transversal component $M_{T,max}$ at $\varphi = 90°$ is given (d., green). A function $\propto 1/t_F$ has further been fitted to the data in a. (gray dashed dotted lines). In order to compare the coercivity of caps with and without EB, the H_C values from Figure 9.2 are added as light blue triangles in b.

bilayer by means of a rotatable magnetic anisotropy which is mediated via interfacial exchange coupling as in the case of the unidirectional anisotropy. Hence, H_C is not only mediated by the intrinsic anisotropy of the ferromagnet as it is written in Equation 2.4.3, but also depends on the portion of rotatable grains (class II) in the antiferromagnetic layer.[MRH22] The described $1/t_F$ dependence is however not clearly visible in Figure 10.3 b. for the flat EB film, which may originate from the fact that the measurements stem from samples with both Si and glass substrates. For the caps with generally higher coercivity, a rather linear reduction of H_C is observable. Comparing the similar t_F dependent course of H_C for the purely ferromagnetic caps (cf. Figure 9.2) with the one for the EB caps, it becomes clear that mainly the cap geometry determines the coercive field's reduction because the remagnetization behavior shifts from onion rotation towards vortex reversal for increasing t_F. This effect dominates over the t_F dependent

influence of the interfacial coupling between antiferromagnetic class II grains' uncompensated moments and the ferromagnet.

The values for $M_{\mathrm{R,f}}$ and $M_{\mathrm{R,b}}$ for the forward/descending and the backward/ascending hysteresis branches plotted in c. visualize the effects of EB on the remanent states. In the flat film, the EB strength is strong enough to pin the remanent remagnetization of both hysteresis branches at positive saturation (+1) when t_{F} is below 30 nm. In the cap array, $M_{\mathrm{R,f}}$ follows a similar course as in the case of ferromagnetic caps (cf. Figure 9.2), with a phase transition between remanent onion and vortex state above 30 nm. This is in agreement with the thickness at which the nucleation field on the descending branch changes from negative to positive values, respectively (c.f dashed brown line in c.).[1] Note that magnetic force microscopy has been proven that caps with $D = 1\,\mu\mathrm{m}$, $t_{\mathrm{F}} = 10\,\mathrm{nm}$ and $t_{\mathrm{AF}} = 30\,\mathrm{nm}$ exhibit the onion texture in remanence in Ref. [TRH21]. Similar measurements are additionally illustrating remanent onion configurations for the here majorly investigated particle size of $D = 500\,\mathrm{nm}$ and a ferromagnetic thickness of 5 nm in Figure 14.1 of the thesis' Appendix.

On the ascending branch, however, $M_{\mathrm{R,b}}$ follows a different course than in the case of purely ferromagnetic caps. Here, the different shape of the caps' hystereses comes into play: For small t_{F} the shape of the hysteresis is so broad with switching fields stretched over a wide magnetic field regime that it is not fully shifted to negative H_{ext} values although the H_{EB} values are comparable to that of the flat film. This has the consequence that the magnetization on the backward/ascending branch does not reach +1 at remanence. Because $|H_{\mathrm{EB}}|$ decreases more strongly with rising t_{F} than H_{C} does, $M_{\mathrm{R,b}}$ is reduced from +0.33 at $t_{\mathrm{F}} = 5\,\mathrm{nm}$ to -0.77 at 20 nm before approaching zero. This corresponds to the increased the vortex stability with increasing t_{F}. For $t_{\mathrm{F}} = 40$ and 50 nm, the EB is already so small that the remanence appears to be symmetric with $M_{\mathrm{R,b}} \approx -M_{\mathrm{R,f}}$ as it is also the case for purely ferromagnetic caps.

Furthermore, the maximum values of M_{T} of the hard axis measurement at $\varphi = 90°$ are displayed as an indication for the reversal path: At high values of $M_{\mathrm{T,max}}$, the remagnetization is dominated by the rotation of onion textures over the EB direction and at small values by vortex reversal. Again, the trend towards a domination of vortex reversal within the cap ensemble is visible for increasing t_{F} which is in agreement with the conclusions of the previously discussed quantities M_{R} and H_{nuc}. Contrastingly, $M_{\mathrm{T,max}}$ remains +1 over the full t_{F} range in the flat EB film.[2] Note, that an extended plot of this summary including also different t_{AF} can be found in Figure 14.2 of the Appendix.

10.2.1 Training and (Zero) Field Cooling of EB Caps

For possible applications of magnetically capped particles, the control of their macroscopic properties, like the remanent states is desirable. For example, the remanent state shall be tuned by engineering the cap material so that it is possible to choose between remanent onion or vortex state. In order to pin the caps with one specific onion texture, a unidirectional anisotropy induced by the EB can in principle be applied to prevent the demagnetization energy-driven

[1] The course of the nucleation and annihilation fields for caps of the here discusses kind can be found in the Appendix of this thesis in Figure 14.3.

[2] For the flat films with $t_{\mathrm{F}} = 5$ and 7 nm, the measurements of M_{T} at 90° were too noisy to be evaluable, therefore the data points are missing.

vortex formation. However, the values for M_{R} in Figure 10.3 reveal that even for the thinnest ferromagnetic thickness (i.e. highest EB), no fixed remanent state is given, that is independent on the caps' magnetic history. Aiming to prepare a sample with magnetic caps for which $M_{\mathrm{R,f}} = M_{\mathrm{R,b}}$ approaching saturation, the EB needs to be further strengthened. For this, a post-deposition field cooling (FC) procedure could be utilized as it is typically also done for EB films or other EB microstructures.[Mei62,SBN06,SAKS09] Depending on the applied magnetic field H_{FC}, the temperature T_{FC} and the process time, certain grains in the antiferromagnetic ensemble can be addressed such that they align parallel with the magnetization of the ideally saturated ferromagnetic layer due to exchange interaction at the interface. After the FC, pinning antiferromagnetic grains belonging to class III contribute to the hereby strengthened EB. It is important to point out that for sufficiently high T_{FC}, the texture which the ferromagnet exhibits at the externally applied field H_{FC} may be imprinted into the antiferromagnet:[SBN06,SAKS09] If H_{FC} is large enough to saturate the ferromagnet, a homogeneous texture will be imprinted, whereas for smaller or even zero H_{FC} (zero field cooling, ZFC) it has been shown in literature that configurations like the vortex texture can be imprinted.[SBN06,ABR21]

Moreover, FC experiments have been performed to EB caps with oxidic antiferromagnets that have a Neél temperature below room temperature (RT).[NKM16] In this case, the sample was cooled in an external magnetic field - starting from RT - to a temperature below the Neél temperature at which subsequently the magnetization reversal was measured. However, in this thesis, IrMn as an alloy with antiferromagnetic properties at RT is used and, hence, the experiments can be performed at RT after cooling the sample from elevated temperatures back to RT in an applied field.

FC at different T_{FC} ($t_{\mathrm{F}} = 30\,\mathrm{nm}$)

In order to systematically study the effects of the described annealing procedure, the magnetization reversal of EB caps with $t_{\mathrm{AF}} = 30\,\mathrm{nm}$ was investigated after different FC procedures had been applied. A layer stack with $t_{\mathrm{F}} = 30\,\mathrm{nm}$ was chosen, since Figure 10.3 indicates the transition between onion and vortex reversal for 'as made' cap array around this thickness. Specifically, the temperature T_{FC} was successively increased from 120 to 300 °C. The latter temperature was not exceeded because significant changes to EB films that may be connected to a reduced melting point for very small antiferromagnetic grains, have been reported at $T_{\mathrm{FC}} = 350\,°\mathrm{C}$ for the here investigated materials.[MHR20] Afterward, the sample's characteristics have been extracted from VMOKE measurements which were acquired after each FC procedure and compared to the data recorded after deposition ('as made'). The extracted quantities are the characteristic fields H_{EB}, H_{C}, H_{ann} and H_{nuc} as well as the remanent magnetizations on both hysteresis branches $M_{\mathrm{R,f/b}}$ of easy axis hystereses and the maximum transversal magnetization $M_{\mathrm{T,max}}$ with regard to the hard axis measurements. Note that the measurements were always performed within a time window of 12 to 30 hours after the respective treatment. In order to exclude the athermal training effect typically observed for EB systems,[OFOVF10] the first remagnetization curve measured after the treatment was omitted in all cases.

The results are displayed in Figure 10.4 a. alongside comparative values for H_{EB}, H_{C} and $M_{\mathrm{T,max}}$ of the EB flat film after selected FC treatments. In b., the magnetization reversal is

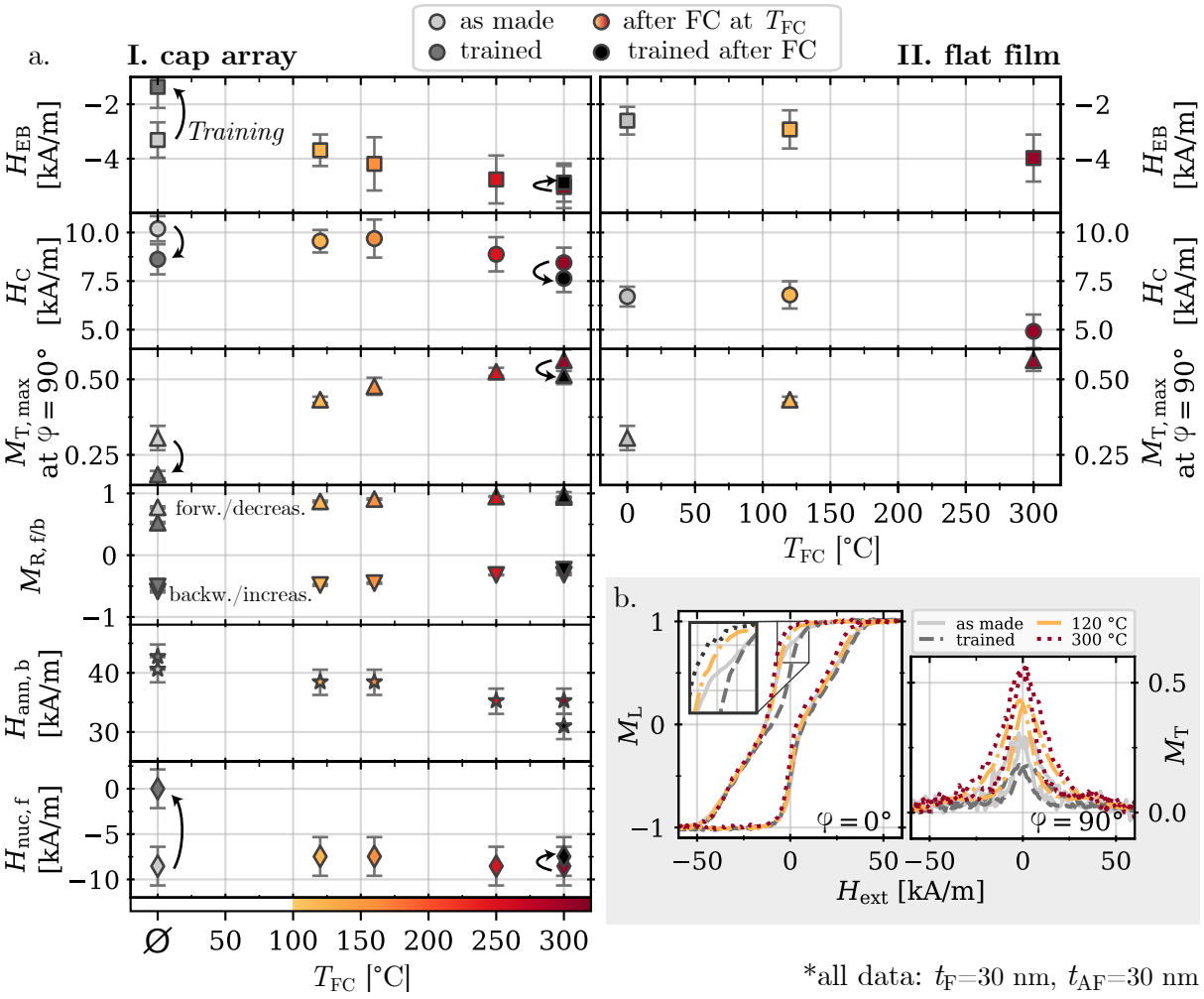

Figure 10.4: Field cooling temperature T_{FC} dependent changes of magnetization reversal characteristics in EB cap arrays and flat EB films are shown in a. For some fields, it is differentiated between the forward/descending (f) and the backward/ascending (b) branch. The hystereses from which the values were extracted were measured on the day after the FC process or after deposition in the case 'as made' (12 to 30 hours later). In addition to the data directly after deposition and FC, the characteristic properties have also been extracted from 'trained' loops. These were measured more than one week after deposition (or after the final FC at 300 °C). During this time the sample had been stored at room temperature and had undergone more than 100 hysteresis loops. For exemplary sample stages, the longitudinal (transversal) magnetization curves are plotted for the easy (hard) axis measurement of the cap array in b.

displayed for exemplary cases, with the longitudinal magnetization component of the easy axis ($\varphi = 0°$) and the transversal component of the hard axis ($\varphi = 90°$) measurements. During the acquisition of this data, it was observed, that the hysteresis shape of cap arrays on the non-field-cooled sample changed over time as the sample had undergone many (>100) hysteresis cycles which were part of other investigations. Therefore, also the data of these 'trained' hysteresis loops is added (gray) for $t_{FC} = \varnothing$. The change of the easy axis reversal between the measurement performed on the day after deposition ('as made') and the 'trained' loop becomes especially obvious for M_L on the descending branch (b.). Besides a reduction of H_{EB}, the nucleation is clearly shifted to larger fields (see $H_{nuc,f}$ in a.), which enlarges the magnetic field regime in which

the vortices are present. For the ascending branch, $H_{\mathrm{nuc,b}}$ remains rather unaffected, however, the vortex stability regime is enlarged due to a rise in $H_{\mathrm{ann,b}}$. The changes are accompanied by a reduction of both $M_{\mathrm{R,f}}$ and $M_{\mathrm{T,max}}$. The reduction of the latter speaks for the fact that with the training of the caps, the vortex core trajectory of the hard axis loop becomes rather centered along the cap, whereas in the case of the higher EB in the 'as made' state, the vortex core had moved along a curved path in order to align more magnetic moments with the EB direction. These curved vortex core routes have previously also been evidenced for EB disks in literature. [SBN06]

Overall, the data implies that by FC the EB strength of the cap arrays can be enhanced as compared to the 'as made' state, while the general reversal mode, which is a vortex reversal in the case of the chosen thicknesses, is preserved. Also, the course of M_{L} at $\varphi = 90°$ maintains the classical vortex reversal shape (not shown). Most importantly, the training related reduction of $|H_{\mathrm{EB}}|$, $M_{\mathrm{R,f}}$ and $M_{\mathrm{T,max}}$ and the change in $H_{\mathrm{nuc,f}}$ and $H_{\mathrm{ann,b}}$ can be revoked with the help of FC. Due to the strengthening of the EB, the remanent magnetization on the descending branch $M_{\mathrm{R,f}}$ changes from 0.5 to 1, while the backward branch remanence is shifted from -0.6 to -0.3, when comparing the data from the 'trained' case and after FC at 300 °C. Simultaneously, the transversal magnetization component shows enhanced maximum values along the course of the hard axis hysteresis measurements, with $M_{\mathrm{T,max}}$ rising from 0.2 to 0.6. Consequently, the vortex reversal must be defined by a more curved trajectory of the vortex core motion for higher T_{FC}. While a reduction of the annihilation field on the ascending branch can be noticed, no significant changes are observed for the respective nucleation field $H_{\mathrm{nuc,b}}$ when compared to the 'as made' state. Nevertheless, appropriate FC facilitates the recovery of the 'as made' nucleation field after the training had caused the caps to nucleate vortices at an earlier stage on the descending branch.

In general, the effects can to some extend be compared to the field-cooled flat bilayer. In both cases, $|H_{\mathrm{EB}}|$ is enhanced, while H_{C} is slightly lowered. Comparable results for EB films were presented in Ref. [MHR20]. The strengthened EB can be explained because antiferromagnetic grains which could not be oriented during the deposition in an external magnetic field can be aligned during the FC process due to the elevated temperature.

As an additional observation, a bend can be seen in the easy axis reversal of the 'as made' caps on the descending branch (see inset of Figure 10.4 b.), which can be attributed to the caps passing through certain transition states prior to the main vortex nucleation. Some of these transition textures have been introduced in section 3.1, like for example *S*-, *C*- or double vortex states. Interestingly, this bend is not observed in the 'trained' cap array and also does not reappear after the FC process has set back the nucleation field. From this it may be concluded, that these transition states are meta stable and, thus, only arise after the deposition. In order to investigate the stability of the field-cooled cap arrays after the final procedure with $T_{\mathrm{FC}} = 300\,°\mathrm{C}$, the sample was purposely subjected to hysteresis cycling and measured again after several weeks. The corresponding data is indicated as 'trained' after FC and implies that training can again affect the cap arrays reversal, however the accompanied changes are less severe than in the case of the training before FC.

FC for different t_F ($T_{FC} = 300\,°C$)

As a result of the T_{FC} dependent study, the strongest changes with the maximum enhancement of $|H_{EB}|$ have been observed for FC at 300 °C and hence this procedure has been applied to samples with EB caps of different ferromagnetic thickness. The easy axis magnetization curves after the FC are compared to the reversal in the 'as made' state in Figure 10.5. For all samples, the FC enhanced the EB shift and reduced the coercivity. Despite this, the remanent magnetization could not even for the thinnest ferromagnetic layer be pinned to one specific texture, as in this case $M_{R,b}$ has been increased from 0 ('as made') to 0.5 (after FC), whereas $M_{R,f} = 1$. Hence, even thinner ferromagnetic layers or an enhanced interfacial exchange coupling would be necessary to reach a hysteresis loop which is fully shifted to the negative magnetic field regime.

For caps with distinct vortex reversal shape ($t_F = 30$ and 50 nm), the FC decreases the field regime of vortex stability: Besides an enhanced $|H_{EB}|$, the nucleation field was reduced/increased on the descending/ascending branch. Additionally, the vortices are annihilated at smaller absolute fields for both remagnetization directions. For $t_F = 30\,nm$, the vortices are present over a magnetic field regime of $(37 \pm 2)\,kA/m$ after the FC, whereas they were stable over a regime of $(40 \pm 1)\,kA/m$ before the procedure. This effect is even more pronounced for $t_F = 50\,nm$, where the FC reduces the vortex stability regime from $(67 \pm 4)\,kA/m$ to $(56 \pm 1)\,kA/m$.[3]

The rightmost panel in Figure 10.5 shows the hysteresis of a cap array with $t_F = 50\,nm$ that had been subjected to an annealing procedure without an external magnetic field applied (ZFC) after the sample had been demagnetized. The ZFC procedure enhances the nucleation field on the forward/descending branch and lowers it on the backward/ascending branch. At the same time, the vortices annihilate at a later stage on the respective branch, which clearly enlarges the caps' vortex stability regime from (62 ± 1) to $(69 \pm 2)\,kA/m$.

In conclusion, we can assume that the FC has a reduction of total energy of the ferromagnetic layer's onion state as a consequence, which is connected to the fact that a homogeneous magnetization texture is imprinted into the antiferromagnetic layer. Contrastingly, ZFC after demagnetization stabilizes vortices. This is due to the *circular EB* that is generated when the ferromagnet hosts a vortex state which aligns the uncompensated interfacial antiferromagnetic moments in a curling texture accordingly by exchange coupling during the cool down.

10.2.2 Analysis of FORC Fingerprints of EB Cap Arrays for Various Ferromagnetic Thicknesses t_F

Because the FORC analysis has proven to be a powerful tool to probe the distribution of properties of ferromagnetically capped particles in subsection 9.1.1, the technique was further applied to the ensembles of EB caps that have previously been field-cooled from 300 °C. For the thicknesses $t_F = 5$, 10, 30 and 50 nm and a fixed antiferromagnetic thickness of 30 nm, the FORC families $M(H_{rev}, H_{ext})$ measured along the sample's easy axis with the LMOKE setup and the respective FORC distributions $\rho(H_{rev}, H_{ext})$ and $\rho(H_i, H_C)$ are shown in Figure 10.6.

The same experimental conditions as in subsection 9.1.1 were used, with a field resolution of $\Delta H_{ext} = \Delta H_{rev} = 1\,kA/m$, the measurement time per point $\Delta t_{meas} = 20\,ms$ and a sweep rate of

[3] The given stability range uncertainty results from the standard deviation of the stability regimes of both branches.

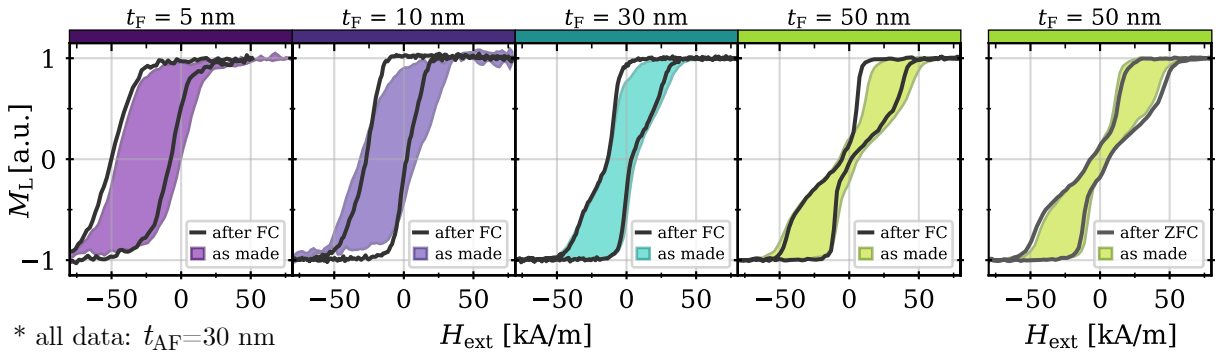

Figure 10.5: The magnetization reversal of cap arrays with the exemplary thicknesses t_F = 5, 10, 30 and 50 nm changes upon FC from T_{FC} = 300 °C. The easy axis hystereses after the annealing procedure are shown alongside the reversal measured previously in the 'as made' state. The rightmost panel indicates the effect of ZFC from 300 °C after demagnetizing the sample.

25 kA/m/s. Each FORC was averaged from multiple measurements N with N = 10 (5, 2, 1) for t_F = 5 nm (10, 30, 50 nm, respectively). For the evaluation, the same filtering (Savitzky-Golay filter of degree 3 for window 5) was applied and also the smoothing factor for the calculation of the FORC distribution was kept at $SF = 8$.

Characteristic features connected to the remagnetization processes of vortex reversal and coherent rotation have been identified in subsection 9.1.1 and are found again in the FORC distributions of the EB caps. The ridge feature connected to rotational processes is visible for thin ferromagnetic layers with t_F = 5 and 10 nm and the FORC distributions for t_F = 10, 30 and 50 nm host the vortex features 1 and 2.

At $\boldsymbol{t_F = 5}$ **nm**, the ridge clearly aligns with the major loop's $H_{EB} = (-33.3 \pm 0.8)$ kA/m on the H_i axis in the transformed distribution (c.). The range it spans along H_i increases for increasing H_C. Moreover, it is stretched from H_C = 5 to 39 kA/m indicating a very wide distribution of coercivities within the probed cap ensemble.

In clear contrast to that, the FORC distribution of the EB cap array with $\boldsymbol{t_F = 50}$ **nm** displays the two familiar features for vortex reversal (cf. subsection 9.1.1). Feature 1 is connected to the nucleation of vortices on the descending branch and their subsequent annihilation. Here, the distribution peaks at H_{ext} = 33 kA/m for reversal fields around the nucleation field $H_{nuc,f}$ = 6 kA/m which was evaluated from the major loop's forward branch. The second feature which is accompanied by a change from negative to positive values is characteristic for the re-nucleation of vortices in an ensemble of which most of the caps are already negatively saturated due to sufficient reversal fields $H_{rev} < -41$ kA/m. The positive portion of feature 2 is located at $H_{ext} = (-14 \pm 4)$ kA/m, whereas the macroscopic nucleation field on the ascending branch is determined as $H_{nuc,b} = -10$ kA/m. This observation indicates that the major loop nucleation fields describe the latest magnetic field at which the vortices nucleate on the respective branch, but cannot describe the distribution of cap properties.

Additionally it shall be mentioned, that the nucleation fields of the major loop's two branches are not symmetric with respect to vanishing external magnetic field as it was the case for purely ferromagnetic caps, where $H_{nuc,f} = -H_{nuc,b}$ (Figure 9.2). Instead, the nucleation events are symmetric around $H_{EB,major} = (-2.4 \pm 0.7)$ kA/m. This has previously been described in literature

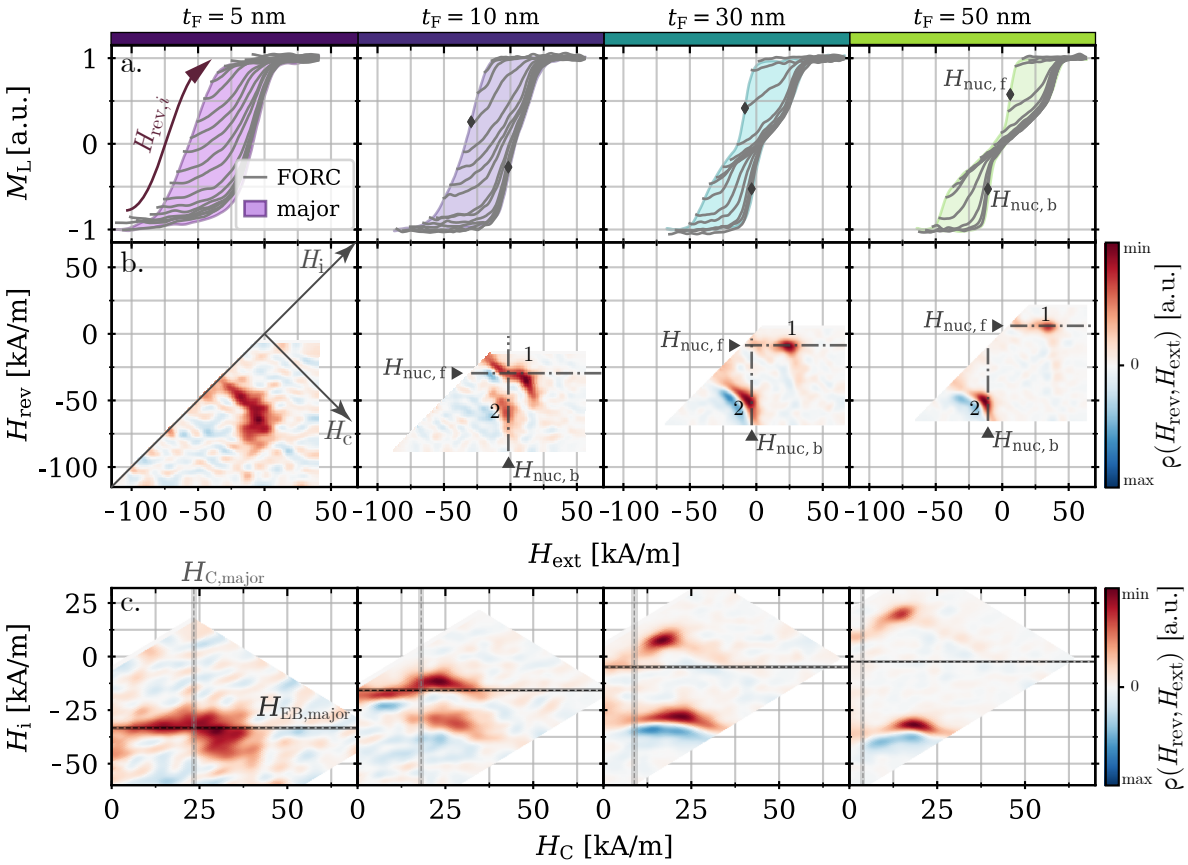

Figure 10.6: FORC analysis for EB cap arrays after FC: For four thicknesses t_F the families of FORCs $M(H_{rev}, H_{ext})$ measured along the sample's easy axis ($\varphi = 0$) are shown (a.) with the corresponding FORC distributions $\rho(H_{rev}, H_{ext})$ (b.). The shading in a. indicates the full major loop and the diagonal arrows in b. shall illustrate the relationship between the coordinate spaces (H_{rev}, H_{ext}) and (H_i, H_C). In c., the FORC distribution is given in the latter coordinate system. The horizontal and vertical dashed lines in c. present the macroscopic values of H_{EB} and H_C, which were extracted from the major loop via Equation 2.4.1 (uncertainty indicated by shaded region). Similarly, the nucleation fields $H_{nuc,f/b}$ (♦) are displayed on the major loop in a., and as dashed dotted lines b.

as a characteristic of the reversal modes for both biased and tilted vortices as introduced in subsection 3.1.1. For both cases, the nucleation asymmetry $\Delta H_{nuc} = H_{nuc,f} + H_{nuc,b} - 2H_{EB}$ has been proposed to be zero,[GH06] whereas a viscous vortex reversal is characterized by $\Delta H_{nuc} \neq 0$.[GYV15] In the present case of $t_F = 50\,nm$, the nucleation asymmetry is determined from the major loop as $\Delta H_{nuc} = (0.2 \pm 0.7)\,kA/m$ which is in agreement with the expectation of a non-viscous reversal due to the choice of $t_{AF} = 30\,nm$. At this antiferromagnetic thickness the amount of rotatable grains (class II) in the antiferromagnetic layer is minimized which in turn prevents viscous reversal processes.

Consistent results are obtained for a thickness of $\boldsymbol{t_F = 30\ nm}$. The features 1 and 2 align similarly with the major loop's nucleation fields as described above, with the features being generally separated by a smaller distance in the distribution diagram due to the fact, that the reduced ferromagnetic thickness diminishes the vortex stability.

Reaching from $t_F = 5$ to $30\,nm$, a transition in the FORC distribution is observable as it has been the case for the ferromagnetic caps presented in Figure 9.3. Interestingly, the phase

transition between the reversal via the rotation of onion states and via vortex formation spans across the thickness of $\boldsymbol{t_F = 10}$ **nm**. For this thickness, the characteristics of both reversal types are visible in the FORC diagram, i.e. the ridge and vortex features. Hence, the caps in the ensemble measured show a mixture of both reversal routes. Similar results have been presented for Fe nanodots with diameters between 50 and 70 nm in literature, where the FORC diagrams for dots with an intermediate size of 58 nm showed a mixture of the named features. [DLR07]

After all, FORC is a suitable tool for the characterization of microstructured samples like the arrays of magnetic caps studied in this thesis. The distribution of properties can qualitatively be compared and conclusions about the degree of inhomogeneity of the structured sample can be drawn.

10.2.3 Visualizing Magnetic Textures in EB Caps with XMCD-PEEM

The samples with different ferromagnetic thicknesses, which were discussed in the scope of FORC analysis in the previous section, have furthermore been investigated by means of XMCD-PEEM with the aim to spatially resolve the magnetization textures within the closely-packed cap arrays.

X-ray Absorption Spectrum of Cobalt

In order to reach maximum contrast in XMCD-PEEM measurements, the corresponding excitation energy must be chosen according to the material that shall be investigated. As CoFe has been used as the ferromagnetic material, the X-ray absorption spectrum for Co has been measured for each sample prior to magnetic imaging. Here, the right handed light's energy was tuned from 770 to 810 eV while the intensity of emitted secondary electrons - as a measure for the absorption - was recorded by the electron detector. The spectra depicted in Figure 10.7 stem from regions with a capped particle monolayer on two different samples for comparison. Both reveal a maximum absorption which corresponds to the L_3 absorption edge. Consequently, the respective energy (e.g. 776.5 eV) was used for the subsequent measurements of the XMCD contrast.

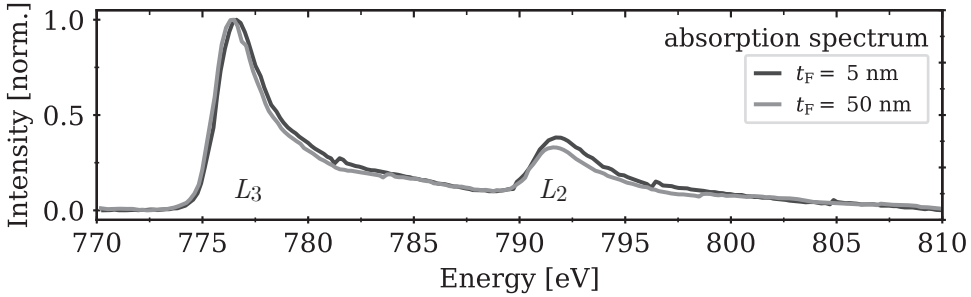

Figure 10.7: Spectra showing the normalized X-ray absorption for two types of EB cap array of different CoFe thickness. The spectra were recorded with circularly polarized light of positive helicity ($L = +\hbar$). The peaks at 776.5 eV and 791.5 eV relate to the absorption from the $2p_{3/2}$ and the $2p_{1/2}$ level into the $3d$ valence band, i.e. the L_3 and L_2 absorption edges, respectively.

XMCD Contrast of EB Cap Ensembles in Remanence

Due to the findings from the FORC analysis for different ferromagnetic thicknesses in subsection 10.2.2, a distribution of magnetic properties is assumed to be present within an array of EB caps. XMCD-PEEM offers the possibility to spatially resolve the magnetization in the cap arrays, and hence, the remanent magnetic textures are studied for different thicknesses t_F in dependence on the magnetic field history. To do so, two images with left- and right-handed circularly polarized light have been acquired at zero field (e.g. after positive saturation) and subsequently, the XMCD asymmetry ζ_{XMCD} has been derived via Equation 6.3.1. While ζ_{XMCD} only contains the desired magnetic information, averaging the two images (i.e., $(I^+ + I^-)/2$) instead yields a characteristic averaged X-ray absorption PEEM image (avg. PEEM). In Figure 10.8, both the averaged XAS and the XMCD asymmetry images (in the following also called XMCD contrast) are illustrated for the thicknesses $t_F = 5$, 10, 30 and 50 nm (I. to IV.). It shall be mentioned, that the sample with $t_F = 10$ nm has been investigated in the 'as made' state, while the other samples, which were investigated in a later beamtime, had been field-cooled prior to the measurements.

The XMCD images in b. and c. were recorded at remanence after the corresponding sample had been exposed to the the largest positive and negative magnetic field that can be applied on the sample holder, respectively. In practice, remanence is reached by applying a small reverse field that re-centers the field of view that was recorded prior to saturation in order to compensate for the yoke's remanence. The magnitude of this magnetic field can only be estimated via a calibration factor from the current that is applied to the sample holder coils and should be treated carefully.[4] If the imaged region is not centered with respect to the sample holder's yoke, the magnetic field will differ from the calculated value. The maximum magnetic field was approximated to be $H_{ext,max} = 88$ kA/m, which is sufficient to saturate cap arrays with $t_F = 10$, 30 and 50 nm (cf. Figure 10.5) but is not high enough to fully negatively saturate the caps with $t_F = 5$ nm due to the layer system's strong EB.

In order to indicate the particle positions, circles have been added to the averaged PEEM images which were subsequently copied to the XMCD contrast image. As a capped sphere creates a shadow for its own backside when the incident X-rays impinge under an angle of 74° with respect to the sample normal, the circles have been positioned in a way, that a particle's bright side in the image faces towards the 'light source'. For further reference, the images are again shown in Figure 14.4 in the Appendix without the circles and with the second averaged PEEM image.

In the XMCD images, the used color map indicates positive magnetization (parallel to $\vec{H}_{ext}$ and $\vec{k}$) as red and negative magnetization (antiparallel to $\vec{H}_{ext}$ and $\vec{k}$) as blue. Maximum $|\zeta_{XMCD}|$ is reached for a collinear arrangement of $\vec{k}$ and $\vec{M}$, whereas it turns zero for their perpendicular alignment.[Bea06] A first observation related to the shown images is that the maximum value of $|\zeta_{XMCD}| \approx 14\,\%$ matches the Cobalt XMCD asymmetry reported in literature ranging from 12 to 20 %.[SWH93,OOC14,Ohl02]

When closely looking at the XMCD contrast within the drawn circles, different patterns can be distinguished: Caps with homogeneously positive magnetization in the onion texture typically posses a positive (red) XMCD on the side which faces towards the X-rays, but show reduced (e.g.

[4] The conversion $H_{ext} \approx I_{coil} \cdot 44\ m^{-1}$ was provided by the experimental scientist based on simulations.

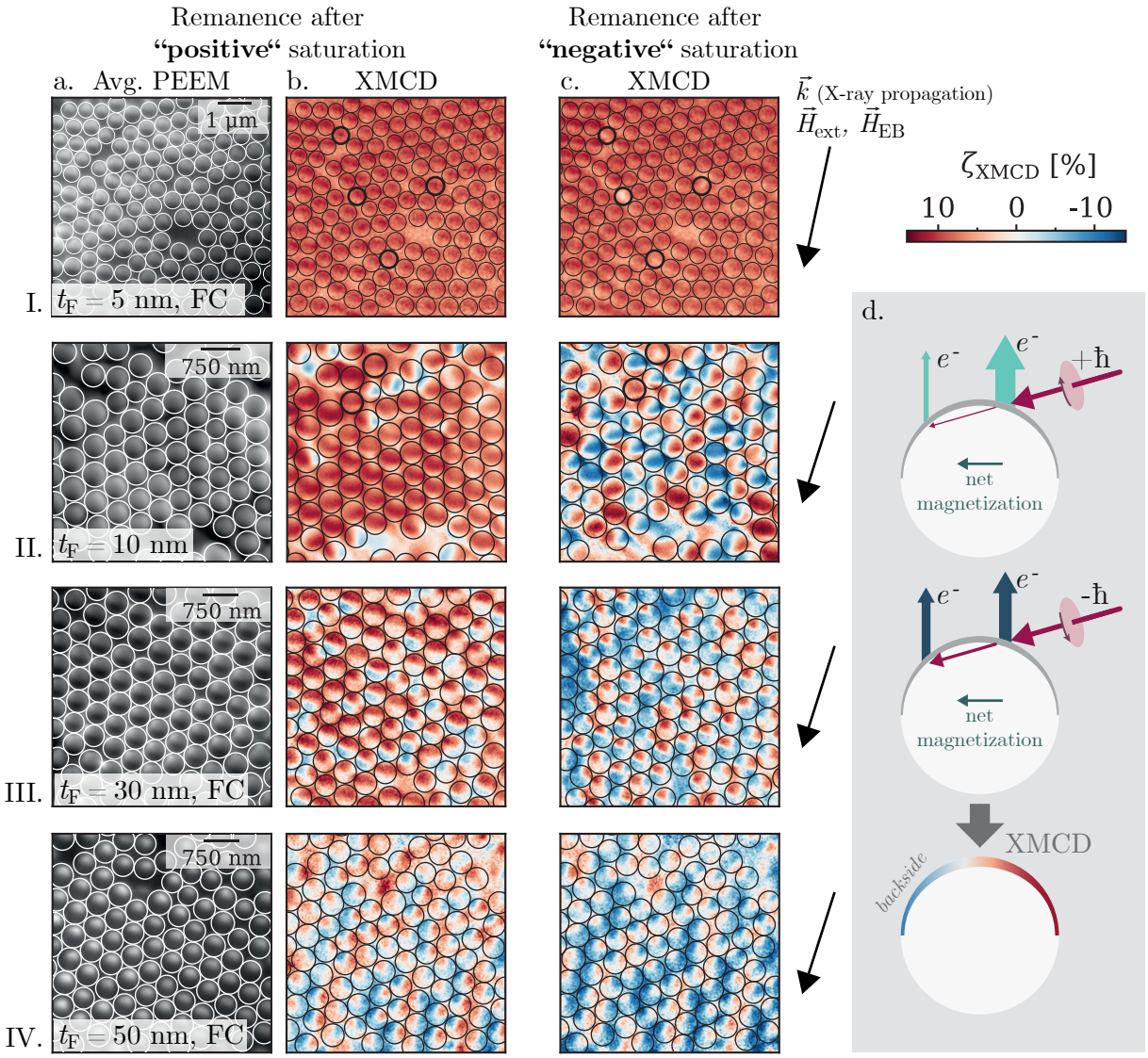

Figure 10.8: Summary of averaged PEEM images (a.) and images of the XMCD asymmetry contrast (b., c.) for samples of EB capped particles ($D = 500\,\mathrm{nm}$) with varying thickness $t_F = 5$, 10, 30 and 50 nm (I. to IV.). The arrow on the right of each row indicates the direction of the incident X-rays (and their k vector) as well as the direction of the applied magnetic fields. ($\vec{k}$ differs slightly for $t_F = 5\,\mathrm{nm}$ due to larger field of view settings during imaging.) Note that the samples were always placed with their EB anisotropy direction parallel to this H_{ext} axis. Column b. shows images taken at zero magnetic field (remanence) after the caps have been exposed to the maximum positive magnetic field that can be applied to the sample holder. Except for $t_F = 5\,\mathrm{nm}$, this magnetic field of approximately 88 kA/m was sufficient to saturate the samples. Images recorded after inverting the maximum magnetic field ('negative') are shown in column c. Circles drawn on top of the averaged PEEM images were copied to the magnetic contrast images in order to locate the caps' positions. In d., an illustration explains the contrast reduction/inversion on the cap's backside: X-rays of the helicity that is less absorbed can be transmitted through the top of the cap to some extent and interact with the backside.

I.b.) or even inverted (e.g. III.b.) values of ζ_{XMCD} on the shaded backside of the sphere. This inversion can be explained due to the magnetization dependent difference in the absorption of X-rays of opposing helicity as illustrated in Figure 10.8 d. The transmittance of X-rays through

the cap is stronger for the less absorbed helicity so that more light of this helicity can contribute to the XMCD on the shadowed side which can consequently invert the contrast. [SKS12]

The second contrast pattern is related to the vortex texture. Recalling the dipolar XMCD contrast in disks with vortices (cf. Figure 3.5), the texture is characterized by ζ_{XMCD} values of opposing sign on the left and right side of the disk, due to the curling of the magnetization. [SAKS09] Along the central line with respect to the propagation direction of the X-rays, ζ_{XMCD} vanishes because the magnetization and $\vec{k}$ are perpendicularly aligned. For the cap geometry, however, a quadrupolar contrast may instead arise as a result of the contrast inversion on the cap's backside and has previously been observed by Streubel *et al.*. [SKS12,SKR16] In case the effect is small enough to only reduce the contrast on the particles' backside, the pattern remains rather dipolar. Under inversion of vortex' circulation sense, this dipolar or quardupolar contrast is inverted accordingly. Note, that the red and blue fraction of a cap's XMCD contrast relate to the net magnetization of the cap projected onto the probing direction. At least on the cap's 'front side', the red:blue ratio can indicate details of the vortex texture, i.e. one of the two fractions will be wider and the white line will appear shifted from the particle center, if the vortex has a shifted core.

Based on the acquired XMCD images, magnetization textures were assigned to the caps' remanent states for the thicknesses $t_{\mathrm{F}} = 10$, 30 and 50 nm. These are illustrated as color coded circles in Figure 10.9, which shall be analyzed together with Figure 10.8 in the context of the measured easy axis hysteresis curves of samples with the same thicknesses in Figure 10.5. Additionally, Figure 10.9 gives the XMCD asymmetry $\bar{\zeta}_{\mathrm{XMCD}} = \zeta_{\mathrm{av}}$ averaged over each image. Although the described effects of contrast inversion do not allow a directly proportional correlation between this value and the net magnetization, the effect of EB is clearly visible for $t_{\mathrm{F}} = 10$ and 50 nm: $\bar{\zeta}_{\mathrm{XMCD}}$ differs for the two remanent states with a larger value after positive saturation.

Remanent Magnetic Textures at Different Layer Thicknesses t_{F}

5 nm In the field-cooled caps with $t_{\mathrm{F}} = 5$ nm, the EB was observed to be strong enough to preserve the caps' positive saturation even after passing zero field on the descending branch (cf. Figure 10.5) which matches the purely red contrast in the XMCD image Figure 10.8 I.b. for 'positive' remanence. Although the MOKE loop revealed that the remanent magnetization on the ascending branch was also positive, $M_{\mathrm{R,b}} \approx 0.5$ is significantly smaller than $M_{\mathrm{R,f}} \approx 1$. This can however not be seen when comparing the XMCD images in Figure 10.8 I.b. and c., where the averaged asymmetry ζ_{av} is 8.3 and 8.2 %, respectively. In principle, both images share the same contrast except for very few caps marked by bold circles. This deviation from the MOKE hysteresis loop is the result of the maximum applicable H_{ext} being insufficient to reach complete negative saturation of the caps on the utilized PEEM sample holder. From the set of FORCs in Figure 10.6, one may now deduce that $H_{\mathrm{ext,max}}$ must have only reached -60 kA/m at the imaged spot rather than the expected -88 kA/m.[5] Regardless of this

[5] $H_{\mathrm{ext,max}}$ can only be nominally reached for a specific sample thickness and at the very center of the sample holder between the yokes. [KSR10] Hence, we deduce that this did not apply to the imaged area.

named difference between the two images and the comparative results from different methods, the caps marked boldly in c. are inspected in detail: These do not show the characteristic quadrupolar vortex pattern but a generally reduced contrast which is a clear indication for the remagnetization of EB caps with $t_F = 5\,nm$ via the rotation of onion textures. Additionally, these caps show differently magnetized onions highlighting the distribution of magnetic properties (i.e. magnetic field range in which onions rotate) which is in accordance with the conclusions drawn from the FORC diagrams.

50 nm Contrastingly, the caps with the thickest CoFe layer ($t_F = 50\,nm$) nucleate vortices before reaching zero field independent of the previous saturation direction ($H_{nuc,f} = 6\,kA/m$, $H_{nuc,b} = -10\,kA/m$). This is well captured by both XMCD contrast images in Figure 10.8 IV.b. and c., where all caps host vortex states. When viewing the full images disregarding the circles, elongated regions of blue and red contrast in an alternating manner can be found that give the impression of a superordinate 'domain' pattern. This pattern can be analyzed regarding the participating cap textures in Figure 10.9. Its appearance is expected to be connected to the dipolar coupling of the vortices as described in the scope of configurational anisotropy in section 3.1. In this work, the particles are mainly oriented in a hexagonal array, where the main symmetry axis only differs from the external magnetic field axis by $\alpha = 8°$. As a consequence, the caps favor to nucleate vortices with the same circulation sense along this line but with an alternating circulation sense between these particle rows. Similar results were obtained by Streubel *et al.* who found periodically arranged rows of vortices in Py cap with alternating circularity for small angles α between the array's main symmetry axis and the the H_{ext} axis.[SKR16] (The effects of array orientation are further discussed in Figure 10.2.3.)

10 and 30 nm The distribution of the caps' magnetic properties is most distinctly highlighted in the XMCD images for $t_F = 10$ and $30\,nm$, where starting from positive saturation most of the caps have not yet nucleated vortices so that 87 and 61 % remain in a 'red' onion texture at remanence, respectively. Accordingly, the nucleation fields $H_{nuc,f}$ have been determined from Figure 10.5 to be (-25 ± 1) and $(-9 \pm 1)\,kA/m$ for $t_F = 10$ (as made) and $30\,nm$ (field-cooled), respectively.

At $t_F = 10\,nm$, it seems that at positive remanence vortices have predominantly nucleated at the boundary of an area with homogeneous lattice orientation. This observation is likely related to the fact that the onion textured cap with a reduced number of neighbors is less stabilized due to magnetostatic interaction. For the remanent state after negative saturation ($t_F = 10\,nm$), the situation is more complex. Both positively as well as negatively magnetized onion states can be found alongside vortex states with both circulation senses. Additionally, two of the caps are homogeneously red colored, but with reduced intensity. Similarly to the observation for $t_F = 5\,nm$, these caps are understood to be in the process of onion rotation where the net magnetization is not yet aligned with $\vec{k}$. However, some circles in Figure 10.8 II. c. host magnetic patterns which cannot be identified clearly and are therefore not taken into consideration

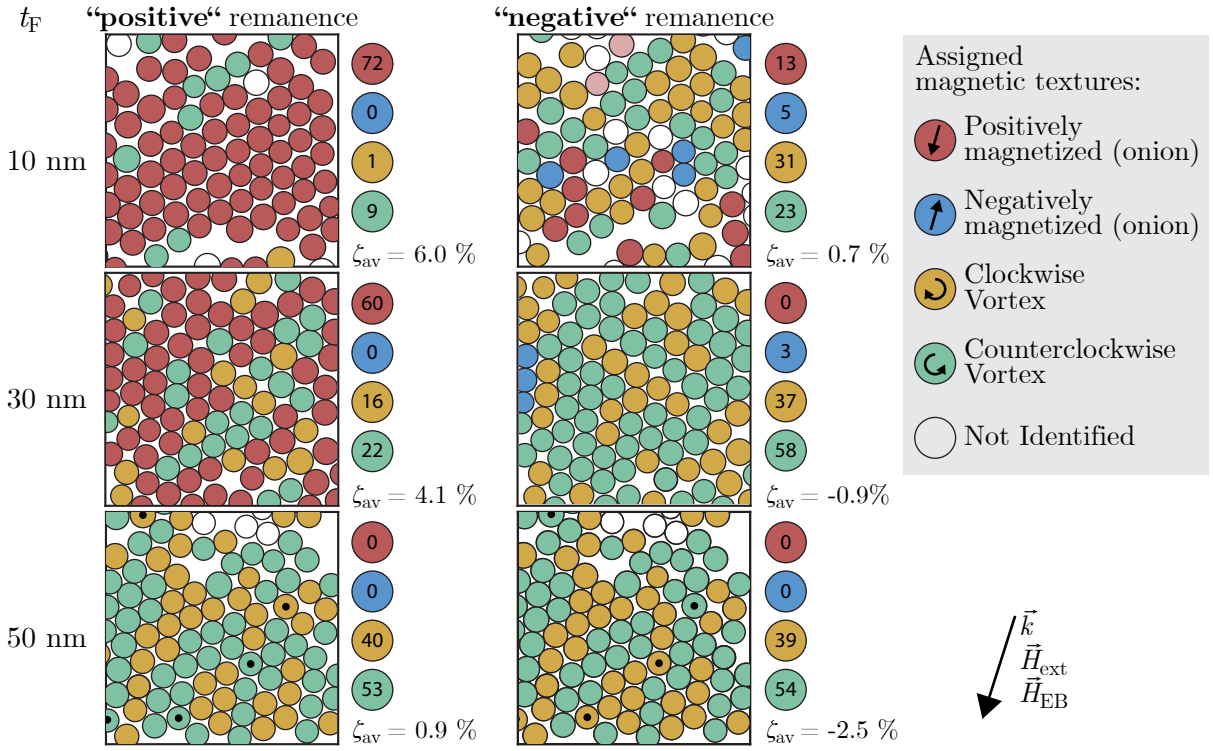

Figure 10.9: The XMCD asymmetry contrast images from Figure 10.8 were used to assign the denoted magnetization textures to the measured EB cap ensembles with t_F = 10, 30 and 50 nm in remanence, both after positive and negative saturation. In addition, the number of each of these textures present in the image is given on its right. Below, the XMCD asymmetry averaged per image in Figure 10.8 is given as ζ_{av}. It shall be emphasized that vortices typically nucleate with the same circulation sense when the direction of the previously applied saturating field has been inverted. The only five excepted particles are marked with black dots.

(not colored in Figure 10.9). These could possibly stem from transition textures like *S*-states or far shifted vortices. Another problem which could lead to difficulties in the identification of the textures are the effects of electrostatic charging during image acquisition. As the particles are made from non-conductive materials and the caps are not perfectly connected to the grounded substrate, the capped particles can accumulate charges when exposed to X-rays even though the caps are to some extent interconnected. Consequently, less secondary electrons escape the sample and contribute to the spatially resolved XMCD contrast. Additionally, these escaping electrons can be deflected on their path towards the detector due to the accumulated charges and as a result, the XMCD signals of neighboring caps superpose which leads to intertwined texture patterns that cannot be clearly identified. Hence, the data and the subsequently assigned textures depicted in Figure 10.9 need to be treated with care.[6]

[6]As a remark, it shall be noted that these effects were predominantly seen in the data of this sample (t_F = 10 nm), which is the only one that had *not* been studied under the use of the synchrotron facility's single bunch mode but in multi bunch mode. In single bunch mode, only one of regularly 400 electron packets circulating in the storage ring is filled which yields only one pulse of synchrotron radiation that is approximately repeated each 800 ns. The resulting 'dark gap' hypothetically reduces the accumulation of charges on the one hand, but comes with the drawback, that longer averaging times on the PEEM detector are necessary to acquire the desired image quality, i.e. to enhance the signal-to-noise ratio. Overall,

From counting the numbers of caps possessing the respective magnetization textures in Figure 10.9, the impression arises, that - independent on the ferromagnetic thickness or magnetic field history - the counterclockwise circulation of vortices is favored over the clockwise. This observation is, however, not reproduced in another XMCD image presented in Figure 10.11 showing a larger field of view, where contrastingly 56 % of vortices curl clockwise. It is therefore accounted that just by chance, the counterclockwise orientation seemed to be more widespread in Figure 10.9.

What is however significant, is the observation of *fixed circularity*. This means that regardless of the magnetic field history (i.e. positive or negative saturation) most of the caps nucleate vortices with the same circulation sense for all three thicknesses $t_F = 10$, 30 and 50 nm, while only 5 caps with $t_F = 50$ nm marked with black dots change from counterclockwise to clockwise or vice versa (Figure 10.9). This observation is accounted to the presence of the antiferromagnetic layer, which lifts the degeneracy of the two circularities. Similar observations have been presented based on Lorentz TEM measurements of EB disks after ZFC in Ref. [TPLH09] (cf. subsection 3.1.1). A fixed circularity imprinted during ZFC in turn means that the nucleation site of a vortex cannot be fixed but has to change when the cap nucleates either from positive or negative saturation. In contrast to EB disks, soft magnetic disks were found to nucleate with a fixed nucleation site but changing circularity which was related to a microstructure governed difference in the two sites' nucleation energies. [TPLH09]

However, in this study, FC has been applied instead of ZFC, which in a simplified picture shall align all uncompensated interfacial antiferromagnetic moments in parallel and should thereby not favor a specific circularity in the ferromagnet. Nevertheless, a possible explanation is sketched in Figure 10.10. Since the magnetic field during FC is sufficient to fully saturate the ferromagnetic layer of the caps, antiferromagnetic grains of class III are expected to be pinned according to the saturated ferromagnet. The uncompensated interfacial moments of rotatable grains of class II can however adapt to the ferromagnetic layer's changing magnetic texture during remagnetization. Collectively, they might viscously enter a curling state once the ferromagnet has nucleated a vortex (2.). This vortex associated to the class II grain ensemble then changes its texture by the motion of its core as it is further 'dragged' by the ferromagnet which is at some point oppositely saturated (3.). During vortex re-nucleation (4.→ 5.), the ferromagnet is now exposed to the shifted vortex texture of the rotatable antiferromagnetic moments. As a result, the circulation sense of the vortex which initially nucleated on the descending branch is also energetically favored for re-nucleation event on the ascending branch.

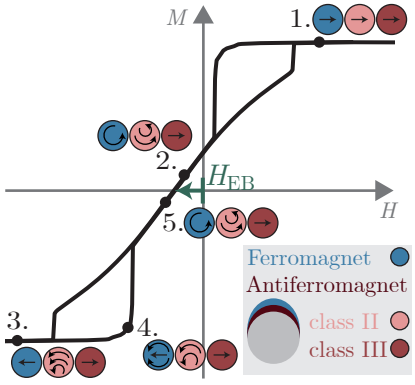

Figure 10.10: Hypothetical mechanism of re-nucleation (4.→ 5.) with fixed circularity mediated by rotatable antiferromagnetic grains.

charging affects the measurements depending on the quality of the sample, especially its conductivity. Measurements on samples with a thinner metallic layer stack generally seemed to further promote charging in some sample areas.

Concluding, the XMCD-PEEM data clearly supports the findings from the FORC analysis. For $t_F = 5\,nm$, the caps remagnetize via rotation of onion textures, whereas they undergo vortex nucleation at $t_F = 30$ and $50\,nm$. For $t_F = 10\,nm$ in negative remanence, the caps show a mixture of the remagnetization paths via onion rotation and vortex reversal, which matches the presence of the FORC features 1 and 2 as well as the ridge feature in Figure 10.6. Only analyzing the sample's major loop would not have yielded these insights, which again underpins the importance of complementing them with methods like FORC and XMCD-PEEM.

Vortex Circulation Patterns in EB Cap Ensembles

From the XMCD contrast of caps with $t_F = 50\,nm$ at remanence, the occurrence of cap rows with same circulation sense was described in Figure 10.2.3. In order to study the effect of vortex circularity coupling also for other array orientations, a position on the sample was chosen at which regions with multiple lattice orientations were found. The data was recorded after the

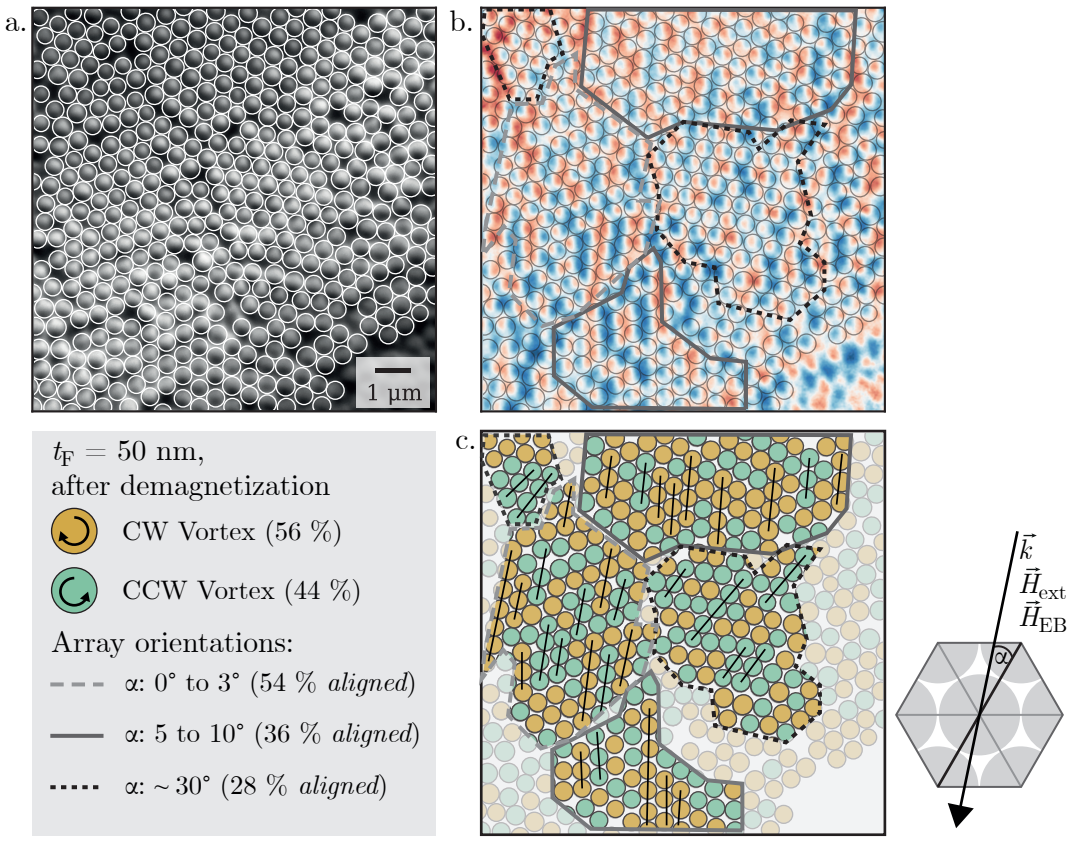

Figure 10.11: For the sample with $t_F = 50\,nm$, images with a wider field of view have been recorded after demagnetizing the sample with the aim to study vortex circularity patterns in areas of various lattice orientation. Again, circles were added to indicate the particle positions in the averaged PEEM image in a. From the XMCD asymmetry contrast image in b., the vortex circulation sense has been extracted and is depicted by the color-coded circles in c. Here, the continuous, dashed and dotted lines are enclosing areas with different orientations of the hexagonal lattice with respect the external magnetic field axis. The percentages given per orientation indicate the ratio of caps in an area that are member of a one of a homo-circular lines (i.e. black lines connecting caps sharing the same circulation sense).

sample had been subjected to a demagnetization procedure. Alongside the averaged PEEM image for a selected array orientation in Figure 10.11 a., the gained XMCD contrast image is shown in b., where subsequently added circles indicate the particle positions. In c., the vortex circulation sense is color coded and regions of consistent hexagonal lattice orientation are enclosed by dashed, dotted and continuous polygons. Within these areas, the lattice orientation angle α was determined as the smallest angle between the external magnetic field axis and one of the three main symmetry axes as shown in the sketch. While $\alpha = 0°$ describes a parallel alignment of the two axes, it can reach 30° at maximum. In order to examine, whether the array orientation with respect to the external field affects the formation of circularity patterns, straight lines are added to c. that connect caps with the same circulation sense (homo-circular line) along the respective hexagonal symmetry axis. The following table summarizes the number of straight lines per length and the total number of particles in the respective group of areas (polygons) categorized via the angle α. The alignment ratio finally indicates the portion of caps which are members of a homo-circular line.

'Length' of straight homo-circular line	$0° \lesssim \alpha \lesssim 3°$	$5° \lesssim \alpha \lesssim 10°$	$\alpha \approx 30$ °
3	7	10	4
4	4	3	2
5	1	0	1
6	0	0	0
7	1	1	0
Total number of caps in area	91	138	88
Caps that are member of a straight line	49	49	25
Alignment ratio	54 %	36 %	28 %

At first sight, the alignment ratio is observed to decrease when the angle α is increased. The closer the array orientation is to a collinear alignment with the external magnetic field axis, the more caps belong to a straight homo-circular line. The origin for this observation is expected to lie in the magnetostatic coupling of the caps.

In section 3.1 this phenomenon has been described within the context of a configurational anisotropy: the formation of transition states that precede the vortex nucleation process in two neighboring disks allows for maximum magnetostatic interaction of the disks and thereby predetermines the sense of circulation of the subsequently nucleated vortex.[JRA09] A pair of non-touching disks would nucleate vortices of same (opposing) circularity after it has been saturated in an external magnetic field parallel (perpendicular) to its long axis.[JRA09] For a honeycomb lattice of Py disks, a pattern of perfectly alternating vortex circularity was experimentally observed and is expected to be based on the magnetostatic coupling of transition states.[VSF17] This can contrastingly not be found in a hexagonal lattice due to the emergence of circulation frustration.[VSF17] Still, homo-circular chains in arrays of disks have been reported in literature, where the neighboring rows have an alternating circulation sense.[VSF17] The frustration in vortex circulation[SMK12] as well as a - to some extent - periodic arrangement of alternating lines with same circulation sense was also observed in hexagonal arrays of Py capped particles for small α.[SKR16] In the cited work, Streubel *et al.* further noticed a zig-zag arrangement of caps with same circulation sense for an angle of 20°, which can however not be found in the image presented

in Figure 10.11. Although no formation of zig-zag lines is observed here, the fraction of caps contributing to a homo-circular straight chain is reduced in comparison to smaller angles α as indicated by the table.

Note that a perfectly periodic arrangement dictated by the magnetostatic coupling of transition states can only occur, when the neighboring caps remagnetize collectively. Due to variations in the caps' geometry and their magnetic environment, their nucleation fields are however distributed over a magnetic field regime as it has been revealed by the FORC analysis. Therefore, the fact that the XMCD image does not clearly show the periodic alteration of homo-circular lines as it has been observed in literature,[SKR16,VSF17] can be related to the distribution of the caps' magnetic properties.

Overall, the measurements imply that the lattice orientation influences the formation of vortex circulation in the individual caps in dependence on their local magnetic neighborhood. The effects can be compared to observations for magnetic disk arrays presented in literature and are related to the magnetostatic coupling of the objects. In contrast to separated micro-structured disks, the caps can, however, also couple via exchange interaction at the touching points of the self-assembled particles. Both magnetostatic and exchange coupling phenomena depend on the caps' curvature, since, e.g., the generated stray fields of onion textures and homogenous magnetized disks differ in their directions which affects the magnetostatic interaction with the respective neighbors. Unfortunately, disentangling the effects of both interactions is beyond the scope of this thesis. Nevertheless, a understanding of the mechanisms of vortex circularity coupling could be approached either by micromagnetic simulations or experimental investigations. For the latter, specifically microstructured samples with magnetically capped particles separated by a variable spacing would need to be designed in order to exclude exchange coupling, and, at very large distances also magnetostatic coupling. The proposed fabrication and magnetic capping of templating micro-spheres at varying distances could be facilitated, e.g., by two-photon lithography and subsequent sputter deposition.

10.3 Vortex Reversal in EB Cap Arrays in Dependence on the Antiferromagnetic Thickness t_{AF}

The vortex reversing caps with a fixed CoFe thickness of $t_F = 30\,nm$ were further investigated under the variation of the antiferromagnetic layer thickness t_{AF}. In addition to the previously presented results with $t_{AF} = 0$ (ferromagnetic caps) and the results for $t_{AF} = 30\,nm$, the thicknesses 5 and 7 nm were chosen. The following table indicates the number of samples N investigated per thickness in the 'as made' condition:

t_{AF} [nm]	0	5	7	30
N (cap array samples)	1	1	2	3

The information about the hystereses shifts H_{EB} and the characteristic fields H_{nuc} and H_{ann} related to vortex nucleation and annihilation, respectively, were extracted as averaged quantities from easy axis MOKE reversal measurements and are illustrated in Figure 10.12 a. and b. Only

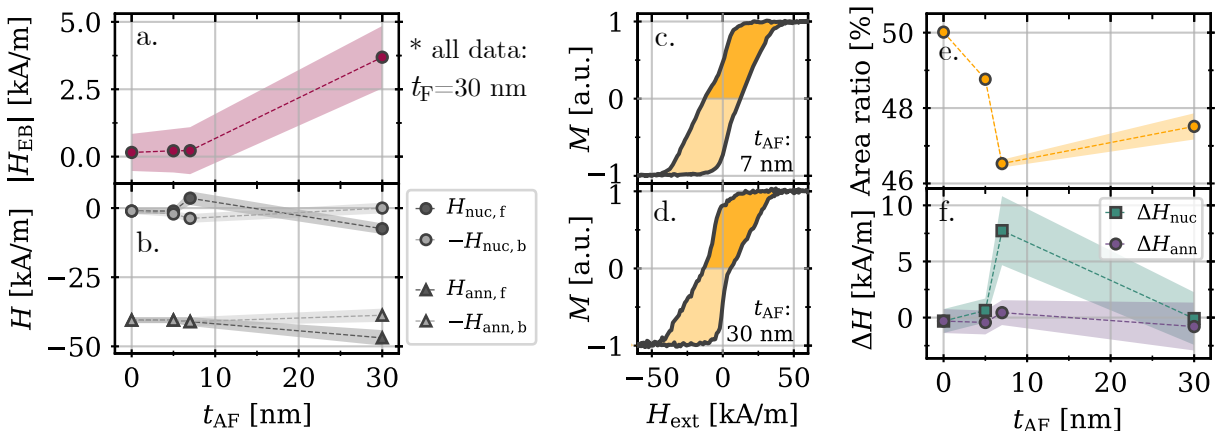

Figure 10.12: Characteristics related to the reversal asymmetry analyzed for 'as made' EB caps with $t_F = 30\,nm$ in dependence of the antiferromagnetic thickness t_{AF}. All inspected hysteresis curves include the characteristic shape of vortex reversal, of which two exemplary ones are depicted in c. and d. In a., $|H_{EB}|$ extracted via Equation 2.4.1 is plotted. Besides, the characteristic fields of vortex nucleation H_{nuc} (○) and annihilation H_{ann} (△) are displayed in b. with respect to the indicated branch (f: forward, descending, b: backward, ascending). The area ratio displayed in e. describes the fraction of the upper colored area indicated in the hysteresis panels in c. with respect to the full loop's area as a measure for the loop's asymmetry. In f., the quantities ΔH_{nuc} (□) and ΔH_{ann} (○) were evaluated that allow a comparison with studies on EB disks [GYV15] and caps [NKM16] presented in literature.

for $t_{AF} = 30\,nm$ a finite non-zero EB can be observed while it vanishes for the smaller thicknesses within the range of uncertainty. This is in contrast to the t_{AF} dependent results presented in Figure 10.1, where for 10 nm thick CoFe layers, the onset of EB already arose at $t_{AF} = 7\,nm$.

When comparing the vortex related characteristic fields, it is observed, that for $t_{AF} = 0$ and 5 nm both $H_{nuc,f/b}$ and $H_{ann,f/b}$ behave symmetrically around zero field. Hence, the reversal for these thicknesses can be categorized as an unbiased vortex reversal based on the sole analysis of the respective major loop (cf. vortex categories in Figure 3.7). In order to classify the caps' remagnetization in the case of 7 nm and 30 nm thick IrMn layers distinguishing between biased, tilted and viscous vortex reversal, exemplary hystereses are plotted in Figure 10.12 c. and d. At first sight, these curves indicate a certainly asymmetric hysteresis shape. The bend around remanence on the descending branch of the caps with $t_{AF} = 30\,nm$ (d.) has previously been observed in the 'as made' curve of another sample with the same layer stack in Figure 10.4 and was accounted to the caps passing through intermediate states directly before the vortex nucleation. This seems, however, not to be the case on the ascending branch.

For $t_{AF} = 7\,nm$, the hysteresis shape differs from the case of 30 nm in the sense, that the vortex shape is less pronounced. The hysteresis looks generally more asymmetric with a larger portion of the loop being located in the range of negative than in the range of positive M. To quantify this, the two areas (upper and lower) enclosed by the curve and the abscissa are colored differently in c. When comparing the two areas, the ratio of the upper area with respect to the full loop's area should be 50 % in a symmetric loop. In panel e., this quantity is plotted over

the antiferromagnetic thickness. For purely ferromagnetic layers, the area ratio is 50 % which fulfills the expectation of a symmetric loop for unbiased caps. Nevertheless, the upper loop area is reduced for finite t_{AF} with a maximum areal asymmetry of 46.5 % at 7 nm.

The described observation of the areal asymmetry is accompanied by nucleation fields $H_{\mathrm{nuc,f}}$ and $H_{\mathrm{nuc,b}}$ behaving asymmetrically with respect to H_{EB}. The antiferromagnetic thickness with a maximum areal asymmetry at 7 nm is the only one for which the nucleation asymmetry is clearly present as it is indicated by ΔH_{nuc} (Equation 3.1.4) in Figure 10.12 f. Hence, the remagnetization for the caps with this layer stack is classified as a viscous vortex reversal. The asymmetry value of $\Delta H_{\mathrm{nuc}} = (7.7 \pm 3.0)\,\mathrm{kA/m}$ is in a range comparable with the value obtained for larger EB caps with $D = 900\,\mathrm{nm}$ by Nissen *et al.*. Note, that they used CoO for the antiferromagnetic layer, which necessitated to measure the reversal at a temperature of 2 K in order to undergo the blocking temperature.[NKM16] For a CoO thickness of 3.5 nm the authors revealed a nucleation asymmetry of $\Delta H_{\mathrm{nuc}} \approx 10.7\,\mathrm{kA/m}$.[NKM16] The result in Figure 10.12 f. can additionally be compared to EB Py disks with a diameter of 1 µm: For the comparable antiferromagnetic alloy $Ir_{20}Mn_{80}$, Gilbert *et al.* found the highest viscosity in the disks' vortex reversal for $t_{\mathrm{AF}} = 5\,\mathrm{nm}$ with $\Delta H_{\mathrm{nuc}} \approx 1.6\,\mathrm{kA/m}$.[GYV15] This value is significantly smaller than for the here presented cap arrays, which can possibly be attributed the three-dimensional shape of the caps as well as the different strength of magnetostatic coupling. Another reason could be a difference in the deposition rate of IrMn which is an important set screw determining distribution of the antiferromagnetic grains' sizes during fabrication and thereby the degree of viscosity mediated by the fraction of rotatable grains of class II.[MHR20]

As introduced in subsection 3.1.1, the reversal of EB disks via the nucleation of a vortex with a tilted core is expected to be accompanied by an asymmetry in the annihilation fields. Both in EB disks and caps, this asymmetry has previously been observed to also depend on the antiferromagnetic thickness.[GYV15,NKM16] Nevertheless, none of the values ΔH_{ann} displayed in Figure 10.12 f. significantly differs from zero, which leads to the conclusion that none of the prepared cap arrays reverses via the tilted vortex path.

As a result, the investigated caps show an unbiased vortex reversal for $t_{\mathrm{AF}} = 0$, whereas they reverse via viscous vortex reversal for $t_{\mathrm{AF}} = 7\,\mathrm{nm}$. For cap arrays with t_{AF} =30 nm, neither a nucleation nor an annihilation asymmetry can be determined in the range of uncertainty. Consequently, their reversal behavior is categorized as a biased vortex reversal from this major loop analysis. The absence of ΔH_{ann} and ΔH_{nuc} also applies for $t_{\mathrm{AF}} = 5\,\mathrm{nm}$, which further shows almost zero H_{EB} and is therefore expected to reverse via an unbiased vortex.

10.3.1 Analysis of FORC Fingerprints of EB Cap Arrays for Various Antiferromagnetic Thicknesses t_{AF}

In order to further study the nucleation events of the EB cap arrays for fixed $t_{\mathrm{F}} = 30\,\mathrm{nm}$ with varied antiferromagnetic thickness, FORC diagrams shall be analyzed. The data is comparable with the results presented in subsection 9.1.1 and subsection 10.2.2, as the same measurement and evaluation parameters were used. The FORC families and respective distributions are depicted in Figure 10.13.

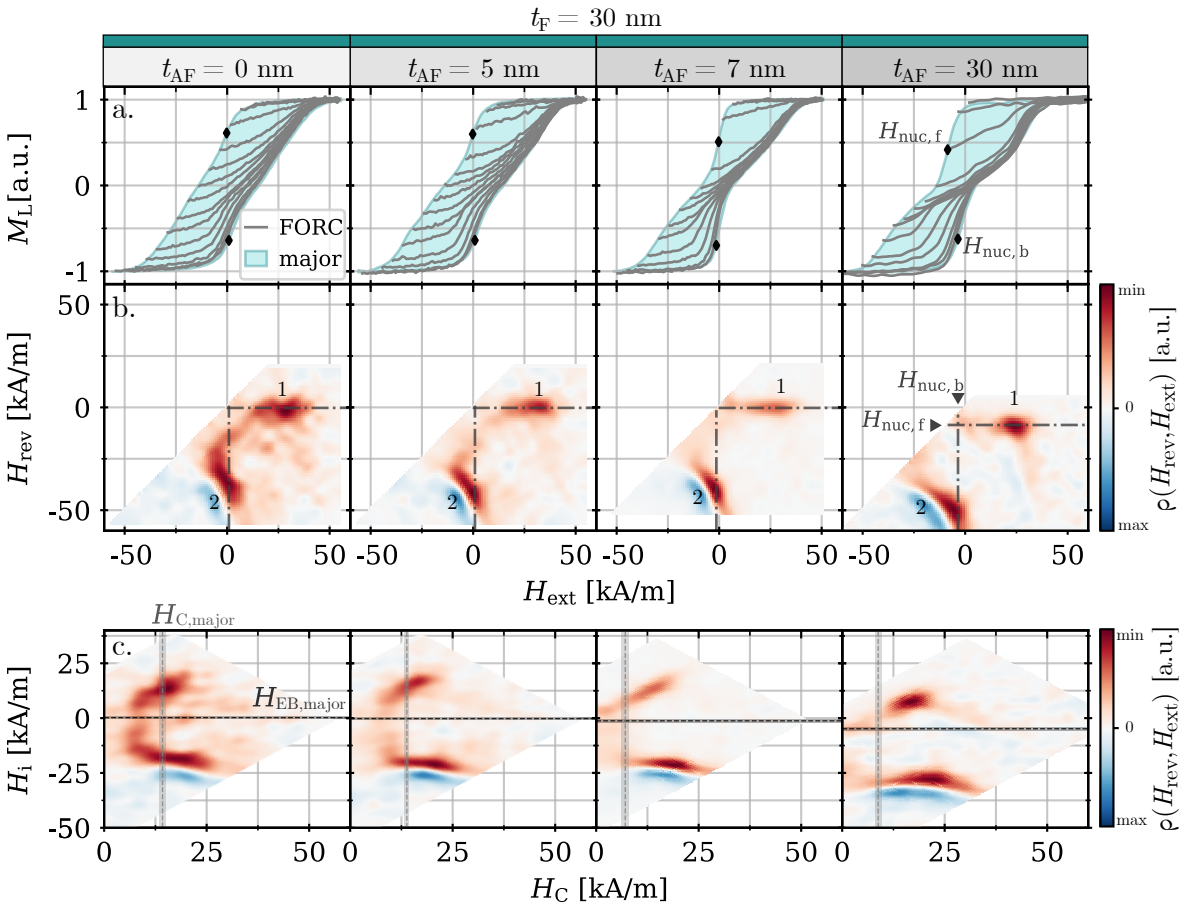

Figure 10.13: For EB cap arrays with t_F =30 nm that are characterized by vortex reversal, FORCs have been recorded after FC in the same manner as previously shown in Figure 10.6. From left to right, the antiferromagnetic thickness is changed from 0 to 30 nm. In a., the families of FORCs $M(H_{rev}, H_{ext})$ measured along the sample's easy axis ($\varphi = 0°$) are displayed. The corresponding FORC distributions $\rho(H_{rev}, H_{ext})$ and $\rho(H_i, H_C)$ are depicted in b. and c., respectively. The major loops' coercivity H_C, loop shift H_{EB} as well as the nucleation fields $H_{nuc,f/b}$ are indicated by dashed and dashed-dotted lines in c. and b., respectively.

Recalling the origin of the features 1 and 2 in the FORC diagram, the results indicate a vortex reversal for all thicknesses t_{AF}. Feature 1 relates to the initial nucleation of vortices on the descending branch and their annihilation on the respective FORCs when approaching positive saturation, whereas feature 2 is connected to the re-nucleation from negatively saturated caps on the ascending branch.

For the purely ferromagnetic cap, i.e. $t_{AF} = 0$, both features share a similar intensity, which speaks for a symmetry in the nucleation process on both branches and is in agreement with the major loop analysis in Figure 10.12. At $t_{AF} = 5$ nm, the intensity of feature 1 is reduced indicating a difference in the nucleation behavior under field inversion. This asymmetry, which contradicts conventional vortex reversal, becomes particularly evident at $t_{AF} = 7$ nm, as feature 1 is only faintly visible. The smaller weight of feature 1 in the FORC diagram shows that the initial nucleation from positive saturation is characterized by less irreversibility than the re-nucleation generating feature 2. A possible explanation for this is connected to the uncompensated interfacial moments of the rotatable grains within the granular antiferromagnetic layer which

cause the nucleation process to be viscous: Just before or during the nucleation of a vortex, the ferromagnetic magnetization texture undergoes small changes which are basically small rotations of ferromagnetic moments. These changes may be stabilized by the antiferromagnet's rotatable grains, as these adapt to the ferromagnetic layer on the time scale of the experiment because their coupling to the ferromagnetic moments exceeds their intrinsic magnetic anisotropy. As a consequence, the process is characterized by less irreversibility since the caps can more easily return to an onion state on the respective FORCs due to this viscous nucleation process. Contrastingly, the nucleation in a purely ferromagnetic cap occurs rather instantaneously due to the missing stabilization of intermediate states by the antiferromagnet's rotatable grains. The additional fact, that the two features differ strongly in their intensity is ascribed to the difference in the antiferromagnetic interface texture on the two branches. Starting from positive saturation, antiferromagnetic grains of both classes II and III are aligned mostly parallel. During reversal, the rotatable grains of class II change their orientation, so that on the ascending hysteresis branch starting from negative saturation, the two types of antiferromagnetic grains possess differently oriented uncompensated moments. Hence, the ferromagnet is differently affected by the interfacial exchange coupling on the two respective branches.

For $t_{\mathrm{AF}} = 30\,\mathrm{nm}$, the features again approach similar intensities and the rather symmetric vortex fingerprint of the transformed distribution $\rho(H_{\mathrm{i}}, H_{\mathrm{C}})$ (c.) is shifted towards negative interaction fields in accordance to the significant shift H_{EB} of the major loop indicated in c. by a dashed horizontal line. It emphasizes that more pinning antiferromagnetic grains of class III are established, which has previously also been observed for EB caps with a thinner ferromagnetic layer in Figure 10.1. The stronger the antiferromagnetic grain volume distribution is shifted to larger grain sizes upon increasing t_{AF}, the more grains are pinning the ferromagnetic layer's magnetization, while the number of rotating grains is reduced. As a consequence, the nucleation processes appear at fields symmetric around H_{EB} (cf. $\Delta H_{\mathrm{nuc}} \approx 0$ in Figure 10.12) and the related features in the FORC distribution gain equal strength.

In conclusion, the transition from a viscous to a classical biased nucleation behavior described for the EB caps clearly depends on the fact, that the antiferromagnetic thickness determines the antiferromagnetic grain ensemble, i.e. the fraction of grains of class II and III. From the FORC data, which indicates a high portion of rotatable grains by a strong asymmetry in the intensities of the two vortex nucleation features, we can deduce that comparably more rotatable grains are hosted in the antiferromagnetic films with thicknesses of 5 and 7 nm. This is in agreement with the MFM analysis of EB disks presented in Ref. [ABR21] where the onset of the viscous behavior accompanied by distorted remanent vortices arose from 4 nm. Approaching larger t_{AF}, the grain volume distribution is shifted towards larger grain sizes which has a reduction of number of rotatable grains as a result. The consequence is that the nucleation again appears to be symmetric with respect to H_{EB} and with FORC features of similar intensity for $t_{\mathrm{AF}} = 30\,\mathrm{nm}$. Hence, the nucleation process is not described as viscous but as a biased vortex reversal for this thickness, which is in agreement with the previous major loop analysis in Figure 10.12.

10.4 Conclusion

Within this chapter, the effects of EB as an additional anisotropy for arrays of magnetic caps have been investigated. At first, EB was successfully introduced in caps by adding an antiferromagnetic layer below the ferromagnetic one, similar as for the case of extended EB films. For cap arrays with thin ferromagnetic layers (10 nm), the dependence of H_C and H_{EB} on the antiferromagnetic thickness compares well with the trends of an extended EB film with the same layer composition (cf. Figure 10.1). The observation that H_{EB} behaves similarly in both systems can be related to the previously confirmed similarity of the distribution of antiferromagnetic grain radii presented in section 7.2.

Similar to ferromagnetic caps, EB caps change their reversal route depending on the ferromagnetic thickness t_F which is in principle connected to the thickness dependence of the demagnetization energy. The transition from the rotation of onion textures to a reversal via vortex nucleation, motion and annihilation was found around $t_F = 10\,\text{nm}$. Characteristics for the easy axis magnetization reversal with respect to t_F were extracted from major loops of caps with an antiferromagnetic thickness expected to sufficiently pin the ferromagnetic layer's magnetization, i.e. $t_{AF} = 30\,\text{nm}$ (cf. section 10.2). Therein, the coercivity was larger in cap arrays than in the extended planar EB film for all thicknesses, whereas both systems show - in the range of uncertainty - the same $H_{EB}(t_F)$ dependency. In addition to the easy axis hysteresis measurements, angular resolved measurements of the reversal have been recorded for specific thicknesses (cf. section 10.1).

In order to study the effects of annealing, FC and ZFC has been applied to 'as made' or 'trained' samples with EB caps of various t_F and $t_{AF} = 30\,\text{nm}$ (cf. subsection 10.2.1). Furthermore, the field-cooled cap arrays were studied with the help of FORC diagrams for various t_F (cf. subsection 10.2.2), which unraveled the distribution of magnetic properties for all t_F, and even a mixture of reversal paths for $t_F = 10\,\text{nm}$.

Exploring EB cap arrays with XMCD-PEEM further allowed to acquire spatially resolved images of the magnetization textures in the individual caps of an the array (cf. subsection 10.2.3). The results match the previously discussed distribution of magnetic properties deduced from the FORC analysis and further reveal that the nucleation and re-nucleation processes are governed by a fixed circularity mechanism.

For a ferromagnetic thickness of $t_F = 30\,\text{nm}$, at which the caps' remagnetization route was characterized as a vortex reversal, an additional study has been performed with respect to the antiferromagnetic thickness t_{AF}. Here, the remagnetization modes *unbiased/classical*, *biased* and *viscous* vortex reversal have been identified via two measures for the major loops' asymmetry and by the strength of the expression of vortex related features in FORC diagrams (cf. section 10.3).

Advantages of FORC Analysis

As inspected previously for purely ferromagnetic caps, also in this chapter, the magnetic properties evaluated from major loops are found to be an average of the local properties. Adding FORC analysis to the experimental toolbox when investigating ensembles of microstructured objects like the capped particles has proven to be very valuable for the following reasons:

- The features in a FORC distribution ($\rho \neq 0$) point to irreversibilities in the reversal process. Depending on the specific FORC *fingerprint*, reversal routes like the rotation of onion textures or vortex reversal can be assigned to the sample.

- The FORC analysis allows to gain insights in the distribution of magnetic properties within an ensemble as it has for example been shown in Figure 9.3, where ferromagnetic caps with $t_F = 10\,nm$ were seen to posses a distribution of coercivities and ferromagnetic caps with $t_F = 40\,nm$ showed a distribution of nucleation fields. These distributions of properties are highlighted by a broadening of the respective FORC feature and cannot be deduced from the often ambiguous analysis of major loops.

- Further, it was seen that the FORC diagrams allow to inspect the degree of reversibility of remagnetization processes, like the vortex nucleation. For EB caps with an intermediate antiferromagnetic thickness of $t_{AF} = 7\,nm$, the nucleation process was identified to be asymmetric under field inversion: It has been observed, that the nucleation on the descending hysteresis branch is less irreversible than on the ascending branch. This was correlated to the amount of rotatable grains in the polycrystalline antiferromagnet, as they mediate the viscosity of reversal processes.[MHR21]

- Finally, it is possible that different reversal routes are present within a measured ensemble. For the EB cap array with $t_{AF} = 30\,nm$ and $t_F = 10\,nm$, the FORC diagram showed a mixture of reversal paths, both rotation of onion states and vortex reversal. Contrastingly, it was not possible to draw this conclusion from the sole major loop study in which all contributions are averaged. We can conclude that FORC offers a technique to deconvolve different reversal routes across any array of structured micro- or nano-magnets which is especially important to unravel the influence of local properties.

11. Anisotropy Engineering for Magnetic Cap Arrays

For practical use of magnetic micro-objects, an essential prerequisite is the control of the magnetization textures within. In technological applications, where they shall store digital information in devices like the proposed vortex random access memory [BKD08], the magnetic state needs (in the best case) to be writable, readable and non-volatile. A second field of application is the already mentioned use of magnetic micro-objects as probes in microfluidic devices for biosensing. Here, the magnetic state of the particle needs to be well known in order to correctly define the magnetic force $\vec{F_{\mathrm{m}}} = \mu_0 \vec{M} \cdot \nabla \vec{H}_{\mathrm{ext}}$ and/or torque $\vec{\tau_{\mathrm{m}}} = \mu_0 \vec{M} \times \vec{H}_{\mathrm{ext}}$ which needs to be generated to initiate a requested actuation. For both, the precise knowledge of the remanent net magnetic moment as well as the range of remagnetization within the experimentally applied magnetic field regime is desired to control and understand the particles' motion and magnetic stability within the required magnetic fields.

When magnetically capped particles are used in microfluidics, they are typically harvested from a sample containing particle arrays. [Reg18,HRT21] However, the simulations in chapter 4 revealed that the exact characteristics of an individual cap cannot be directly deduced from the properties of caps interacting in an array. As a consequence, this deviation necessitates the investigation of individual capped particles, which will be the subject of chapter 12.

Nevertheless, studying magnetic cap arrays clearly points to trends of reversal paths and remanent magnetic states with respect to the cap geometry and the used materials. The radius and the thickness of a ferromagnetic cap determine its demagnetization energy, for which the consequences on the remagnetization behavior were studied in chapter 9 and e.g. in Refs. [SEG12, Str15, NMK15]. On the other hand, the choice of ferromagnetic material can change the strength of the intrinsic magnetic anisotropy which will be discussed in this chapter. Moreover, it has been shown in the course of chapter 10 that a (local) unidirectional anisotropy (EB) can be induced when an additional antiferromagnetic layer is incorporated to share an interface with the ferromagnetic layer. To tune the exchange-biased caps' magnetic properties, it has been identified that FC defines a unidirectional and ZFC a circular EB.

For a templating particle diameter of $D = 500\,\mathrm{nm}$, the easy axis magnetization reversal was measured with the LMOKE setup for different material compositions based on the soft and a hard ferromagnetic alloys, NiFe and CoFe, respectively. The caps have either been prepared by field-growth ($H_{\mathrm{depo}} = 28\,\mathrm{kA/m}$) or sputtered in the absence of a magnetic field ($H_{\mathrm{depo}} = 0$).

Based on these four types of ferromagnetic caps, the effect of EB was further studied by adding an additional antiferromagnetic IrMn layer of 30 nm thickness. Hence, eight different types of magnetically capped particles were fabricated where the dimensions like radius and thickness remained constant. For all samples, a ferromagnetic thickness of $t_F = 10\,\text{nm}$ was chosen as the transition regime between a reversal governed by the rotation of onion states and the vortex reversal was found to lie around this thickness (cf. Figure 10.6). For the EB cap arrays, FC was applied to the field-grown samples whereas a demagnetization routine and subsequent ZFC was applied to the field-free-grown samples. The recorded easy axis hysteresis curves are shown in Figure 11.1 and will be discussed in the following.

Considering the top row at first, the use of CoFe (c.) instead of NiFe (a.) increases the saturating fields (note the difference in the depicetd range of H_{ext}) which is related to the larger intrinsic magnetic anisotropy and the higher exchange stiffness of CoFe. The coercivity of these cap arrays further increases, when the material is deposited in a magnetic field (b., d.). This observation matches the expectations for field-growth induced anisotropy. For example, deposition in a saturating magnetic field induces a uniaxial magnetic anisotropy of $\sim 140\,\text{J/m}^3$ in the face-centered-cubic (fcc) structured alloy NiFe that typically exhibits a negligible magnetic anisotropy.[CO55] In contrast to the easy axis hysteresis curves in the case of CoFe (c., d.), the characteristic vortex reversal shape can be identified for NiFe (a., b.). For the field-grown CoFe caps of the here chosen thickness $t_F = 10\,\text{nm}$ (d.), the reversal via the rotation of onion textures has previously been evidenced by FORC measurements in subsection 9.1.1.

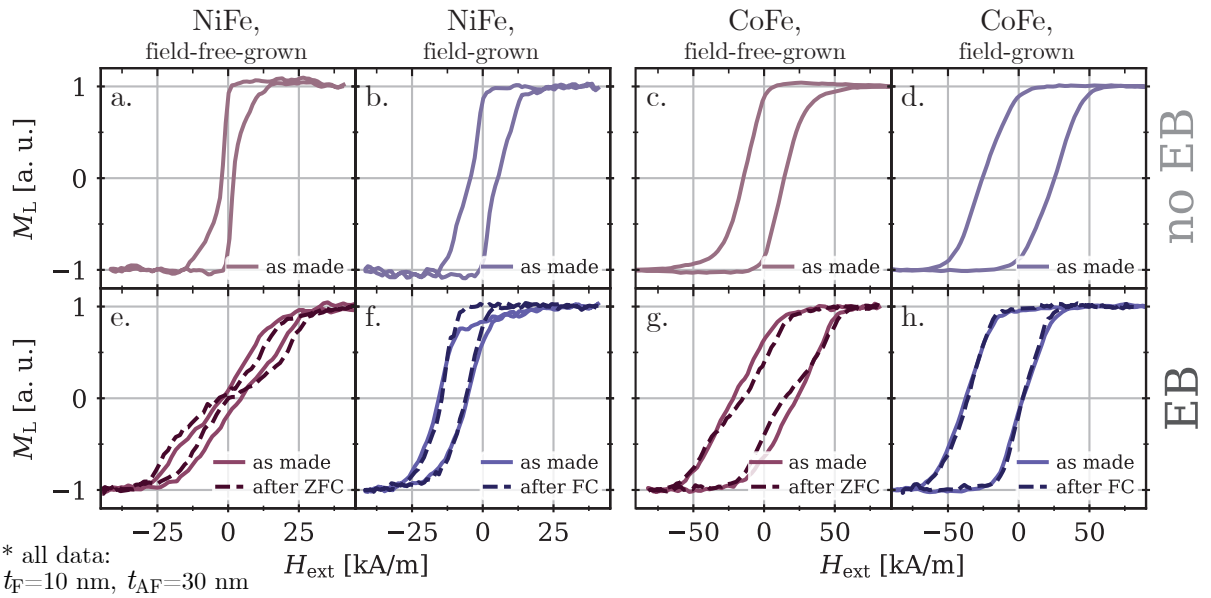

Figure 11.1: Easy axis magnetization reversal of magnetic cap arrays with a particle diameter of $D = 500\,\text{nm}$ for purely ferromagnetic (a. - d.) and exchange-biased (e. - h.) layer stacks. Soft magnetic Permalloy, NiFe, was used on the left, wile hard magnetic CoFe was deposited on the caps measured in the right column. Note the different range of the x-axis. Additionally, it is differentiated between caps that have been deposited in the presence (field-grown) or the absence (field-free-grown) of an external magnetic field. All measurements termed 'as made' were performed without (zero-) field-cooling the sample but after a storage time of roughly one year.

The lower row of hysteresis loops in Figure 11.1 refers to caps with EB. Only for the deposition in a magnetic field (f., h.), the characteristic hysteresis shift and the accompanying difference in the remanent magnetization of both branches ($M_{\mathrm{R,f}} \neq -M_{\mathrm{R,b}}$) is observed, whereas the reversal remains centered around zero with $M_{\mathrm{R,f}} \approx -M_{\mathrm{R,b}}$ for the field-free-grown layers (e., g.).

Interestingly, the field-grown EB caps from NiFe do not indicate the vortex reversal shape as compared to the purely ferromagnetic counterparts, but show a rather asymmetric reversal (f.). This asymmetry is further enhanced upon FC, which does, however, not enhance the EB field shift determined from the curve's intersections with the x-axis but generally 'lifts' the remanent magnetization $M_{\mathrm{R,f}}$ on the the descending branch from 0.85 to approximately 1 and $M_{\mathrm{R,f}}$ on the the ascending branch from 0.6 to 0.85. The fact that here, the FC does not enhance H_{EB} for both field-grown NiFe and CoFe could be related to the long storage time between the deposition and the remagnetization measurement. The effect of storage related stabilization of the EB due to the thermally activated relaxation of pinning antiferromagnetic grains, aligning their uncompensated interfacial moments in accordance to the ferromagnetic layer's remanent magnetization, is well known from flat EB films.[PR02] As for the here presented investigations, the samples were stored for approximately one year at room temperature, it is expected that a major part of the antiferromagnetic grain ensemble mediating the EB shift is already set, and that the number of class III grains cannot be further increased. As a result, the effects of FC are less prominent than shortly after the fabrication.

The observed asymmetry of the (*supposedly* easy-axis) hysteresis of field-grown NiFe EB caps might originate from a misalignment of the external magnetic field with respect to the sample's easy axis (defined by H_{depo}) as it has been reported for flat EB films, where the differences in the remagnetization behavior of the two branches have been evidenced to be crucially determined by the measurement angle.[CSH05] More precisely, Jiménez *et al.* revealed that the angular dependent reversal asymmetry of EB films with NiFe as a ferromagnet takes only positive values, whereas it has a zero crossing when the ferromagnet has a stronger anisotropy such as Co.[JCS09] This asymmetry arises in the angular regime of irreversible processes but turns zero in the reversible regime, i.e. for purely rotational remagnetization processes. For ferromagnets with vanishing intrinsic anisotropy like NiFe, the authors connect this to a non-collinear orientation of the ferromagnetic anisotropy axis and the unidirectional anisotropy axis. This deviation from a strictly collinear alignment results in the reorientation of the ferromagnetic magnetization configuration due to a magnetic coupling frustration at the not perfectly flat interface shared with the antiferromagnetic layer.[JCS09] In the case of the here discussed EB caps, the asymmetry is clearly present for NiFe (f.), but not recognizable for CoFe (h.). In order to quantify the asymmetry and its angular dependence as shown in Ref. [JCS09], angular resolved measurements of both the longitudinal and the transversal magnetization component, i.e. VMOKE measurements, are inevitable.

The most dominant change between the hysteresis shape of ferromagnetic and EB caps is seen for field-free-grown NiFe (e.), where the vortex stability regime is more than doubled from $|H_{\mathrm{nuc}} - H_{\mathrm{ann}}| = 15\,\mathrm{kA/m}$ for the pure NiFe caps to $37\,\mathrm{kA/m}$ for the EB NiFe caps after ZFC.

Similarly, the hysteresis of the field-free-grown EB caps from CoFe changes its shape upon ZFC (g.). From the 'as made' major loop curve, a reversal based on rotation of onion states could

be deduced at first sight, whereas the curve exhibits the characteristic kinks indicating vortex reversal after ZFC. Here, it is important to note that the occurrence of a vortex shaped hysteresis from this sample after ZFC is only possible when the reversal behavior of the 'as made' sample *did* include the nucleation of vortices. This is a prerequisite, because these vortex textures can only be imprinted to the underlying antiferromagnet which later on promotes the characteristic vortex shape accompanied by an enlarged vortex stability regime, if the demagnetization procedure leaves the cap array in a state with nucleated vortices. This result again points to the importance to study ensembles like magnetic cap arrays by different methods instead of just relying on conclusions drawn from possibly ambiguous major loops. Here, a FORC analysis would be a valuable addition as from the above observations it can be assumed that the cap ensemble exhibits a mixture of reversal paths and a very broad distribution of nucleation and annihilation fields. A FORC diagram could give these insights and clarify whether the major loop to which one would - in first instance - assign a rotational behavior, just appears with a smoothed shape where the individual reversal routes are actually averaged over the ensemble.

In conclusion, the reversal paths, the magnetic field range for the reversal, and the occupied magnetic states in remanence can be tuned by anisotropy engineering based on the following factors affecting certain energetic contributions in the context of the micromagnetic description as introduced in section 2.1:

- The cap geometry determines the demagnetization energy.
- The choice of material determines both the exchange energy and the magnetic anisotropy energy.
- The magnetic field during deposition can induce an additional uniaxial anisotropy energy.
- Last but not least, the introduction of EB adds a specific exchange bias energy which may be tuned by a post-deposition annealing procedure like FC. Specifically, ZFC may introduce a locally varying exchange bias energy.

12. Studying Individual Magnetic Janus Particles

So far, all presented experimental results purely considered the behavior of capped particles arranged in close-packed monolayers. Nevertheless, for possible applications in microfluidics, individual capped particles are desired to be used. In this field of research, a particle with two sides of different properties is typically called a Janus particle (JP). The name refers to the roman god 'Janus' who is the god of beginnings, transitions and endings and therefore often depicted with two faces. Although the term was introduced for particles possessing one hydrophobic and one hydrophilic side,[CFR89] it is nowadays used for many different kinds of two-sided particles including magnetically capped particles.

When working with magnetic JPs, we shall recall that the micromagnetic simulations in chapter 4 suggest severe differences in the remagnetization behavior of an individual ferromagnetic cap or caps in an array. For the chosen geometry, especially the remanent magnetization was seen to differ in the way that the individual cap showed a stable vortex state while a cap surrounded by its six neighbors remains in an onion state. Consequently, studying arrays of magnetically capped particles does not allow to draw direct conclusions for the single particle characteristics.

Although methods to investigate individual magnetic JPs are rare, some experimental options shall be listed:

- A technique called dynamic cantilever magnetometry (DCM) has been established to measure the hysteresis of individual magnetic objects like magnetic nanotubes mounted on an oscillating cantilever.[WRB12,GWR16,MGW18] The method has been applied to the ferromagnetic and EB capped particles prepared for this thesis by Philipp *et al.* in Ref. [PGR21]. The derived results shall be summarized in section 12.1 after a short introduction to the method.

- Brandt *et al.* isolated a single capped particle from an array by removing all surrounding particles with the help of FIB milling. Subsequently, they studied spin wave modes in the magnetic cap by pump-probe MOKE measurements.[BRG13]

- Rahm *et al.* performed micro-Hall magnetometry on an individual disk that was structured by electron beam lithography directly on the micro-Hall sensor.[RBU03] In order to study magnetically capped particles this way, the self-assembly could be performed starting with a low concentration of the templating particles in solution which results in a low density of rather distributed and not monolayered particles on the chip. By chance one particle

could possibly be positioned on the sensor so that similar experiments could be performed. Unfortunately, sputter deposition subsequent to the assembly process would also cover the sensor itself which renders this option rather unsuited. Also FIB milling all particles in a monolayer except one as described above is undesired as it would likely also destroy the sensor itself. A less destructive route would be to transfer a capped particle from an array onto the sensor with the help of a micromanipulator, as it is similarly done in DCM.

- In XMCD-PEEM experiments, imaging individual caps is also possible. Especially for small and rather transparent objects, the object's shadow can give additional insights in the magnetization textures.[SKS12] Since the X-rays are incident under an angle of 74° with respect to the sample normal, the shadow cast is longer than the object itself, which allows to identify the texture within very small capped particles (30 nm) with the help of this 'tail' contrast.[SKS12] As this technique only applies to objects that are rather transparent, for larger capped particles the magnetization texture has to be studied directly from the cap (not the shadow). The larger the particles, however, the stronger are the charging effects, which can complicate the analysis, e.g. when only a small signal is generated by the caps which is then superposed by the background created by the less-charged substrate (c.f. Figure 12.1). Additionally, hysteresis measurements are comparatively complicated due to the fact that a magnetic field applied in the PEEM setup deflects the course of secondary electrons which necessitates demanding adjustments regarding the focusing unit in order to guide them towards the detector.

In a digression, a brief description will be given of similar XMCD-PEEM experiments that have been carried out in the course of this work. In Figure 12.1, XMCD asymmetry contrast images recorded for particles capped with an EB layer with $t_F = 10\,\mathrm{nm}$ are shown. While only one of the capped particles can be treated as an individual, the other ones are close enough to each other that magnetostatic interactions are expected. Aside of the averaged PEEM image which is stitched together from two measurements, the respective XMCD images are shown for three magnetic field configurations. In the images of the remanent states in b. and c., the sample has previously been positively and negatively saturated, respectively. In d., a magnetic field of $-17\,\mathrm{kA/m}$ was applied during imaging after negative saturation. From the averaged PEEM image, the effect of charge accumulation on the particles is emphasized by their dark appearance as compared to the surrounding area. The underlying substrate is also covered by the studied magnetic film and therefore creates a usually unwanted background in the respective XMCD image. The presence of EB becomes obvious from the fact, that the residual film magnetization is not inverted between positive and negative remanence in b. and c. Unfortunately, the EB film in c. has subdivided into domains and therefore creates a complex XMCD pattern. This background superposes the XMCD contrast created by the caps, which renders it very difficult to derive pure information on the cap magnetization. Hence, the information in the corresponding XMCD images shall be treated with care, as the contrast within the marked circles can originate from both, the caps as well as the flat EB film. Nevertheless, in b. and d., some of the caps can be assigned magnetic textures. The presence of both onion and vortex states suggests that a cap as an individual remagnetizes via vortex nucleation, and that caps resembling an onion have not yet undergone nucleation. However, the reversal via coherent rotation cannot be excepted for the

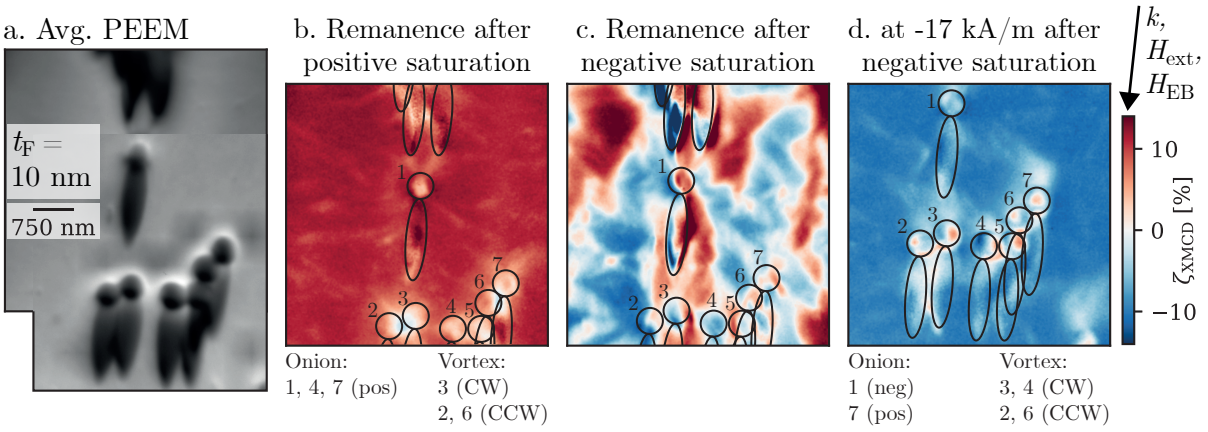

Figure 12.1: XPEEM data of EB capped particles ($D = 500\,\text{nm}$, $t_F = 10\,\text{nm}$, $t_{AF} = 30\,\text{nm}$, 'as made') which are not arranged in a close-packed array. The averaged PEEM image in a. is stitched together from two measurements. The corresponding XMCD images are shown for positive and negative remanence in b. and c., whereas a magnetic field of $-17\,\text{kA/m}$ was applied during imaging after negative saturation in d.

caps not hosting vortices. This is reminiscent of the results of FORC measurements on EB cap arrays, where both remagnetization routes were also found for this ferromagnetic layer thickness. The doublet of caps 2 and 3 furthermore shows that - regardless of the magnetization history - the pair of vortices is formed with opposing circulation sense as it was previously suggested by simulations of disks in Figure 3.3, when the doublet's long axis does not coincide with the H_{ext} axis. Similar as for EB cap arrays in Figure 10.2.3, it is seen, that the caps undergo a nucleation mechanism with EB induced fixed circularity but changing nucleation site as previously presented for EB disks.[TPLH09] In order to remove the undesired background information of the flat film, pre-structuring the sample via FIB should be considered in the future so that only the remaining particles can be measured individually.

12.1 Dynamic Cantilever Magnetometry

In DCM, a soft cantilever is driven to oscillate at its resonance frequency f with a fixed amplitude in a feedback loop with the help of a piezoelectric actuator.[GWR16] As indicated in the sketch in Figure 12.2 a., the cantilever to which the magnetic micro- or nanoobject (sample) has been attached oscillates around an axis parallel to y in the presence of an externally applied magnetic field $\vec{H}_{ext}$ which direction can be rotated within the xz-plane by a maximum of $\vartheta_H = 117°$. The measured quantity is the cantilever's resonance frequency shift $\Delta f = f - f_0$, where f_0 denotes the resonance frequency at $H_{ext} = 0$. The shift results from the magnetic torque τ_m acting on the investigated object due to $\vec{H}_{ext}$.

Practically, the object of interest, i.e. a JP, is picked up from the respective substrate with the help of a micromanipulator and afterwards glued to the apex of an ultrasoft single-crystal Si cantilever with epoxy glue under an optical microscope.[GWR16] The cantilever deflection is measured by a fiber interferometer via laser light being reflected from a wider paddle region on the cantilever (s. Figure 12.2 a.).[GWR16]

By setting up the cantilever's equation of motion, the authors of Ref. [WRB12] and Ref.

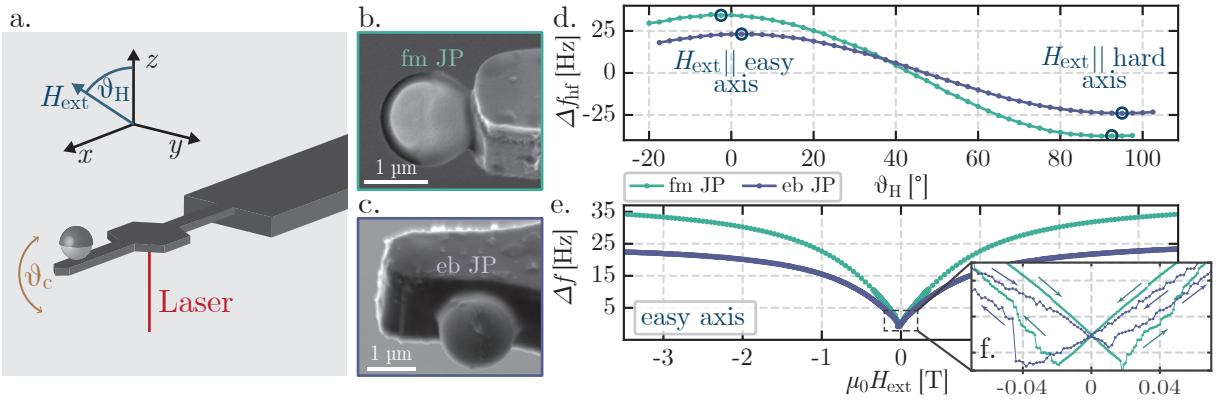

Figure 12.2: a. Sketch of a JP attached to a cantilever in a DCM setup with the respective coordinate system. SEM images in b. and c. were recorded after the ferromagnetic (fm) and the exchange-biased (eb) JPs were glued to the cantilever, respectively. The high-field frequency shift Δf_{hf} in d. was measured while changing the angle ϑ_H, i.e. the direction of $\vec{H}_{ext}$ with $\mu_0|\vec{H}_{ext}| = 3.5\,T$. At the angle of the therein determined easy axis, the hysteresis measurements depicted in e. were performed for both JP types. The hysteretic behavior is visible in the inset f, where arrows indicate the field sweep direction. Reused (and adapted) from [PGR21], with the permission of AIP Publishing.

[GWR16] derive Δf from the energy E of this magnet-on-cantilever system, to which both the mechanical energy related to the cantilevers mechanical properties as well as the sample's magnetic energy E_m contribute. As a result, Δf depends on the second derivative of E_m with respect to the cantilever deflection ϑ_c:

$$\Delta f = \frac{f_0}{2k_0 l_e^2}\left(\frac{\partial^2 E_m}{\partial \vartheta_c^2}\Big|_{\vartheta_c=0}\right). \tag{12.1.1}$$

Here, the cantilever is approximated as a harmonic oscillator, and its effective spring constant is k_0, its effective length in the fundamental mode is l_e and ϑ_c is the angle of its free end describing the deflection.[GWR16] The shift in resonance frequency is caused by a hardening or softening of the cantilever, connected to positive and negative values in Δf, respectively. In the simplest model, E_m can be described with the help of a Stoner-Wolfahrth ansatz for samples behaving like a macro spin, which is in general true for high applied external fields. In contrast to that, the sample can posses rather complex magnetization configurations in the low-field regime, which cannot be treated by a coherently rotating group of magnetic moments as in the Stoner-Wohlfarth approach. As a consequence, interpreting the DCM results in the low-field regime necessitates micromagnetic simulations that yield the total magnetic energy E_m per applied field. The frequency shift $\Delta f(H_{ext})$ can be simulated when the second derivative of E_m with respect to ϑ_c is approximated by the finite difference between both the cantilever's resting position and a slightly deflected alignment ($\delta\vartheta_c \neq 0$):[MGW18]

$$\frac{\partial^2 E_m}{\partial \vartheta_c^2}\bigg|_{\vartheta_c=0} \approx \frac{E_m(\delta\vartheta_c) - 2E_m(0) + E_m(-\delta\vartheta_c)}{(\delta\vartheta_c)^2} \tag{12.1.2}$$

With this second order derivative and the experimental values of f_0, k_0 and l_e, the frequency shift is retrieved in dependence of the magnetic field for all magnetization configurations simulated

according to Equation 12.1.1.[MGW18] Correlating the simulated and the experimental data, then allows to assign magnetization textures and the transitions between them to specifically applied magnetic fields. Note that the process typically requires multiple iterations in the micromagnetic modeling until the experimental results are matched, as details from the sample's geometry, its anisotropies and its orientation with respect to the cantilever's coordinate system have to be tuned precisely. Another important parameter is the saturation magnetization, which can, however, be estimated beforehand from fits of the Stoner-Wolfahrth approach to the DCM data in the high magnetic field regime.[GWR16] More details on the DCM method and the related modeling approaches can be found in Refs. [WRB12, GWR16, MGW18].

12.1.1 Hystereses of Individual Janus Particles

The following results have been acquired by the PoggioLab at the University of Basel within a close collaboration and are published in Ref. [PGR21]. A ferromagnetic and an EB JP both with a diameter of $D = 1.5\,\mu\text{m}$ were glued to two cantilevers. The layer stack of the particles' caps consist of a 10 nm Cu, 30 nm of IrMn (only for EB JP), 10 nm of CoFe and a 10 nm thick Si capping. After recording SEM images of the respective particle on the cantilever shown in Figure 12.2 b. and c., each sample was investigated by DCM. Note the particle orientations in these images that were later on considered in the simulations: In the case of the ferromagnetic JP, the cap faces towards the right side, while the cap of the EB JP is oppositely oriented.

In order to first determine the JPs' easy and hard axis, the frequency shifts measured with the maximum magnetic field $\mu_0 H_{\text{ext}} = 3.5\,\text{mT}$ under variation of its angle ϑ_{H} are shown in Figure 12.2 d. In this high-field limit, $\Delta f(H_{\text{ext}})$ approaches an asymptote, whereby a maximum and a minimum in $\Delta f_{\text{hf}}(\vartheta_{\text{H}})$ appear along the object's easy and hard directions, respectively. By sweeping H_{ext} under these two angles $\vartheta_{\text{H,easy}}$ and $\vartheta_{\text{H,hard}}$, magnetic hystereses $\Delta f(H_{\text{ext}})$ can be recorded that contain specific features in the low-field regime characteristic for the progression of the caps' magnetic textures.

The easy axis measurements of both JP types are given in Figure 12.2 e. Both show a typical V-shaped curve with asymptotic behavior at high external magnetic fields as it was also obtained from modeling the DCM response of a single-domain elliptical object in a Stoner-Wohlfarth approach that considers an effective shape anisotropy and the Zeeman energy for E_{m}.[WRB12,GWR16] The asymptotes for large positive and negative magnetic fields are symmetric for the ferromagnetic JP, while they are asymmetric with a difference of 0.9 Hz in Δf_{hf} for $\pm 3.5\,\text{T}$ due to the unidirectional anisotropy in the EB JP. The ferromagnetic JP starts to reverse its magnetization symmetrically on both branches of the reversal at $\pm 20\,\text{mT}$ which is recognizable from the point where $\Delta f(H_{\text{ext}})$ changes its slope from negative to positive in reverse field. Contrastingly for the EB JP, the reversal is initiated at $-44\,\text{mT}$ on the descending branch but at 12 mT on the ascending branch. The easy axis measurements of both JP types are given in Figure 12.2 e. Both show a typical V-shaped curve with asymptotic behavior at high external magnetic fields as it was also obtained from modeling the DCM response of a single-domain elliptical object in a Stoner-Wohlfarth approach that considers an effective shape anisotropy and the Zeeman energy for E_{m}.[WRB12,GWR16] The asymptotes for large positive and negative magnetic fields are symmetric for the ferromagnetic JP, while they are asymmetric

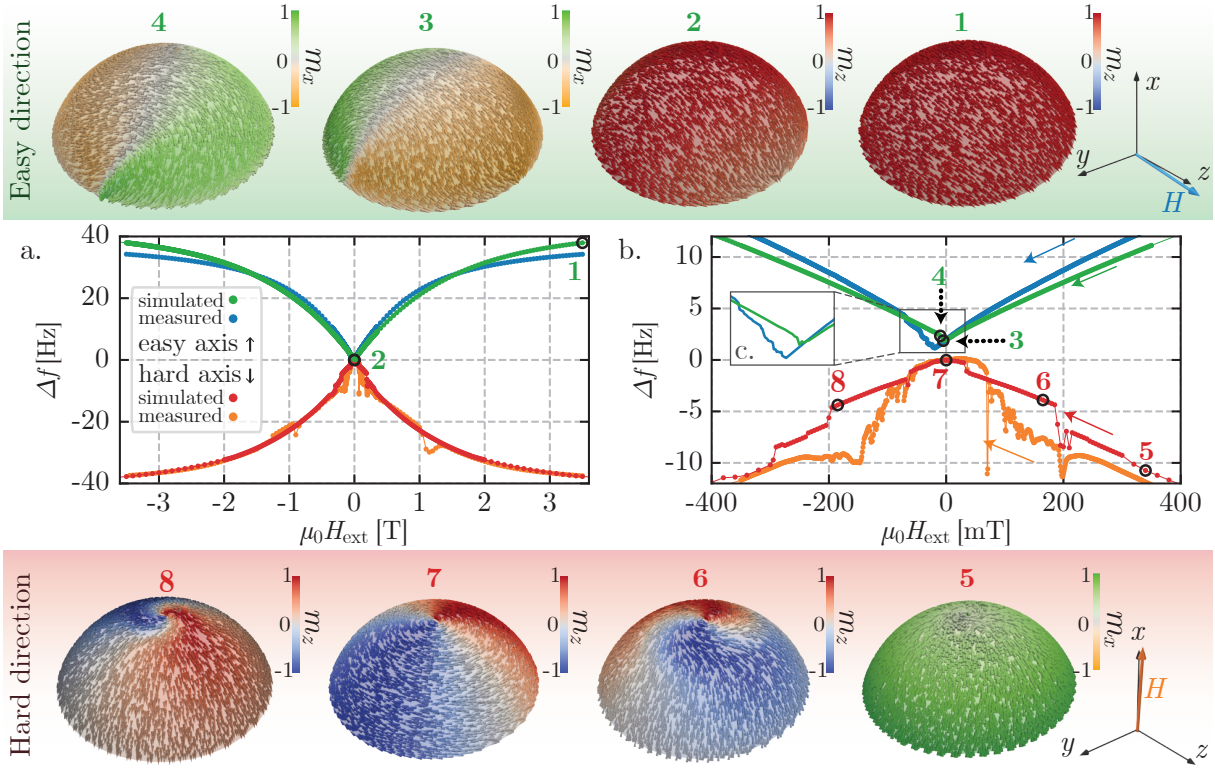

Figure 12.3: Simulated and measured DCM data for both hard and easy axis for a ferromagnetic JP (a.) with detail views on the low-field regime (b. and c.). Above and below, the magnetic configurations are given with numbers indicating the respective fields in a. and b. In b., the easy axis curves have been offset by 2 Hz for visibility reasons. Reused (and adapted) from [PGR21], with the permission of AIP Publishing.

with a difference of 0.9 Hz in Δf_{hf} for ± 3.5 T due to the unidirectional anisotropy in the EB JP. The ferromagnetic JP starts to reverse its magnetization symmetrically on both branches of the reversal at ± 20 mT which is recognizable from the point where $\Delta f(H_{\mathrm{ext}})$ changes its slope from negative to positive in reverse field. Contrastingly for the EB JP, the reversal is initiated at -44 mT on the descending branch but at 12 mT on the ascending branch.

To match the measured data to simulations, the hard and easy axis magnetization reversals of both JPs' caps have been modeled using the finite-element software *Nmag*.[FFB07] Here, the geometry was designed to consider the thickness gradient observable in the FIB image in Figure 7.1 g. Additionally, the discretized mesh of the cap was chosen to be a hemispherical shell truncated from the equator which shall account for the observation from SEM images in Figure 12.2 where the cap is seen to not perfectly cover the particle by half. The width of this 'truncation belt' and the orientation of the particle on the cantilever (azimuthal and polar angle for orientation with respect to the defined coordinate system) were tuned in an iterative process to match the experimental progression of $\Delta f(H_{\mathrm{ext}})$ at high magnetic fields for both layer stacks. This truncation has a change in shape anisotropy and the demagnetization factor as a consequence, because the spherical halfshell in principle gradually approaches a disk shape with increasing truncation width. A detailed description of the adjustment of simulation parameters is found in the supplementary material of Ref. [PGR21].

Ferromagnetically Capped Particle

Starting with the ferromagnetically capped particle, the experimental DCM data is shown alongside the simulated curve for both the easy and the hard direction reversal in Figure 12.3 (forward, descending branch only). For selected magnetic fields, the magnetization textures derived from the simulation are further illustrated. Note that depending on the texture, either the out-of-equatorial-plane component of the magnetization (m_x in this coordinate system, green-yellow) or the in-equatorial-plane component (m_z, red-blue) are indicated by the color coding.

For the easy axis hysteresis (top), most moments remain aligned with the easy direction starting from saturation (1) until remanence, where an onion texture (2) is found. Shortly after remanence, at about $-5\,\mathrm{mT}$ the cap enters a S-state from which it remagnetizes (3 to 4). Although this progression was found during simulations, slight parameter variations resulted in a vortex nucleation rather than the reversal via an S-state. This vortex state is further the cap's energetic ground state with a magnetic energy that is 101 aJ smaller than for the onion state.[PGR21] Hence, it is expected that over time and in the presence of disturbances that the simulations do not consider, the cap relaxes to a vortex state at remanence. In the experimental Δf curve, several kinks are present which are not found in the simulated course (c.f. inset Figure 12.3 c.). These switching events could be an indication for the hopping of the vortex core.[PGR21] A possible reason for the cap not entering a vortex state in the simulation could be that the cell size of the discredited mesh was not chosen small enough and that the steps in the magnetic field are too large around the possible nucleation point.

For the hard axis, the experimental data does not follow a W-shaped course as expected from the Stoner-Wohlfarth approach[PGR21] but an inverted V-shape. This deviation can be explained from the object's curvature due to which the local demagnetization field depends on the polar coordinate. Hence, the field magnitude for which the reorientation of magnetic moments takes place strongly depends on their position within the cap which has the V-shape as a consequence.[PGR21] When studying the simulated hard axis curve and the respective images of the magnetic textures, the moments are seen to rotate towards their local easy direction. In configuration 5, the moments at the top have started to rotate into the zy-plane in order to be locally aligned parallel to the surface and already curl around the cap's center. Contrastingly, the moments in the equatorial region remain aligned with H_ext as this still allows a parallel-to-surface orientation. The vortex texture grows towards smaller magnetic fields (6). At magnetic fields below 300 mT, kinks in Δf indicate the vortex motion, which however already starts below 1.5 T in the experiment, where the vortex is expected to hop from one to another pinning site. At remanence (7), a global vortex state has evolved that again shrinks upon increasing the magnetic field in the inverse direction (8). The alignment of the magnetic moments with H_ext starts from the equator and the vortex has fully vanished at $-1.8\,\mathrm{T}$.

Exchange-biased Capped Particle

Similar DCM hysteresis curves are also obtained for the EB JP, for which the experimental and simulated data of the descending branch is shown in Figure 12.4. Again, the easy axis curve possesses a V-shape, whereas the hard axis loop indicates the inverted V-shaped course.

The remanent state in the easy axis case is an onion state (2), that transitions through an S-state (3) which is accompanied by a rise in Δf visible in the simulated data in Figure 12.4 b. The experimental data similarly indicates only one switching event, which is however located at more negative magnetic fields. This deviation originates from the fact, that the EB is only considered by a unidirectional anisotropy adding a EB shift but not influencing the coercivity. As expected for the EB JP, these switching events are not symmetric around zero field for the two branches like it was for the ferromagnetically capped particle (c.f. Figure 12.2 f.). As a vortex reversal is typically accompanied by smaller switching events (e.g. vortex hopping) like they are observed in Figure 12.3, the reversal is likely consistent with the simulated transition via S-states.

For magnetic fields applied along the hard axis, the moments start to rotate from the H_{ext} axis towards a parallel-to-surface alignment when reducing the magnetic field from saturation. As it was the case for the ferromagnetic JP, a small vortex forms at the JP's top/center at 1.34 T (not shown) which expands when further lowering the field. However, in contrast to the ferromagnetic JP, the vortex is more and more shifted towards one side (4) rather than occupying the full cap. The vortex exits the cap at a magnetic field of 5 mT and hence, an onion state is present in remanence (5). The direction of this onion's net magnetization is parallel to the unidirectional anisotropy. At reverse fields, the cap builds a domain wall (6) that rotates when further sweeping the field towards negative saturation until it is transferred to a vortex state which vanishes at -1.36 T.

It shall be noted that the hard axis DCM curves of experiment and simulation posses both irregularities in the lower field regime that cannot be directly matched. Hence, no clear conclusions on the progression of magnetic states during the hard axis reversal can be drawn except for the remanent state being an onion state which aligns with the EB direction.

Conclusion

As a result, the analysis of hard and easy axis DCM measurements suggests that a ferromagnetically capped particle exhibits a vortex state at remanence, independent of the magnetic field history. The simulations yield a vanishing normalized magnetic moment $M/(M_{\mathrm{S}}V) \approx 0.03$ in the case of the vortex on the hard axis loop and a value of 0.64 for the onion on the easy axis loop, which is however assumed to not be stable.

The EB JP is contrastingly determined to maintain the onion state with a normalized magnetic moment of $M/(M_{\mathrm{S}}V) \approx 0.89$ and 0.71 for the hard and easy direction magnetic history, respectively.

These results clearly indicate that the introduction of EB by an additional antiferromagnetic layer (if thick enough, c.f. Figure 10.1) can stabilize the onion state in magnetic caps up to diameters of at least the here shown 1.5 µm.

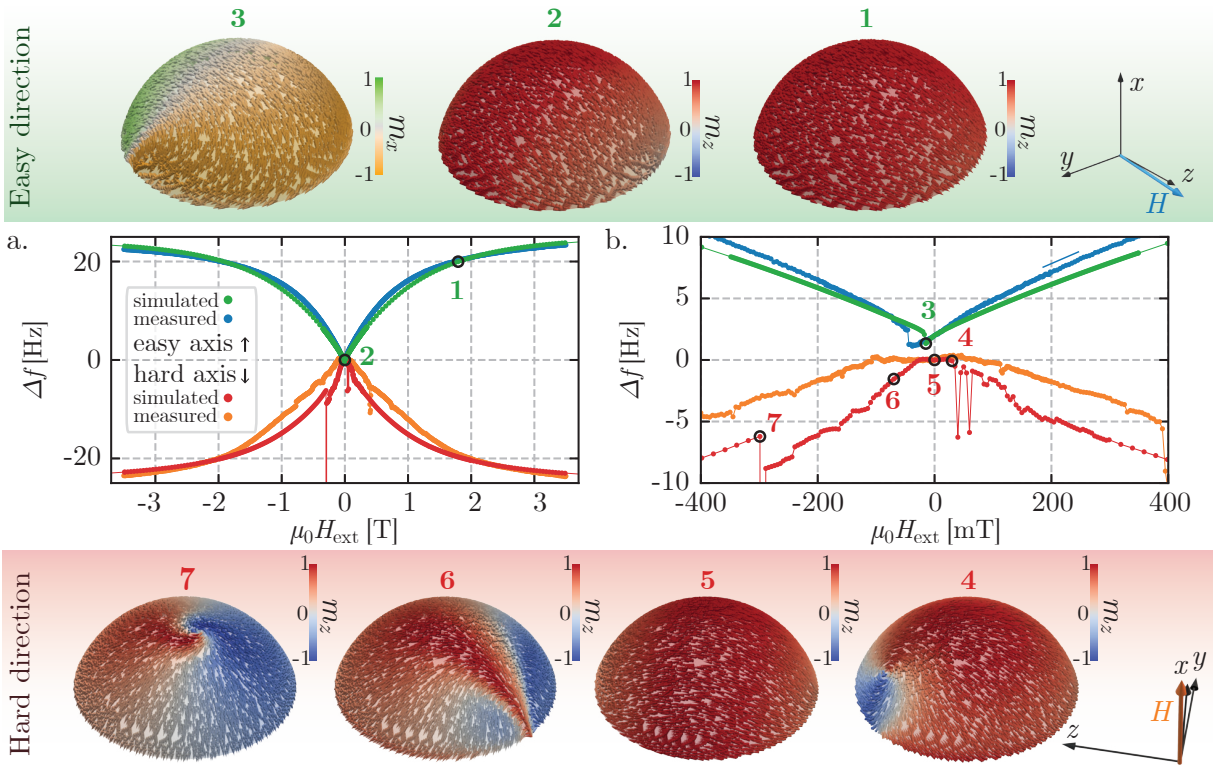

Figure 12.4: Data for EB JP, caption from Figure 12.3 applies. Reused (and adapted) from [PGR21], with the permission of AIP Publishing.

For the usage as magnetic probes in lab-on-a-chip prototypes, superparamagnetic particles are commonly applied.[RLL16] These are magnetized by the presence of an applied field and can consequently be actuated by magnetic force. There are however applications in which a fixed remanent moment may be desired in order to enable the control via magnetic torque by the application of an external magnetic field.[EMS16] EB JPs can be promising candidates which offer this remanent onion state and can therefore be actuated to perform translatory and rotatory motion by magnetic force and torque, respectively.[HRT21] This and other aspects regarding the remote control of magnetic particle motion will be discussed in chapter 13.

13. Microfluidic Application Examples

13.1 Remote-Controlled Transport of Magnetic Particles

The controlled motion of spherical magnetic particles in a microfluidic environment is vastly explored for the design of bioanalytic and diagnostic tools. Generally, these magnetic microparticles are capable to be actuated by a magnetic field $\vec{H}_{\text{eff}}$. The particles' motion - often referred to as magnetophoresis [YES07,LVS17,UMCO20] - is induced by a magnetic force

$$\vec{F}_{\text{m}} = -\mu_0(\vec{m}_{\text{MP}} \cdot \vec{\nabla}) \cdot \vec{H}_{\text{eff}} \tag{13.1.1}$$

which is exerted to the magnetic particle (MP) or bead with a magnetic moment $\vec{m}_{\text{MP}}$. Instead of using magnetic field gradients generated by large laboratory magnets, the use of micromagnetic arrays has been established for lab-on-a-chip applications. [RLL16] Therein, the micro- or nanoparticles are actuated in microfluidic containers or channels on a centimeter-sized chip. A chip with a magnetic substrate can be designed to generate comparably high magnetic field gradients in localized areas emerging from magnetic domains or magnetic microstructures like wires or disks. [RLL16,EKH15] As a consequence, the particles can perform certain functions of a lab-on-a-chip system including, for example, mixing of the fluid for enhanced diffusion, [HLG12] and collecting analyte molecules that specifically interact with a capture molecule immobilized on the particle surface. Based on the particles' remotely-controllable transport, the captured analytes including e.g., proteins, viruses and cells can then be separated from other molecules in the sampled liquid and consequently be guided to a detection area on the chip. For the particles' detection, an important concept to mention relies on magnetoresistive sensor elements. [RMB12]

A transport concept presented by Holzinger *et al.* shall be briefly explained in the following, where superparamagnetic particles are moved due to a dynamic transformation of their magnetic potential energy landscape. [HKB15] For the generation of a magnetic stray field landscape with spatially confined magnetic field gradients, a substrate which is topographically flat but magnetically patterned is utilized. This substrate consists of an EB layer system, which has been engineered using ion bombardment induced magnetic patterning (IBMP) to posses adjacent micrometer wide stripe domains with opposing in-plane magnetization separated by domain walls in a head-to-head and tail-to-tail configuration. [HKB15] For reference, the magnetic stray fields in a plane above the substrate surface are depicted with the according magnetization directions in the domains in Figure 13.2 d. These inhomogeneous magnetic stray fields emerging from the domain walls cause the capture of MPs due to the magnetic force presented by Equation 13.1.1. Superposing these stray fields with periodically changing external magnetic fields dynamically

transforms the MPs' potential energy landscape. In particular, a magnetic field H_z pointing outwards from the substrate plane lifts the energetic degeneracy of the two domain wall types, so that it is energetically preferred for the MP to be located above head-to-head but not above the tail-to-tail domain walls. Inverting H_z subsequently changes the position of the energetic minima to the tail-to-tail domain walls.[HKB15] In order to transport the formed particle rows in a **directed** fashion it is necessary to further transform the effective magnetic field in a way that upon H_z inversion the position of the closest potential energy minimum is reached by a motion in the desired transport direction. For this, the energy minima are slightly displaced from the domain wall position by the help of an additional time-dependent magnetic field H_x. The rows of particles will move into the positive x-direction for an initially positive H_x at their steady-state velocity induced by the magnetic force F_m.[HKB15] As a result, alternating external magnetic field pulses in both $z-$ and $x-$ direction, where $H_x(t)$ is phase-shifted by a quarter period with respect to $H_z(t)$, can be used to realize a step-wise motion of MPs from one domain wall to the next. As the MP's steady-state velocity is determined by the ratio between magnetic force (c.f. Equation 13.1.1) and the drag force according to STOKES' law, there is a critical frequency for the external magnetic field sequence above which the particles cannot follow the laterally shifted energetic minimum in the given time.[HKB15]

Besides the above described mechanism, other transport concepts[WAA10,DDH12,YES07] have been established based on the use of superparamagnetic particles, e.g. particles with a magnetic core and a polymeric shell. These are characterized to have zero magnetic moment in the absence of a magnetic field (on the experimental timescale), and thus, they can only be actuated by a magnetic field because they are simultaneously magnetized by the latter. In the following section, we turn towards the use of anisotropic particles with remanent magnetic moment, i.e. magnetic Janus particles (JPs). These particles are retrieved from the fabrication of magnetically capped particle arrays by a so-called harvesting process, where they are collected from the substrate by mechanical scratching with a pipette and dispersed in distilled water for the subsequent use in microfluidic experiments.

13.2 Motion of Magnetically Capped Janus Particles

Superparamagnetic particles adapt to changes in the orientation of an external magnetic field H_{ext} either by Néel relaxation, i.e. the reorientation of the object's magnetic moments, or by Brownian relaxation, i.e. the physical rotation of the whole particle.[DLS14] Alternatively, both relaxation processes can occur when the time constants for the individual mechanisms are comparable. For EB JPs that have caps with a fixed remanent magnetic moment, Brownian relaxation is the governing mechanism, if H_{ext} is small enough to not induce a magnetization reversal. As a result, a rotating magnetic field can cause the particle to rotate accordingly.[EMS16,Reg18] A rotational JP motion is called synchronous, if the particle rotation frequency $\vec{\omega}$ equals the external magnetic field frequency $\vec{\omega}_{ext}$. This applies if the magnetic torque $\vec{\tau}_M = \vec{m}_{MP} \times \mu_0 \vec{H}_{ext}$ exceeds the viscous torque $\vec{\tau}_D = -8\pi \cdot r^3 \cdot \eta_l \vec{\omega} \cdot b_{corr}$ as shown in Figure 13.1 a. Here, r is the particle radius, η_l the liquid's viscosity, and $b_{corr}(r, z)$ is a distant dependent correction factor for the rotation in the vicinity of a wall, i.e. the bottom of the microfluidic container.[LMK09]

Therefore, EB JPs are rendered to be valuable microprobes for bioassays in which the coupling of a potential analyte causes an increase of the hydrodynamic radius that will clearly affect the particle's motion dynamics. Here, it plays an important role that the viscous torque depends on r^3 while the drag force depends on r. Hence, the rotational motion dynamics of a particle is supposed to be more strongly affected upon the immobilization of analyte molecules to its surface than the translocation. In general, the frequency limit ω_c for a synchronous rotation is determined from balancing τ_M and τ_D:[YBG15]

$$\omega_c = \frac{|\vec{m}_{MP}| \cdot \mu_0 |\vec{H}_{ext}| \mu_0}{8\pi \cdot r^3 \cdot \eta_l \cdot b_{corr}}. \tag{13.2.1}$$

A possible coupling event between analyte and particle thus induces a change in the hydrodynamic radius and further a change of the rotational lag γ or even the loss of synchronization ($\omega < \omega_{ext}$).[Reg18]

Both image series in Figure 13.1 b. and c. were recorded with a high-speed camera in a light microscope setup and depict the rotation of an EB JP with a diameter of 1.5 µm dispersed in water, where the magnetic cap can be identified as the JP's side with darker appearance. The cap is composed of the same layer stack as the EB JP investigated by DCM in section 12.1, i.e. Cu(5 nm)/IrMn(30 nm)/CoFe(10 nm)/Si(10 nm). A quadrupolar electromagnet was used to generate the rotating field with $\mu_0|\vec{H}_{ext}| = 2\,\mathrm{mT}$ by a superposition of two homogeneous magnetic fields $H_{ext} \cdot \hat{y}$ and $H_{ext} \cdot \hat{x}$, both modulated by a cosine function and phase shifted by 90°. The rotational behavior was recorded for the exemplary frequencies $\omega_{ext}/(2\pi) = f_{ext} = 5$ and 45 Hz. From the image sequences it can be seen, that the JP synchronously follows the rotation (with a here unknown phase lag γ) for the small frequency, whereas it performs a tumbling motion for the higher frequency. For this asynchronous case, the JP completes only three full rotations within five periods of the external field rotation, while it rotates back and forth in between. In order to gain quantitative information from the videos, the orientation of the particle cap projected onto the two-dimensional substrate plane has been tracked with the software *Video Spot Tracker*.[Vid] For both experiments, the tracked angle and the frequency derived from the particle's rotational velocity $f_{JP} = 2\pi\omega$ is plotted against the periods of the external magnetic field rotation in Figure 13.1 d. In the synchronous case, the angle and average frequency of the JP coincide with the external magnetic field angle and frequency, respectively. For the asynchronous case, the phase lag is increased over time and the JP's average frequency f_{JP} is smaller than f_{ext}. The previously described tumbling is indicated by the negative values of f_{JP}, which highlights a reciprocating rotational motion.

Besides the described rotational experiments, similar JPs with a diameter of 3 µm were studied in the scope of translatory actuation. Specifically, the transport concept introduced in section 13.1 (Ref. [HKB15]) was applied to EB JPs by Huhnstock *et al.* for a prototypical stripe domain pattern of 5 µm width.[HRT21] In this work, a directed particle transport with comparably high steady-state velocities is demonstrated for EB JPs instead of the superparamagnetic particles that were used in Ref. [HKB15]. From the microscope recordings it was observed, that the JPs' translatory motion during a transportation step towards the neighboring domain wall is accompanied by a rotation. The JP rotates around an axis parallel to the substrate surface

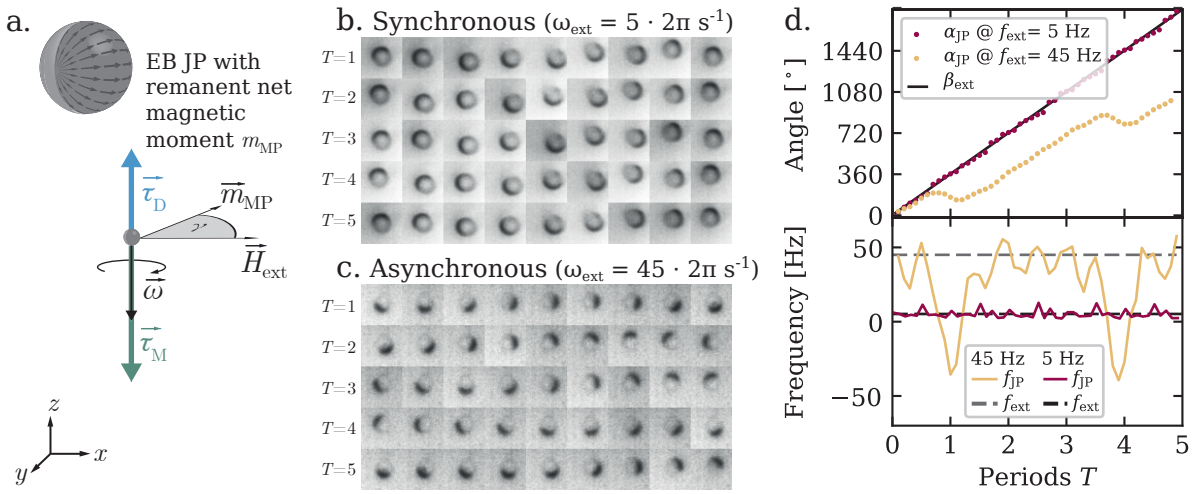

Figure 13.1: The sketch in a. shows the magnetic and viscous torque, $\vec{\tau}_M$ and $\vec{\tau}_D$, respectively, acting on an EB JP in a fluid exposed to a rotating magnetic field in the xy-plane. The JP's net magnetic moment $\vec{m}_{MP}$ in point-dipole approximation is abstracted from the orientation of the onion texture within the thin film cap. The anti-clockwise rotating magnetic field causes an anti-clockwise rotation of the JP with an angular velocity $\vec{\omega}$. The phase lag between the orientation of the cap's magnetic moment and the magnetic field is indicated by the angle γ. The time resolved microscopic data of a EB JP exposed to a rotating magnetic field with $\mu_0|\vec{H}_{ext}| = 2\,\mathrm{mT}$ in b. and c. was recorded for two different rotational frequencies of the external magnetic field $\omega_{ext}/2\pi = 5\,\mathrm{Hz}$ and $45\,\mathrm{Hz}$. The five rows show the evolution of the particle orientation for five successive periods T of the external magnetic field rotation, where each row resembles one field rotation. In d., the tracked angle of the JP's cap orientation is given as a function of full field rotation periods T alongside the extracted frequencies. More information on rotational experiments of Janus particles are presented in the author's master thesis: *Physical Characterization and Motion Dynamics of Exchange-Biased Janus Particles* (2018).[Reg18]

normal upon a sign change in the external magnetic field H_x applied parallel to sample plane. Moreover, it was found that the angular regime spanned by this particle reorientation decreases from 180° to about 45° when the external field pulse frequency is increased. This is the case as the rotational velocity is maintained while the time span for the rotation is effectively reduced before the next inversion in H_z induces the subsequent transport step.[HRT21] Furthermore, the corresponding rotational velocity scales with the strength of the applied magnetic field pulse (H_x).[HRT21] Finally, the authors discuss, how changing the external magnetic pulse frequency and the field amplitude therefore allows to access different motion regimes, where either rotational *or* translatory motion occurs *or* a combination of both motion types.[HRT21]

13.3 Towards Biosensing: Actuating Magnetic Particles in Physiological Media

This section summarizes the article 'Transport Efficiency of Biofunctionalized Magnetic Particles Tailored by Surfactant Concentration' which was prepared during this PhD period. More details on the experimental methods and the theoretical model are given in the original manuscript and the supporting information of Ref. [RHE21] published in 2021 in *Langmuir*.

In realistic lab-on-a-chip applications, biomolecular target molecules like antigens shall be captured by surface-functionalized magnetic particles.[WAA10] For this, a suitable recognition molecule, e.g. an antibody, that specifically and sensitively interacts with the analyte molecule is immobilized to the particle surface by a biochemical coupling reaction.[EKH15] A transportation mechanism like the one introduced in the previous section can therefore be used to guide the functionalized particle towards a chip area with a sample of a human body fluid (e.g. urine or blood) from where the analyte molecule is captured. Subsequently, the particle - including the captured molecule - is transported to a detection unit on this chip.

The prototype concepts for magnetic particle actuation have been typically developed for pure water as the particles' liquid environment,[YES07,HKB15,DTK11,EKH15] however, proteins functionalized to a particle surface would denaturate therein, hence, loosing their functionality. Instead, physiological liquids, i.e. buffered solutions, are required as dispersion media, because they preserve the correct structure of the protein and consequently its function. Nevertheless, the physical properties of these fluids like the viscosity, permittivity, the ionic strength, and consequently a surface's electrochemical potential differ from those of pure water. The hereby affected surface forces are therefore mediated by the choice of the dispersion medium. This consideration becomes especially crucial when particles are supposed to be actuated close to a substrate surface. The dispersion medium is not only a passive carrier liquid for the particles but influences their colloidal stability and their surface sticking probability. The equilibrium distances between two particles and between a particle and substrate are determined by the balance of acting forces. In order to derive the steady-state distance of a particle, surface forces, buoyancy, gravitation, and magnetic forces have to be taken into account. As a result, the properties mediating these forces must be investigated carefully in order to realize the particles' transport and avoid particle agglomeration and their adsorption to the substrate surface.

Regardless of the type of magnetic particle used in microfluidics, the development of a corresponding biosensing device based on the here presented transport concept must ensure three factors, that are:

1. The biomolecules of interest (both analyte and immobilized capture molecule) need to be stable during the process in the respective liquid medium.

2. The magnetic particles shall not agglomerate or stick to the underlying substrate in this medium, so that...

3. ... the number of mobile particles is maximized for an efficient transportation. Tracking the motion of *many* particles in parallel is desired in a biosensor in order to gain statistically sound results from a sufficiently large data set.

As a consequence, any biofunctionalized magnetic particle (BMP) transport needs to be optimized in the sense that parameter spaces have to be determined for the respective liquid medium. Experimentally, agglomeration and sticking was found to be minimized by the help of surfactants, which are added in a specific concentration and affect the surface forces.[OB17,GRF05,JGB10] Based on these observations, a prototype system shown in Figure 13.2 a. with GFP-functionalized superparamagnetic particles was developed. After the biochemical coupling protocol was found

for the immobilization of green fluorescent protein (GFP) to the particle surface, the transport of the acquired BMP was studied under variation of the concentration of an additional surfactant. Here, the anionic surfactant sodium dodecyl sulfate (SDS), for which data are well available,[SRS12,KWR17,SA09] was used during the particle transport in phosphate buffered saline (PBS). The particle's directed transport was achieved by the dynamic transformation of their magnetic potential energy landscape based on the concept described in Ref. [HKB15] (c.f. section 13.1). The experimental setup including the microfluidic chamber, Helmholtz coils for the generation of the external magnetic field and the microscopic unit is described along with the biochemical coupling protocol for the immobilization of GFP in the methods section of Ref. [RHE21] . Based on the above concept, the cited publication presents average BMP transport velocities in dependence of SDS concentration, where data from transport experiments is compared to velocities derived via a theoretical model. In addition, the remaining fluorescence has been monitored over timescales of days as a measure for the stability of the protein's function.

The mentioned model predicts BMP trajectories for the described stepwise transport and considers multiple factors affecting the BMP: The effective magnetic field $\vec{H}_{\mathrm{eff}}$ as a superposition of the sample's magnetic stray field landscape and the externally applied field pulses, the surfactant's influence on the viscous properties of the liquid and the surface forces determining the particle substrate separation. The distance dependent magnetic stray fields shown in Figure 13.2 d. were calculated from magnetization patterns simulated with the object oriented micromagnetic framework (OOMMF). The steady state-distances z'_{BMP} shown in Figure 13.3 b. were determined from the balance of the magnetic force $F_{\mathrm{m}}(z)$ and the surface forces, i.e. the electrostatic force $F_{\mathrm{el}}(z')$ and the van der Waals force $F_{\mathrm{vdW}}(z')$, for a BMP positioned above a domain wall. As the electrostatic force depends on the ionic strength of the liquid and the zeta potential of the two interacting surfaces (BMP and substrate), its distant dependent course changes when using PBS instead of water. The surfactant SDS further influences the zeta potential where the concentration dependence is shown in Figure 13.3 a. Moreover, the addition of SDS affects the liquid viscosity η_{l} shown in Figure 13.3 c. which was determined by a linear fit from the experimental data of Ref. [KWR17].

By balancing the magnetic force $F_{\mathrm{m}}(x, z_{\mathrm{b}})$ and the opposing drag force $F_{\mathrm{d}}(x, z'_{\mathrm{b}})$ at a given time t, the momentary steady-state velocity of a BMP

$$\vec{v}_{\mathrm{BMP}}(x, z', t) = -\frac{\mu_0(\vec{m}_{\mathrm{BMP}}(x, z, t) \cdot \vec{\nabla}) \cdot \vec{H}_{\mathrm{eff}}(x, z, t)}{6 \cdot \pi \cdot r \cdot \eta_{\mathrm{l}} \cdot f_{\mathrm{d}}(z')} \tag{13.3.1}$$

can be calculated in dependence of its lateral position x with respect to the micromagnetic pattern under consideration of the steady-state separation z'_{BMP}.[WSFX05,HKB15] Here, r is the BMP radius, f_{d} is a distance-dependent drag force coefficient,[WSFX05] and $\vec{m}_{\mathrm{BMP}}$ is the particle's magnetic moment which can be calculated in point-dipole approximation (Ref. [RHE21] Suppl. Info.).[YKK04] Based on Equation 13.3.1, the step-like trajectories of BMP are constructed by calculating the momentary velocity at each time interval ($\Delta t = 10\,\mu\mathrm{s}$) of the simulation as

$$x_{\mathrm{BMP}}(t_{i+1}) = x_{\mathrm{BMP}}(t_i) + \vec{v}_{\mathrm{BMP}}(x_{\mathrm{BMP},i}, z', t_i) \cdot \Delta t + x_{\mathrm{rw}} \tag{13.3.2}$$

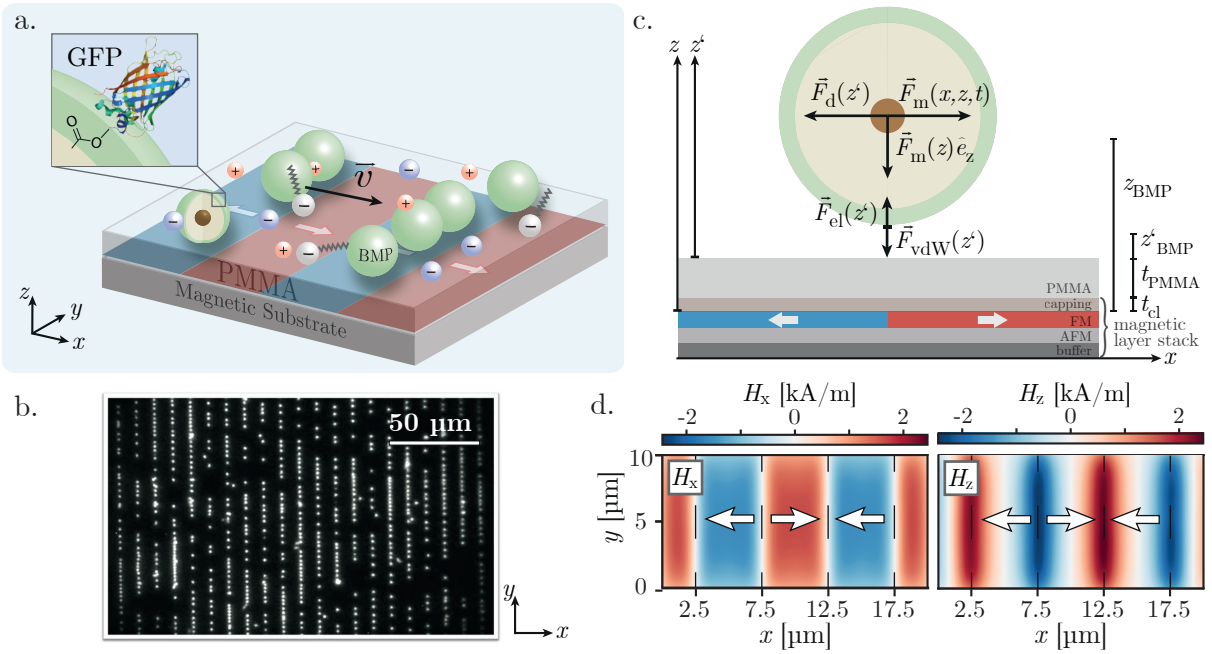

Figure 13.2: a. Sketch of the prototype system for the investigation of the transport of superparamagnetic core-shell particles with biochemically immobilized green fluorescent protein (GFP), not drawn to scale. The substrate consists of a parallel stripe magnetic domain pattern with opposing magnetizations in adjacent domains (5 µm width) covered by a polymeric spacer layer (PMMA) with the thickness $t_{\mathrm{PMMA}} = 700\,\mathrm{nm}$. The liquid environment of the particle is a physiological buffer (indicated by red and blue ions +/-) to guarantee protein stability, while the colloidal stability is realized via specific concentrations of the surfactant sodium dodecyl sulfate (DS- is indicated with zig-zag alkyl chains). b. Frame of a transport video recorded with a fluorescence microscope indicating the fluorescent BMPs in rows aligned parallel to the substrate's domain walls. c. Relevant forces on a BMP (GFP surface in light green and magnetic core in brown) for the theoretical description. Along the vertical axis, the electrostatic ($F_{\mathrm{el}}(z')$), van der Waals ($F_{\mathrm{vdW}}(z')$) and magnetic force ($\vec{F}_{\mathrm{m}}(z)\hat{e}_{\mathrm{z}}$) are indicated, from the balance of which the stationary distance is derived. The distance dependent forces determining the particle velocity are pointing horizontally: the drag force ($\vec{F}_{\mathrm{d}}(z')$) and the time and position dependent magnetic force ($\vec{F}_{\mathrm{m}}(x,z,t)$) which actuates the BMP. The magnetic substrate consists of a buffer layer, an EB bilayer and a capping layer of the thickness t_{cl}. Please note the relation between the distance z' to the surface and the distance to the ferromagnetic layer, $z = r + z' + t_{\mathrm{cl}} + t_{\mathrm{PMMA}}$. d. The magnetic stray field components H_{x} and H_{z} in the xy-plane were computed at z_{BMP}=1.328 µm above the EB stripe array (steady-state distance z_{BMP} in PBS with $c_{\mathrm{SDS}} = 1$ w%). Domain walls are drawn as dashed black lines and white arrows refer to the magnetization directions. Adapted and reprinted with permission from Reginka *et al.*, Langmuir **37** (2021).[RHE21] Copyright 2021 American Chemical Society.

with the distance x_{rw} accounting for the particle's Brownian motion.

To gain comparable velocities from the simulated and experimental trajectories, mean step velocities were extracted for both. Due to the quality of the particles' positional data which was determined from microscope recordings via the tracking software *AdaPT* [DHK21], the momentary particle velocities from the derivatives of the x-trajectory were too noisy for an adequate analysis. Instead, a Gaussian error function was fitted to each step of the trajectory $x(t)$. From the function's derivative, the mean step velocity $\overline{v}_{\mathrm{BMP}}$ was deduced, which is plotted in Figure 13.3 e. for both the experimental and the simulated trajectories.

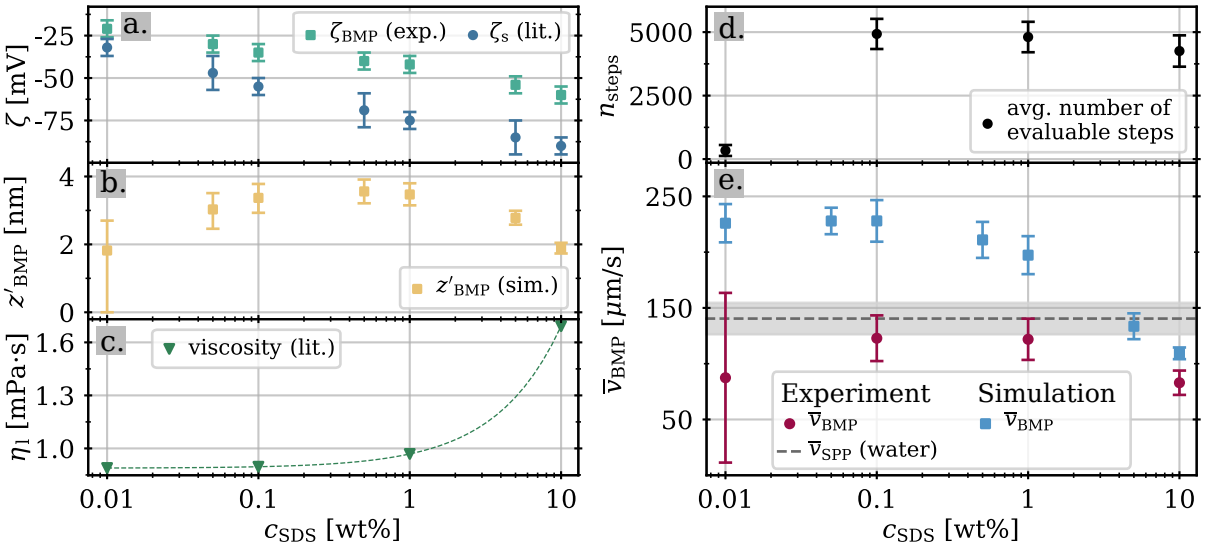

Figure 13.3: Dependence of the BMP transport on the surfactant concentration c_{SDS}. The zeta potential values ζ_{s} of the PMMA substrate are taken from [KWR17] while the values for the prepared BMPs ζ_{BMP} were experimentally obtained by dynamic light scattering. The model yields steady-state separations z'_{BMP} between the substrate surface and the BMPs via the balancing of the considered forces (b.). The SDS concentration dependent progression of the viscosity η_{l} in c. is taken from [KWR17]. The average number of steps n_{steps} in d. describes how many transport steps were successfully evaluable from the transport videos. In e., experimentally and theoretically determined values of the mean step velocities $\overline{v}_{\mathrm{BMP}}$ during BMP transport at room temperature are given. The average step velocity of plain superparamagnetic particles (SPP) dispersed in water (no PBS, no SDS) is given as a reference. Adapted and reprinted with permission from Reginka *et al.*, Langmuir **37** (2021). [RHE21] Copyright 2021 American Chemical Society.

From the interplay of attractive and repulsive forces, the steady-state distance z'_{BMP} determined by the model are displayed in Figure 13.3 b. for BMPs immersed in phosphate buffered saline (PBS) under variation of the surfactant concentration ($c_{\mathrm{SDS}} = [0, 0.01, 0.1, 1, 10]$ w%). While the averaged steady-state separation of the plain particle and a PMMA surface in water was retrieved to be z'_{P} =148.5 nm within the error margins [0, 309] nm, the model reveals a much smaller distance between a BMP in PBS, i.e. z'_{BMP} =1.3 nm within the error margins of [0,2.3] nm. As the typical surface roughness of spin coated PMMA was experimentally determined to be larger than this value, [Sem07] the particles will likely stick to the PMMA surface. The reduced distance when switching to the BMP-PBS system is related to the reduction of the absolute zeta potential of a BMP in PBS with $\zeta = -15\,\mathrm{mV}$ as compared to a plain particle in water with $\zeta = -69\,\mathrm{mV}$. The PMMA surface shows a zeta potential ζ_{s} of $-35\,\mathrm{mV}$ in water and of $-32\,\mathrm{mV}$ in PBS. [KWR17] Hence, the BMP in PBS experiences less electrostatic repulsion from the PMMA surface than the plain particle in water because the ions in the buffer shield the surfaces electrochemically. This theoretical consideration explains why plain particles in water were identified as mobile and showed transport velocities up to 223 µm/s in the experiment, while biofunctionalized particles could not be actuated at all in PBS.

To prevent the BMPs from being adhered to the PMMA surface, SDS was added in different

concentrations ($c_{\mathrm{SDS}} = [0, 0.01, 0.1, 1, 10]$ w%), which increases the surfaces' negative charge density and thereby both zeta potentials are reduced for increased surfactant concentration as shown in Figure 13.3 a. Consequently, the attractive and repulsive forces acting on the BMPs are balanced at larger distances as depicted in Figure 13.3 b. However, this increase is only observed for c_{SDS} up to 0.5 w%, whereas z'_{BMP} drops for higher concentrations which is related to an increase of the solutions' ionic strength. Subsequently, the values of z'_{BMP} derived from the model were used to compute the particles' step velocity during the transport. In Figure 13.3 e., the simulated mean step velocities $\overline{v}_{\mathrm{BMP}}$ are presented as a function of the SDS concentration alongside the experimentally determined values. As an additional measure for the transport efficiency, the number of evaluable transport steps n_{steps} was averaged over all videos recorded for the respective SDS concentration and is shown in Figure 13.3 d. (10 to 14 videos per concentration).

Next, the resulting transport velocities and the values of n_{steps} under addition of SDS shall be discussed:
For a BMP in PBS at 0.01 w% SDS, a steady-state distance of $z'_{\mathrm{BMP}} = 1.8$ nm (error margins [0,2.7] nm) was theoretically obtained which subsequently results in a simulated velocity of around 223 µm/s. This value is however expected to be unrealistically high, because the lower error margin of z'_{BMP} is zero speaking for an adhered particle and because the surface roughness of spin coated PMMA [Sem07] is expected to be larger than the distance of 1.8 nm. This explains why the majority of BMPs was not seen to be mobile in the experiments as the number of successfully evaluated steps corroborates. Increasing c_{SDS} causes larger steady-state distances so that less sticking occurs. For concentrations between 0.1 and 10 w%, the average number of evaluable steps is independent of c_{SDS} considering the margins of uncertainty, but it is overall enhanced compared to 0.01 w% SDS. A side effect of this enhanced transport efficiency for $c_{\mathrm{SDS}} > 0.01$ w% are the reduced margins of uncertainty for the experimental velocities which are evaluated from more mobile particles.
In general, the simulated velocities seem to be overpredicted when compared to the experiment. Possible reasons for this are discussed in Ref. [RHE21] and include the systematic overestimation of the magnetic force based on the micromagnetic simulation of the EB stripe array.
Despite this overestimation, the trend of the velocities is qualitatively described by the model: The theoretical velocity drops from 226 to 195 µm/s when increasing c_{SDS} from 0.1 to 1 w%. On the one hand, this is due to the higher separation and thus a reduced magnetic force actuating the particle. On the other hand, the drag force on the BMP increases because a higher SDS concentration enhances the liquid's viscosity [KWR17] as illustrated in Figure 13.3 c. Although the distance between BMP and the substrate's magnetic layer again decreased at c_{SDS} =10 w%, the even more strongly enhanced viscosity causes the reduction of the calculated step velocity down to 108 µm/s. This effect is also well visible in the experimental result.

Overall, with the above described prototype system of an EB stripe patterned substrate, GFP functionalized superparamagnetic particles and a liquid environment based on PBS and SDS, an optimized transport efficiency and mean step velocities of up to 123 µm/s were accomplished for an SDS concentration between 0.1 and 1 w%. With the addition of SDS to the physiologic

buffer solution, the BMP's velocities are comparable to the velocity of plain superparamagnetic particles dispersed in water which was experimentally determined to be $\overline{v}_{\mathrm{SPP}} = (140 \pm 14)\,\mu\mathrm{m/s}$ for the same substrate and the same external magnetic field sequence. Furthermore, the BMP were stored in the PBS-SDS solutions over the timescale of 8 days during which transport experiments were performed repeatedly under a fluorescence microscope in order to investigate the fluorescence of the GFP immobilized to the particles' surface. Although SDS is a prominent surfactant for the denaturation of proteins,[LTM11] the GFP function remained intact as visible by its fluorescence throughout all transport experiments regardless of the SDS concentration and the storage time. This protein stability can be accounted to an entropic effect based on the immobilization itself preventing the protein's unfolding/denaturation.[KRP08]
The findings of this study can be transferred when an actual analyte shall be captured from the solution by a capture molecule (e.g. an antibody) that is immobilized to the particle surface. However, expecting the same transportation yield for a different surface functionalization than the here presented GFP-functionalization can be misleading. For such a more realistic biosensing concept, it is inevitable to optimize the biofunctionalized particles' properties and the properties of the liquid medium simultaneously in order to adjust the transport characteristics.

13.4 Outlook

Combining the insights collected from section 13.2 and section 13.3 will allow to design a microfluidic transport experiment in which a magnetic JP with a biofunctionalized surface performs both translatory and rotatory motion based on the transport concept of dynamically altered magnetic field landscapes. In order to achieve this, a biochemical coupling protocol needs to be found in which a biomolecule like an antibody is covalently bound to, e.g., the the non-magnetic side of the fabricated JPs' surface. Using templating particles with a COOH-functionalization on their surface will likely enable the immobilization of GFP other proteins in a similar coupling protocol as the one presented in Ref. [RHE21].

Again, a strategy will need to be found for the adjustment of the JP-substrate distance in order to avoid surface sticking for several reasons: Due to the JPs remanent magnetic moment, the magnetic forces are different as in the case of superparamagnetic particles. Another reason is, that the JPs have a different (so far higher) mass and a center-of-mass deviating from the geometrical center[HRT21] which causes a changed influence of gravitation. Additionally, the metallic surface properties and consequently the surface forces are expected to differ from the here studied case of fully surface-functionalized particles.

Finally, for each set of binding partners, i.e., target and capture molecule, the transport concept must meet their requirements for the liquid environment. Consequently, the transport must be tuned according to the particle-substrate spacing and transport efficiency based on the choice of materials and liquids.

14. Summary and Conclusion

Within the last decade, significant attraction has been drawn to magnetic objects of curvilinear, or more specifically circular, tubular or spherical geometry. Magnetic caps, i.e. thin magnetic films that adopt the shape of a hollow hemisphere, are showpieces in this field of research, as they can be easily fabricated by thin film deposition onto self-assembled spherical microparticles. With a focus on in-plane magnetized films, this thesis explores not only ferromagnetic but also exchange-biased hemispherical caps. In general, the exchange bias is an interface effect that expresses itself as an additional unidirectional magnetic anisotropy in a thin ferromagnetic film that is in contact with an antiferromagnetic layer. In order to study this phenomenon, which is well known from planar extended thin film systems, in the scope of curved magnetic films, the refinement of existing and the development of new fabrication and characterization routes is inevitable. Aside of these technical aspects, the thesis at hand delivers insights into the magnetic textures and the magnetization reversal mechanisms of mainly magnetic cap arrays, but also of individual caps. A strong focus is put on the impact of the participating layers' thicknesses and post-fabrication annealing techniques on the caps' magnetic characteristics. Thereby, it is intended to investigate how the magnetic textures expressed by the caps can be deliberately tailored *during* as well as modified *after* fabrication.

The thesis opens with an introduction to general **fundamentals of magnetism** including a description of the exchange bias effect in chapter 2, followed by a summary of the current state of research regarding **magnetism in circular and spherical geometries**, i.e. disks and caps, in chapter 3. Here, micromagnetic simulations have been added to communicate the commonly observed magnetic textures, namely vortex and onion, within individual disks or caps and the important principles of their remagnetization. Chapter 4 dives deeper into the **micromagnetic modeling** of individual ferromagnetic caps and those arranged in a hexagonal lattice, where the latter are experimentally more easily accessible than individual or deliberately distributed caps. This theoretical perspective revealed severe differences in the behavior of individual caps and those in an array, as the latter have shown to stabilize magnetic onion textures and thereby prevent vortex formation due to magnetostatic coupling. Additionally, the simulations indicate a dependence of the cap array's magnetization reversal on the angle between the lattice symmetry and the externally applied magnetic field. This led to the conclusion that measurements of realistic samples which contain a variety of orientations and even defects or a distribution of cap sizes are expected to similarly reveal a distribution of macroscopic magnetic properties. How realistic samples for this thesis have been experimentally prepared in a combination of a self-assembly process for the templating spheres and sputter deposition of the selected layer

systems, is described in the **fabrication** protocol in chapter 5. Subsequently, the utilized **characterization techniques** are introduced in chapter 6, differentiating between structural and magnetic methods where the latter include Kerr magnetometry and photoemission electron microscopy with magnetic contrast obtained from X-ray magnetic circular dichroism.

In order to visualize the **structural morphology** of both the overall sample and the individual caps, chapter 7 is dedicated to images recorded by light, scanning electron and helium ion microscopy. As the resolution of the acquired helium ion micrographs was sufficient to resolve the granular structure of the exchange-biased layer system deposited onto the spheres, a thorough grain size analysis is presented. Based on the retrieved grain size distributions, conclusions about the layer growth could be drawn that allowed for the formulation of two major assumptions: Firstly, the structural nature of the curved film is in agreement with a study on planar systems of similar composition presented in literature for which reason it can be expected that the magnetic properties of both species, caps and extended films, follow similar rules connected to the antiferromagnetic layer's granular structure. Secondly, the results suggest a perpendicular-to-surface growth. Thus, it can be hypothesized that the exchange bias and the associated unidirectional magnetic anisotropy - as a local, microscopic property mediated by exchange coupling between interfacial ferromagnetic and antiferromagnetic moments - does not point strictly parallel to the substrate plane, but follows the curved surface of the cap.

Before the investigations regarding the magnetic properties of cap arrays are presented, chapter 8 discusses important **practical aspects** that need to be taken into account for the interpretation of magneto-optical measurements. Building on these technical considerations, the analysis of the **remagnetization of ferromagnetic cap arrays** is presented in chapter 9, where easy axis hysteresis loops are assigned specific magnetization reversal paths in dependence on the ferromagnetic layer thickness. This classification into different remagnetization phases is underpinned by the study of so-called magnetic *fingerprint* diagrams determined from measured sets of first-order reversal curves (FORC). Next, the **remagnetization of exchange-biased cap arrays** is studied in dependence on both the ferromagnetic and the antiferromagnetic layer thickness in chapter 10. After a brief analysis of the reversal behavior in dependence on the measurement angle, mainly easy axis hysteresis loops have been investigated. From these, especially the macroscopic magnetic quantities with a focus on the exchange bias shift and the coercive field are compared for the flat, extended layer system and the system deposited on the particle array. The results evidence that an additional unidirectional anisotropy can successfully be introduced to a ferromagnetic cap when it is in direct contact to an antiferromagnetic layer. Further, they indicate that the ferromagnetic thickness affects not only the demagnetization energy of the caps' magnetic states and consequently the energetic preference of either the vortex or the onion texture, but also determines the strength of the exchange bias as it is well known from planar bilayers.[MB57,MKS87,RZ07] These actually competing effects are further studied with regard to annealing in the presence or the absence of an external magnetic field, i.e. field cooling. While it is found that field cooling stabilizes the onion texture in the magnetic caps, zero field cooling results in the imprinting of a circular EB and therefore stabilizes the vortex state instead. Ensembles of exchange-biased caps with different thicknesses of the participating layers were further analyzed in the scope of the FORC formalism where the extracted fingerprints provide

information on the distribution of magnetic properties such as coercive and nucleation fields for those arrays that reverse via the formation of vortices. As FORC distributions offer information on the degree of reversibility of certain remagnetization events like the nucleation of a vortex, it was possible to differentiate between two modes of *viscous* and simply *biased* reversal in dependence on the antiferromagnetic film thickness. Interestingly, the FORC diagram of one specific cap array ($t_F = 10\,nm$ and $t_{AF} = 30\,nm$) also exhibited a mixture of reversal paths, which indicates that delicate changes in the individual caps' geometry and their local neighborhood situation can affect their remagnetization process as it was partly suggested by the previously conducted micromagnetic simulations (cf. chapter 4). In this context, the advantages of the FORC method are elaborated as the described observations would not have been detected from a simple major loop analysis. As a complementing approach to investigate the presence of different magnetic textures in arrays of exchange-biased caps with different ferromagnetic thicknesses, images of the magnetic contrast were recorded with a photoemssion electron microscope (PEEM) by exploiting the X-ray magnetic circular dichroism (XMCD). Differences in the images recorded at remanence after positive and negative saturation reveal the nature of exchange bias. Moreover, the observation that vortex reversing caps tend to remagnetize with a fixed circulation sense was reasoned by the following hypothesis: Thermally unstable antiferromagnetic grains viscously adopt the magnetization configuration within the ferromagnetic layer during its reversal and remain in a partly curled state which subsequently predetermines the circulation sense of the vortex which re-nucleates in the ferromagnetic layer.

Intended as a practical guidance for **anisotropy engineering** in magnetic cap arrays, chapter 11 compares how the choice of ferromagnetic material, the presence of a magnetic field during deposition, the introduction of exchange bias, and possible post-fabrication annealing procedures affect the caps' reversal paths, the magnetic field range for the reversal, and the occupied magnetic states at remanence.

In order to shed light onto the behavior of **individual magnetic caps**, chapter 12 shortly presents exemplary XMCD PEEM images of non-arranged exchange-biased caps. In addition, the results of a study utilizing the method of dynamic cantilever magnetometry are summarized, where the magnetization reversal of a ferromagnetic and an exchange-biased capped particle are compared in close correlation with micromagnetic simulations. Heading towards possible applications, these individual magnetically capped particles can be collected from a sample and dispensed in a liquid, e.g. water, so that they - as magnetic Janus particles - can be utilized as magnetic probes or carriers in microfluidic experiments. Therefore, chapter 13 serves as an outlook for the use of magnetically functionalized particles in **microfluidic applications**, where actuation concepts for both Janus particles and superparamagnetic beads are presented. The thesis closes with a study that investigates how the transport efficiency of superparamagnetic beads in a physiological buffer liquid can be tuned with the help of a surfactant. Also for magnetic Janus or other magnetic particles, the thereby gained insights are transferable when similar magnetic probes shall be employed in a physiological environment for the detection of biologically relevant molecules in future lab-on-a-chip devices.

Both general key aspects regarding magnetic hollow hemispheres and the major conclusions drawn from the investigations of the present thesis are summarized in the following:

- ▷ Regarding magnetic characterization, the use of complementary methods is inevitable when studying micro- or nanostructured magnetic systems such as partly irregular arrays of magnetic caps. Inspecting the magnetization reversal of cap arrays - possibly also in dependence on the measurement angle - necessitates the thorough structural characterization of the probed sample region. Apart of integral methods for hysteresis measurements, other techniques should be taken into consideration that allow to spatially resolve the microscopic magnetization textures and to retrieve how the magnetic properties of the ensemble are generally distributed. In this thesis, the collected set of methods contained the visualization of magnetic states of individual caps in an array by XMCD PEEM images and the analysis of the magnetic properties' distributions by the FORC formalism.

- ▷ There is a set of magnetization textures that can be exhibited by magnetic caps: The most prominent ones are the vortex and the onion texture, while *S*- and *C*- states can form as transition textures. The two main routes along which a cap remagnetizes are the *rotation of an onion state* and the *nucleation, motion and eventual annihilation of a vortex*.

- ▷ Investigating three-dimensional and especially curved magnetic objects demands to build up an understanding of the prevailing contributions of the system's free energy. In the case of magnetic caps, the remagnetization route and the exhibited textures depend on the demagnetization energy determined by the cap geometry in the first place. In the present thesis, this is mainly studied by the variation of the ferromagnetic layer's thickness, while literature reports that also the radius of the templating particle crucially influences these characteristics.[SKR16,BRG13] Additionally, inter-particle magnetostatic and exchange coupling affect a cap's magnetic state when it is situated in an array. This has been estimated to some extent in chapter 4 with the help of micromagnetic simulations and in subsection 10.2.3 by the analysis of remanent vortex circulation patterns recorded with XMCD PEEM.

- ▷ When comparing the exchange-biased caps for a sufficiently thick antiferromagnetic layer to their purely ferromagnetic counterparts, the exchange bias effect mainly shifts the hysteresis but does *not* change the caps' reversal path itself. Nevertheless, it has been evidenced that the interface effect can be exploited to manipulate the caps' remanent states. Specifically, a post-deposition annealing process in the presence or in the absence of an external magnetic field promotes onion or vortex states in remanence, respectively.

- ▷ The exchange bias shift as a macroscopic magnetic quantity that can be extracted from measured hysteresis loops was found to be rather independent on the structural aspect of the films' curved modulation on the array of particles, as its ferromagnetic thickness dependence presented in chapter 10 is comparable with the one of the flat and extended exchange-biased bilayers. Moreover, the structural analysis of the caps' surface in chapter 7 led to the conclusion that the antiferromagnetic grain size distribution is comparable for both the flat and the curved film which in turn reasons that also curved exchange bias

systems can be interpreted in the context of the established models describing flat polycrystalline systems. Therein, the prevailing exchange-bias-related anisotropies, namely the fixed unidirectional and the time-dependent rotational magnetic anisotropy, are connected with the number of thermally stable and thermally unstable grains in the granular antiferromagnet.[MGM16,MHR20] It has been found that the antiferromagnetic layer's thickness significantly affects the type of reversal in exchange-biased cap arrays generally remagnetization via vortex formation, as the ratio between thermally stable and unstable grains can be tuned by scaling the grains' height under the assumption of columnar grain growth for the utilized set of deposition parameters.[MRH22] Similar to observations regarding the viscous behavior of flat bilayers,[MHR21]the remagnetization modes of unbiased, viscous as well as biased vortex reversal could be deliberately addressed by the choice of the antiferromagnetic layer thickness (cf. section 10.3).

Throughout this thesis, experimental parameter ranges were presented in which the properties of magnetic caps can be tailored at room temperature based on the templating particles' size, the layers' thicknesses, the ferromagnetic material, the introduction of exchange bias, and post-deposition treatments. Based on this tool box, it will be possible to identify routes to engineer the remagnetization paths as well as the magnetic textures exhibited by magnetic caps, or other three-dimensional curved nanostructures.

Publications

1. M. Mirzaee-Kakhki, A. Ernst, D. de las Heras, M. Urbaniak, F. Stobiecki, A. Tomiţa, R. Huhnstock, I. Koch, J. Gördes, A. Ehresmann, D. Holzinger, **M. Reginka** and T. M. Fischer: *Colloidal trains*
   Soft Matter **16** 1594-1598 (2020)
   https://doi.org/10.1039/C9SM02261A

2. Ł. Frąckowiak, P. Kuświk, G.D., Chaves-O'Flynn, M. Urbaniak, M. Matczak, P.P. Michałowski, A. Maziewski, **M. Reginka**, A. Ehresmann and F. Stobiecki: *Magnetic Domains without Domain Walls: A Unique Effect of He+ Ion Bombardment in Ferrimagnetic Tb/Co Films*
   Physical Review Letters **124** 047203 (2020)
   https://doi.org/10.1103/PhysRevLett.124.047203

3. M. Merkel, R. Huhnstock, **M. Reginka**, D. Holzinger, M. Vogel, J. Zehner, and K. Leistner and A. Ehresmann: *Interrelation between polycrystalline structure and time-dependent magnetic anisotropies in exchange-biased bilayers*
   Physical Review B **102** 144421 (2020)
   https://link.aps.org/doi/10.1103/PhysRevB.102.144421

4. M. Mirzaee-Kakhki, A. Ernst, D. de las Heras, M. Urbaniak, F. Stobiecki, J. Gördes, **M. Reginka**, A. Ehresmann and T. M. Fischer: *Simultaneous polydirectional transport of colloidal bipeds*
   Nature Communications **11** 4670 (2020)
   https://doi.org/10.1038/s41467-020-18467-9

5. A. Tomiţa, **M. Reginka**, R. Huhnstock, M. Merkel, D. Holzinger, and A. Ehresmann: *Magnetic textures in hemispherical thin film caps with in-plane exchange bias*
   Journal of Applied Physics **129** 015305 (2021)
   https://doi.org/10.1063/5.0033772

6. Ł. Frąckowiak, F. Stobiecki, G.D., Chaves-O'Flynn, M. Urbaniak, M. Schmidt, M. Matczak, A. Maziewski, **M. Reginka**, A. Ehresmann and P. Kuświk: *Subsystem domination influence on magnetization reversal in designed magnetic patterns in ferrimagnetic Tb/Co multilayers*
   Scientific Reports **11** 1041 (2021)
   https://doi.org/10.1038/s41598-020-80004-x

7. M. Urbaniak, M. Matczak,G. D., Chaves-O'Flynn, **M. Reginka**, A. Ehresmann and P. Kuświk: *Domain wall motion induced magnetophoresis in unpatterned perpendicular magnetic anisotropy Co layers with Dzyaloshinskii-Moriya interactions*
Journal of Magnetism and Magnetic Materials **519** 167454 (2021)
https://doi.org/10.1016/j.jmmm.2020.167454

8. **M. Reginka**, H. Hoang, Ö. Efendi, M. Merkel, R. Huhnstock, D. Holzinger, K. Dingel, B. Sick, D. Bertinetti, F. W. Herberg, and A. Ehresmann: *Transport Efficiency of Biofunctionalized Magnetic Particles Tailored by Surfactant Concentration*
Langmuir **37** 8498-8507 (2021)
https://doi.org/10.1021/acs.langmuir.1c00900

9. S. Philipp, B. Gross, **M. Reginka**, M. Merkel, M. M. Claus, M. Sulliger, A. Ehresmann, and M. Poggio: *Magnetic hysteresis of individual Janus particles with hemispherical exchange biased caps*
Applied Physics Letters **119** 222406 (2021)
https://doi.org/10.1063/5.0076116

10. R. Huhnstock, **M. Reginka**, A. Tomiţa, M. Merkel, K. Dingel, D. Holzinger, B. Sick, M. Vogel, and A. Ehresmann: *Translatory and rotatory motion of exchange-bias capped Janus particles controlled by dynamic magnetic field landscapes*
Scientific Reports **11** 21794 (2021)
https://doi.org/10.1038/s41598-021-01351-x

11. I. Koch, M. Langner, D. Holzinger, M. Merkel, **M. Reginka**, R. Huhnstock, A. Tomiţa, C. J. Caballero, A. Greiner, and A. Ehresmann: *3D Arrangement of Magnetic Particles in Thin Polymer Films Assisted by Magnetically Patterned Exchange Bias Layer Systems*
Particle and Particle Systems Characterization **38** 2100072 (2021)
https://doi.org/10.1002/ppsc.202100072

12. M. Merkel, R. Huhnstock, **M. Reginka**, M. Vogel, H. Głowinski, P. Kuświk, and A. Ehresmann: *Viscous magnetization decrease in first-order reversal curves induced by rotatable magnetic anisotropy in polycrystalline exchange-biased bilayers*
Physical Review B **104** 214406 (2021)
https://doi.org/10.1103/PhysRevB.104.214406

13. M. Merkel, **M. Reginka**, R. Huhnstock, and A. Ehresmann: *Polycrystalline exchange-biased bilayers: Magnetically effective vs. structural antiferromagnetic grain volume distribution*
Physical Review B **106** 014403 (2022)
https://doi.org/10.1103/PhysRevB.106.014403

14. K. Volkova, J. Heupel, S. Trofimov, F. Betz, R. Colom, R.W. MacQueen, S. Akhundzada, **M. Reginka**, A. Ehresmann, J.P. Reithmaier, S. Burger, C. Popov and B. Naydenov *Optical and Spin Properties of NV Center Ensembles in Diamond Nano-Pillars*
Nanomaterials **12** 1516 (2022)
https://doi.org/10.3390/nano12091516

Bibliography

[Abe19] Abert, C. *Micromagnetics and spintronics: models and numerical methods.* The European Physical Journal B, 92(6), 120 (2019).

[ABR21] Arekapudi, S. S. P. K., B. Böhm, L. Ramasubramanian, F. Ganss, P. Heinig, S. Stienen, C. Fowley, K. Lenz, A. M. Deac, M. Albrecht and O. Hellwig. *Direct imaging of distorted vortex structures and magnetic vortex annihilation processes in ferromagnetic/antiferromagnetic disk structures.* Physical Review B, 103(1), 14405 (2021).

[AEL07] Altbir, D., J. Escrig, P. Landeros, F. S. Amaral and M. Bahiana. *Vortex core size in interacting cylindrical nanodot arrays.* Nanotechnology, 18(48) (2007).

[Aha88] Aharoni, A. *Elongated single-domain ferromagnetic particles.* Journal of Applied Physics, 63(12), 5879 (1988).

[AHG05] Albrecht, M., G. Hu, I. L. Guhr, T. C. Ulbrich, J. Boneberg, P. Leiderer and G. Schatz. *Magnetic multilayers on nanospheres.* Nature Materials, 4(3), 203 (2005).

[ALS10] Amaladass, E., B. Ludescher, G. Schütz, T. Tyliszczak, M. S. Lee and T. Eimüller. *Nanospheres generate out-of-plane magnetization.* Journal of Applied Physics, 107(5), 10 (2010).

[BA98] Barna, P. B. and M. Adamik. *Fundamental structure forming phenomena of polycrystalline films and the structure zone models.* Thin Solid Films, 317(1-2), 27 (1998).

[BBK11] Berkov, D. V., C. T. Boone and I. N. Krivorotov. *Micromagnetic simulations of magnetization dynamics in a nanowire induced by a spin-polarized current injected via a point contact.* Physical Review B, 83(5), 1 (2011).

[BBV02] Bekaert, J., D. Buntinx, C. Van Haesendonck, V. V. Moshchalkov, J. De Boeck, G. Borghs and V. Metlushko. *Noninvasive magnetic imaging and magnetization measurement of isolated mesoscopic Co rings.* Applied Physics Letters, 81(18), 3413 (2002).

[Bea06] Beaurepaire, E. *Magnetism: A Synchrotron Radiation Approach.* Springer (2006).

[BGLB13] Biziere, N., C. Gatel, R. Lassalle-Balier, M. C. Clochard, J. E. Wegrowe and E. Snoeck. *Imaging the Fine Structure of a Magnetic Domain Wall in a Ni Nanocylinder*. Nano Letters, 13(5), 2053 (2013).

[BKD08] Bohlens, S., B. Krüger, A. Drews, M. Bolte, G. Meier and D. Pfannkuche. *Current controlled random-access memory based on magnetic vortex handedness*. Applied Physics Letters, 93(14), 142508 (2008).

[BKS05] Bergmann, L., R. Kassing, C. Schaefer and S. Blügel. *Festkörper*. Lehrbuch Der Experimentalphysik. De Gruyter (2005).

[BMC09] Bermdez Urẽa, E., Y. Mei, E. Coric, D. Makarov, M. Albrecht and O. G. Schmidt. *Fabrication of ferromagnetic rolled-up microtubes for magnetic sensors on fluids*. Journal of Physics D: Applied Physics, 42(5) (2009).

[Bor] *Boris computational spintronics*. `https://www.boris-spintronics.uk`. Accessed: 2021-11-30.

[BRG13] Brandt, R., R. Rückriem, D. Gilbert, F. Ganss, T. Senn, K. Liu, M. Albrecht and H. Schmidt. *Size-dependent magnetization switching characteristics and spin wave modes of FePt nanostructures modes*. J. Appl. Phys., 113 (2013).

[CFR89] Casagrande, C., P. Fabre, E. Raphaël and M. Veyssié. *Janus Beads: Realization and Behaviour at Water/Oil Interfaces*. Europhysics Letters (EPL), 9(3), 251 (1989).

[CG97] Chikazumi, S. and C. Graham. *Physics of ferromagnetism*. International series of monographs on physics. Oxford University Press (1997).

[CGS19] Campuzano, S., M. Gamella, V. Serafín, M. Pedrero, P. Yáñez-Sedeño and J. M. Pingarrón. *Magnetic Janus Particles for Static and Dynamic (Bio)Sensing*. Magnetochemistry, 5(3) (2019).

[Cho97] Chou, S. Y. *Patterned magnetic nanostructures and quantized magnetic disks*. Proceedings of the IEEE, 85(4), 652 (1997).

[CKA99] Cowburn, R. P., D. K. Koltsov, A. O. Adeyeye, M. E. Welland and D. M. Tricker. *Single-domain circular nanomagnets*. Physical Review Letters, 83(5), 1042 (1999).

[CO55] Chikazumi, S. and T. Oomura. *On the Origin of Magnetic Anisotropy Induced by Magnetic Annealing*. Journal of the Physical Society of Japan, 10(10) (1955).

[Coe10a] Coey, J. M. D. In *Magnetism and Magnetic Materials*, Kapitel Ferromagnetism and exchange, pages 128–194. Cambridge: Cambridge University Press (2010).

[Coe10b] Coey, J. M. D. In *Magnetism and Magnetic Materials*, Kapitel Experimental methods, pages 333–373. Cambridge: Cambridge University Press (2010).

[CSH05] Camarero, J., J. Sort, A. Hoffmann, J. M. García-Martín, B. Dieny, R. Miranda and J. Nogués. *Origin of the asymmetric magnetization reversal behavior in exchange-biased systems: Competing anisotropies*. Physical Review Letters, 95(5), 1 (2005).

[CVA16] Clercq, J. D., A. Vansteenkiste, M. Abes, K. Temst and B. V. Waeyenberge. *Modelling exchange bias with MuMax3.* Journal of Physics D: Applied Physics, 49(43), 435001 (2016).

[DaCR19] Daeng-am, W., P. Chureemart, A. Rittidech, L. J. Atkinson, R. W. Chantrell and J. Chureemart. *Micromagnetic model of exchange bias: effects of structure and AF easy axis dispersion for IrMn/CoFe bilayers.* Journal of Physics D: Applied Physics, 53(4), 045002 (2019).

[DDH12] Donolato, M., B. T. Dalslet and M. F. Hansen. *Microstripes for transport and separation of magnetic particles.* Biomicrofluidics, 6(024110), 1 (2012).

[De 92] De Gennes, P.-G. *Soft Matter (Nobel Lecture).* Angewandte Chemie International Edition, 31(7), 842 (1992).

[DHK21] Dingel, K., R. Huhnstock, A. Knie, A. Ehresmann and B. Sick. *AdaPT: Adaptable Particle Tracking for Spherical Microparticles in Lab on Chip Systems.* Computer Physics Communications, page 107859 (2021).

[DLR07] Dumas, R. K., C. P. Li, I. V. Roshchin, I. K. Schuller and K. Liu. *Magnetic fingerprints of sub- 100 nm Fe dots.* Physical Review B, 75(13), 1 (2007).

[DLS14] Dieckhoff, J., A. Lak, M. Schilling and F. Ludwig. *Protein detection with magnetic nanoparticles in a rotating magnetic field.* Journal of Applied Physics, 115(2), 024701 (2014).

[DTK11] Donolato, M., A. Torti, M. Kostesha, M. Deryabina, E. Sogne, P. Vavassori, M. F. Hansen and R. Bertacco. *Magnetic domain wall conduits for single cell applications.* Lab on Chip, 11, 2976 (2011).

[EEW06] Ehresmann, A., D. Engel, T. Weis, A. Schindler, D. Junk, J. Schmalhorst and V. Höink. *Fundamentals for magnetic patterning by ion bombardment of exchange bias layer systems.* Phys. Status Solidi B, 36(1), 29 (2006).

[EGR14] Eslami, S., J. G. Gibbs, Y. Rechkemmer, J. van Slageren, M. Alarcón-Correa, T.-C. Lee, A. G. Mark, G. L. J. A. Rikken and P. Fischer. *Chiral Nanomagnets.* ACS Photonics, 1(11), 1231 (2014).

[EJE05] Ehresmann, A., D. Junk, D. Engel, A. Paetzold and K. Röll. *On the origin of ion bombardment induced exchange bias modifications in polycrystalline layers.* Journal of Physics D: Applied Physics, 38(6), 801 (2005).

[EKH15] Ehresmann, A., I. Koch and D. Holzinger. *Manipulation of Superparamagnetic Beads on Patterned Exchange-Bias Layer Systems for Biosensing Applications.* Sensors, pages 28854–28888 (2015).

[EMS16] Erb, R. M., J. J. Martin, R. Soheilian, C. Pan and J. R. Barber. *Actuating Soft Matter with Magnetic Torque.* Advanced Functional Materials, 26(22), 3859 (2016).

[ESW11] Ehresmann, A., C. Schmidt, T. Weis and D. Engel. *Thermal exchange bias field drift in field cooled MnIr/CoFe thin films after 10 keV He ion bombardment.* Journal of Applied Physics, 109(023910) (2011).

[FC72] Fulcomer, E. and S. H. Charap. *Thermal fluctuation aftereffect model for some systems with ferromagnetic-antiferromagnetic coupling.* Journal of Applied Physics, 43(10), 4190 (1972).

[FFB07] Fischbacher, T., M. Franchin, G. Bordignon and H. Fangohr. *A Systematic Approach to Multiphysics Extensions of Finite-Element-Based Micromagnetic Simulations: Nmag.* IEEE Transactions on Magnetics, 43(6), 2896 (2007).

[FIK11] Fischer, P., M. Y. Im, S. Kasai, K. Yamada, T. Ono and A. Thiaville. *X-ray imaging of vortex cores in confined magnetic structures.* Physical Review B, 83(21) (2011).

[FKCO20] Frąckowiak, Ł., P. Kuświk, G. D. Chaves-O'Flynn, M. Urbaniak, M. Matczak, P. P. Michałowski, A. Maziewski, M. Reginka, A. Ehresmann and F. Stobiecki. *Magnetic Domains without Domain Walls: A Unique Effect of He + Ion Bombardment in Ferrimagnetic Tb / Co Films.* Physical Review Letters, 124(4), 047203 (2020).

[FO15] Fischer, P. and H. Ohldag. *X-rays and magnetism.* Reports on Progress in Physics, 78(9) (2015).

[Fon59] Foner, S. *Versatile and Sensitive Vibration-Sample Magnetometer.* The Review of scientific instruments, 30(7), 550 (1959).

[FT65] Feldtkeller, E. and H. Thomas. *Structure and energy of Bloch lines in thin ferromagnetic films (DE: Struktur und Energie von Blochlinien in dünnen ferromagnetischen Schichten).* Physik der kondensierten Materie, 4(1), 8 (1965).

[Gau17] Gaul, A. M. *Erzeugung remanent stabiler Domänenmuster in austauschverschobenen Dünnschichtsystemen mittels Heliumionenmikroskopie Dissertation.* Dissertation, Universität Kassel (2017).

[Get08] Getzlaff, M. *Fundamentals of Magnetism.* Springer-Verlag (2008).

[GH06] Guslienko, K. Y. and A. Hoffmann. *Field evolution of tilted vortex cores in exchange-biased ferromagnetic dots.* Physical Review Letters, 97(10), 1 (2006).

[GKS14] Gaididei, Y., V. P. Kravchuk and D. D. Sheka. *Curvature effects in thin magnetic shells.* Physical Review Letters, 112(25), 1 (2014).

[GNO02] Guslienko, K. Y., V. Novosad, Y. Otani, H. Shima and K. Fukamichi. *Magnetization reversal due to vortex nucleation, displacement, and annihilation in submicron ferromagnetic dot arrays.* Physical Review B, 65(2), 244141 (2002).

[GRF05] Gunnarsson, K., P. E. Roy, S. Felton, J. Pihl, P. Svedlindh, S. Berner, H. Lidbaum and S. Oscarsson. *Programmable Motion and Separation of Single Magnetic Particles on Patterned Magnetic Surfaces.* Advanced Materials, 17, 1730 (2005).

[Gus01] Guslienko, K. Y. *Magnetic anisotropy in two-dimensional dot arrays induced by magnetostatic interdot coupling.* Physics Letters, Section A: General, Atomic and Solid State Physics, 278(5), 293 (2001).

[GWR16] Gross, B., D. P. Weber, D. Rüffer, A. Buchter, F. Heimbach, A. Fontcuberta I Morral, D. Grundler and M. Poggio. *Dynamic cantilever magnetometry of individual CoFeB nanotubes.* Physical Review B, 93(6), 1 (2016).

[GYV15] Gilbert, D. A., L. Ye, A. Varea, S. Agramunt-Puig, N. del Valle, C. Navau, J. F. López-Barbera, K. S. Buchanan, A. Hoffmann, A. Sánchez, J. Sort, K. Liu and J. Nogués. *A new reversal mode in exchange coupled antiferromagnetic/ferromagnetic disks: distorted viscous vortex.* Nanoscale, 7(21), 9878 (2015).

[Ham03] Hamrle, J. *Magneto-optical determination of the in-depth magnetization profile in magnetic multilayers.* Dissertation (2003).

[HDY09] Hernandez, S. C., J. Dou, C. Yu, M. J. Pechan, L. Folks, J. A. Katine and M. J. Carey. *Exchange-coupled suppression of vortex formation in permalloy nanodot chain arrays.* Journal of Applied Physics, 105(7) (2009).

[HHF03] Hamrle, J., J. Hamrle, J. Ferré, J. P. Jamet, V. Repain, V. Repain, G. Baudot and S. Rousset. *Vicinal interface sensitive magneto-optical Kerr effect: Application to Co/Au(322).* Physical Review B, 67(15), 1 (2003).

[HHK03] Ha, J. K., R. Hertel and J. Kirschner. *Micromagnetic study of magnetic configurations in submicron permalloy disks.* Physical Review B, 67, 1 (2003).

[HKB15] Holzinger, D., I. Koch, S. Burgard and A. Ehresmann. *Directed Magnetic Particle Transport above Artificial Magnetic Domains Due to Dynamic Magnetic Potential Energy Landscape Transformation.* ACS Nano, 9(7), 7323 (2015).

[HLG12] Holzinger, D., D. Lengemann, F. Göllner, D. Engel and A. Ehresmann. *Controlled movement of superparamagnetic bead rows for microfluid mixing.* Applied Physics Letters, 100(15) (2012).

[Hof04] Hoffmann, A. *Symmetry driven irreversibilities at ferromagnetic-antiferromagnetic interfaces.* Physical Review Letters, 93(9), 1 (2004).

[HRT21] Huhnstock, R., M. Reginka, A. Tomita, M. Merkel, K. Dingel, D. Holzinger, B. Sick, M. Vogel and A. Ehresmann. *Translatory and rotatory motion of exchange-bias capped Janus particles controlled by dynamic magnetic field landscapes.* Scientific Reports, 11(1), 21794 (2021).

[HS98] Hubert, A. and R. Schäfer. *Magnetic Domains, The Analysis of Magnetic Microstructures.* Springer (1998).

[IFH17] Im, M. Y., P. Fischer, H. S. Han, A. Vogel, M. S. Jung, W. Chao, Y. S. Yu, G. Meier, J. I. Hong and K. S. Lee. *Simultaneous control of magnetic topologies for reconfigurable vortex arrays.* NPG Asia Materials, 9(2), 1 (2017).

[IIP12] Ivanov, Y. P., A. I. Il'In, E. V. Pustovalov, K. V. Nefedov and L. A. Chebotkevich. *Effect of the shape anisotropy and configurational anisotropy on the magnetic structure of ferromagnetic nanodots.* Physics of Metals and Metallography, 113(3), 222 (2012).

[JA04] Jubert, P. O. and R. Allenspach. *Analytical approach to the single-domain-to-vortex transition in small magnetic disks.* Physical Review B, 70(14), 1 (2004).

[JCJ94] Jungblut, R., R. Coehoorn, M. T. Johnson, J. aan de Stegge and A. Reinders. *Orientational dependence of the exchange biasing in molecular-beam-epitaxy-grown Ni80 Fe20 / Fe50 Mn50 bilayers (invited).* Journal of Applied Physics, 75(10), 6659 (1994).

[JCS09] Jiménez, E., J. Camarero, J. Sort, J. Nogués, N. Mikuszeit, J. M. García-Martín, A. Hoffmann, B. Dieny and R. Miranda. *Emergence of noncollinear anisotropies from interfacial magnetic frustration in exchange-bias systems.* Physical Review B, 80(1), 1 (2009).

[JDM03] Jung, H. S., W. D. Doyle and S. Matsunuma. *Influence of underlayers on the soft properties of high magnetization FeCo films.* Journal of Applied Physics, 93(10 2), 6462 (2003).

[JGB10] Johansson, L., K. Gunnarsson, S. Bijelovic, K. Eriksson, A. Surpi, E. Göthelid, P. Svedlindh and S. Oscarsson. *A magnetic microchip for controlled transport of attomole levels of proteins.* Lab on a Chip, 10, 654 (2010).

[JRA09] Jain, S., Y. Ren, A. O. Adeyeye and N. Singh. *Configurational anisotropy and control of magnetic vortex chirality in arrays of circular Ni80 Fe20 nanoscale dots.* Physical Review B, 80(13), 1 (2009).

[KHP12] Kuschel, T., J. Hamrle, J. Pištora, K. Saito, S. Bosu, Y. Sakuraba, K. Takanashi and J. Wollschläger. *Magnetic characterization of thin Co50Fe50 films by magnetooptic Kerr effect.* Journal of Physics D: Applied Physics, 45(49) (2012).

[KKL98] Kleiber, M., F. Kümmerlen, M. Löhndorf, A. Wadas and D. Weiss. *Magnetization switching of submicrometer Co dots induced by a magnetic force microscope tip.* Physical Review B, 58(9), 5563 (1998).

[KKP10] Kimling Née Moser, J., V. Kunej, H. F. Pernau, E. Scheer and M. Albrecht. *Magnetoresistive effects in Co/Pd multilayers on self-assembled nanoparticles (invited).* Journal of Applied Physics, 107(9), 449 (2010).

[KRP08] Knotts IV, T. A., N. Rathore and J. J. D. Pablo. *An Entropic Perspective of Protein Stability on Surfaces.* Biophysical Journal, 94, 4473 (2008).

[KRV16] Kravchuk, V. P., U. K. Rößler, O. M. Volkov, D. D. Sheka, J. Van Den Brink, D. Makarov, H. Fuchs, H. Fangohr and Y. Gaididei. *Topologically stable magnetization states on a spherical shell: Curvature-stabilized skyrmions.* Physical Review B, 94(14), 1 (2016).

[KSR10] Kronast, F., J. Schlichting, F. Radu, S. K. Mishra, T. Noll and H. A. Dürr. *Spin-resolved photoemission microscopy and magnetic imaging in applied magnetic fields.* Surface and Interface Analysis, 42(10-11), 1532 (2010).

[KSS12] Kravchuk, V. P., D. D. Sheka, R. Streubel, D. Makarov, O. G. Schmidt and Y. Gaididei. *Out-of-surface vortices in spherical shells.* Physical Review B, 85(14), 1 (2012).

[Kub13] Kubitscheck, U., editor. *Fluorescence microscopy : from principles to biological applications.* Wiley-VCH, Weinheim (2013).

[Kus11] Kuschel, T. *Magnetic anisotropy of transition metal based thin films investigated by magnetooptic Kerr effect.* Dissertation (2011).

[Kus19] Kusano, E. *Structure-Zone Modeling of Sputter-Deposited Thin Films: A Brief Review.* Applied Science and Convergence Technology, 28, 179 (2019).

[KV16] Kronast, F. and S. Valencia Molina. *SPEEM: The photoemission microscope at the dedicated microfocus PGM beamline UE49-PGMa at BESSY II.* Journal of large-scale research facilities JLSRF, 2, 1 (2016).

[KVLD03] Kläui, M., C. A. F. Vaz, L. Lopez-Diaz and J. A. C. Bland. *Vortex formation in narrow ferromagnetic rings.* Journal of Physics Condensed Matter, 15(21) (2003).

[KWR17] Khademi, M., W. Wang, W. Reitinger and D. P. J. Barz. *Zeta Potential of Poly(methyl methacrylate) (PMMA) in Contact with Aqueous Electrolyte - Surfactant Solutions.* Langmuir, 33(40), 10473 (2017).

[LDS14] Liu, X. M., J. Ding, N. Singh, G. Shimon and A. O. Adeyeye. *Magnetization dynamics of coupled Ni80Fe20 dots: Effects of configurational anisotropy and dipolar coupling.* Applied Physics Letters, 105(5), 1 (2014).

[LEA06] Landeros, P., J. Escrig, D. Altbir, M. Bahiana and J. D'Albuquerque e Castro. *Stability of magnetic configurations in nanorings.* Journal of Applied Physics, 100(4) (2006).

[Lep20] Lepadatu, S. *Boris computational spintronics - High performance multi-mesh magnetic and spin transport modeling software.* Journal of Applied Physics, 128(24) (2020).

[LLL15] Lu, C., X. Liu, Y. Li, F. Yu, L. Tang, Y. Hu and Y. Ying. *Multifunctional Janus Hematite-Silica Nanoparticles: Mimicking Peroxidase-Like Activity and Sensitive Colorimetric Detection of Glucose.* ACS Applied Materials & Interfaces, 7(28), 15395 (2015).

[LLN01] Lebib, A., S. P. Li, M. Natali and Y. Chen. *Size and thickness dependencies of magnetization reversal in Co dot arrays.* Journal of Applied Physics, 89(7), 3892 (2001).

[LMK09] Leach, J., H. Mushfique, S. Keen, R. Di Leonardo, G. Ruocco, J. M. Cooper and M. J. Padgett. *Comparison of Faxén's correction for a microsphere translating or rotating near a surface.* Physical Review E - Statistical, Nonlinear, and Soft Matter Physics, 79(2) (2009).

[LPE05] Li, Z.-P., O. Petracic, J. Eisenmenger and I. K. Schuller. *Reversal behavior of exchange-biased submicron dots.* Applied Physics Letters, 86(072501) (2005).

[LPM06] Li, Z. P., O. Petracic, R. Morales, J. Olamit, X. Batlle, K. Liu and I. K. Schuller. *Asymmetric reversal in inhomogeneous magnetic heterostructures.* Physical Review Letters, 96(21), 1 (2006).

[LPN01] Li, S. P., D. Peyrade, M. Natali, A. Lebib, Y. Chen, U. Ebels, L. D. Buda and K. Ounadjela. *Flux closure structures in cobalt rings.* Physical Review Letters, 86(6), 1102 (2001).

[LTM11] Lee, A., S. K. Y. Tang, C. R. Mace and G. M. Whitesides. *Denaturation of Proteins by SDS and Tetraalkylammonium Dodecyl Sulfates.* Langmuir, 27, 11560 (2011).

[LVS17] Lim, B., P. Vavassori, R. Sooryakumar and C. Kim. *Nano / micro-scale magnetophoretic devices for biomedical applications.* Journal of Physics D: Applied Physics, 50(033002) (2017).

[LYY16] Lee, K., Y. Yi and Y. Yu. *Remote Control of T Cell Activation Using Magnetic Janus Particles.* Angewandte Chemie - International Edition, 55(26) (2016).

[Mal87] Malozemoff, A. P. *Random-field model of exchange anisotropy at rough ferromagnetic-antiferromagnetic interfaces.* Physical Review B, 35(7) (1987).

[MB56] Meiklejohn, W. H. and C. P. Bean. *Classics in Magnetics A New Magnetic Anisotropy.* Conference on Magnetism and Mag- netic Materials, 37(6), 3866 (1956).

[MB57] Meiklejohn, W. H. and C. P. Bean. *New Magnetic Anisotropy.* Physical Review Letters, 105(5), 904 (1957).

[MBUS08] Makarov, D., E. Bermúdez-Ureña, O. G. Schmidt, F. Liscio, M. Maret, C. Brombacher, S. Schulze, M. Hietschold and M. Albrecht. *Nanopatterned CoPt alloys with perpendicular magnetic anisotropy.* Applied Physics Letters, 93(15), 153112 (2008).

[Mei62] Meiklejohn, W. *Exchange Anisotropy-A Review.* Journal of Applied Physics, 33(3) (1962).

[MFO95] Micheletto, R., H. Fukuda and M. Ohtsu. *A Simple Method for the Production of a Two-Dimensional, Ordered Array of Small Latex Particles.* Langmuir, 11(9), 3333 (1995).

[MGM16] Müglich, N. D., A. Gaul, M. Meyl, A. Ehresmann, G. Götz, G. Reiss and T. Kuschel. *Time-dependent rotatable magnetic anisotropy in polycrystalline exchange-bias systems : Dependence on grain-size distribution.* Physical Review B, 94, 1 (2016).

[MGW18] Mehlin, A., B. Gross, M. Wyss, T. Schefer, G. Tütüncüoglu, F. Heimbach, A. Fontcuberta Morral, D. Grundler and M. Poggio. *Observation of end-vortex nucleation in individual ferromagnetic nanotubes.* Physical Review B, 97(13), 1 (2018).

[MHR20] Merkel, M., R. Huhnstock, M. Reginka, D. Holzinger, M. Vogel, A. Ehresmann, J. Zehner and K. Leistner. *Interrelation between polycrystalline structure and time-dependent magnetic anisotropies in exchange-biased bilayers.* Physical Review B, 102(14), 144421 (2020).

[MHR21] Merkel, M., R. Huhnstock, M. Reginka, M. Vogel, A. Ehresmann, H. Głowinski and P. Kuświk. *Viscous magnetization decrease in first-order reversal curves induced by rotatable magnetic anistropy in polycrystalline exchange-biased bilayers.* Physical Review B, 104, 214406 (2021).

[MKS87] Mauri, D., E. Kay, D. Scholl and J. K. Howard. *Novel method for determining the anisotropy constant of MnFe in a NiFe/MnFe sandwich.* Journal of Applied Physics, 62(7), 2929 (1987).

[MLSA05] Mejía-López, J., P. Soto and D. Altbir. *Asymmetric reversal of the hysteresis loop in exchange-biased nanodots.* Physical Review B, 71(10), 2 (2005).

[MP10] Mihajlovic, G. and M. Patrick. *Temperature dependent nucleation and annihilation of individual magnetic vortices.* Appl. Phys. Lett., 96(112501), 1 (2010).

[MPF01] Mougin, A., S. Poppe, J. Fassbender, B. Hillebrands, G. Faini, U. Ebels, M. Jung, D. Engel, A. Ehresmann and H. Schmoranzer. *Magnetic micropatterning of FeNi/FeMn exchange bias bilayers by ion irradiation.* Journal of Applied Physics, 89(11 II), 6606 (2001).

[MRH22] Merkel, M., M. Reginka, R. Huhnstock and A. Ehresmann. *Polycrystalline exchange-biased bilayers: Magnetically effective vs. structural antiferromagnetic grain volume distribution.* Physical Review B, 106, 014403 (2022).

[MSvdB21] May, A., M. Saccone, A. van den Berg, J. Askey, M. Hunt and S. Ladak. *Magnetic charge propagation upon a 3D artificial spin-ice.* Nature Communications, 12(1), 1 (2021).

[Müg16] Müglich, N. D. *Exchange-Bias-Dünnschichtsysteme: Charakterisierung, Modellierung und Anwendung.* Dissertation, Universität Kassel (2016).

[MVK22] Makarov, D., O. M. Volkov, A. Kákay, O. V. Pylypovskyi, B. Budinská and O. V. Dobrovolskiy. *New Dimension in Magnetism and Superconductivity: 3D and Curvilinear Nanoarchitectures.* Advanced Materials, 34(3), 2101758 (2022).

[MZK21] Mourkas, A., A. Zarlaha, N. Kourkoumelis and I. Panagiotopoulos. *Curvature induced stabilization of vortices on magnetic spherical sector shells.* Journal of Magnetism and Magnetic Materials, 524(November 2020), 167676 (2021).

[NGS02] Novosad, V., K. Y. Guslienko, H. Shima, Y. Otani, S. G. Kim, K. Fukamichi, N. Kikuchi, O. Kitakami and Y. Shimada. *Effect of interdot magnetostatic interaction on magnetization reversal in circular dot arrays.* Physical Review B, 65(6), 1 (2002).

[Nis16] Nissen, D. *Magnetic Vortices in Closely Packed Cap Structures.* Dissertation, UniversitÃ¤t Augsburg (2016).

[NK12] Nečas, D. and P. Klapetek. *Gwyddion: an open-source software for SPM data analysis.* Central European Journal of Physics, 10, 181 (2012).

[NKM16] Nissen, D., O. Klein, P. Matthes and M. Albrecht. *Exchange-biased Py/CoO vortex structures: Magnetization reversal, cooling-field dependence, and training.* Physical Review B, 94(13), 1 (2016).

[NMK15] Nissen, D., D. Mitin, O. Klein, S. S. Arekapudi, S. Thomas, M.-Y. Im, P. Fischer and M. Albrecht. *Magnetic coupling of vortices in a two- dimensional lattice.* Nanotechnology, 26 (2015).

[NOK99] Nemoto, A., Y. Otani, S. G. Kim, K. Fukamichi, O. Kitakami and Y. Shimada. *Magnetoresistance and planar Hall effects in submicron exchange-coupled NiO/Fe19Ni81 wires.* Applied Physics Letters, 74(26), 4026 (1999).

[NS99] Nogués, J. and I. K. Schuller. *Exchange bias.* Journal of Magnetism and Magnetic Materials, 192(2), 203 (1999).

[NSL05] Nogués, J., J. Sort, V. Langlais, V. Skumryev, S. Suriñach, J. S. Muñoz and M. D. Baró. *Exchange bias in nanostructures.* Physics Reports, 422, 65 (2005).

[NWE07] Notte, J., B. Ward, N. Economou, R. Hill, R. Percival, L. Farkas and S. McVey. *An introduction to the helium ion microscope.* AIP Conference Proceedings, 931(2007), 489 (2007).

[OB17] Ouk, M. and G. S. Beach. *Superparamagnetic microbead transport induced by a magnetic field on large-area magnetic antidot arrays.* Journal of Magnetism and Magnetic Materials, 444, 218 (2017).

[OFOVF10] O'Grady, K., L. Fernandez-Outon and G. Vallejo-Fernandez. *A new paradigm for exchange bias in polycrystalline thin films.* Journal of Magnetism and Magnetic Materials, 322(8), 883 (2010).

[Ohl02] Ohldag, H. *Exchange Coupling of Co and Fe on Antiferromagnetic NiO Investigated By Dichroism X-Ray Absorption Spectromicroscopy.* Dissertation, Heinrich-Heine-Universität Düusseldorf (2002).

[OLLV12] Otálora, J. A., J. A. López-López, P. Vargas and P. Landeros. *Chirality switching and propagation control of a vortex domain wall in ferromagnetic nanotubes.* Applied Physics Letters, 100(7), 072407 (2012).

[OOC14] Ohresser, P., E. Otero, F. Choueikani, K. Chen, S. Stanescu, F. Deschamps, T. Moreno, F. Polack, B. Lagarde, J. P. Daguerre, F. Marteau, F. Scheurer, L. Joly, J. P. Kappler, B. Muller, O. Bunau and P. Sainctavit. *DEIMOS: A beamline dedicated to dichroism measurements in the 350-2500 eV energy range.* Review of Scientific Instruments, 85(1) (2014).

[OSO02] Okuno, T., K. Shigeto, T. Ono, K. Mibu and T. Shinjo. *MFM study of magnetic vortex cores in circular permalloy dots: Behavior in external field.* Journal of Magnetism and Magnetic Materials, 240(1-3), 1 (2002).

[PDD20] Pip, P., C. Donnelly, M. Döbeli, C. Gunderson, L. J. Heyderman and L. Philippe. *Electroless Deposition of Ni-Fe Alloys on Scaffolds for 3D Nanomagnetism.* Small, 16(44), 1 (2020).

[PGR21] Philipp, S., B. Gross, M. Reginka, M. Merkel, M. M. Claus, M. Sulliger, A. Ehresmann and M. Poggio. *Magnetic hysteresis of individual Janus particles with hemispherical exchange biased caps.* Applied Physics Letters, 119(22), 222406 (2021).

[PLG14] Phatak, C., Y. Liu, E. B. Gulsoy, D. Schmidt, E. Franke-Schubert and A. Petford-Long. *Visualization of the Magnetic Structure of Sculpted Three-Dimensional Cobalt Nanospirals.* Nano Letters, 14(2), 759 (2014).

[PNB02] Prejbeanu, I. L., M. Natali, L. D. Buda, U. Ebels, A. Lebib, Y. Chen and K. Ounadjela. *In-plane reversal mechanisms in circular Co dots.* Journal of Applied Physics, 91(10 I), 7343 (2002).

[PR02] Paetzold, A. and K. Röll. *Thermally activated self-alignment of exchange coupling in NiO / NiFe bilayers.* Journal of Applied Physics, 91(10), 7748 (2002).

[PRS05] Pike, C. R., C. A. Ross, R. T. Scalettar and G. Zimanyi. *First-order reversal curve diagram analysis of a perpendicular nickel nanopillar array.* Physical Review B, 71(13), 1 (2005).

[PSN00] Pokhil, T., D. Song and J. Nowak. *Spin vortex states and hysteretic properties of submicron size NiFe elements.* Journal of Applied Physics, 87(9), 6319 (2000).

[RBU03] Rahm, M., J. Biberger, V. Umansky and D. Weiss. *Vortex pinning at individual defects in magnetic nanodisks.* Journal of Applied Physics, 93(10 2), 7429 (2003).

[Reg18] Reginka, M. *Physical Characterization and Motion Dynamics of Exchange-Biased Janus Particles.* Dissertation, Universität Kassel (2018).

[RHE21] Reginka, M., H. Hoang, Ö. Efendi, M. Merkel, R. Huhnstock, D. Holzinger, K. Dingel, B. Sick, D. Bertinetti, F. Herberg and A. Ehresmann. *Transport efficiency of biofunctionalized magnetic particles tailored by surfactant concentration.* Langmuir, 37(28), 8498 (2021).

[RHS02] Ross, C. A., M. Hwang, M. Shima, J. Y. Cheng, M. Farhoud, T. A. Savas, H. I. Smith, W. Schwarzacher, F. M. Ross, M. Redjdal and F. B. Humphrey. *Micromagnetic behavior of electrodeposited cylinder arrays.* Physical Review B, 65(14), 1 (2002).

[RHZ14] Roberts, A. P., D. Heslop, X. Zhao and C. R. Pike. *Understanding fine magnetic particle systems through use of first-order reversal curve diagrams.* Reviews of Geophysics, 52(4), 557 (2014).

[RKLD01] Rothman, J., M. Kläui, L. Lopez-Diaz, C. A. Vaz, A. Bleloch, J. A. Bland, Z. Cui and R. Speaks. *Observation of a Bi-domain state and nucleation free switching in mesoscopic ring magnets.* Physical Review Letters, 86(6), 1098 (2001).

[RLL16] Rampini, S., P. Li and G. U. Lee. *Micromagnet arrays enable precise manipulation of individual biological analyte-superparamagnetic bead complexes for separation and sensing.* Lab on a Chip, 16(19), 3645 (2016).

[RMB12] Rapoport, E., D. Montana and G. S. D. Beach. *Integrated capture, transport, and magneto-mechanical resonant sensing of superparamagnetic microbeads using magnetic domain walls.* Lab Chip, 12, 4433 (2012).

[RSB03] Rahm, M., M. Schneider, J. Biberger, R. Pulwey, J. Zweck, D. Weiss and V. Umansky. *Vortex nucleation in submicrometer ferromagnetic disks.* Applied Physics Letters, 82(23), 4110 (2003).

[RZ07] Radu, F. and H. Zabel. *Exchange Bias Effect of Ferro-/Antiferromagnetic Heterostructures*, volume 227. Springer-Verlag (2007). URL `http://link.springer.com/10.1007/978-3-540-73462-8`.

[SA09] Saeed, I. A. and S. S. Ashraf. *Denaturation studies reveal significant differences between GFP and blue fluorescent protein.* International Journal of Biological Macromolecules, 45, 236 (2009).

[SAKS09] Salazar-Alvarez, G., J. J. Kavich, J. Sort, A. Mugarza, S. Stepanow, A. Potenza, H. Marchetto, S. S. Dhesi, V. Baltz, B. Dieny, A. Weber, L. J. Heyderman, J. Nogués and P. Gambardella. *Direct evidence of imprinted vortex states in the antiferromagnet of exchange biased microdisks.* Applied Physics Letters, 95(1), 10 (2009).

[Sav64] Savitzky, A.; Golay, M. J. E. *Smoothing and Differentiation.* Anal. Chem, 36(8), 1627 (1964).

[SBN06] Sort, J., K. S. Buchanan, V. Novosad, A. Hoffmann, G. Salazar-Alvarez, A. Bollero, M. D. Baró, B. Dieny and J. Nogués. *Imprinting vortices into antiferromagnets.* Physical Review Letters, 97(6), 1 (2006).

[SBP08] Sort, J., K. S. Buchanan, J. E. Pearson, A. Hoffmann, E. Menéndez, G. Salazar-Alvarez, M. D. Baró, M. Miron, B. Rodmacq, B. Dieny and J. Nogués. *Tailoring the magnetization reversal of elliptical dots using exchange bias (invited).* Journal of Applied Physics, 103(7) (2008).

[SEG12] Sapozhnikov, M. V., O. L. Ermolaeva, B. G. Gribkov, I. M. Nefedov, I. R. Karetnikova, S. A. Gusev, V. V. Rogov, B. B. Troitskii and L. V. Khokhlova. *Frustrated magnetic vortices in hexagonal lattice of magnetic nanocaps.* Physical Review B, 85(5) (2012).

[Sem07] Semaltianos, N. G. *Spin-coated PMMA films.* Microelectronics Journal, 38(6-7), 754 (2007).

[SFK16] Streubel, R., P. Fischer, F. Kronast, V. P. Kravchuk, D. D. Sheka, Y. Gaididei, O. G. Schmidt and D. Makarov. *Magnetism in curved geometries.* Journal of Physics D: Applied Physics, 49(36), 363001 (2016).

[SHAR12] Sandig, O., J. Herrero-Albillos, F. M. Römer, N. Friedenberger, J. Kurde, T. Noll, M. Farle and F. Kronast. *Imaging magnetic responses of nanomagnets by XPEEM.* Journal of Electron Spectroscopy and Related Phenomena, 185(10), 365 (2012).

[SHC05] Sort, J., A. Hoffmann, S. H. Chung, K. S. Buchanan, M. Grimsditch, M. D. Baró, B. Dieny and J. Nogués. *Magnetization reversal in submicron disks: Exchange biased vortices.* Physical Review Letters, 95(6), 1 (2005).

[SHHRD20] Sanz-Hernández, D., A. Hierro-Rodriguez, C. Donnelly, J. Pablo-Navarro, A. Sorrentino, E. Pereiro, C. Magén, S. McVitie, J. M. de Teresa, S. Ferrer, P. Fischer and A. Fernández-Pacheco. *Artificial Double-Helix for Geometrical Control of Magnetic Chirality.* ACS Nano, 14(7), 8084 (2020).

[Shi00] Shinjo, T. *Magnetic Vortex Core Observation in Circular Dots of Permalloy.* Science, 567(August), 1998 (2000).

[SHI15] Streubel, R., L. Han, M. Y. Im, F. Kronast, U. K. Rößler, F. Radu, R. Abrudan, G. Lin, O. G. Schmidt, P. Fischer and D. Makarov. *Manipulating topological states by imprinting non-collinear spin textures.* Scientific Reports, 5, 1 (2015).

[SHK14] Streubel, R., L. Han, F. Kronast, A. A. Ünal, O. G. Schmidt and D. Makarov. *Imaging of buried 3D magnetic rolled-up nanomembranes.* Nano Letters, 14(7), 3981 (2014).

[SHO02] Schneider, M., H. Hoffmann, S. Otto, T. Haug and J. Zweck. *Stability of magnetic vortices in flat submicron permalloy cylinders.* Journal of Applied Physics, 92(3), 1466 (2002).

[SHZ00] Schneider, M., H. Hoffmann and J. Zweck. *Lorentz microscopy of circular ferromagnetic permalloy nanodisks.* Applied Physics Letters, 77(18), 2909 (2000).

[SKF15] Streubel, R., F. Kronast, P. Fischer, D. Parkinson, O. G. Schmidt and D. Makarov. *Retrieving spin textures on curved magnetic thin films with full-field soft X-ray microscopies.* Nature Communications, 6(May), 1 (2015).

[SKR16] Streubel, R., F. Kronast, C. F. Reiche, T. Mühl, A. U. Wolter, O. G. Schmidt and D. Makarov. *Vortex circulation and polarity patterns in closely packed cap arrays.* Applied Physics Letters, 108(4) (2016).

[SKS12] Streubel, R., V. P. Kravchuk, D. D. Sheka, D. Makarov, F. Kronast, G. Oliver, R. Streubel, V. P. Kravchuk, D. D. Sheka, D. Makarov, F. Kronast, O. G. Schmidt and Y. Gaididei. *Equilibrium magnetic states in individual hemispherical permalloy caps.* Applied Physics Letters, 132419(September 2012) (2012).

[SKS13] Sheka, D. D., V. P. Kravchuk, M. I. Sloika and Y. Gaididei. *Equilibrium states of soft magnetic hemispherical shell.* Spin, 3 (2013).

[SLM14] Streubel, R., J. Lee, D. Makarov, M. Y. Im, D. Karnaushenko, L. Han, R. Schäfer, P. Fischer, S. K. Kim and O. G. Schmidt. *Magnetic microstructure of rolled-up single-layer ferromagnetic nanomembranes.* Advanced Materials, 26(2), 316 (2014).

[SM99] Stiles, M. D. and R. D. McMichael. *Model for exchange bias in polycrystalline ferromagnet-antiferromagnet bilayers.* Phys. Rev. B, 59, 3722 (1999).

[SMK12] Streubel, R., D. Makarov, F. Kronast, V. Kravchuk, M. Albrecht and O. G. Schmidt. *Magnetic vortices on closely packed spherically curved surfaces.* Physical Review B, 85(17) (2012).

[SRS12] Sokalingam, S., G. Raghunathan, N. Soundrarajan and S.-g. Lee. *A Study on the Effect of Surface Lysine to Arginine Mutagenesis on Protein Stability and Structure Using Green Fluorescent Protein.* PLoS ONE, 7(7) (2012).

[SS06] Stöhr, J. and H. C. Siegmann. *Magnetism: From fundamentals to nanoscale dynamics*, volume 152. Springer-Verlag (2006).

[SSAB06] Sort, J., G. Salazar-Alvarez, M. D. Baró, B. Dieny, A. Hoffmann, V. Novosad and J. Nogús. *Controlling magnetic vortices through exchange bias.* Applied Physics Letters, 88(4), 1 (2006).

[Str15] Streubel, R. *Imaging Spin Textures on Curved Magnetic Surfaces.* Dissertation, Technische Universität Chemnitz (2015).

[SV90] Soille, P. and L. M. Vincent. *Determining watersheds in digital pictures via flooding simulations.* In M. Kunt, editor, *Visual Communications and Image Processing '90: Fifth in a Series*, volume 1360, pages 240 – 250. International Society for Optics and Photonics, SPIE (1990). URL `https://doi.org/10.1117/12.24211`.

[SVM17] Sander, D., S. O. Valenzuela, D. Makarov, C. H. Marrows, E. E. Fullerton, P. Fischer, J. McCord, P. Vavassori, S. Mangin, P. Pirro, B. Hillebrands, A. D. Kent, T. Jungwirth, O. Gutfleisch, C. G. Kim and A. Berger. *The 2017 Magnetism Roadmap.* Journal of Physics D: Applied Physics, 50(36) (2017).

[SW48] Stoner, E. C. and E. Wohlfarth. *A mechanism of magnetic hysteresis in heterogeneous alloys.* Philosophical Transactions of the Royal Society of London. Series A, Mathematical and Physical Sciences, 240 (1948).

[SWH93] Stöhr, J., Y. Wu, B. D. Hermsmeier, M. G. Samant, G. R. Harp, S. Koranda, D. Dunham and B. P. Tonner. *Element-specific magnetic microscopy with circularly polarized X-rays.* Science, 259(5095), 658 (1993).

[TCSV19] Teixeira, A., S. Castillo-Sepúlveda, S. Vojkovic, J. Fonseca, D. Altbir, A. Núñez and V. Carvalho-Santos. *Analysis on the stability of in-surface magnetic configurations in toroidal nanoshells.* Journal of Magnetism and Magnetic Materials, 478, 253 (2019).

[TH88] Tonner, B. P. and G. R. Harp. *Photoelectron microscopy with synchrotron radiation.* Review of Scientific Instruments, 59(6), 853 (1988).

[TPLH09] Tanase, M., A. K. Petford-Long, O. Heinonen, K. S. Buchanan, J. Sort and J. Nogués. *Magnetization reversal in circularly exchange-biased ferromagnetic disks.* Physical Review B, 79(1), 014436 (2009).

[TRH21] Tomita, A., M. Reginka, R. Huhnstock, M. Merkel, D. Holzinger and A. Ehresmann. *Magnetic textures in hemispherical thin film caps with in-plane exchange bias.* Journal of Applied Physics, 129(1) (2021).

[UMCO20] Urbaniak, M., M. Matczak, G. Chaves-O'Flynn, M. Reginka, A. Ehresmann and P. Kuświk. *Domain wall motion induced magnetophoresis in unpatterned perpendicular magnetic anisotropy Co layers with Dzyaloshinskii-Moriya interactions.* Journal of Magnetism and Magnetic Materials, 519, 167454 (2020).

[UMH06] Ulbrich, T. C., D. Makarov, G. Hu, I. L. Guhr, D. Suess, T. Schrefl and M. Albrecht. *Magnetization reversal in a novel gradient nanomaterial.* Physical Review Letters, 96(7), 1 (2006).

[USK16] Ueltzhöffer, T., R. Streubel, I. Koch, D. Holzinger, D. Makarov, O. G. Schmidt and A. Ehresmann. *Magnetically Patterned Rolled-Up Exchange Bias Tubes: A Paternoster for Superparamagnetic Beads.* ACS Nano, 10(9), 8491 (2016).

[VFP16] Van De Wiele, B., S. Fin, M. Pancaldi, P. Vavassori, A. Sarella and D. Bisero. *Magnetization reversal in magnetic dot arrays: Nearest-neighbor interactions and global configurational anisotropy.* Journal of Applied Physics, 119(20) (2016).

[VFS14] Van De Wiele, B., S. Fin, A. Sarella, P. Vavassori and D. Bisero. *How finite sample dimensions affect the reversal process of magnetic dot arrays.* Applied Physics Letters, 105(16) (2014).

[VFT05] Vopsaroiu, M., G. V. Fernandez, M. J. Thwaites, J. Anguita, P. J. Grundy and K. O'Grady. *Deposition of poly crystalline thin films with controlled grain size.* Journal of Physics D: Applied Physics, 38(3), 490 (2005).

[VGG05] Vopsaroiu, M., M. Georgieva, P. J. Grundy, G. Vallejo Fernandez, S. Manzoor, M. J. Thwaites and K. O'Grady. *Preparation of high moment CoFe films with controlled grain size and coercivity.* Journal of Applied Physics, 97(10), 2003 (2005).

[Vid] *Video Spot Tracker, CISMM at UNC-CH.* `https://cismm.web.unc.edu/resources/software-manuals/video-spot-tracker-manual/`. Accessed: 2022-01-25.

[VKB06] Vaz, C. A., M. Kläui, J. A. Bland, L. J. Heyderman, C. David and F. Nolting. *Fundamental magnetic states of disk and ring elements.* Nuclear Instruments and Methods in Physics Research, Section B: Beam Interactions with Materials and Atoms, 246(1), 13 (2006).

[VKM19] Volkov, O. M., F. Kronast, I. Mönch, M.-a. Mawass, A. Kákay, J. Fassbender and D. Makarov. *Experimental and Theoretical Study of Curvature Effects in Parabolic Nanostripes.* Phys. Status Solidi RRL, 1800309, 1 (2019).

[VNA16] Vojkovic, S., A. S. Nunez, D. Altbir and V. L. Carvalho-Santos. *Magnetization ground state and reversal modes of magnetic nanotori.* Journal of Applied Physics, 120(3) (2016).

[VSF17] Velten, S., R. Streubel, A. Farhan, N. Kent, M. Y. Im, A. Scholl, S. Dhuey, C. Behncke, G. Meier and P. Fischer. *Vortex circulation patterns in planar microdisk arrays.* Applied Physics Letters, 110(26), 1 (2017).

[VZM04] Vavassori, P., N. Zaluzec, V. Metlushko, V. Novosad, B. Ilic and M. Grimsditch. *Magnetization reversal via single and double vortex states in submicron Permalloy ellipses.* Physical Review B, 69(21), 3 (2004).

[WAA10] Weddemann, A., C. Albon, A. Auge, F. Wittbracht, P. Hedwig, D. Akemeier, K. Rott, D. Meißner, P. Jutzi and A. Hütten. *How to design magneto-based total analysis systems for biomedical applications.* Biosensors and Bioelectronics, 26(4), 1152 (2010).

[Was12] Waser, R. *Nanoelectronics and Information Technology - Advanced Electronic Materials and Novel Devices.* Wiley-VCH, 3 edition (2012).

[WHB18] Williams, G., M. Hunt, B. Boehm, A. May, M. Taverne, D. Ho, S. Giblin, D. Read, J. Rarity, R. Allenspach and S. Ladak. *Two-photon lithography for 3D magnetic nanostructure fabrication.* Nano Research, 11 (2018).

[WRB12] Weber, D. P., D. Rüffer, A. Buchter, F. Xue, E. Russo-Averchi, R. Huber, P. Berberich, J. Arbiol, A. Fontcuberta I Morral, D. Grundler and M. Poggio. *Cantilever magnetometry of individual Ni nanotubes.* Nano Letters, 12(12), 6139 (2012).

[WRZ10] Westphalen, A., A. Remhof and H. Zabel. *Magnetization reversal of microsized Fe elliptic rings.* Journal of Magnetism and Magnetic Materials, 322(5), 481 (2010).

[WSFX05] Wirix-Speetjens, R., W. Fyen, K. Xu, J. De Boeck and G. Borghs. *A force study of on-chip magnetic particle transport based on tapered conductors.* IEEE Transactions on Magnetics, 41(10), 4128 (2005).

[WWB02] Wachowiak, A., J. Wiebe, M. Bode, O. Pietzsch, M. Morgenstern and R. Wiesendanger. *Direct observation of internal spin structure of magnetic vortex cores.* Science, 298(5593), 577 (2002).

[WYW11] Wang, Y. X., N. N. Yang, M. B. Wei, Y. J. Zhang, H. B. Liu and J. H. Yang. *Enhanced exchange bias of isolated Co/CoO nanocaps.* Journal of Alloys and Compounds, 509(23), 6626 (2011).

[YAK12] Yan, M., C. Andreas, A. K'akay, F. Garc'ia-S'anchez and R. Hertel. *Chiral symmetry breaking and pair-creation mediated Walker breakdown in magnetic nanotubes.* Applied Physics Letters, 100(25), 252401 (2012).

[YAS21] Yang, J., C. Abert, D. Suess and S.-K. Kim. *Intrinsic DMI-free skyrmion formation and robust dynamic behaviors in magnetic hemispherical shells.* Scientific Reports, 11, 3886 (2021).

[YBG15] Yan, J., S. C. Bae and S. Granick. *Rotating crystals of magnetic Janus colloids.* Soft Matter, 11(1), 147 (2015).

[YES07] Yellen, B. B., R. M. Erb, H. S. Son, R. Hewlin and G. U. Lee. *Traveling wave magnetophoresis for high resolution chip based separations.* Lab on a Chip, 7, 1681 (2007).

[YKK04] Yoon, M., Y. Kim, Y. M. Kim, H. Yoon, V. Volkov, A. Avilov, Y. J. Park and I. W. Park. *Superparamagnetism of transition metal nanoparticles in conducting polymer film.* Journal of Magnetism and Magnetic Materials, 272-276(SUPPL. 1), 2003 (2004).

[YKS15] Yershov, K. V., V. P. Kravchuk, D. D. Sheka and Y. Gaididei. *Controllable vortex chirality switching on spherical shells.* Journal of Applied Physics, 117(8), 083908 (2015).

[YM05] Young, R. J. and M. V. Moore. *Dual-beam (FIB-SEM) systems techniques and automated applications* (2005).

[YSG16] Yi, Y., L. Sanchez, Y. Gao and Y. Yu. *Janus particles for biological imaging and sensing.* The Analyst, 141(12), 3526 (2016).

[ZWM09] Zhang, Y. J., Y. X. Wang, X. D. Meng, Y. Liu, X. Ding and J. H. Yang. *Exchange bias of NiO/FeNi ordered nanocaps on curved substrate.* Journal of Applied Physics, 105(8) (2009).

Appendix

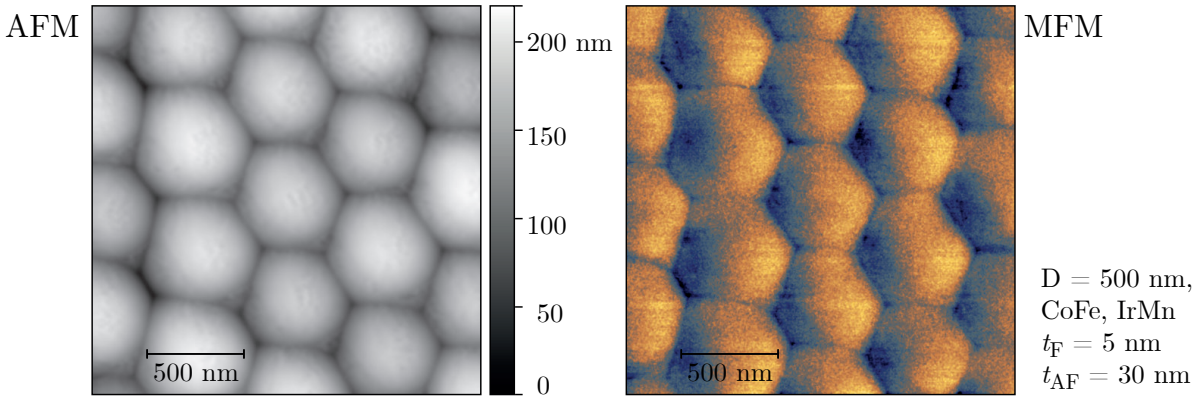

Figure 14.1: Exemplary images of the topography (left) and the magnetic charge contrast (right) of 'as made' EB capped particles with $D = 500\,\text{nm}$, $t_F = 5\,\text{nm}$ and $t_{AF} = 30\,\text{nm}$ measured at zero field (after positive saturation). The magnetic force microscopic (MFM) image on the right was recorded by tracing the atomic force microscopic (AFM) topography signal with a magnetic tip in a contouring manner (MFM scan relative tip height: 55 nm). Each cap exhibits a magnetic charge contrast which is characteristic for an onion state in which the magnetization follows the cap's curvature from left (dark) to right (bright). We have reported similar results for larger EB caps with $D = 1\,\mu\text{m}$, $t_F = 10\,\text{nm}$ and $t_{AF} = 30\,\text{nm}$ composed of the same materials.[TRH21] For the therein shown data, a thorough analysis and discussion can be found in the master thesis of this dissertation's author: *Physical Characterization and Motion Dynamics of Exchange-Biased Janus Particles* (2018).

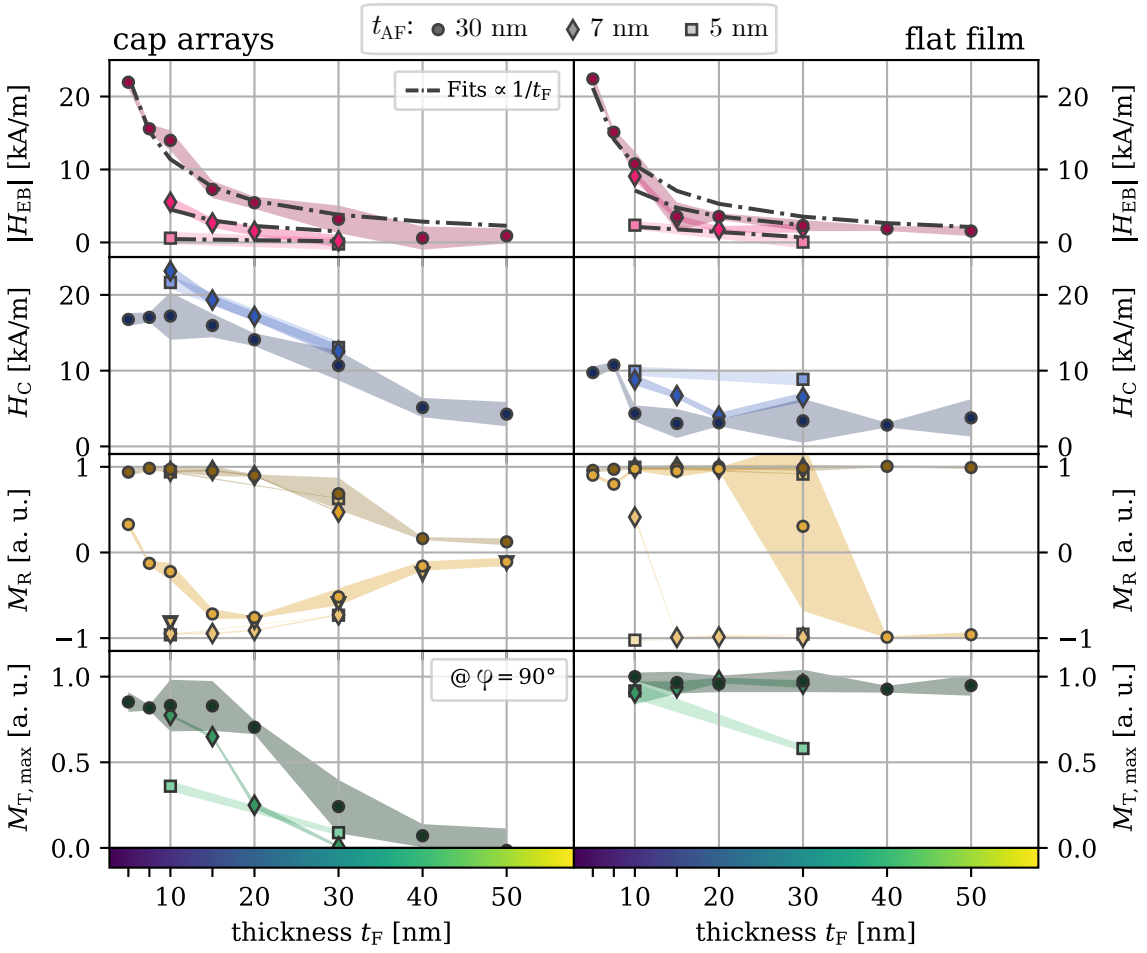

Figure 14.2: Summarized characteristics of the easy axis magnetization reversal ($\varphi = 0$) of both EB cap arrays and a flat bilayer in dependence on the ferromagnetic thickness t_F for a set of antiferromagnetic thicknesses t_{AF}: the absolute EB shift $|H_{EB}|$ (a., red), the coercivity H_C (b., blue) and the remanent longitudinal magnetization M_R with respect to the two hysteresis branches (c., ocker). Additionally, the maximum value of the transversal component $M_{T,max}$ at $\varphi = 90°$ is given (d., green). Fit functions $\propto 1/t_F$ are added in a. (gray dashed dotted lines).

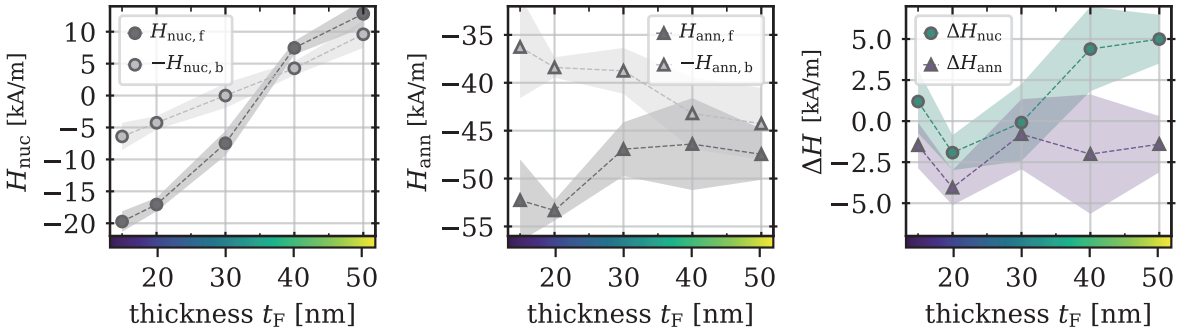

Figure 14.3: Characteristic fields of vortex reversing EB cap arrays with $t_{AF} = 30\,\text{nm}$ in dependence on the ferromagnetic thickness t_F: nucleation and annihilation fields H_{nuc} are shown for both branches of the easy axis hystereses ($\varphi = 0$). The dashed vertical line represents the transition from negative to positive values of H_{nuc} on the descending branch. In addition, ΔH_{nuc} and ΔH_{ann} were evaluated as quantities reflecting the reversal asymmetry. ΔH_{nuc} and ΔH_{ann} can be compared with the t_{AF} dependent study presented in Figure 10.12.

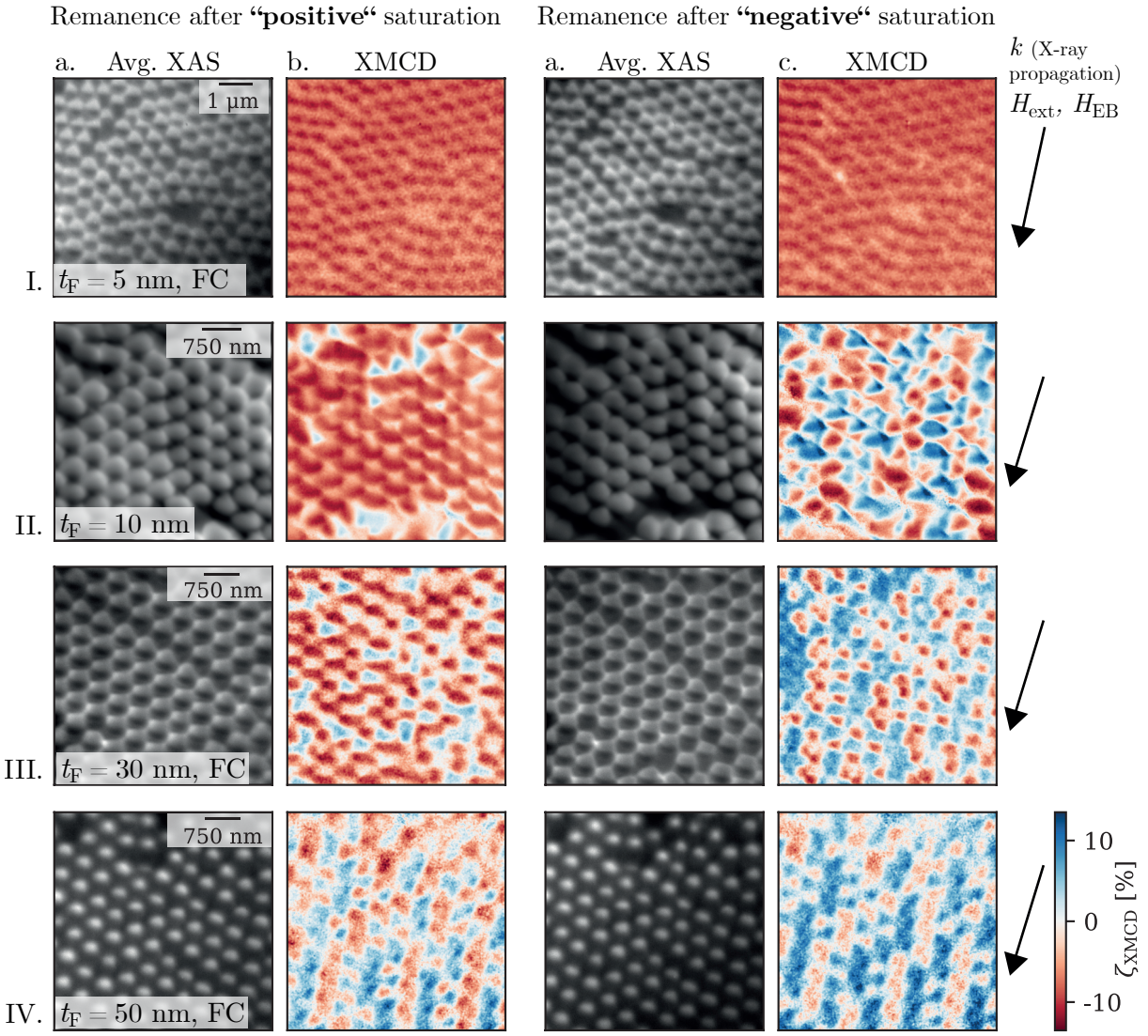

Figure 14.4: Summary of averaged PEEM images (a.,c.) and images of the XMCD asymmetry contrast (b., d.) for samples of EB capped particles ($D = 500\,\mathrm{nm}$) with varying thickness $t_\mathrm{F} = 5$, 10, 30 and 50 nm (I. to IV.). The arrow on the right of each row indicates the direction of the incident X-rays (and their k vector) as well as the direction of the applied magnetic fields. Columns a. and b. show images taken at zero magnetic field (remanence) after the caps have been exposed to the maximum positive magnetic field that can be applied to the sample holder. Images recorded after inverting the maximum magnetic field ('negative') are shown in columns c. and d.

Acknowledgements

At the end of this thesis, I would like to express my thanks to some important people who have supported me along the way.

First and foremost, my thanks go to my doctoral supervisor Prof. Dr. Arno Ehresmann for giving me the opportunity and the resources to research my topic in your group and eventually to do a PhD. Thank you for your support, which often went beyond the purely scientific. Furthermore, I would like to thank Prof. Dr. Manfred Albrecht for taking over the role as second examiner and Prof. Dr. Gustavo Pastor as well as Prof. Dr. Thomas Giesen for their participation in the examination board.

Besides the financial support by the Helmholtzzentrum Berlin, there are some people who made the success of the XMCD PEEM measurements at BESSY possible: A big thanks goes to Dr. Florian Kronast, Dr. Mohamad-Assaad Mawass, Nina Novakovic-Marinkovic, and Dr. Sergio Valencia Molina for excellent support on two beamtimes and to my colleagues from Kassel Rico Huhnstock, Maximilian Merkel, and Sapida Akhundzada for their commitment - day and night.

Moreover, I am very thankful for a great joint project with the Poggio Lab at the University of Basel. Simon Philipp, Dr. Boris Gross, Matthias Claus, Marc Sullinger, and Prof. Dr. Martino Poggio made it possible to get to know the individual Janus particle from a completely new perspective. Thanks for the great cooperation!

Studying the structural aspects of the particles further demanded expertise in microscopy techniques. Here, my special thanks go to Dr. Kai Arstila who performed HIM measurements with me on a Saturday afternoon at the university of Jyväskylä, and to Prof. Dr. Thomas Kusserow for cutting the particles in half and imaging them at the FIB-SEM in the Institute of Nanostructure Technologies and Analytics, INA. For clean room work in the INA, I furthermore received valuable support from Anita Friedrichsen, Dr. Annette Becker, Eireen Käkel and Florian Schnabel, thank you.

Besides the work on the magnetically capped particles, I also really enjoyed the project of biofunctionalized magnetic particle transport. Therefore, many thanks go to our collaborators in the biochemistry department at the university of Kassel, especially to Dr. Daniela Bertinetti and Prof. Dr. Friedrich Herberg. I also want to acknowledge Kristina Dingel and

Prof. Dr. Bernhard Sick for developing the powerful tracking software *AdaPT*. Most importantly, this project was only possible due to the dedicated and profound work of Hai Hoang and Özge Efendi for which I am truly grateful.

Scientific work today enormously depends on computer-based tools, and therefore I would like to thank all developers of freely available software, like *AdaPT*, *Boris Computational Spintronics*, *Gwyddion*, LaTeX, *Nmag*, *Python*, and *VideoSpotTracker*, but also each and everyone who contributes in the respective communities.

In order to conduct successful research in the home laboratories, also administrative and technical tasks arise: Here my thanks go to Andreas Nehls and Arne Schröder for contributing their technical know-how, and to Andrea Wecker who supports us in all bureaucratic matters. Last but not least, a research group only functions, as each PhD learns from their colleagues. I want to greatly acknowledge Dr. Alexander Gaul, Dr. André Knie, Dr. Dennis Holzinger, Dr. Henning Huckfeldt, Dr. Iris Koch, and Dr. Timo Ueltzhöffer for everything they taught us junior scientists about magnetism, good scientific practice and team work. In this context, I want to thank my closest companions and irreplaceable friends Rico Huhnstock and Maximilian Merkel for everything that we have mastered together in the last years!

Finally, I want to thank my parents who have always honestly and truly supported me with open ears, good advice and love on this scientific journey.